

Symmetry-Enhanced Hybrid Thermoacoustic Models of Annular and Can-Annular Combustors

Matthias Häringer

Vollständiger Abdruck der von der TUM School of Engineering and Design
der Technischen Universität München zur Erlangung des akademischen
Grades eines
Doktors der Ingenieurwissenschaften
genehmigten Dissertation.

Vorsitz:

Prof. Dr. Chiara Manfletti

Prüfende der Dissertation:

1. Prof. Wolfgang Polifke, Ph.D.
2. Prof. James R. Dawson, Ph.D.
3. Prof. Dr.-Ing. Andreas Huber

Die Dissertation wurde am 29.01.2024 bei der Technischen Universität München eingereicht
und durch die TUM School of Engineering and Design am 07.06.2024 angenommen.

Abstract

Thermoacoustic combustion instabilities (TCI) are a major concern in the development of gas turbine combustion systems. These instabilities lead to a growth of acoustic and heat release fluctuations, which eventually form a limit-cycle (LC) oscillation. Depending on the LC amplitude, TCI may impair the operational range or even cause structural damage to the combustor. Most modern gas turbines are equipped with annular or can-annular combustion systems, which comprise multiple identical sectors arranged equidistantly around the engine circumference. Due to their size and complexity, the numerical and experimental prediction of LC oscillations in these multi-burner configurations is particularly challenging.

This thesis exploits the symmetry of (can-)annular configurations to develop two types of models, which allow efficient prediction of LC oscillations. Both model types are hybrid in nature, resolving only one burner/flame zone using large-eddy simulation (LES). The remaining parts of the combustion system are represented as a low-order model (LOM). The first model directly exploits the particular eigenmode structure of systems with discrete rotational symmetry that follows from Bloch-wave theory. The computational domain is limited to one sector, and a symmetry condition accounts for the remaining parts of the system. The model can predict LC oscillations of an isolated mode order. To overcome the limitations of the assumed Bloch-symmetry, the second model explicitly resolves the remaining sectors in the LOM. The required LOMs of nonlinear flame dynamics are adapted during the simulation of the self-excited system to match the dynamics observed in the LES. This avoids the costly a priori identification of nonlinear flame models. Both model types are validated using a generic can-annular system and an annular test-rig and can predict LC oscillations with reasonable accuracy and at significantly reduced computational cost compared to established modeling frameworks.

The idea of limiting the computational domain to one single sector by employing symmetry conditions is also transferred to experimental single-can test-rigs. Based on Bloch-wave theory, this thesis proposes a strategy to tune the acoustic terminations of a single-can test-rig to experimentally investigate thermoacoustic properties of individual azimuthal mode orders of an entire can-annular combustion system. The developed strategy avoids the high experimental effort associated with using pressurized full can-annular test-rigs for thermoacoustic investigations.

Lastly, this thesis extends an existing method for calibrating global chemical reaction mechanisms based on the production rates of the major species in a detailed mechanism. The calibration focuses on correctly predicting flame dynamics. Calibrating global reaction mechanisms becomes increasingly important due to the growing use of fuel blends, for which reduced or global mechanisms are unavailable. This method lays the foundation for limiting the computational effort in predicting LC oscillations with the numerical tools developed by providing computationally efficient reaction mechanisms.

Kurzfassung

Thermoakustische Verbrennungsinstabilitäten (TCI) sind eine wesentliche Herausforderung bei der Entwicklung von Gasturbinenbrennkammern. Diese Instabilitäten führen zu einem Anwachsen von akustischen Fluktuationen und Wärmefreisetzungsschwankungen, die schließlich eine Grenzyklusschwingung (LC) entwickeln. Abhängig von der LC-Amplitude können TCI den Betriebsbereich beeinträchtigen oder sogar strukturelle Schäden an der Brennkammer verursachen. Die meisten modernen Gasturbinen sind mit annularen oder Can-annularen Verbrennungssystemen ausgestattet, welche eine Zahl an identischen Sektoren umfassen, die gleichverteilt um den Umfang der Gasturbine angeordnet sind. Aufgrund ihrer Größe und Komplexität ist die numerische und experimentelle Vorhersage von LC-Schwingungen in diesen Mehrbrennerkonfigurationen eine besondere Herausforderung.

In dieser Arbeit wird die Symmetrie dieser Systeme ausgenutzt, um zwei Arten von Modellen zu entwickeln, die eine effiziente Vorhersage von LC-Schwingungen ermöglichen. Beide Modelltypen lösen nur eine Brenner-/Flammenzone mittels Large-Eddy-Simulation (LES) auf und sind damit hybrider Natur. Die übrigen Teile des Verbrennungssystems werden als Modell niedriger Ordnung (LOM) dargestellt. Das erste Modell nutzt direkt die spezielle Eigenmodenstruktur von Systemen mit diskreter Rotationssymmetrie, die sich aus der Bloch-Wellen Theorie ergibt. Der Rechenbereich ist auf einen einzigen Sektor beschränkt und eine Symmetriebedingung berücksichtigt die übrigen Teile des Systems. Das entwickelte Modell kann LC-Schwingungen einer isolierten Modenordnung vorhersagen. Um die Einschränkungen der angenommenen Bloch-Symmetrie zu überwinden, löst das zweite Modell die verbleibenden Sektoren explizit im LOM auf. Die erforderlichen LOMs der nichtlinearen Flammendynamik werden während der Simulation des selbsterregten Systems so angepasst, dass sie die in der LES beobachtete Dynamik bestmöglich abbilden. Dies vermeidet die kostspielige a priori Identifikation von nichtlinearen Flammenmodellen. Beide Modelltypen werden anhand eines generischen Can-annularen Systems und eines annularen Prüfstands validiert und sind in der Lage, LC-Schwingungen mit angemessener Genauigkeit und mit deutlich geringeren Rechenkosten vorherzusagen, als dies bei etablierten Modellierungsansätzen der Fall ist.

Der Ansatz den Rechenbereich durch Symmetriebedingungen auf einen einzigen Sektor zu beschränken, wird auch auf experimentelle Can-annulare Testrigs übertragen. Basierend auf der Bloch-Wellen Theorie wird in dieser Arbeit eine Strategie zur Anpassung der akustischen Randbedingungen eines Einzel-Can-Prüfstandes vorgeschlagen, um die thermoakustischen Eigenschaften einzelner azimuthaler Modenordnungen eines kompletten Can-annularen Brennkammersystems experimentell zu untersuchen. Die entwickelte Strategie vermeidet den hohen experimentellen Aufwand, der mit der Verwendung eines druckbeaufschlagten, vollen Can-annularen Prüfstandes für thermoakustische Untersuchungen verbunden ist.

Schließlich erweitert diese Arbeit eine bestehende Methode zur Kalibrierung globaler chemischer Reaktionsmechanismen basierend auf den Produktionsraten der wichtigsten Spezies in einem detaillierten Mechanismus. Ein wesentliches Ziel der Kalibrierung ist die korrekte Vorhersage der Flammendynamik. Die Kalibrierung globaler Reaktionsmechanismen wird aufgrund der zunehmenden Verwendung von Brennstoffmischungen, für die keine reduzierten oder globalen Mechanismen verfügbar sind, immer wichtiger. Durch die Bereitstellung recheneffizienter Reaktionsmechanismen legt diese Methode den Grundstein für die Begrenzung des Rechenaufwands bei der Vorhersage von LC-Schwingungen mit den entwickelten numerischen Werkzeugen.

Vorwort

Diese Arbeit entstand hauptsächlich während meiner Zeit an der Professur für Thermofluid-dynamik. Zuvorderst gilt mein Dank meinem Doktorvater Professor Wolfgang Polifke. Du warst mir mit deiner offenen, menschlichen Art, deiner tiefen Fachkenntnis und deinem ehrlichen Interesse an der Forschung stets ein Vorbild. Du gabst mir jederzeit die Freiheiten auch unkonventionelle Ansätze zu verfolgen und hast es aber trotzdem verstanden meine Forschung in die richtigen Bahnen zu lenken. Es liegt maßgeblich an deiner Leitung, dass am Institut eine kollegiale und konstruktive Arbeitsatmosphäre herrscht, die mich immer gerne an die Promotionszeit zurückdenken lässt.

Für die gute Atmosphäre waren natürlich noch weitere Personen verantwortlich. Ich bin dankbar für all die klugen und spannenden Menschen, die ich während meiner Zeit am Institut kennenlernen durfte. Trotzdem will ich einige Personen hervorheben, die meine Zeit am Lehrstuhl besonders geprägt haben. Da ist zuallererst meine wunderbare Bürokollegin Feli. Du hast mich durch die Höhen und Tiefen einer Promotion, sowie durch den Stress vor Paper-Deadlines begleitet. Gemeinsam mit euch, Gerrit und Thomas, kam der Spaß am Doktorandendasein nie zu kurz (auch wenn es mit der Bar aufd' Nacht leider nichts geworden ist). Lieber Guillaume und Abdulla, ich habe die tiefgründigen Gespräche mit euch sehr genossen und bin froh, dass ihr mir immer mit eurem Rat zur Seite standet. Dir Moritz, und der gesamten Fußballer- und Sportler-Truppe, danke ich für die sportlichen, der Brotzeitgruppe für die kulinarischen Höhepunkte jeder Woche.

Ohne die Unterstützung meiner Eltern, die mir mein Studium ermöglicht haben, hätte diese Arbeit nicht entstehen können. Ihr seid für mich da wenn ich euch brauche und lasst mich ansonsten einfach machen. Dafür bin ich euch zutiefst dankbar.

Zu guter Letzt, der Dank an meine Partnerin Maria. Du bist und warst mein Anker und hast mir jederzeit den Rücken frei gehalten, auch wenn du oft selbst dafür zurückstecken musstest. Ohne deinen unermüdlichen Einsatz, vor allem auch in der letzten Phase dieser Arbeit, wäre das alles nicht möglich gewesen. Ich danke dir von Herzen.

Miriam, mein Sonnenschein, danke, dass es dich gibt.

Acknowledgment

The financial support from the Research Association for Combustion Engines (Forschungsvereinigung Verbrennungskraftmaschinen e. V. – FVV, project number: 6012700) is gratefully acknowledged. The author gratefully acknowledges the computational and data resources provided by the Leibniz Supercomputing Centre (www.lrz.de).

The contribution of Alexander Eder, who set up and run the LES simulation for the identification of the FTF of the annular test-rig (see Sec. 5.3.2.3), is gratefully acknowledged.

Acknowledgment

Contents

1	Introduction	1
2	Governing Equations	5
2.1	Reactive Flow Equations	5
2.2	Linear Acoustics	6
3	Hybrid CFD/LOM Modeling of (Can-)Annular Configurations	9
3.1	On the Need for a Symmetry-Enhanced Hybrid Model	9
3.2	Thermoacoustics of (Can-)Annular Combustors	11
3.2.1	General Characteristics	11
3.2.2	Consequences of Symmetry on Thermoacoustic Mode Structure	14
3.2.2.1	Bloch-Wave Theory	14
3.2.2.2	Equivalent Reflection Coefficient	16
3.3	Strategies to Couple CFD and LOM	17
3.3.1	State-Space Modeling of Acoustic Systems	17
3.3.1.1	Relation to Linear ODE	18
3.3.1.2	Relation to Transfer Function	18
3.3.1.3	Relation to Discretized PDE	19
3.3.2	Theory of Characteristic-Based State-Space Boundary Conditions	20
3.3.2.1	Navier-Stokes Characteristic Boundary Conditions	20
3.3.2.2	Locally One-Dimensional Inviscid Relations	21
3.3.2.3	Characteristic-Based State-Space Boundary Conditions	23
3.3.3	Low-Mach v' - Q' Coupling	24
3.3.4	Selection of the Coupling Framework	25
3.4	Hybrid Model Architectures	25
3.4.1	Time domain Bloch-Wave Approach	25
3.4.2	ROLEX Model	27
3.5	Flame Modeling	29
3.5.1	Coupling Nonlinear Flame Models and Acoustic LOM	30
3.5.2	Model Structure and Online Parameter Identification	30
3.6	Application of the Proposed Hybrid Models	33
4	Calibrating Global Reaction Mechanisms	37
5	Investigated Validation Cases	41
5.1	Numerical Setup	41
5.1.1	Solver and Setup for Laminar Cases	41

5.1.2	LES Solver and Numerical Setup	42
5.2	Generic Laminar 4-Burner System	43
5.2.1	Case Setup	43
5.2.2	Hybrid Model Results	45
5.3	NTNU Annular Rig	47
5.3.1	Case Setup	47
5.3.2	Results	48
5.3.2.1	Single-Sector LES	48
5.3.2.2	Low-Order Model	50
5.3.2.3	Identification of Linear Flame Dynamics	51
5.3.2.4	Hybrid Model Results	51
6	Contextualization and Discussion of Publications	57
6.1	Numerical Limit Cycle Prediction in (Can-)Annular Configurations	57
6.1.1	Overview of Nonlinear Flame Models	57
6.1.2	Discussion of Available Thermoacoustic Model Setups	60
6.2	Thermoacoustic Tuning of Single-Can Test-Rigs	63
6.3	Calibrating Global Reaction Mechanisms	63
7	Summary of Papers	65
7.1	Time Domain Bloch Boundary Conditions for Efficient Simulation of Thermoacoustic Limit-Cycles in (Can-)Annular Combustors	66
7.2	Hybrid CFD/Low-Order Modeling of Thermoacoustic Limit Cycle Oscillations in Can-Annular Configurations	67
7.3	A Strategy to Tune Acoustic Terminations of Single-Can Test-Rigs to Mimic Thermoacoustic Behavior of a Full Engine	68
7.4	Large Eddy Simulation of the Dynamics of Lean Premixed Flames Using Global Reaction Mechanisms Calibrated for CH ₄ -H ₂ Fuel Blends	69
8	Conclusion and Outlook	71
	Bibliography	72
	List of Figures	85
	Appendices	
.1	PAPER_BLOCH	93
.2	PAPER_ROLEX	103
.3	PAPER_TESTRIG	113
.4	PAPER_MECH	124

1 Introduction

According to the “Paris Agreement”, the members of the United Nations aim at “*holding the increase in the global average temperature to well below 2°C above pre-industrial levels and pursuing efforts to limit the temperature increase to 1.5°C above pre-industrial levels*” [1]. Achieving this goal requires a fundamental transformation of our lifestyle, the economy, and especially how we satisfy our energy demands. Within subsequent decades, renewable sources such as wind and solar energy must substitute essentially all fossil power plants. Due to their fluctuating nature, these renewable sources must be supplemented with long-term and large-scale energy storage systems, which, however, are not expected to be available in time with the required capacities. Due to their quick-start ability, wide operational range, and their - relative to other fossil power plants - low specific CO₂ emissions, gas turbine power plants may serve as an interim solution to compensate for the fluctuating supply from renewable sources [2]. In the long run, energy storage by “Power-to-Gas” technologies necessitates gas turbine power plants to convert chemically stored energy to electrical energy [3, 4].

Modern land-based gas turbines are typically equipped with lean premixed combustors [5–7]. These lean systems feature very low NO_x emission levels, which comply with strict regulations but are prone to thermoacoustic combustion instabilities (TCI) [8]. These instabilities emerge from constructive feedback of unsteady heat release and the acoustics of the combustion system and result in a growth of acoustic and heat release fluctuations. Eventually, nonlinear phenomena of flame dynamics saturate this growth and lead to the formation of a limit cycle (LC) oscillation. Depending on the amplitudes, these LC oscillations may impair combustion performance or even cause structural damage to the combustor. To assess the impact of TCI, it is desirable to predict the stability and LC amplitude already in the design phase of a combustor.

Most combustion systems for land-based and aircraft gas turbines are of annular or can-annular type. The high practical relevance of these combustor types leads to growing interest in the scientific community, reflected by an increasing number of multi-can [9–16] and annular [17–22] test-rigs. The characteristic feature of these systems is that they comprise multiple individual burners, which are arranged equidistantly around the circumference of the engine and are coupled acoustically [23–25]. Therefore, the individual burners can interact, and the complete configuration gives rise to azimuthal modes extending over all burners around the circumference [10, 26, 27]. Due to the coupling of the individual sectors in (can-)annular configurations, it is not possible to model TCI by considering only one sector without further means [28–30].

Modeling TCI in (can-)annular configurations is particularly challenging because of their complexity and sheer size. Hitherto, several methods have been developed to predict stability properties and LC amplitudes of such systems. They range from simplified (semi-)analytical treatment [31–33] and acoustic network models [34–36] over linearized conservation equations as the inhomogeneous Helmholtz equation [37] to high fidelity LES simulations solving the complete set of nonlinear governing equations [38–42]. The latter inherently include nonlin-

ear flame-flow interaction and nonlinear flame dynamics, thus accounting for the formation of LC oscillations. However, the computational cost to simulate a complete applied configuration using high fidelity LES is tremendous [39], which inhibits its widespread use in the industrial development process.

In contrast, (semi-)analytical and reduced-order methods are crucial to gain fundamental understanding but can often not represent the complexity of real systems. To predict LC oscillations, these methods typically rely on data-driven models of the nonlinear flame dynamics, which are costly to determine or even not available at all [43]. A common approach to model nonlinear flame dynamics is the *flame describing function* (FDF) [44, 45], which is an amplitude-dependent extension of the linear *flame transfer function* (FTF). However, the FDF is costly to determine for practical configurations [46], and its “*weakly nonlinear*” approach lacks essential nonlinear features, such as mode interaction and the generation of higher harmonics [47]. Artificial Neural Networks (ANN) recently showed promising results in reproducing nonlinear flame dynamics [43, 48–50]. However, training ANNs requires relatively long time series, which are costly to produce. Additionally, these models suffer from poor predictive capability if used outside the range of training data [50].

Hybrid models offer a powerful alternative to the above-mentioned modeling strategies. These model types combine two or more sub-models, typically with differing levels of fidelity. They are particularly efficient for multi-scale and multi-physics problems such as TCI. The principal idea is to employ high-fidelity models only where necessary and represent the remaining system by computationally efficient models of lower fidelity. In the context of TCI, a high-fidelity CFD simulation may resolve the small turbulent and chemical scales relevant in the vicinity of the flame. The CFD may be coupled to a (low-order) acoustic model, solving for the large acoustic scales in the entire combustion system. Numerous implementations of said strategy are found in the literature [51–58].

Recent studies [59, 60] employ Bloch-wave theory [61] to exploit the symmetry properties of the considered annular and can-annular multi-burner systems to efficiently model TCI by limiting the computational domain to one single sector of the complete configuration. However, these models rely on (possibly nonlinear) data-driven flame models with the drawbacks mentioned above. The present thesis brings together hybrid modeling and symmetry considerations to combine the advantages of both approaches.

Three publications constitute the core of this cumulative thesis: In PAPER_BLOCH [29] (reproduced in App. .1), we combine the hybrid modeling framework developed by Jaensch *et al.* [58] with the Bloch-wave approach to form hybrid nonlinear time domain models of (can-)annular combustors. Based on the same symmetry considerations, in PAPER_TESTRIG [30] (reproduced in App. .3), we propose a strategy to utilize single-can test-rigs for representing thermoacoustics of a full can-annular combustor. Although very powerful, the Bloch-wave approach is subject to severe restrictions, which are not always met in practice. The third publication PAPER_ROLEX [62] (reproduced in App. .2) proposes a more generally applicable hybrid model for (can-)annular combustors: a CFD simulation (LES) of one burner segment or flame zone is coupled to a low-order model (LOM) of the remaining system. By exploiting the system’s symmetry, the coupled low-order nonlinear flame models are adapted *on the fly*, based on the flame dynamics observed in the CFD simulation. Figure 1.1 illustrates the gist of the two numerical modeling approaches developed within the thesis.

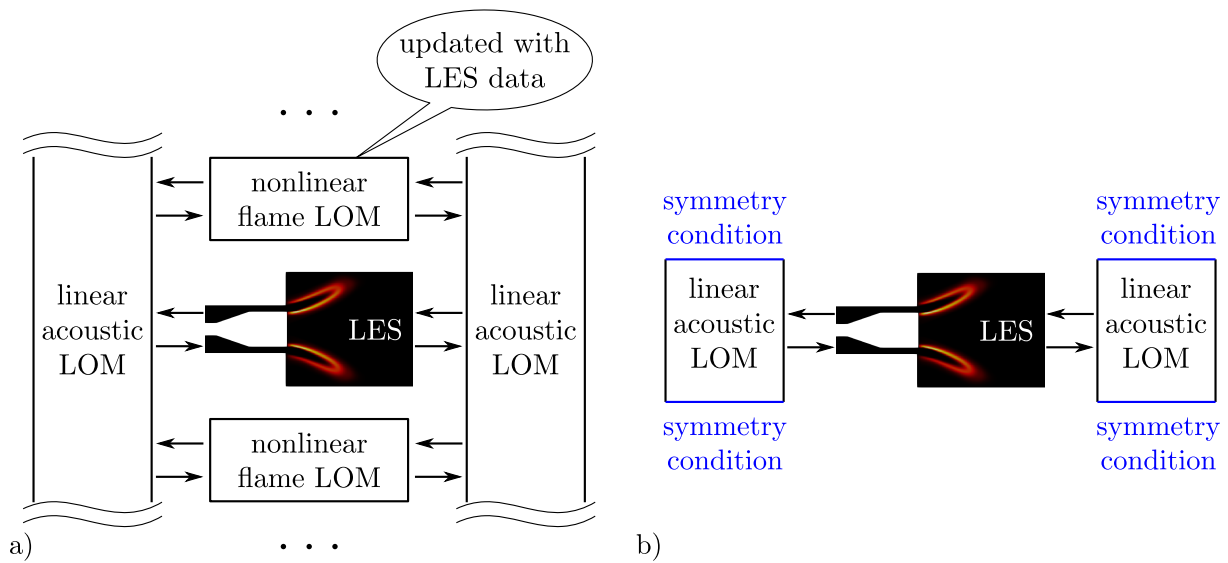


Figure 1.1: Hybrid models developed within this thesis: a) CFD simulation (LES) of one burner/flame zone coupled to a LOM of the remaining system. Nonlinear flame models are adapted on the fly according to the dynamics observed in LES. b) LES of one burner/flame zone coupled to a LOM including symmetry conditions.

The fourth publication PAPER_MECH [63] included in App. .4 extends a method for calibrating global chemical reaction mechanisms with particular attention to a correct representation of flame dynamics. The method presented there provides a crucial ingredient for an accurate and efficient reactive LES and thus lays the foundation for the application of the numerical models developed in PAPER_BLOCH and PAPER_ROLEX.

The remainder of this thesis guides through these four publications and aims to link their developments to each other and to the existing literature (see Chpt. 6). After presenting the fundamental governing equations in Chpt. 2, the characteristics of (can)-annular systems and the theory behind the hybrid modeling of these configurations is reviewed in Chpt. 3. This chapter also introduces the basic concepts of the hybrid modeling strategies developed. Chapter 4 discusses the method employed for calibrating global reaction mechanisms. Chapter 5 presents unpublished results of applying the hybrid models developed to a can-annular and an annular test-rig.

2 Governing Equations

2.1 Reactive Flow Equations

The compressible reactive flow equations are the basic governing equations in thermoacoustics. They comprise conservation of mass (2.1), momentum (2.2), energy (2.3), and species (2.4), which describe the change of fluid composition due to chemical reactions [64]. The ideal gas law (2.5) links pressure p with temperature T and density ρ via the specific gas constant $R = \mathcal{R}/M$, where $\mathcal{R} = 8.314\text{J/molK}$ is the universal gas constant and M is the molar mass of the gas mixture.

$$\frac{\partial \rho}{\partial t} + \nabla \cdot (\rho \mathbf{u}) = 0 \quad (2.1)$$

$$\frac{\partial (\rho \mathbf{u})}{\partial t} + \nabla \cdot (\rho \mathbf{u} \mathbf{u}) = -\nabla p + \nabla \cdot \left(\mu \left[\nabla \mathbf{u} + (\nabla \mathbf{u})^T - \frac{2}{3} (\nabla \cdot \mathbf{u}) \mathbf{I} \right] \right) \quad (2.2)$$

$$\frac{\partial (\rho h)}{\partial t} + \nabla \cdot (\rho \mathbf{u} h) = \frac{\partial p}{\partial t} + \nabla \cdot (\alpha \nabla h) + \omega_q \quad (2.3)$$

$$\frac{\partial (\rho Y_i)}{\partial t} + \nabla \cdot (\rho \mathbf{u} Y_i) = \nabla \cdot (D_i \nabla Y_i) + \omega_i \quad (2.4)$$

$$p = \rho R T, \quad (2.5)$$

Equations (2.1)-(2.4) assume Fick's and Fourier's law for mass and heat diffusion and Newton's law of viscosity. Species transport due to temperature gradients (Soret effect) is neglected. The energy equation (2.3) neglects contributions from mechanical work and the heat flux resulting from diffusion of species with different enthalpy. ω_q is the only volumetric heat source considered and results from chemical reactions. \mathbf{u} is the velocity vector, h the specific enthalpy, t is time, μ is the dynamic viscosity, α is the thermal diffusivity, \mathbf{I} is the identity tensor. Y_i is the mass fraction and D_i the diffusion coefficient of species i in the mixture. The production rate ω_i of species i is obtained from solving a chemical reaction mechanism. Details about the reaction mechanisms employed are found in Chpt. 4, in Sec. 5.1, and the PAPER_MECH reproduced in App. 4.

Equations (2.1)-(2.5) inherently include the generation and propagation of acoustic waves. This complicates their numerical solution. In case acoustic waves are not of interest and the Mach number is sufficiently small ($\text{Ma} < 0.3$, which is typically fulfilled in gas turbine combustors), the set of equations (2.1)-(2.3) can be simplified. In the low-Mach number formulation [65], the pressure p is split into a dynamic p_d and a thermodynamic p_t part. The spatial variation of p_t is negligible for small Mach numbers. Assuming constant ambient pressure $p_{t,\infty} = \text{const.}$, the thermodynamic part of the pressure is uniform in space $\nabla p_t \approx 0$ and constant in time $\partial p_t / \partial t = 0$ in the entire domain. Only the thermodynamic part is relevant in the energy equation and the

ideal gas law. The governing equations in low-Mach formulation write

$$\frac{\partial \rho}{\partial t} + \nabla \cdot (\rho \mathbf{u}) = 0 \quad (2.6)$$

$$\frac{\partial(\rho \mathbf{u})}{\partial t} + \nabla \cdot (\rho \mathbf{u} \mathbf{u}) = -\nabla p_d + \nabla \cdot \left(\mu \left[\nabla \mathbf{u} + (\nabla \mathbf{u})^T - \frac{2}{3} (\nabla \cdot \mathbf{u}) \mathbf{I} \right] \right) \quad (2.7)$$

$$\frac{\partial(\rho h)}{\partial t} + \nabla \cdot (\rho \mathbf{u} h) = \nabla \cdot (\alpha \nabla h) + \omega_q \quad (2.8)$$

$$\frac{\partial(\rho Y_i)}{\partial t} + \nabla \cdot (\rho \mathbf{u} Y_i) = \nabla \cdot (D_i \nabla Y_i) + \omega_i \quad (2.9)$$

$$p_t = \rho R T. \quad (2.10)$$

Note that in equations (2.6)-(2.10) the density still depends on the non-constant temperature, and thus, the material derivative of density is generally $\frac{D\rho}{Dt} \neq 0$.

The low-Mach formulation generally permits a much larger time step Δt for the numerical solution. The Courant number $Co = |\mathbf{u}| \Delta t / \Delta x$, which governs the time step, is related to the flow velocity. In the compressible formulation (2.1)-(2.5) the Courant number $Co = (c + |\mathbf{u}|) \Delta t / \Delta x$ is related to the speed of sound c , which is usually one order of magnitude larger than $|\mathbf{u}|$ [65]. Additionally, the low-Mach formulation avoids the use of sophisticated boundary conditions, which are necessary for the correct treatment of acoustic waves [66] (see Sec. 3.3.2). However, the low-Mach formulation alone can not represent TCI, as it misses the acoustic feedback.

2.2 Linear Acoustics

The considerations below follow the representation in [67] and are intended to give a brief overview. A detailed introduction into acoustics is found, e.g., in [68]. The acoustic governing equations are derived starting from the compressible conservation equations of mass (2.1), momentum (2.2), and energy (2.3) of a fluid with fixed composition (no species equations, $\omega_q = 0$). Linear acoustics describe small perturbations q' of flow quantities $q = \bar{q} + q'$ around a reference value \bar{q} . Acoustic perturbations are assumed to be isentropic, which eliminates the diffusive terms in the energy and momentum equation. Inserting the ansatz $q = \bar{q} + q'$ into the governing equations and neglecting higher order terms as well as gradients in the mean flow yields for mass and inviscid momentum conservation:

$$\frac{\partial \rho'}{\partial t} + \bar{\mathbf{u}} \cdot \nabla \rho' + \bar{\rho} \nabla \cdot \mathbf{u}' = 0 \quad (2.11)$$

$$\bar{\rho} \left(\frac{\partial \mathbf{u}'}{\partial t} + \bar{\mathbf{u}} \cdot (\nabla \cdot \mathbf{u}') \right) + \nabla p' = 0. \quad (2.12)$$

With the assumption of isentropic fluctuations, the pressure and density fluctuation are linked

$$p' = \frac{\partial p}{\partial \rho} \Big|_s \rho' = c^2 \rho' \quad (2.13)$$

via the speed of sound $c = \sqrt{\gamma R \bar{T}}$, where $\gamma = c_p / c_v$ denotes the ratio of isobaric and isochoric heat capacity.

Combining Eqs. (2.11),(2.12), and (2.13) yields the acoustic wave equation

$$\left(\frac{\partial}{\partial t} + \bar{\mathbf{u}} \cdot \nabla\right)^2 p' - c^2 \nabla^2 p' = 0. \quad (2.14)$$

Assuming planar one-dimensional wave propagation, the acoustic Riemann invariants

$$f = \frac{1}{2} \left(\frac{p'}{\bar{\rho}c} + u' \right) \quad (2.15)$$

$$g = \frac{1}{2} \left(\frac{p'}{\bar{\rho}c} - u' \right) \quad (2.16)$$

are a solution of the wave equation (2.14). They describe characteristic waves traveling upstream and downstream with a propagation speed $c \pm u$, respectively. The acoustic pressure and velocity fluctuations are retrieved from reverting Eqs. (2.15),(2.16):

$$\frac{p'}{\bar{\rho}c} = f + g \quad (2.17)$$

$$u' = f - g. \quad (2.18)$$

Acoustic boundary conditions can be characterized by a complex-valued, frequency-dependent reflection coefficient $R(s)$. It relates the amplitude and phase of the reflected wave to the incident wave. The reflection coefficient at the upstream R_u and downstream R_d side is defined as

$$R_u(s) = \frac{\hat{f}}{\hat{g}} \quad (2.19)$$

$$R_d(s) = \frac{\hat{g}}{\hat{f}}, \quad (2.20)$$

where $\hat{(\cdot)}$ denotes the Laplace transform and $s = \sigma + i\omega$ is the Laplace variable with the growth-rate σ and the angular frequency ω .

3 Hybrid CFD/LOM Modeling of (Can-)Annular Configurations

3.1 On the Need for a Symmetry-Enhanced Hybrid Model

The prohibitive computational cost of compressible reactive LES simulations of typical thermoacoustic systems promotes the use of reduced-order (ROM) or low-order models (LOM)¹. A wide variety of LOMs are commonly employed: On one side of the spectrum are network models, which combine and interconnect analytical [31, 32, 69, 70] or numerical [71, 72] solutions of simple elements to represent the actual system in idealized form. On the other side are 3D acoustic solvers, based on the acoustic Helmholtz-Equation [37, 73] or the linearized Euler (LEE) [74] or Navier-Stokes Equations (LNSE) [75–77]. All these models are based on simplifications of the governing equations Eqs. (2.1)-(2.5) and thus contain unclosed terms. These terms arise, most importantly, from the heat release fluctuation resulting from flow-flame-flow feedback (“*flame dynamics*”), but possibly also from other phenomena such as the generation and dissipation of acoustic energy from acoustic-hydrodynamic interaction. The closure models employed range from simple analytical or empirical relations (common for acoustic losses [78]) to separate more or less complex sub-models.

As flame dynamics are decisive for the thermoacoustic characteristics of a system, the flame requires a more sophisticated treatment by a separate sub-model to achieve quantitative accuracy. Coupling a sub-model of flame dynamics with an acoustic LOM constitutes a hybrid thermoacoustic model. A wide variety of flame models are used, depending on the objective of the specific study (see Sec. 6.1.1 for an overview).

The most sophisticated nonlinear flame model is a reactive LES simulation because it relies on the least model assumptions. If well set up, the LES simulation of the flame region is expected to closely resemble the “true” flame dynamics. No other flame model available shows the same level of accuracy, generality, and robustness (see Sec. 6.1.1). From this perspective, it is straightforward to directly couple an LES simulation of the flame region with a LOM representing the acoustics of the system considered. This thesis implements the two coupling strategies developed by Jaensch *et al.* [58]. Details about the two methods are found in Sec. 3.3. Both strategies proved to predict thermoacoustic limit-cycle (LC) oscillations at comparable accuracy to a compressible reactive LES of the entire combustion system. As the LES domain of the hybrid approaches is limited to the immediate vicinity of the flame, this accuracy can be achieved at drastically reduced computational cost compared to the full LES.

Even when applying the hybrid approach of Jaensch *et al.* [58], the computational cost of sim-

¹A LOM is built based on first principals, but with fewer degrees of freedom compared to a high fidelity model, whereas a ROM is generated by model order reduction of a high fidelity model

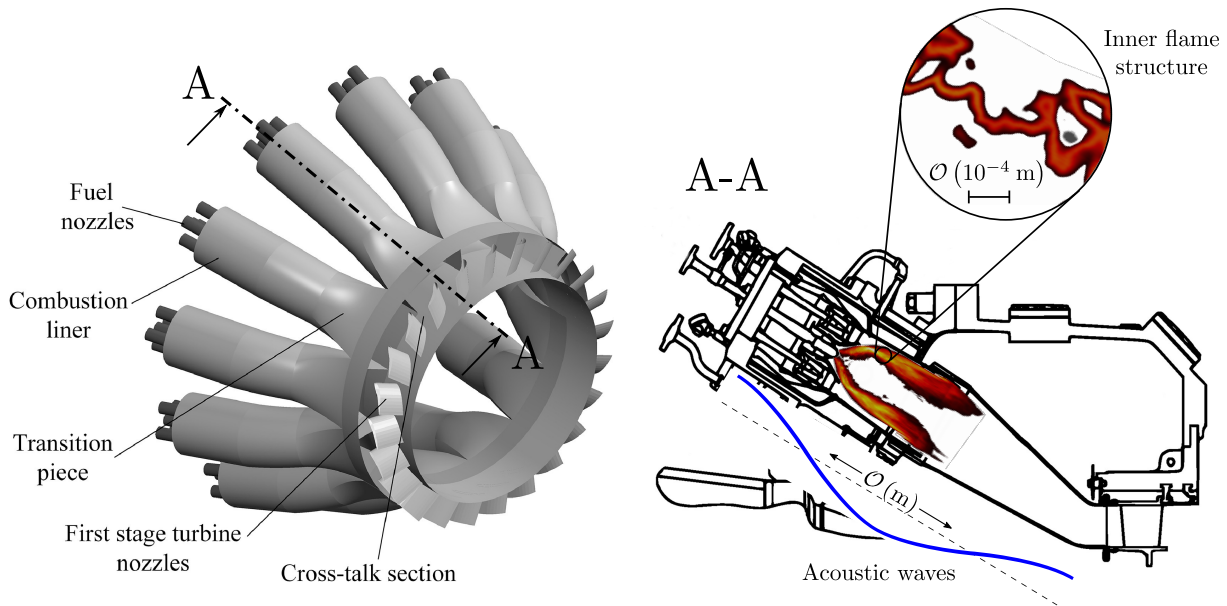


Figure 3.1: Dimensions of an applied can-annular combustor. The image on the left shows the assembly of the individual cans (adopted from [10]). The image on the right shows a cut-plane through one can, illustrating the relevant flame and acoustic length scales (adopted from [79]).

ulating LC oscillations of an entire annular or can-annular combustion system of applied relevance is tremendous. Firstly, this is because of the large volume of one burner/flame zone. In a large-size can-annular combustion system [6], the volume of one can is in the order of 0.1 m^3 . At the same time, the computational grid of the LES has to be sufficiently fine to resolve the thin reaction layer and the main turbulent structures. Depending on the operating condition, a cell edge length of less than 1 mm may be required in the flame region, resulting in up to 100 million computational cells for one single burner/flame. Secondly, a (can)-annular combustion system comprises multiple burners, typically between 12 and 30. Figure 3.1 illustrates the dimensions and the relevant thermoacoustic length scales for an applied can-annular system. Directly using the approach of Jaensch *et al.* [58] would mean resolving all cans by reactive LES and coupling them to an acoustic LOM of the remaining parts of the combustion system. Even though only the immediate burner/flame region has to be resolved in LES, the cell count would be in the order of billions. Such a simulation would be feasible (at least in the near future) but is considered not practicable in the design phase of a new combustor, which is characterized by small evolutionary changes in geometry and boundary conditions and thus requires frequent adaption of the simulation setup.

Can-annular and annular combustors comprise several nominally identical sectors. Due to the interactions between these sectors (see Sec. 3.2), it is impossible to model thermoacoustics of the entire configuration by considering only one sector/can without further means. Nevertheless, nominally identical sectors imply nominally identical flames and identical (nonlinear) dynamics. Although this does *not always* imply identical in-output behavior of each flame (see Sec. 3.2 for a detailed discussion), this symmetry property can be exploited to create more effi-

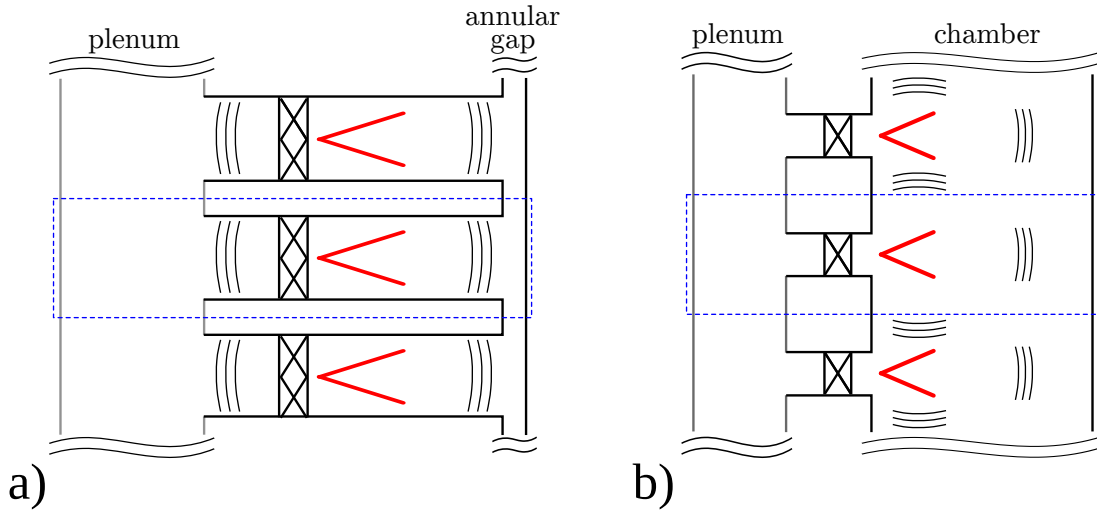


Figure 3.2: Sketch of a can-annular (left) and annular configuration (right). The blue box indicates one sector of the respective configuration.

cient hybrid models of (can)-annular combustors, where the LES domain is limited to one single burner/flame zone.

The following sections illustrate the specific thermoacoustic characteristics of annular and can-annular combustors and their implications on the hybrid, symmetry-enhanced modeling strategies developed within this thesis. The employed coupling strategies between LES and LOM are discussed, and all variants of the hybrid modeling framework for (can)-annular configurations developed within this thesis are presented. Finally, the individual steps necessary to simulate LC oscillations following the proposed strategies are summarized.

3.2 Thermoacoustics of (Can-)Annular Combustors

3.2.1 General Characteristics

Can-annular combustors are widely used in large-scale land-based gas turbines for power production. Almost any recent aero-engine gas turbine is equipped with an annular combustor. Both annular and can-annular combustors are multi-burner configurations, which comprise several nominally identical sectors - each containing one burner/flame zone - arranged around the circumference of an engine. Figure 3.2 schematically illustrates those two setups.

In annular configurations (see Fig. 3.2b)), the compressor outlet plenum feeds the individual injector tubes. The individual flames are located in one single chamber of annular shape terminated by the vanes of the first turbine stage. In real gas turbines, the flow through the vanes of the first turbine stage is choked or close to choked, depending on the operating point. Acoustically, this termination can be reasonably well approximated by a real-valued reflection coefficient $R \lesssim 1$ close to one [80]. In the scope of this thesis, any acoustic losses through the turbine are neglected, and an ideal closed-end acoustic boundary condition at the turbine inlet is assumed [81]. Due to the common chamber, the individual flames experience strong acoustic

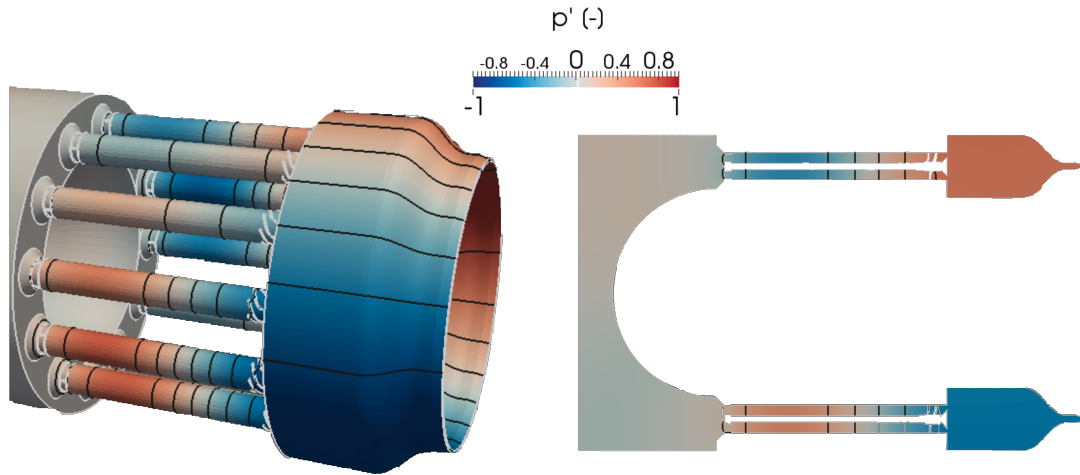


Figure 3.3: Acoustic pressure field for the first order azimuthal chamber mode of the annular test-rig considered within this thesis. Right side: cut-plane through center of the configuration (A. Ghani, personal communication, January 17th, 2019).

coupling. Additionally, coupling through the plenum may also be relevant. The difference in speed of sound in plenum (“cold” fresh gases) and chamber (hot burnt products) and possibly different radii leads to a separation in “*plenum modes*” and “*chamber modes*”, where most of the acoustic activity is found in the plenum or chamber, respectively, as well as “*mixed modes*”, where both participate equivalently [32].

The relatively large axial and radial dimension of the chamber results in a generally three-dimensional acoustic field. Formally, this is expressed by the acoustic Helmholtz number

$$\text{He} = \frac{\omega L}{c}, \quad (3.1)$$

where L is a characteristic length. If $\text{He} \ll 1$, a distance L is considered *acoustically compact* for the frequency ω , i.e., any gradient of the acoustic variables can be neglected across the distance L and the acoustic travel time is negligible. The axial and radial extent of a typical annular combustion chamber is *in general not* acoustically compact for all frequencies of interest², meaning that the radial and axial component of the acoustic field can *generally* not be neglected by the acoustic model employed. However, given the characteristic dimensions of annular combustors, the most relevant low-frequency modes can be well approximated by pure axial or azimuthal modes, reducing the complexity of the required acoustic model [32, 34, 37]. Figure 3.3 exemplifies such an approximately one-dimensional acoustic pressure field of the first-order azimuthal mode in the chamber of the annular test-rig considered in Sec. 5.3.

As the flames are not separated from each other by a solid structure, flame-flame interaction is possible [19, 82]. Moreover, the flames may react not only to axial velocity fluctuations u' in the injector tube but also to the transverse velocity fluctuation v' of the azimuthal component of the acoustic field in the chamber. Several studies (e.g., see [83, 84]) suggest that the contribution of transverse excitation to the overall heat release rate fluctuation is negligibly small. The leading term of the response of an axis-symmetric flame to v' is of second order, causing frequency

²The focus is on low to medium frequency TCI

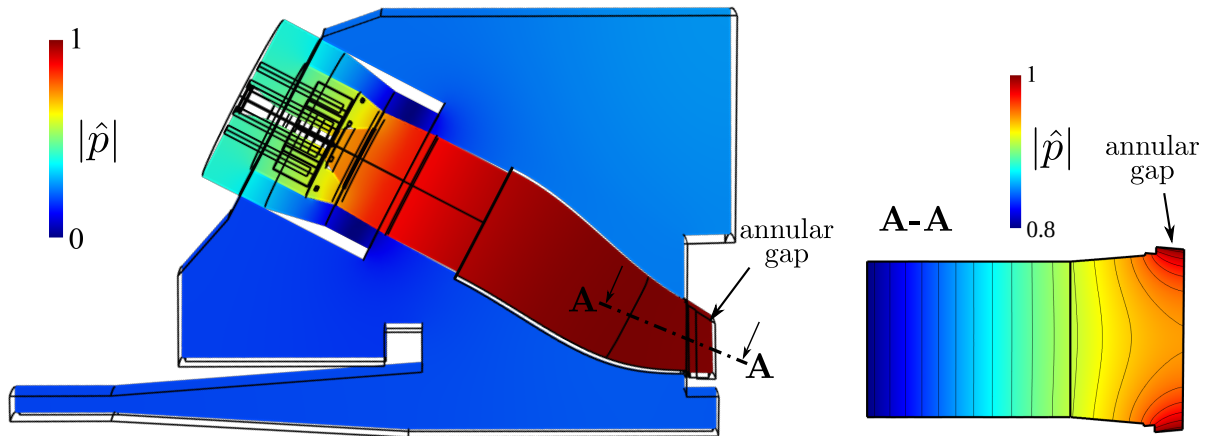


Figure 3.4: Acoustic pressure field for the first order azimuthal mode of the can-annular configuration considered in PAPER_TESTRIG. Left side: Mid cut-plane through can and plenum. Right side: Cut-plane through can in the vicinity of the annular gap (note the different limits of the color map).

doubling. However, unfavorable resonance conditions can lead to coupling with higher order modes and may result in significant amplitudes despite the overall weak flame response to v' [85]. In the scope of this thesis, transverse forcing is neglected but can be integrated into the modeling framework developed without essential difficulties.

In contrast to annular combustors, the individual flames in can-annular configurations are well separated, making any direct flame-flame interaction or transverse forcing impossible, at least for the considered low to intermediate frequency range. Nevertheless, the individual flames are coupled acoustically via the common compressor exit plenum feeding all cans and via a small cross-talk area in front of the turbine inlet, called annular gap. Typically, the vast area ratio between plenum and can inlet essentially decouples plenum and cans [6], resulting in secondary importance of can-can coupling via the plenum [30]. Though stronger than the coupling via the plenum, can-can coupling via the small annular gap is much weaker than the acoustic coupling of the individual flames in an annular combustor. This weak coupling, however, gives rise to azimuthal modes extending over the entire circumference and involving all cans simultaneously [26].

The cans are typically relatively long and narrow compared to the acoustic wavelengths in the frequency range considered. Formally, the acoustic Helmholtz number is very small $He \ll 1$ if the can diameter is considered as characteristic length L . This is typically not the case if the length of the can is considered as characteristic length. As seen in Fig. 3.4, the acoustic field within the cans is essentially one-dimensional and planar and similar to that of an isolated single can. In the vicinity of the annular gap, however, can-can coupling manifests itself by a generally 3-dimensional acoustic field with a dominant azimuthal component. These 2D/3D effects at the annular gap are commonly lumped into a Rayleigh conductivity [86] or a characteristic length of the annular gap [87] to represent them in a 1D acoustic model.

The relatively weak can-can coupling leads to a phenomenon called “*mode-clustering*” [28, 88]: From the perspective of a single can, the coupling with the neighboring cans via plenum and annular gap slightly affects the acoustic boundary conditions compared to an isolated single

can. The modes of various azimuthal orders introduced by this weak coupling have closely spaced frequencies and growth rates. They are generally close to the respective axial mode of an isolated single can. Mode clustering increases the likelihood of nonlinear interactions, such as synchronization between the modes of one cluster. Another result of the weak coupling is the phenomenon of *mode localization*, which means that a slight perturbation of the symmetry of the configuration may drastically affect the symmetry of the thermoacoustic mode shapes [89–91]. Both must be accounted for when developing a hybrid model for can-annular configurations.

Despite their differences, both annular and can-annular systems share the same topology and symmetry. In both systems, several individual burners/flames are coupled by a ring-shaped common connection at the upstream and downstream sides. Disregarding small geometrical features such as igniters or diagnostic systems, which are usually mounted only in specific sectors/cans, both systems feature a discrete rotational and possibly also reflectional symmetry. The latter may be broken in annular configurations in the presence of a significant mean flow in azimuthal direction [92, 93]. Effects of nonlinear flame dynamics may break both reflectional and rotational symmetry at high oscillation amplitudes [94–96]. The implications of symmetry and symmetry breaking on the modeling strategy proposed are discussed in detail in Sec. 3.2.2 and 3.5.

3.2.2 Consequences of Symmetry on Thermoacoustic Mode Structure

3.2.2.1 Bloch-Wave Theory

The discrete rotational symmetry of (can)-annular systems emerges from the number N of identical sectors - in the following denoted *unit cell* - which are arranged equidistantly around the circumference of the engine. In an annular combustor, the unit cell comprises one burner/flame and the respective sector of the chamber and plenum (see Fig. 3.2b)). In a can-annular combustor, the unit cell comprises one can and the respective sector of the compressor exit plenum and the annular gap (see Fig. 3.2a)).

The (thermo-)acoustic eigenmodes of systems exhibiting such symmetry have a special structure. Applying the Bloch-wave theorem [61], the acoustic pressure associated to the eigenmodes can be written as [59]

$$\hat{p}(\mathbf{x}) = \Psi(\mathbf{x}) e^{im\phi}, \quad \text{with} \quad m = \begin{cases} -\frac{N}{2} + 1, \dots, 0, \dots, \frac{N}{2} & N \text{ even} \\ -\frac{(N-1)}{2}, \dots, 0, \dots, \frac{N-1}{2}, & N \text{ odd.} \end{cases} \quad (3.2)$$

Here \hat{p} is the acoustic pressure in frequency domain, and $\mathbf{x} = (r, \phi, z)$ is the position vector comprised of the radial, circumferential, and axial coordinate. Ψ is a function that is identical in all N unit cells, m is called the *Bloch-wave number*. Up to mode order $N/2$, the absolute value $|m|$ of the Bloch-wave number is identical to the azimuthal mode order. All higher azimuthal mode orders $|m| > N/2$ can be readily expressed with the given set $m = -(N/2-1), \dots, -1, 0, 1, \dots, N/2$ of Bloch-wave numbers and are thus included in Eq. (3.2). For example, the azimuthal mode order $N/2 + 1$ is represented by the Bloch-wave number $m = N/2 - 1$, mode order $N/2 + 2$ by $m = N/2 - 2$, and mode order N by $m = 0$. Equation (3.2) thus includes *all* eigenmodes.

Depending on m , the modes can be classified into *axial modes* ($m = 0$), so-called *push-pull modes* ($m = N/2$)³, which feature a pressure field of alternating sign in adjacent unit cells, and modes of Bloch-wave number $m = \pm 1, \dots, \pm(N/2 - 1)$, which designate modes spinning in the (anti-)clockwise direction [28].

Equation (3.2) has important implications on modeling: once the function $\Psi(\mathbf{x})$ is known in the unit cell, the eigenmodes can be directly computed from Eq. (3.2) by inserting the respective m . Thus, the eigenmodes of the respective m can be computed based on only one unit cell by imposing pseudo-periodic “*Bloch boundary conditions*” (BBC) [29, 59]

$$\hat{p}\left(r, \phi = \phi_0 + \frac{\pi}{N}, z\right) = \hat{p}\left(r, \phi = \phi_0 - \frac{\pi}{N}, z\right) e^{im\frac{2\pi}{N}} \quad (3.3)$$

for the acoustic variables at the azimuthal interfaces. The solution in the entire configuration can be extrapolated from the computed solution in the unit cell according to Eq. (3.2). The Bloch-wave approach is originally employed in frequency domain to efficiently compute eigenmodes and the associated eigenfrequencies [59] or - combined with an FDF modeling nonlinear flame dynamics - LC amplitudes [60] of systems featuring discrete rotational symmetry.

If the azimuthal mean flow is negligible, the discrete rotational symmetry also induces reflectional symmetry. This assumption is often justified, in particular for can-annular configurations. As a result, modes of Bloch-wave number $\pm m$ of spinning modes $m \neq 0 \wedge m \neq N/2$ merely differ by their direction of rotation. They describe two linearly independent eigenmodes, which share a common eigenvalue of algebraic multiplicity 2 and are thus degenerate. In this case, it is sufficient to consider only positive $m = 0, \dots, N/2$ for linear stability analysis. If such a degenerate mode pair is linearly unstable, linear theory alone cannot predict the acoustic wave structure emerging [33]. The time domain pressure field resulting for a degenerated mode pair with Bloch-wave number m writes

$$p(\mathbf{x}, t) = \text{Re} \left\{ \Psi(\mathbf{x}) e^{i\omega t} \left(a_1 e^{im\phi} + a_2 e^{-im\phi} \right) \right\}, \quad (3.4)$$

where the coefficients a_1 and a_2 are the respective amplitudes of the anticlockwise and clockwise spinning waves. If the counter-rotating modes have identical amplitudes $a_1 = a_2$, they result in an azimuthally standing wave with a nodal line at a fixed azimuthal position. In case the growth of either of the modes suppresses its counterpart ($a_1 = 0$ or $a_2 = 0$) the result is a rotating wave whose nodal line is azimuthally spinning with the speed of sound c . Everything in between is also possible and observed in practice: from a mixed wave pattern, where both modes have non-zero but different amplitudes at the same time, to periodic switching of the rotation direction [22, 94, 95]. In contrast, axial ($m = 0$) and push-pull modes ($m = N/2$) do not come in pairs and thus feature a unique characteristic wave structure, even in the nonlinear regime.

If the considered system comprises only elements with linear dynamics, it does not matter whether the degenerate mode pair results in a standing, spinning, or mixed wave pattern. All patterns have the same frequency and growth rate, and the dynamics of linear elements do not depend on amplitude. Flames, however, feature nonlinear dynamics in the relevant amplitude range. If an azimuthally standing wave ($a_1 = a_2$) emerges from a degenerate mode pair, some

³Only existing in configurations with an even number N of unit cells

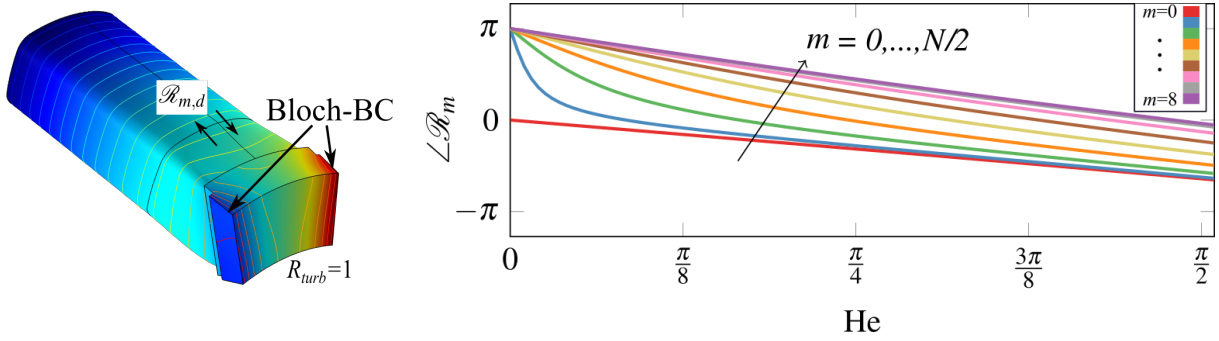


Figure 3.5: Equivalent reflection coefficient of the can-annular system considered in [30]. Left side shows the downstream part of a can, including the respective section of the annular gap, as well as the reference location of $\mathcal{R}_{m,d}$. Right side shows the phase of $\mathcal{R}_{m,d}$.

flames are subjected to higher oscillation amplitudes than others. This leads to different nonlinear saturation of the flame response around the circumference and ultimately breaks the symmetry of the system. The type of symmetry break, in turn, decides together with stochastic forcing from turbulent combustion noise the standing or spinning wave pattern emerging [94, 95, 97]. Therefore, at finite amplitudes, the Bloch-wave approach in Eq. (3.2) can only describe azimuthally spinning waves ($a_1 = 0$ or $a_2 = 0$) or axial $m = 0$ and push-pull modes ($m = N/2$), which maintain symmetry.

3.2.2.2 Equivalent Reflection Coefficient

Equation (3.3) describes the acoustic boundary conditions on the cutting interfaces of the unit cell. They may be imposed not only for computing eigenmodes but also for deriving *equivalent reflection coefficients* \mathcal{R}_m for annular and especially can-annular systems [28, 87, 88]. The reflection coefficient defined at the in- or outlet of a can represents the cumulative acoustic response of all remaining cans of the system. The equivalent reflection coefficient \mathcal{R}_m depends on the acoustics of the coupling interfaces and the Bloch-wave number m . By that, it assumes a synchronization pattern of order m according to Eq. (3.2) throughout the system. Although \mathcal{R}_m lumps the response of all remaining cans, it does not depend on the can acoustics and the generally unknown flame response, making it very attractive for hybrid modeling. Figure 3.5 exemplifies the equivalent reflection coefficient of the $N = 16$ can-annular system considered in PAPER_TESTRIG. The phase of $\mathcal{R}_{m,d}$ is plotted over $He = \omega d/c$, where d is the azimuthal distance of neighboring cans. It shows a characteristic pattern, similarly found in different configurations [28, 87, 88]. The gain is trivially given as 1 for the considered $R_{turb} = 1$.

This thesis introduces a direct coupling between CFD simulation and equivalent reflection coefficient, thereby developing a time domain formulation of BBC [29]. This modeling strategy is further discussed in Sec. 3.4.1 and in PAPER_BLOCH reproduced in App. .1 Additionally, a framework to employ Bloch-wave theory, and in particular the equivalent reflection coefficient \mathcal{R}_m , to single-can testing was developed. Details about the developed strategy and results of a numerical validation case are found in PAPER_TESTRIG reproduced in App. .3.

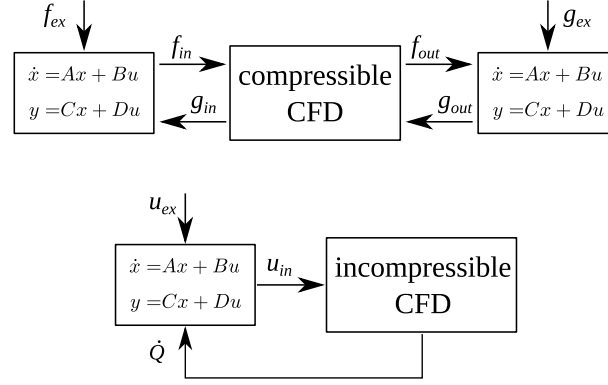


Figure 3.6: Strategies employed in this study to couple CFD and LOM. CBSBC illustrated at the top, low-Mach $v' - Q'$ coupling at the bottom. The inputs f_{ex} , g_{ex} and u_{ex} allow external forcing of the system.

3.3 Strategies to Couple CFD and LOM

The coupling between LES and LOM is a crucial ingredient of the hybrid models developed. Within this thesis, the two approaches used in [58] - “*Characteristic-Based State-Space Boundary Conditions*” (CBSBC) [98] and low-Mach $v' - Q'$ coupling [53] - are employed and implemented in the open-source software package OpenFOAM [99]. The two approaches are illustrated in Fig. 3.6. In both frameworks, the acoustic LOM is represented as a state-space model (see Sec. 3.3.1). CBSBC, described in Sec. 3.3.2, couple a fully compressible CFD simulation with an acoustic LOM of the *remaining* system. The low-Mach $v' - Q'$ framework described in Sec. 3.3.3 couples a low-Mach CFD simulation with an acoustic LOM of the *entire* system. Both approaches have their advantages and limits of applicability, which are discussed in Sec. 3.3.4.

3.3.1 State-Space Modeling of Acoustic Systems

Any linear time-invariant system can be represented as a state-space model of the following form:

$$\dot{x}(t) = Ax(t) + Bu(t) \quad (3.5)$$

$$y(t) = Cx(t) + Du(t) \quad (3.6)$$

Here, x is the state vector, describing the system’s state at time t , u are the inputs of the system, and y are its outputs. The system matrix A governs the system’s internal dynamics. Its eigenvalues determine the free/unforced evolution of the system state and, in particular, the stability of the system. B represents the impact of external inputs on the system state. The system output is linked to the state vector with the output (or measurement) matrix C . D accounts for possible direct feed-through from in- to output.

The state-vector x of a given system may represent physical quantities (such as the acoustic wave amplitude at a given location), but it does not necessarily have to. The state-space formulation of a system is not unique. In fact, there are infinitely many representations, which can be transformed into each other by $x = Tz$, where T is a non-singular square matrix and z is the new

state vector. The system dynamics are solely governed by the eigenvalues of the system matrix A and are invariant to state transformations [100].

Various in- and outputs can be defined for the same system, measuring different quantities of interest without changing the system dynamics. Let the state-space matrix A describe the dynamics of a given acoustic system: By properly choosing the in- and output matrices B and C , the model may represent the reflection coefficient of the acoustic system considered at a given location. By adjusting the in- and output matrices B and C , the state-space model with the same system matrix A may, for example, represent the reflection coefficient of the same system at a different location or model the system's response to an external input. The following sections describe three popular ways to obtain a state-space representation of an acoustic system.

3.3.1.1 Relation to Linear ODE

A linear time-invariant system can be represented by the general ordinary differential equation (ODE)

$$\frac{d^n y(t)}{dt^n} + \dots + a_1 \frac{dy(t)}{dt} + a_0 y(t) = \frac{d^q u(t)}{dt^q} + \dots + b_1 \frac{du(t)}{dt} + b_0 u(t) \quad (3.7)$$

with a given set of initial conditions for y and its time derivatives. For simplicity, we only consider systems with a single input u and output y , but the considerations can be readily extended to multiple in- and outputs. After defining a state vector x with components $x_n = \frac{d^{n-1}y(t)}{dt^{n-1}}$ we can re-write Eq. (3.7) and arrive at the state-space representation Eq. (3.5) and (3.6), where the system matrices are given by [100]

$$A = \begin{bmatrix} 0 & 1 & 0 & \dots & 0 \\ 0 & 0 & 1 & \dots & 0 \\ \vdots & \vdots & \vdots & \ddots & \\ 0 & 0 & 0 & \dots & 1 \\ -a_0 & -a_1 & -a_2 & \dots & -a_{n-1} \end{bmatrix}, \quad B = \begin{bmatrix} 0 \\ 0 \\ \vdots \\ 0 \\ 1 \end{bmatrix} \quad (3.8)$$

$$C = [b_0 - b_n a_0, \quad b_1 - b_n a_1, \quad \dots, \quad b_{n-1} - b_n a_{n-1}], \quad D = b_n$$

if $q = n$. In case $q < n$, C and D simplify to

$$C = [b_0 \quad b_1 \quad \dots \quad b_q \quad 0 \quad \dots \quad 0], \quad D = 0. \quad (3.9)$$

Note that the above system can be transformed into a new state representation of arbitrary form. In turn, every state-space representation can be brought to the above form and equivalently be represented as an n -th order ODE, where n is the dimension of the state-vector x . To summarize, any acoustic system described by a general linear ODE in Eq. (3.7) can easily be converted into a state-space system.

3.3.1.2 Relation to Transfer Function

A given state-space system can be represented as a transfer function in frequency domain [100]. Equivalently, a measured (or modeled) transfer function or a rational fit of a system's frequency response can be represented as a state-space model in the form of Eqs. (3.5),(3.6).

Assume a system described by a transfer function (or frequency response model) of the following form

$$G(s) = \frac{b_q s^q + b_{q-1} s^{q-1} + \dots + b_1 s + b_0}{a_n s^n + a_{n-1} s^{n-1} + \dots + a_1 s + a_0}, \quad (3.10)$$

where s is the Laplace variable $s = \sigma + i\omega$. This transfer function follows from the Laplace transformation of Eq. (3.7) and is thus the frequency domain representation of the system governed by this ODE. Therefore, the state-space representation in Eqs. (3.8) still holds.

In turn, given a state-space model in the form of Eq. (3.5) and (3.6), the corresponding transfer function writes

$$G(s) = C(sI - A)^{-1} B + D. \quad (3.11)$$

Note that the denominator of the transfer function $G(s)$ is the characteristic polynomial of the system matrix A , i.e., the eigenvalues of the A -matrix show up as poles of the transfer function. Regarding in-output behavior, the transfer function and state-space representation of a linear time-invariant system are completely equivalent. In a transfer function formulation, an unfortunate choice of the in- and outputs may cause pole-zero cancellations, which hide internal dynamics, while the eigenvalues are always visible in the state-space formulation. In the state-space representation, various in-output relations (and thus transfer functions) of the same system can be easily obtained by modifying the matrices B and C . In that sense, the state-space representation is a more complete description of the system dynamics, while a transfer function only shows a particular in-/output behavior of a system.

To summarize, every transfer function or frequency domain model given in the rational form Eq. (3.10) can be easily written as a state-space model. In case the considered transfer function has a different form or if, for example, only measured frequency response data are available, a rational function of the form Eq. (3.10) can be fitted to the data and converted to a state-space model.

3.3.1.3 Relation to Discretized PDE

The spatial discretization of linearized partial differential equations (PDE) can be translated to a state-space representation similar to Eq. (3.5) and Eq. (3.6). Depending on the discretization scheme, the time derivative of the state vector \dot{x} may have to be multiplied by a so-called *mass matrix* E [101]. This, however, does not affect the above-mentioned general framework.

The acoustics of complex geometries may be modeled using 1D, 2D, or 3D codes implementing linearized governing equations (Helmholtz, LEE, LNSE). Spatial discretization of the PDE, for example, through the finite volume or the finite element method, yields a system of linear ODEs, which can be re-arranged into state-space form as shown in Sec. 3.3.1.1.

Commercial and Open Source tools, which are frequently used to implement linearized acoustic equations, either directly support the export of the state-space matrices A, B, C, D, E (e.g., Comsol Multiphysics) [101] or allow the implementation of this feature (e.g., FEniCS). The (thermo-) acoustic network model taX [72]⁴, which is used in this thesis, is based on the inter-

⁴code available at <https://gitlab.lrz.de/tfd/taX>

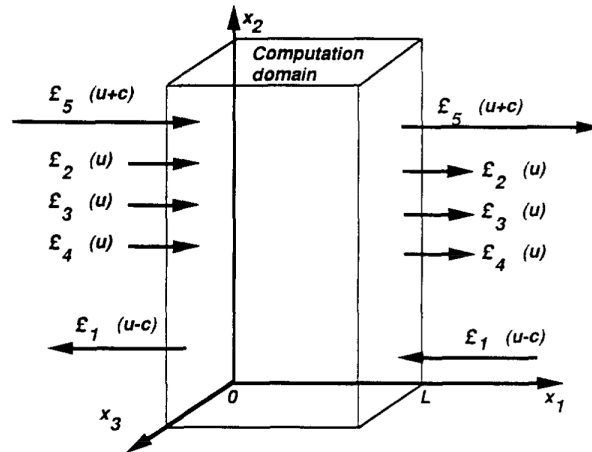


Figure 3.7: Subsonic in- and outlet boundary with characteristic waves traveling normal to boundaries. Reproduced from [66].

connection of individual elements represented as state-space models and supports their direct export [72, 101].

3.3.2 Theory of Characteristic-Based State-Space Boundary Conditions

Characteristic-Based State-Space Boundary Conditions (CBSBC) [98] are based on the *Navier-Stokes Characteristic Boundary Conditions* (NSCBC) proposed by Poinso *et al.* [66], and in particular on the fully non-reflective version of the *Locally One-Dimensional Inviscid* (LODI) boundary conditions proposed by Polifke *et al.* [102]. In this section, the theory behind CBSBC is briefly reviewed.

3.3.2.1 Navier-Stokes Characteristic Boundary Conditions

In incompressible flows, mass, momentum, energy, and species are transported only by mean flow and dissipative processes. Fully compressible flows, however, additionally feature transport by acoustic waves. Thus, numerical boundary conditions (BC) for compressible flows have to account not only for the mean flow but also for the acoustic characteristics of the domain boundaries. In particular, the numerical BC must represent the reflection and transmission of acoustic waves at the boundaries of the configuration considered.

To address this, Poinso *et al.* [66] proposed the NSCBC, which relies on a characteristic decomposition of the governing equations Eqs (2.1)-(2.3) at the domain boundaries. Figure 3.7 shows an exemplary computational domain with an in- and outlet normal to x_1 located at $x_1 = 0$ and $x_1 = L$, respectively. The characteristic decomposition of the Navier-Stokes equations leads to five characteristic waves $\mathcal{L}_1, \dots, \mathcal{L}_5$ traveling normal to (and through) the boundaries.

The characteristic waves $\mathfrak{L}_1, \dots, \mathfrak{L}_5$ are related to the primitive flow variables like

$$\mathfrak{L}_1 = (u_1 - c) \left(\frac{\partial p}{\partial x_1} - \rho c \frac{\partial u_1}{\partial x_1} \right) = -2\rho c \frac{\partial g}{\partial t} \quad (3.12)$$

$$\mathfrak{L}_2 = u_1 \left(c^2 \frac{\partial \rho}{\partial x_1} - \frac{\partial p}{\partial x_1} \right) \quad (3.13)$$

$$\mathfrak{L}_3 = u_1 \frac{\partial u_2}{\partial x_1} \quad (3.14)$$

$$\mathfrak{L}_4 = u_1 \frac{\partial u_3}{\partial x_1} \quad (3.15)$$

$$\mathfrak{L}_5 = (u_1 + c) \left(\frac{\partial p}{\partial x_1} + \rho c \frac{\partial u_1}{\partial x_1} \right) = -2\rho c \frac{\partial f}{\partial t}. \quad (3.16)$$

\mathfrak{L}_1 and \mathfrak{L}_5 are related to the upstream and downstream traveling acoustic waves and linked with the acoustic Riemann invariants f and g as shown in Eq. (3.12) and (3.16). \mathfrak{L}_2 is the entropy wave convected with the mean flow velocity u_1 . \mathfrak{L}_3 and \mathfrak{L}_4 represent transversal velocity fluctuations transported with the mean flow, i.e., these waves account for the transport of vorticity. For subsonic flow speeds $u_1 < c$, as assumed in Fig. 3.7, four waves are entering the domain at the inlet, while one wave (the upstream traveling acoustic wave \mathfrak{L}_1) is leaving the domain. Four waves are leaving the domain at the outlet, while \mathfrak{L}_1 is entering the domain.

A well-posed BC has to prescribe all waves entering the domain at the boundary considered, while all waves leaving the domain are solely governed by the flow inside the domain. The general strategy to set a physical BC (such as an arbitrary condition for pressure, velocity, etc.) in the NSCBC framework is to determine the incoming waves \mathfrak{L}_i that lead to the physical condition prescribed. The outwards traveling waves are computed from the solution inside the domain. Afterward, the full set of characteristic waves can be used to determine conditions for all remaining primitive physical variables. This strategy leads to consistent conditions for all flow variables and, most importantly, makes acoustic (and entropy and vorticity) waves directly accessible.

3.3.2.2 Locally One-Dimensional Inviscid Relations

Using the full Navier-Stokes Equations, it is generally impossible to determine the characteristic waves \mathfrak{L}_i that correspond to arbitrary physical conditions. Assuming the flow at the boundary to be locally one-dimensional and inviscid leads to the LODI-relations. Now, the characteristic

waves are directly connected to the temporal variations of the primitive variables:

$$\frac{\partial \rho}{\partial t} + \frac{1}{c^2} \left[\mathfrak{L}_2 + \frac{1}{2} (\mathfrak{L}_5 + \mathfrak{L}_1) \right] = 0 \quad (3.17)$$

$$\frac{\partial p}{\partial t} + \frac{1}{2} (\mathfrak{L}_5 + \mathfrak{L}_1) = 0 \quad (3.18)$$

$$\frac{\partial u_1}{\partial t} + \frac{1}{2\rho c} (\mathfrak{L}_5 - \mathfrak{L}_1) = 0 \quad (3.19)$$

$$\frac{\partial u_2}{\partial t} + \mathfrak{L}_3 = 0 \quad (3.20)$$

$$\frac{\partial u_3}{\partial t} + \mathfrak{L}_4 = 0. \quad (3.21)$$

These relations can be used to determine the incoming waves from physical conditions, while the outgoing wave is calculated from the flow inside. After determining the characteristic waves, they are substituted into the NSCBC relations (see [66]) to determine all remaining primitive variables, which are not directly set by the physical condition.

Assuming that viscous and multi-dimensional effects are negligible directly at the boundary (this assumption is valid if the boundary is sufficiently far away from regions with strong vorticity [66]), the LODI-relations (3.17)- (3.21) can be used directly to evaluate primitive variables at the boundary from given characteristic waves. This is particularly useful for setting specific acoustic BCs, i.e., for prescribing certain \mathfrak{L}_1 or \mathfrak{L}_5 . Note, however, that the LODI framework can also be used to prescribe entropy or vorticity conditions.

Acoustically non-reflecting boundary conditions are of particular interest, e.g., for system identification purposes [103]. Theoretically, a non-reflective condition enforces an incoming wave of $\mathfrak{L}_1 = 0$ (outlet) or $\mathfrak{L}_5 = 0$ (inlet). This, however, leads to an under-determined system because the outlet pressure in Eq. (3.18) or the inlet velocity in Eq. (3.19) is solely governed by the outgoing wave, i.e., only dependent on the flow inside the domain with no value prescribed from outside. This results in a drift of the mean value caused by turbulent fluctuations or even by numerical inaccuracies.

A solution to that problem is to add a relaxation term to the incoming wave [66]

$$\mathfrak{L}_1 = \sigma (p - p_T) \quad (3.22)$$

$$\mathfrak{L}_5 = \sigma (u - u_T), \quad (3.23)$$

which ensures that the inlet velocity and/or the outlet pressure exponentially approaches the target value u_T and p_T . This formulation is no longer fully non-reflective. As shown by Polifke *et al.* [102], the BC is even fully reflective for frequencies approaching zero. This issue can be resolved by subtracting the pressure or velocity fluctuation caused by (plane) acoustic waves from the relaxation term (“*plane-wave-masking*”). An acoustically non-reflective formulation is thus [102]

$$\mathfrak{L}_1 = \sigma (p - \rho c (f + g) - p_T) \quad (3.24)$$

$$\mathfrak{L}_5 = \sigma (u - (f - g) - u_T). \quad (3.25)$$

To apply relations (3.24) and (3.25), the (plane) acoustic waves f and g traveling outwards the domain have to be measured. This is achieved with a characteristic based filter [102], illustrated

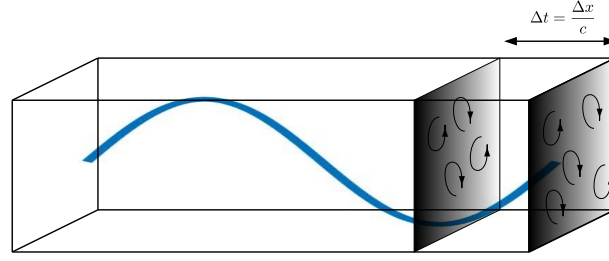


Figure 3.8: Characteristic-based filtering to obtain the acoustic waves leaving the domain.

in Fig. 3.8. The acoustic pressure p_a and velocity u_a fluctuations are computed by averaging pressure and velocity fluctuations over cut-planes parallel to the boundary plane. As the traveling speed of the acoustic waves is known and is different from the convection speed of turbulent fluctuations, multiple parallel planes can be considered for the averaging (see Fig. 3.8), which effectively cancels out the influence of turbulent fluctuations.

Finally, the LODI-relations with plane-wave masking can impose arbitrary acoustic excitation from outside the domain on a fully non-reflective BC. Following Eq. (3.12) and (3.16), adding external acoustic forcing f_{bc} and g_{bc} at a non-reflective boundary condition results in incoming waves given by

$$\mathcal{L}_1 = \sigma(p - \rho c(f + g_{bc}) - p_T) - 2\rho c \frac{\partial g_{bc}}{\partial t} \quad (3.26)$$

$$\mathcal{L}_5 = \sigma(u - (f_{bc} - g) - u_T) - 2\rho c \frac{\partial f_{bc}}{\partial t}. \quad (3.27)$$

Note that at this stage, the boundary is still fully non-reflective. The incoming acoustic wave is not linked to the outgoing wave but is given by (independent) external forcing.

3.3.2.3 Characteristic-Based State-Space Boundary Conditions

Based on the non-reflective LODI relations with external excitation Eq. (3.26) and (3.27), arbitrary reflection coefficients R_{in} and R_{out} (or equivalently impedances Z_{in} and Z_{out}) are imposed at the inlet and outlet by linking the yet external acoustic waves f_{bc} and g_{bc} with the outwards traveling waves

$$\hat{f}_{bc} = \hat{g} R_{in} = \hat{g} \frac{Z_{in} + 1}{Z_{in} - 1} \quad (3.28)$$

$$\hat{g}_{bc} = \hat{f} R_{out} = \hat{f} \frac{Z_{out} - 1}{Z_{out} + 1}. \quad (3.29)$$

Assuming that the prescribed reflection coefficients $R(s)$ are a linear time-invariant system, they can be represented as a state-space model (see Sec. 3.3.1). This leads to the CBSBC proposed by Jaensch *et al.* [98].

In summary, the CBSBC is a fully non-reflective LODI-BC (using plane-wave-masking), for which the incoming acoustic wave (or external forcing in the LODI framework) is linked to the outwards traveling wave by a state-space model. This is illustrated in Fig. 3.9 for an exemplary

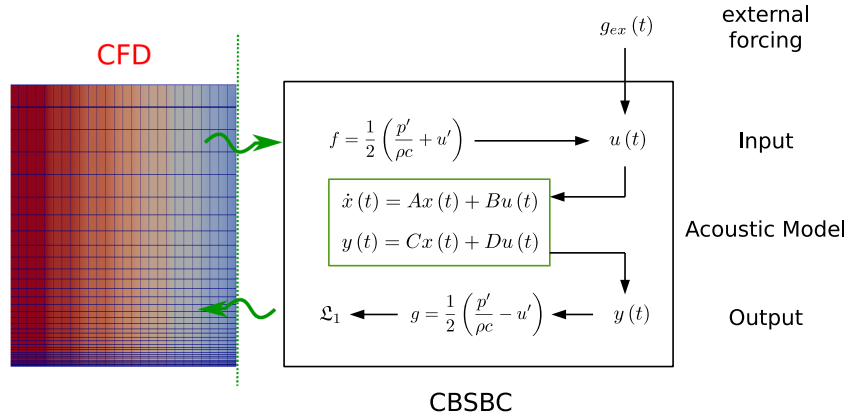


Figure 3.9: CBSBC for an outlet boundary. The state-space model in the green box represents the imposed reflection coefficient.

outlet BC. The f wave leaving the CFD domain serves as input for the state-space model, together with a possible additional external forcing g_{ex} . Consequently, for a CBSBC outlet the in- and outputs of the state-space system in Eqs. (3.5),(3.6) are

$$\begin{aligned} u &= [f_{out}, g_{ex}] \\ y &= [g_{out}]. \end{aligned} \quad (3.30)$$

The in- and outputs of a CBSBC inlet are defined accordingly. Note that further external inputs can easily be appended to the input vector of the state-space model. Solving the state-space system yields the inwards traveling wave g_{out} at the outlet, which is imposed on the CFD simulation by the LODI relation (3.26).

In some configurations, the acoustic systems coupled at the in- and outlet may not be separated but may be one monolithic system. This is, for example, the case in can-annular combustors, when can-can coupling via both annular gap and plenum is considered. In this case, the in- and output equations of the coupled state-space system contain the characteristic waves from both the inlet and outlet:

$$\begin{aligned} u &= [f_{out}, g_{ex}, g_{in}, f_{ex}] \\ y &= [g_{out}, f_{in}]. \end{aligned} \quad (3.31)$$

3.3.3 Low-Mach v' - Q' Coupling

The coupling of a low-Mach CFD simulation solving Eqs. (2.6)-(2.10) to an acoustic LOM is conceptually much simpler than the compressible coupling described in Sec. 3.3.2. There are no acoustic waves in the low-Mach CFD, which have to be treated consistently by the boundary conditions, and the coupling relies on primitive physical variables only. At first glance, it seems counter-intuitive that a low-Mach simulation, which lacks the description of acoustic waves, can simulate the flame response to acoustic excitation. However, flames of gaseous fuels are insensitive to pressure fluctuations, and acoustic waves only interact via the velocity fluctuations they induce [104]. Such types of flames are denoted as “*velocity-sensitive*” in the following. If the velocity-sensitive flame considered is acoustically compact with $He \ll 1$ (characteristic

length being the flame length), the flame response to acoustic waves can be well approximated by the response to inlet velocity fluctuations in a low-Mach simulation. The imposed velocity fluctuations are equivalent to the velocity fluctuations that the acoustic waves would induce in a fully compressible medium [105].

As illustrated in Fig. 3.6 bottom, the coupled state-space model is fed with the recorded heat-release rate fluctuation \dot{Q}' . The LOM incorporates Rankine-Hugoniot jump conditions for pressure and velocity across the flame to convert the heat release rate fluctuation to sound waves [106]. The output of the state-space model is the velocity fluctuation v' and is imposed at the inlet of the CFD:

$$\begin{aligned} u &= [\dot{Q}', u_{ex}] \\ y &= [v']. \end{aligned} \quad (3.32)$$

Again, further external inputs u_{ex} can easily be appended to the input vector of the state-space model. Unlike in the CBSBC coupling, the coupled LOM has to account for the acoustics of the *entire* system, including the CFD domain.

3.3.4 Selection of the Coupling Framework

CBSBC, and particularly the underlying LODI framework, are generally limited to plane acoustic waves traveling perpendicular to the coupling interfaces. Note, however, that this restriction does not apply *within* the domain of the LOM, as the coupled state-space model Eqs. (3.5),(3.6) may as well represent a 3D acoustic field. The low-Mach $v' - Q'$ coupling is limited to acoustically compact CFD domains with $He \ll 1$ because acoustic waves are not resolved in the CFD. In turn, it is not restricted to plane waves at the interface of CFD and LOM, as the imposed velocity fluctuations can have an arbitrary non-uniform spatial distribution.

For annular configurations, which typically do not feature plane waves at the domain interfaces (see Fig. 3.2 b), the low-Mach approach is thus better suited, also because the burner/flame zone is comparatively short and thus acoustically compact even for high frequencies. In turn, the cans in typical can-annular setups are relatively long and, thus, not acoustically compact in the relevant frequency range. Coupling via CBSBC is thus preferred because the restriction on plane waves at the coupling interface is not a severe limitation in can-annular setups. If both approaches are applicable, the low-Mach coupling is preferred because the numerical setup of a low-Mach number CFD simulation is less demanding.

3.4 Hybrid Model Architectures

3.4.1 Time domain Bloch-Wave Approach

Section 3.2.2 introduced the equivalence reflection coefficient \mathcal{R}_m , which is a direct consequence of the Bloch-wave structure of thermoacoustic modes in (can-)annular configurations with discrete rotational symmetry. In PAPER_BLOCH, we propose a straightforward way to exploit this symmetry in hybrid models of (can-)annular combustors. A LOM including BBC is

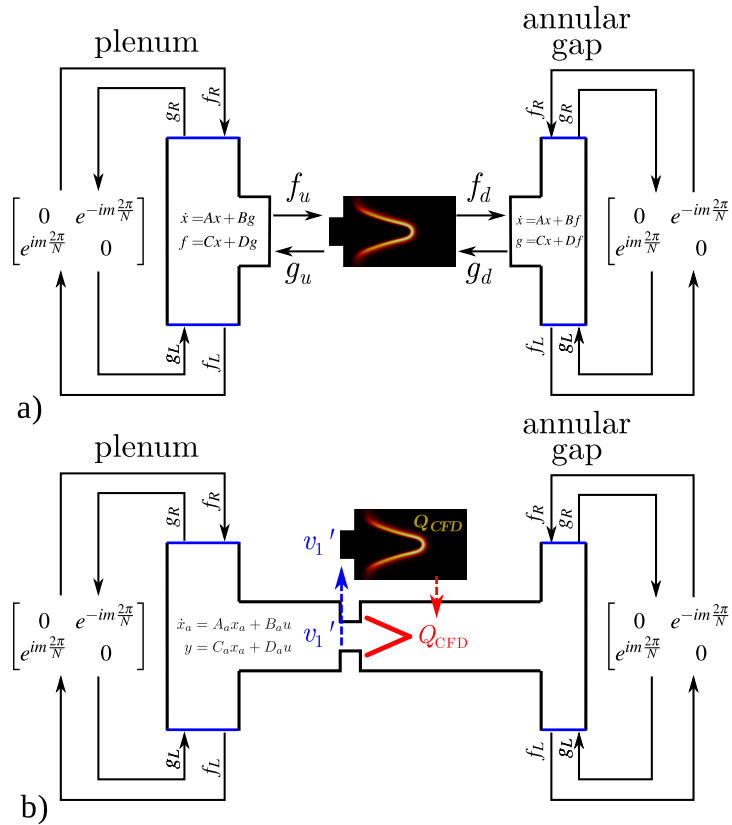


Figure 3.10: Developed time domain BBC model setups. a) coupling via CBSBC, b) low-Mach $v' - Q'$ coupling. Though illustrated for a can-annular configuration, those setups are, in principle, also applicable to annular configurations.

lumped into an equivalent reflection coefficient \mathcal{R}_m and coupled to a CFD simulation of one single burner/flame zone using the coupling frameworks described in Sec. 3.3. Figure 3.10 displays the model architecture for both compressible (a) and low-Mach CFD simulation (b). This yields a nonlinear time domain model of an isolated azimuthal mode order m of a (can-)annular configuration. If the inherent assumptions of the Bloch-wave theorem are fulfilled, this strategy is a direct approach to exploit the symmetry of the systems studied. It allows computing LC oscillations by resolving only one single burner/flame zone or one can. Further details about the derivation and the implementation of the method, as well as a validation case study, are found in PAPER_BLOCH reproduced in App. .1.

While the developed time domain Bloch-wave approach yields very accurate results if its inherent assumptions are fulfilled [29, 62], the limits of applicability are quite strict:

- discrete rotational symmetry of the configuration considered, which is maintained even during large amplitude LC oscillations
- no interaction of modes of different azimuthal orders, as solely the azimuthal mode order $|m|$ considered is present in the simulation
- multiple simulations/experiments are necessary to assess the stability and to model the LC of all mode orders

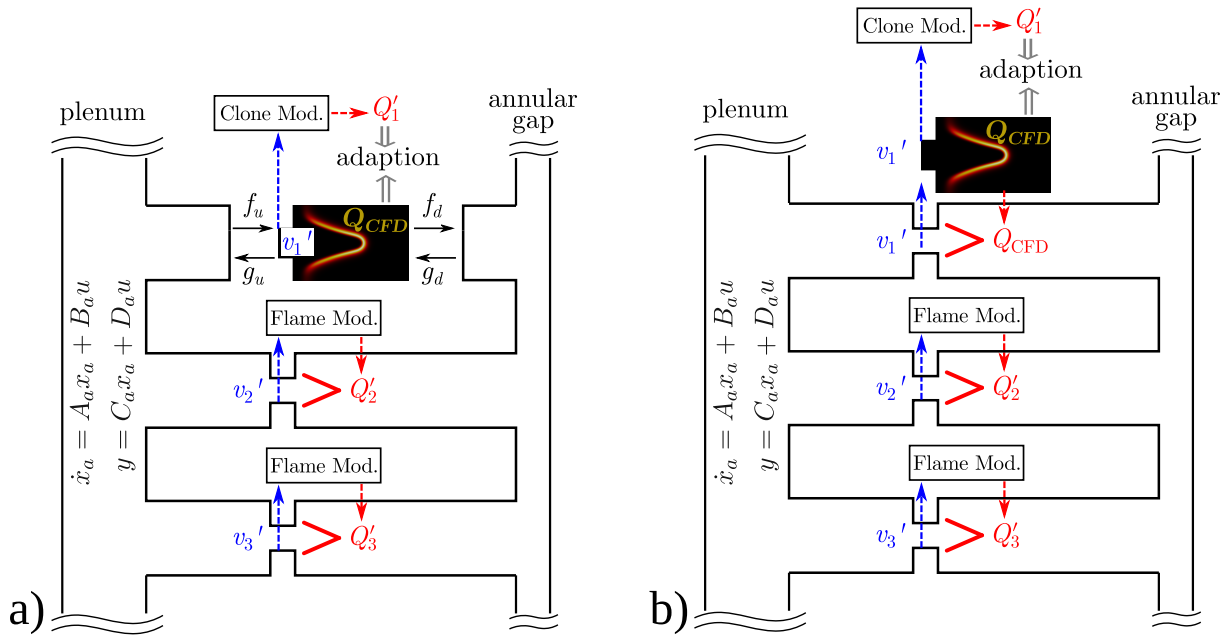


Figure 3.11: Developed ROLEX model setup. a) coupling via CBSBC, b) low-Mach $v' - Q'$ coupling. Though illustrated for a can-annular configuration, those setups are also applicable to annular configurations.

However, these assumptions are not always justified. Even if the geometry and the mean flow of the configuration studied feature a discrete rotational symmetry, this symmetry may break during large amplitude LC oscillations as explained in Sec. 3.2.2. In this case, the time domain Bloch-wave approach still yields an estimation of the LC oscillation of the configuration studied. However, the Bloch-wave approach fails to predict the occurrence of symmetry breaking. It cannot capture the effect of symmetry breaking and possible nonlinear interactions of individual azimuthal mode orders. Instead, the result will be that of an isolated azimuthal mode order in a perfectly symmetrical configuration.

3.4.2 ROLEX Model

To overcome the limitations of the time domain Bloch-wave approach, in PAPER_ROLEX we developed a more general hybrid model, which does not rely on the Bloch symmetry. The model explicitly resolves all burners/flames or cans. This comes with the advantage that all azimuthal mode orders are present in one model, but at the cost that nonlinear flame models are required to represent the dynamics of the flames, which the CFD does not resolve. Details of the hybrid model developed and a numerical validation case are discussed in depth in PAPER_ROLEX reproduced in App. .2. In the following, the gist of the method is outlined.

Figure 3.11 illustrates two versions of the hybrid modeling strategy developed, which differ in their coupling strategy. In Fig. 3.11a), CFD and LOM are coupled via CBSBC, in Fig. 3.11b) via the low-Mach $v' - Q'$ framework. In both versions, only one burner/flame zone or one can is resolved by CFD. The remaining parts of the combustion system, including all remaining

flames, are represented as LOM. This type of model is in the following denoted as ROLEX⁵. As detailed in Sec. 3.3, the acoustics are represented as a linear state-space model. The nonlinear flame models are coupled to the linear acoustic LOM similarly to the CFD simulation. A costly a priori identification of a generally valid, quantitatively accurate nonlinear flame model would shatter the efficiency of the entire approach. Instead, by exploiting the symmetry of the configuration, the flame models are adapted *on the fly*, based on the flame dynamics observed in the CFD simulation. The resulting flame models will, in general, only be valid in the vicinity of the simulated trajectory of the self-excited system, and the proposed approach will not yield a general nonlinear flame model, which is valid for all frequencies, amplitudes, and operating conditions. However, this is not the goal of the proposed strategy, as the focus here is on predicting the stable LC of the system considered.

The online adaption routine of the flame models employed is described in Sec. 3.5 and in greater detail in PAPER_ROLEX. Up to now, the only restriction on the type of nonlinear flame model is that it must represent the correct *linear* flame dynamics in the limit of zero amplitude. This ensures that the complete configuration features the correct linear stability properties. The linear flame model must thus be identified prior to the simulation of the self-excited system. Note that the computational resources needed for identifying a linear flame model are orders of magnitude smaller than for a generally valid nonlinear flame model.

Without loss of generality, the nonlinear flame models are assumed to be parameterized by a set of coefficients stored in the vector s . The online identification of the parameters s is based on a “clone model”. It has the same structure as the other flame models and is solved with the input being the reference velocity v_1' recorded in the CFD simulation. This indirect route via the “clone model” is necessary because, in general, the acoustic state in the individual burners or cans differ from each other. Even in the case of perfect Bloch-symmetry, the individual sectors are phase-shifted by $e^{im\phi}$, according to Eq. (3.2). If symmetry is broken (for example due to azimuthally standing waves), even the amplitude levels at the individual flames differ, leading to different nonlinear saturation. This prevents a direct identification of the individual flame models based on the CFD observation. By comparing the heat release output of “clone model” and CFD, the nonlinear model parameters s are identified and subsequently applied to all flame models.

The model structures shown in Fig. 3.11 suffer from one flaw: they introduce (artificial) asymmetry into the modeled system. As the flame models will not perfectly represent the actual flame dynamics, the one can or burner/flame resolved by CFD will differ from the modeled burners or cans. In unfortunate circumstances, this symmetry break may strongly impact the predicted LC oscillations. As stated in Sec. 3.2.1, can-annular configurations are susceptible to perturbations of their symmetry. For example, the artificial asymmetry introduced may lead to mode localization, which may not be present in the actual configuration.

An alternative, symmetry-preserving setup illustrated in Fig. 3.12 was developed to address this issue. Here, the “clone model” and CFD switch places, and the CFD is fed with the input(s) recorded at the respective position(s) in the LOM. The CFD simulation now solely serves the purpose of providing reference data for the parameter identification. The output of the CFD is not coupled back into the LOM. Instead, the self-excited system is now solely represented by

⁵acronym of “**R**educed-**O**rders **L**ES model of self-**E**Xcited combustion instabilities in (can-)annular systems”

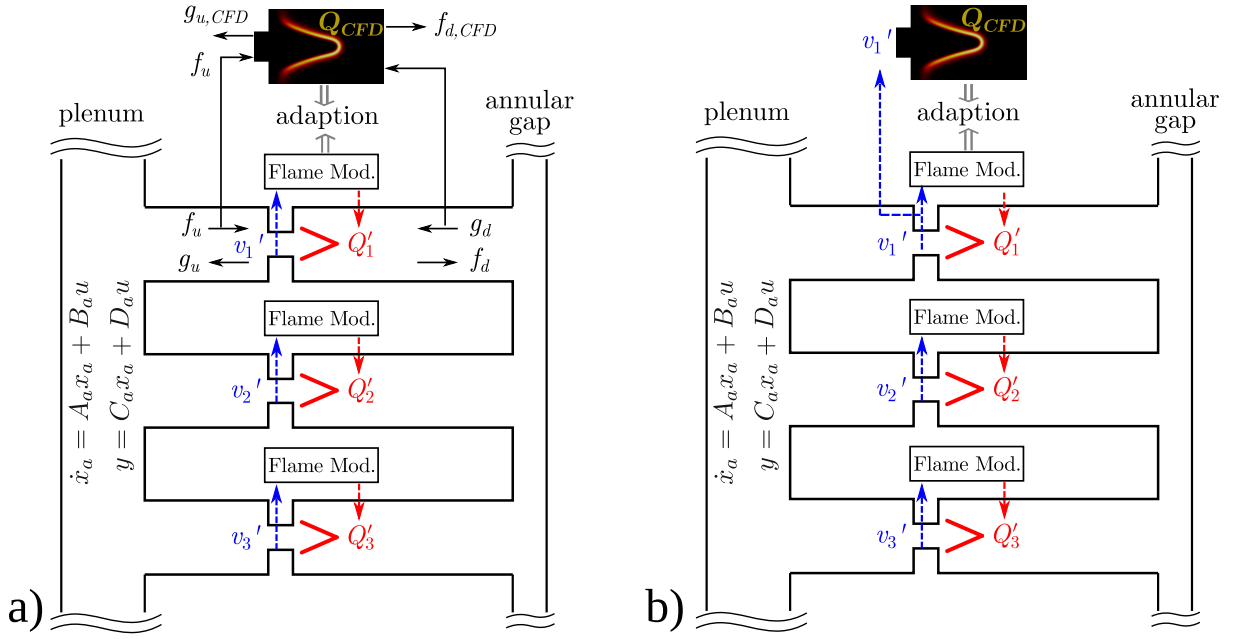


Figure 3.12: Developed symmetry preserving ROLEX model setup. a) coupling via CBSBC, b) low-Mach $v' - Q'$ coupling. Compared to the setup published in PAPER_ROLEX and shown in Fig. 3.11, “Clone model” and CFD switch places.

the LOM, which ensures the correct symmetry properties of the modeled system.

Generally, the model structure shown in Fig. 3.12 is superior because it maintains the correct symmetry properties. If applicable (see Sec. 3.3), the low-Mach, symmetry preserving setup in Fig. 3.12b) is recommended. The compressible symmetry-preserving setup suffers from the fact that the CFD domain on its own exhibits internal thermoacoustic dynamics. For example, the uncoupled CFD domain may be thermoacoustically unstable due to an unstable intrinsic thermoacoustic (ITA) mode [107, 108]. In this case, the compressible symmetry-preserving setup can not be used because the system trajectory simulated in the CFD quickly deviates from that of the remaining burners or cans represented by the LOM. If the compressible setup must be used (in case of a non-compact flame), the original setup in Fig. 3.11a) is recommended unless it has been ensured that the CFD domain itself is thermoacoustically stable.

3.5 Flame Modeling

All models developed that do not rely on Bloch-symmetry (see Fig. 3.11 and Fig. 3.12) require a nonlinear flame model to represent the dynamics of the flames not resolved by the CFD. The flame models are intended to be updated on the fly during the simulation of the self-excited system. This poses specific requirements on the models and their integration in the LOM coupled to the CFD, which will be reviewed in the following. Further details are found in PAPER_ROLEX reproduced in App. .2. A broader overview of common nonlinear flame models and their identification and a comparison with the model employed here follows in Sec. 6.1.1.

3.5.1 Coupling Nonlinear Flame Models and Acoustic LOM

The approaches presented in Sec. 3.3 couple a linear (thermo-)acoustic state-space model to a compressible or low-Mach CFD simulation. Such a linear state-space model could seamlessly incorporate a linear flame model. There are various common state-space representations of a (linear) FTF [109], which can be interconnected with the remaining system like any other linear building block. In the present context, however, the coupled LOM needs to be *nonlinear* because it has to include the nonlinear dynamics of the flames that the LES does not resolve.

Without modifying the gist of the coupling strategies, nonlinear flame models can be included in the LOM by appending the in- and outputs of the coupled state-space models in Eq. (3.30) or in Eq. (3.32), similar to the treatment of external inputs. In the case of a CBSBC inlet, for example, the in- and outputs not only contain the acoustic waves crossing the interface and possibly some external forcing f_{ex} but are appended by the in- and outputs of the individual flame models:

$$\begin{aligned} u &= [g_{in}, f_{ex}, \dot{Q}'_1, \dots, \dot{Q}'_n] \\ y &= [f_{in}, v'_1, \dots, v'_n]. \end{aligned} \quad (3.33)$$

Here, the outputs of flame model “1” to “ n ”, the modeled heat release rates $\dot{Q}'_1, \dots, \dot{Q}'_n$, are appended to the inputs of the acoustic state-space model. The inputs of the flame models, the velocity fluctuations at the respective flame reference positions v'_1, \dots, v'_n , are appended to the outputs of the acoustic model. In this way, the nonlinear flame models are connected to the linear acoustic model, but their in- and outputs are directly accessible.

3.5.2 Model Structure and Online Parameter Identification

Up to this point, the structure of the employed flame models has not yet been determined. In fact, by appending the in- and outputs of the linear acoustic model as shown in Eq. (3.33), it can be combined with any conceivable flame model that yields the integrated heat release rate and is formulated in time domain. However, the specific requirements of the present purpose limit the models that can be considered. They must

- feature nonlinear dynamics, particularly saturation of gain (and possibly change in phase) for high input amplitudes. Other nonlinear effects, such as the generation of higher harmonics and cross-frequency coupling, are desired but less important.
- accurately represent linear dynamics (in the limit of zero input amplitude) for a wide frequency range. This ensures the correct stability properties of the system considered.
- depend only on a few free parameters because the amount of training data available during online identification is limited.
- allow training of the free model parameters without heavy computations, as this would slow down the entire simulation.

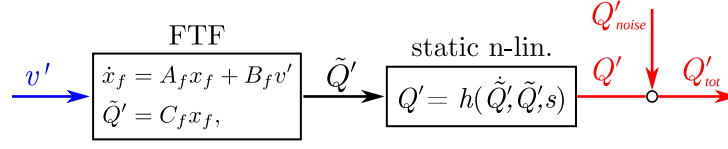


Figure 3.13: Wiener-type flame model comprising a linear time-invariant dynamic part (FTF) and a static nonlinear function correcting the linear model output \tilde{Q}' .

Out of the wide variety of possible flame models (see Sec. 6.1.1 and Fig. 6.1 for an overview), a *Wiener-type* block structured model [110–112] best fits the requirements above. The Wiener model structure adapted to the present context is illustrated in Fig. 3.13. It comprises a linear dynamic model, here a FTF represented as a linear state-space model, followed by a static (algebraic) nonlinear function, which corrects the linear model output.

The FTF $F(\omega) = \hat{Q}'/\hat{v}$, constitutes the linear dynamic model part and describes the linearized flame response \tilde{Q}' over the relevant frequency range. It is provided in advance and not modified during the simulation of the self-excited system. This ensures that the linear stability properties of the configuration considered are correctly represented. The FTF can either be computed in advance by employing the CFD/SI technique [103], measured in an experimental test-rig, or modeled [65]. The coefficients of the nonlinear algebraic function $h(\tilde{Q}', \dot{\tilde{Q}}', s)$ are stored in the parameter vector s . They are repeatedly updated based on comparing the deterministic model output Q' and the CFD observation during the simulation of the self-excited system. This continuously improves the prediction quality of the nonlinear flame models.

The nonlinear algebraic function $h(\tilde{Q}', \dot{\tilde{Q}}', s)$ may take various forms. As it is the only nonlinear part of the flame model, it determines its nonlinear features such as saturation at high amplitudes, interaction of different frequencies, and scattering to higher harmonics. For the cases considered in the scope of this thesis, the function

$$Q' = h(\tilde{Q}', \dot{\tilde{Q}}', s) = \frac{2}{s_1\pi} \arctan\left(\frac{s_1\pi}{2}\tilde{Q}'\right) + s_2\tilde{Q}'\dot{\tilde{Q}}' \quad (3.34)$$

performed well. It converts the linear model output \tilde{Q}' and its time derivative $\dot{\tilde{Q}}' := d\tilde{Q}'/dt$ into the non-linear flame model output Q' . The time derivative of the linear model output $\dot{\tilde{Q}}'$ is directly accessible from the state-space model representation of the FTF. The first term in Eq. (3.34) accounts for nonlinear saturation and generation of odd harmonics. The second term creates second harmonics and creates a sawtooth-shaped signal (see Fig. 3.14), like it is often observed in high-amplitude LC oscillations (see e.g. [113]). This term was first proposed by Purwar *et al.* [85] in the context of nonlinear flame response to transverse excitation.

The deterministic nonlinear model output Q' is superposed with a stochastic Q'_{noise} , which models turbulent combustion noise. Q'_{noise} is computed by solving a noise model with uniform white noise as input [114]. If no noise model is provided, $Q'_{noise} = 0$.

In its current form in Eq. (3.34), the static nonlinear function can not modify the phase of the linear model output. This may cause problems for certain configurations where the phase of the flame response is strongly amplitude-dependent. A variant of Eq. (3.34), which introduces

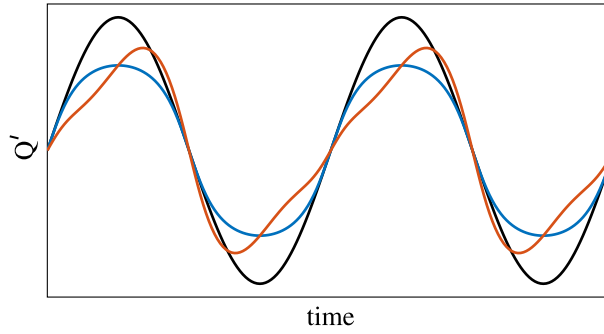


Figure 3.14: Output of static non-linear function Eq. (3.34) (red) with exemplary $s = [1, -0.4]$ and sinusoidal input signal (black). Blue curve shows the saturation term only.

a constant phase-shift depending on s_3 , writes

$$Q' = h(\tilde{Q}', \dot{\tilde{Q}}', s) = \frac{2}{s_1\pi} \arctan\left(\frac{s_1\pi(\tilde{Q}' + s_3\dot{\tilde{Q}}')}{2\sqrt{1+s_3^2}}\right) + s_2 \frac{(\tilde{Q}' + s_3\dot{\tilde{Q}}')(\dot{\tilde{Q}}' - s_3\tilde{Q}')}{1+s_3^2} \quad (3.35)$$

Different ways of introducing a phase shift are conceivable. If necessary, higher-order terms can introduce further higher harmonics.

The output of the static nonlinear function is controlled by the tuning parameters s_1 and s_2 (and possibly additional parameters). These parameters are identified by solving the nonlinear least squares problem

$$s = \operatorname{argmin}\left(h\left(\tilde{Q}'|_{0 \rightarrow t}, \dot{\tilde{Q}}'|_{0 \rightarrow t}, s\right) - Q_{CFD}|_{0 \rightarrow t}\right)^2. \quad (3.36)$$

Here, $\tilde{Q}'|_{0 \rightarrow t}$, $\dot{\tilde{Q}}'|_{0 \rightarrow t}$ and $Q_{CFD}|_{0 \rightarrow t}$ denote the time-series of linear “clone model” output, its time derivative, and the observation from CFD recorded from initial time zero to current time t (c.f. Figs. 3.11,3.12). Note that no dynamic model has to be solved during the optimization step. The cost function solely involves evaluating an algebraic function with stored inputs. The least-squares problem in Eq. (3.36) is solved repeatedly after a prescribed update period τ . This constantly improves the estimation of the model parameters s_1 and s_2 as the amplitude in the CFD changes and affects the dynamics of the flame. After identifying the “clone model” parameters, s_1 and s_2 are applied to all flame models.

The performance of the flame model employed is assessed by comparing the outputs of the (tuned) “clone model” and the CFD for all inputs encountered in the simulation of the self-excited system. A good model must accurately predict nonlinear saturation of the fundamental frequency component, as this governs the LC amplitude. Depending on the focus of the particular study, another quality criterion may be the correct representation of the first few higher harmonics. For all cases considered within this thesis, a flame model employing the static non-linear function in Eq. (3.34) was sufficient for the present purpose.

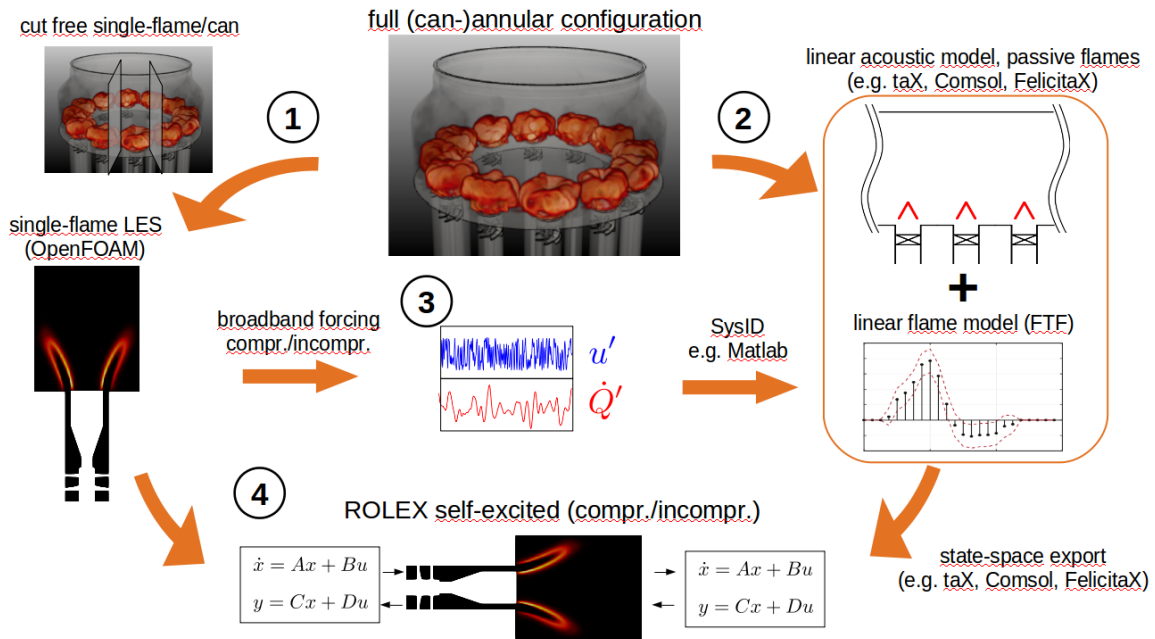


Figure 3.15: Individual steps necessary to set up and simulate LC of (can-)annular configurations with the proposed ROLEX model.

3.6 Application of the Proposed Hybrid Models

Two types of symmetry-enhanced hybrid models have been presented in this chapter: The time domain Bloch-wave approach (see Fig. 3.10) and the ROLEX model (see Fig. 3.11 and Fig. 3.12). Both model types are, in principle, capable of predicting LC oscillations of (can-)annular configurations but are subject to different restrictions and have a different focus. The present section summarizes the steps necessary to apply the hybrid models to predict LC oscillations of a real (can-)annular configuration. Afterward, the limitations of each model are discussed.

Figure 3.15 visualizes the steps necessary to apply the ROLEX model proposed. The steps include pre-processing to provide all required model ingredients and the actual simulation of the self-excited hybrid model. They are:

1. Cut the full (can-)annular configuration considered at appropriate locations to obtain the CFD domain of the hybrid model. Generally, the CFD domain has to include one flame in its entirety, even when exposed to high pulsation amplitudes. If compressible coupling is used, the acoustic field must be plane at the cutting interfaces. In the case of the low-Mach setup, the cut-free domain has to be acoustically compact. Set up the CFD (LES) and validate the predicted mean flow (if possible).
2. Construct a linear acoustic state-space representation of the configuration considered (see Sec. 3.3). The flames are considered as passive temperature jumps. The heat release rates and the velocity at the reference positions of the individual flames are selected as in- and outputs to couple the nonlinear flame models. Additional in- and outputs are the variables that couple the CFD domain (f and g waves in the compressible and v' and Q' in the

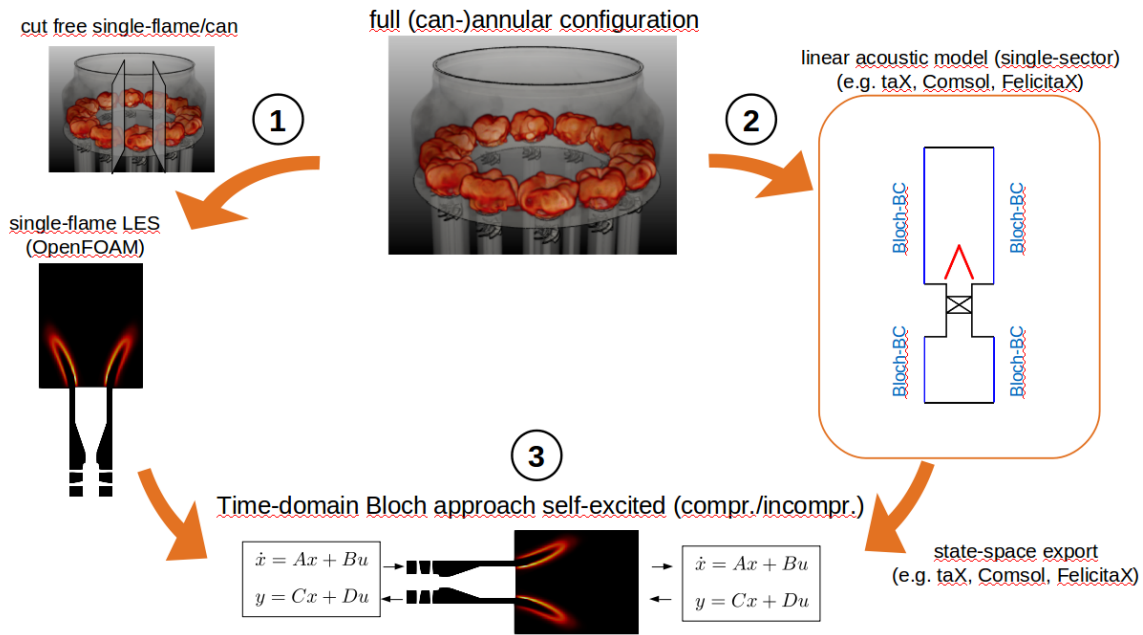


Figure 3.16: Individual steps necessary to set up and simulate LC of (can-)annular configurations with the proposed time domain Bloch-wave approach.

low-Mach case).

3. Identify the FTF, which serves as the linear part of the flame model employed (see Fig. 3.13). The FTF can be computed using the CFD/SI technique by broadband forcing of the CFD domain cut free in step 1. Alternatively, an experimentally measured or modeled FTF can be used.
4. Combine all model ingredients and simulate the hybrid model of the self-excited system.

Figure 3.16 visualizes the steps necessary to apply the time domain Bloch-wave approach. They are:

1. Set up the single-flame CFD simulation. Same as for the ROLEX approach.
2. Construct a linear acoustic state-space representation of one sector of the configuration considered (see Sec. 3.3). Depending on the type of coupling (CBSBC or low-Mach $v' - Q'$), the acoustic model represents the parts of the sector that are not resolved by CFD or the entire sector with the flame considered as passive temperature jump. Select the azimuthal mode order m and apply the corresponding BBC from Eq. (3.3). The in- and outputs of the LOM are the variables that couple the CFD domain (f and g waves in the compressible and v' and Q' in the low-Mach case).
3. Combine LOM and CFD and simulate the hybrid model of the self-excited system.
4. Repeat from 2. for all azimuthal mode orders of interest

The ROLEX model includes all modes of the system considered in one simulation and does not assume a certain symmetry of the modes. It can, in principle, account for nonlinear phenomena such as mode interaction, symmetry breaking, and mode localization, and it can predict the wave structure emerging from degenerate modes (standing/spinning). However, preparing the hybrid model involves multiple steps, most notably identifying a linear flame model, which requires some computational resources prior to the actual simulation. Additionally, the model heavily relies on the nonlinear flame model employed. Although the flame LOMs are continuously adapted to match the real flame dynamics, they are restricted by their pre-defined model structure. For example, the block-structured models employed here rely on the separability of a linear dynamic and a nonlinear static part, which is not always justified. Using more sophisticated models is possible but may come at the cost of a more complex or less robust online adaptation. In general, whether the model employed can correctly represent all important nonlinear features of the investigated system cannot be assessed in advance. Only a thorough posterior comparison of CFD and flame model output will hint at whether the flame model employed is appropriate.

In contrast, the time domain Bloch approach requires less preparation, as it does not need the knowledge of linear flame dynamics. A high-fidelity CFD simulation directly resolves the only flame present in the hybrid model. Flame dynamics are thus represented in the best possible way. However, a single simulation run only covers one azimuthal mode order m . If the stability and the LC amplitudes of each mode order shall be investigated, multiple simulation runs are necessary. Nonlinear phenomena involving multiple mode orders cannot be captured. Symmetry breaks, as well as their effects, are not predictable using this approach.

4 Calibrating Global Reaction Mechanisms

A chemical reaction mechanism is required to close the energy and species source terms in Eqs. (2.3),(2.4). Detailed chemical reaction mechanisms (DM) are very accurate but involve dozens to hundreds of species and hundreds to thousands of reactions. Additionally, the production rates of individual species differ by several orders of magnitude, which makes the resulting system of equations very stiff. The use of DM in LES is thus considered impractical. One way of reducing the computational effort is to use global chemical reaction mechanisms (GM). A GM is an empirical reaction scheme that represents only the formation and consumption of major species based on only a few reactions. The reactions involved are calibrated to best represent the production rate of the considered major species and to match global flame properties such as the laminar flame speed s_L and flame thickness δ_L . This calibration, however, is typically only valid for one specific fuel composition and a narrow range of operating conditions.

The turbulent validation case considered in Sec. 5.3 is operated with a CH₄-H₂- mixture, for which, to the author's knowledge, no GM is available. This section outlines the basic principles of the calibration method used to obtain a GM for a given operating condition. A more detailed description, including a thorough analysis of the performance of the resulting GM, is found in PAPER_MECH reproduced in App. 4.

The proposed approach improves a method developed by Polifke *et al.* [115]. A chemical mechanism is a set of reactions with reaction rates \mathbf{r}_l , with $l = 1, \dots, L$, where L is the number of reactions of the mechanism. These reactions generate or consume species C_i , with $i = 1, \dots, N$, where N is the number of species of the mechanism. The sum of reactions that convert individual species into each other and constitute the chemical mechanism write

$$\sum_{i=1}^N \nu'_{il} C_i \leftrightarrow \sum_{i=1}^N \nu''_{il} C_i; l = 1, \dots, L, \quad (4.1)$$

where ν'_{il} and ν''_{il} are the forward and backward stoichiometric coefficients of species C_i in reaction l .

With the above definitions, the net rate of production of species C_i , denoted ω_i , is the sum of the production rate of species C_i in each reaction

$$\omega_i = \sum_{l=1}^L \nu_{il} r_l, \quad (4.2)$$

where $\nu_{il} = \nu''_{il} - \nu'_{il}$ follows from the stoichiometric coefficients in the reaction scheme. The volumetric heat release rate ω_q of the chemical reactions writes

$$\omega_q = - \sum_{l=1}^L h_l r_l, \quad (4.3)$$

where h_l is the standard enthalpy of reaction. Note that for an exothermic reaction $h_l < 0$ and the corresponding $\omega_q > 0$.

Equations (4.2) and 4.3 can be written in matrix form

$$\mathbf{p} = \mathbf{M}\mathbf{r}, \quad (4.4)$$

where the species production rates and the heat release rate are collected to form the production rate vector

$$\mathbf{p} = [\omega_1, \dots; \omega_N, \omega_q]. \quad (4.5)$$

The matrix \mathbf{M} is of size $(N + 1) \times L$ and its coefficients are given by v_{il} and h_l .

The goal of the following considerations is to reduce a detailed mechanism, which comprises a large number of species and reactions, to a global mechanism, comprising only a few reactions L_g and species N_g , with $L_g \ll L$ and $N_g \ll N$. This involves finding a (reduced) set of reaction rates \tilde{r}_l with $l = 1, \dots, L_g$, which yields production rates p_i with $i = 1, \dots, N_g + 1$ of the species in the global mechanism that match the production rates of these species in the detailed mechanism.

Directly obtaining reaction rates \tilde{r}_l from a given set of production rates p_i would require the inversion of the reaction scheme in Eq. (4.4). This is generally impossible because the matrix \mathbf{M} is not quadratic. A DM usually has more reactions than species, while for a GM, it is the opposite. The system of Eqs. (4.4) is thus overdetermined for a GM. Polifke *et al.* [115] address this issue by selecting only a sub-set of L_g so-called principal species, from which the reaction rates \tilde{r}_l are obtained.

In PAPER_MECH, we generalize this approach by solving Eq. (4.4) for the unknown target reaction rates \tilde{r}_l of the global mechanism by employing the weighted least squares method

$$\tilde{\mathbf{r}} = (\mathbf{M}^T \mathbf{W} \mathbf{M})^{-1} \mathbf{M}^T \mathbf{W} \mathbf{p}, \quad (4.6)$$

where \mathbf{W} is a diagonal matrix containing user-defined weights. In case a number L_g of selected production rates are weighted with $w_i = 1$, while the weighting of all other production rates is $w_i = 0$, the method reduces to the original approach by Polifke *et al.* [115]. The weighting is especially useful for normalizing the production rate vector \mathbf{p} , which is otherwise dominated by the comparably large value of the heat release rate ω_q . Additionally, species of special interest for the case considered can be weighted higher to improve the accuracy of their prediction. Lastly, carefully choosing the weighting helps smoothing the resulting target reaction rates \tilde{r}_l such that they can be easily fitted with the chosen ansatz.

Now that the target reaction rates \tilde{r}_l are defined, the last step is to match these rates by tuning the coefficients of a presumed functional form of the reaction rates \hat{r}_l of the GM. A usual ansatz for this functional form is the rate law

$$\hat{r}_l = k_{fl} \prod_{i=1}^N [C_i]^{\tilde{v}'_{il}} - k_{rl} \prod_{i=1}^N [C_i]^{\tilde{v}''_{il}}, \quad (4.7)$$

where the reaction rate depends on the molar species concentrations $[C_i]$. An Arrhenius temperature dependence is used for the forward rate coefficients k_{fl}

$$k_{fl} = A_l T^{b_l} \exp\left(-\frac{E_{A,l}}{RT}\right), \quad (4.8)$$

where A_l is the pre-exponential factor, b_l is the temperature exponent, and $E_{A,l}$ is the activation energy of reaction l . If the reaction considered is reversible, the thermodynamic equilibrium constant $K_{eq,l}$ links the forward and backward rate coefficient

$$K_{eq,l} = \frac{k_{fl}}{k_{rl}}. \quad (4.9)$$

Otherwise, the backward rate coefficient in (4.7) is $k_{rl} = 0$. In a DM, the species concentration exponents $\tilde{\nu}_{nl}$ in Eq. (4.7) are the stoichiometric coefficients ν_{il} of the elementary reactions. For the GM, these exponents are additional tuning parameters. To summarize, $\tilde{\nu}_{il}, A_l, b_l, E_{A,l}$ are the free parameters that have to be calibrated to match the target reaction rates \tilde{r}_l obtained from Eq. (4.6). To find the free coefficients, the cost function f_l

$$f_l = \left\langle \left| \ln \left(\left| \frac{\hat{r}_l(n)}{\tilde{r}_l(n)} \right| \right) \right| \left| \frac{\tilde{r}_l(n)}{\max(\tilde{r}_l)} \right|^\eta \right\rangle, \quad (4.10)$$

which represents the deviation of the Arrhenius-based reaction rate \hat{r}_l from the target reaction rate \tilde{r}_l on a logarithmic scale, is minimized. n represents the grid point on which the target reaction rates \tilde{r}_l are computed and $\langle \dots \rangle$ is the average carried out over all grid points n .

According to Polifke *et al.* [115], the production rate vector \mathbf{p} in Eq. (4.6) used to compute the target reaction rates $\tilde{r}_l(n)$ for Eq. (4.10) is obtained by solving a freely propagating laminar 1D flame with a DM at a specific operating condition (pressure, temperature of educts, equivalence ratio). This yields the target reaction rates $\tilde{r}_l(n)$ over all grid points of the 1D flame solution. This approach is also used in the present work. However, the production rates can, in principle, also be obtained from different flame-type solutions with the DM or for multiple operating conditions. These production rates may be appended to the production rates \mathbf{p}_{1D} obtained from the freely propagating flame

$$\mathbf{p} = [\mathbf{p}_{1D}, \mathbf{p}_s, \mathbf{p}_h, \dots], \quad (4.11)$$

to get a more general result for the reaction rates. The grid points n now also involve other operating conditions and/or other flame solutions such as, for example, flames with strain \mathbf{p}_s and/or heat loss \mathbf{p}_h .

5 Investigated Validation Cases

The hybrid models presented in Sec. 3 were developed and validated based on a generic laminar 4-can burner called “*Rohrbrennkammer 4*” (RBK4). The models developed were also applied to an experimental annular combustion test-rig operated at NTNU (the “Intermediate Pressure Annular Combustor” [116]), for which experimental measurements of LC oscillations are available [113]. The results of the time domain Bloch-wave approach applied to the RBK4 combustor are published in PAPER_BLOCH. The application of the compressible ROLEX model from Fig. 3.11a) to the RBK4 combustor is presented in PAPER_ROLEX.

This section presents the unpublished results of applying the hybrid models developed to additional cases. First, the solver and the numerical setups of the considered cases are outlined. Afterward, the results of the low-Mach, symmetry-preserving ROLEX model (see Fig. 3.12b)) applied to the RBK4 combustor are presented. The section concludes with applying the low-Mach, symmetry-preserving ROLEX model and the time domain Bloch-wave approach to the NTNU annular rig.

5.1 Numerical Setup

5.1.1 Solver and Setup for Laminar Cases

The CFD simulations of the laminar RBK4 cases employ a modified version of the solver `rhoReactingFoam` from the open-source finite-volume toolbox `OpenFoam`¹ [99]. Depending on the version, the solver implements either the compressible governing equations (2.1)-(2.5) or the low-Mach formulation (2.6)-(2.10). The solver was developed and validated by Stefan Jaensch within a previous research project [117]. The main difference to the standard `rhoReactingFoam` solver is the modeling of the species diffusion coefficients D_i , which is here based on species-specific Schmidt numbers $D_i = \nu / Sc_i$, whereas the standard solver assumes equal Sc-Numbers for all species.

The dynamic viscosity μ and the heat diffusivity α are computed from Sutherland’s law. The chemical source terms ω_i and ω_q are obtained by solving the global two-step BFER reaction mechanism for methane-air combustion [118].

The PIMPLE algorithm is employed to solve the pressure-velocity coupling for the compressible cases, and the PISO [119] algorithm is used for low-Mach cases. A second-order implicit time integration scheme is used. The time step is fixed at $\Delta t = 5 \cdot 10^{-7}$ s, which yields a hydrodynamic CFL number of less than 0.1. Spatial discretization is done by blending a second-order

¹Version 4.x, available at <https://github.com/OpenFOAM/OpenFOAM-4.x>

central difference and an upwind scheme using a Sweby limiter [119].

5.1.2 LES Solver and Numerical Setup

The turbulent reactive flow solver employed is a modified version of `reactingFoam` from OpenFoam [99]. The solver and the turbulence-chemistry interaction model were mainly developed and implemented by Alp Albayrak within a previous research project [65]. The LES solver implements the filtered low-Mach governing equations

$$\frac{\partial \tilde{\rho}}{\partial t} + \nabla \cdot (\tilde{\rho} \tilde{\mathbf{u}}) = 0 \quad (5.1)$$

$$\frac{\partial (\tilde{\rho} \tilde{\mathbf{u}})}{\partial t} + \nabla \cdot (\tilde{\rho} \tilde{\mathbf{u}} \tilde{\mathbf{u}}) = -\nabla \tilde{p}_d + \nabla \cdot \left([\mu + \mu_T] \left[\nabla \tilde{\mathbf{u}} + (\nabla \tilde{\mathbf{u}})^T - \frac{2}{3} (\nabla \cdot \tilde{\mathbf{u}}) \mathbf{I} \right] \right) \quad (5.2)$$

$$\frac{\partial (\tilde{\rho} \tilde{h})}{\partial t} + \nabla \cdot (\tilde{\rho} \tilde{\mathbf{u}} \tilde{h}) = \nabla \cdot \left([\mathcal{F} \mathcal{E} \alpha + (1 - \mathcal{S}) \alpha_T] \nabla \tilde{h} \right) + \frac{\mathcal{E}}{\mathcal{F}} \omega_q \quad (5.3)$$

$$\frac{\partial (\tilde{\rho} \tilde{Y}_i)}{\partial t} + \nabla \cdot (\tilde{\rho} \tilde{\mathbf{u}} \tilde{Y}_i) = \nabla \cdot \left(\left[\mathcal{F} \mathcal{E} \frac{\mu}{Sc_i} + (1 - \mathcal{S}) \frac{\mu_T}{Sc_T} \right] \nabla \tilde{Y}_i \right) + \frac{\mathcal{E}}{\mathcal{F}} \omega_i \quad (5.4)$$

$$p_t = \tilde{\rho} R \tilde{T}, \quad (5.5)$$

where $(\tilde{\cdot})$ is the filtering operator. μ_T and α_T denote the turbulent viscosity and thermal diffusivity resulting from sub-grid scale fluctuations. The WALE turbulence model [120] is employed to compute μ_T based on the resolved fields (see [65] for further details on the turbulence modeling). Turbulent thermal and mass diffusivity α_T and D_T are modeled by assuming a constant turbulent Prandtl $Pr_T = \frac{\mu_T}{\rho \alpha_T} = 0.6$ and Schmidt number $Sc_T = \frac{\mu_T}{\rho D_T} = 0.6$ for each species. As in the laminar solver, individual but constant laminar Schmidt numbers Sc_i are provided for each species i . The same solution algorithm and numerical schemes as in the laminar case are employed. The time step is fixed at $\Delta t = 2.5 \cdot 10^{-7}$ s, ensuring a hydrodynamic CFL number below 0.3. Reactions are modeled using the 3-step global mechanism from `PAPER_MECH` calibrated to the present operating point. Table 5.1 shows the resulting mechanism parameters (c.f. Eq. (4.8) and Eq. (4.1)).

Table 5.1: Parameters of the global 3-step mechanism calibrated for the operating point of the NTNU annular rig. SI units.

	A	b	T_a	ν'_{CH_4}	ν'_{H_2}	ν'_{O_2}
R1	$1.56 \cdot 10^8$	0.003	10861	0.63	–	0.52
R2	$5.26 \cdot 10^8$	0.006	11618	–	–	0.5
R3	$1.14 \cdot 10^9$	0.005	9088	–	1.0	0.5

An extended version of the dynamic thickened flame model [121, 122] models turbulent combustion. The laminar flame thickness δ_L is artificially thickened by the factor \mathcal{F} introduced in Eqs. (5.4) and (5.3). The thickened flame cannot account for the effects of turbulent flame wrinkling caused by eddies smaller than the thickened flame width. This is corrected by introducing

the efficiency function \mathcal{E} . The dynamic thickened flame model aims to modify the governing equations only in the immediate vicinity of the reaction zone. This is achieved by introducing a sensor function \mathcal{S} . The thickening factor and efficiency function read

$$\mathcal{F} = 1 + \left(n \frac{\Delta_x}{\delta_L} - 1 \right) \underbrace{\tanh \left(\beta_1 \frac{\Omega}{\Omega_0} \right)}_{\mathcal{S}}, \quad (5.6)$$

$$\mathcal{E} = \left[1 + \min \left(\mathcal{F}, \Gamma \frac{u'_\Delta}{s_L} \right) \right]^{\beta_3}, \quad (5.7)$$

where Γ is a function depending on the resolved velocity field, u'_Δ represents the flame filtered sub-grid scale rms velocity (see [122]) and Δ_x is the LES filter width. A prescribed number of $n = 7$ cells resolve the thickened flame front. An Arrhenius-like function Ω is used to track the flame region and is defined as

$$\Omega = Y_F^{n_F} Y_O^{n_O} \exp \left(-\beta_2 \frac{T_a}{T} \right) \quad (5.8)$$

where T_a is the activation temperature and Ω_0 denotes the maximum of the Arrhenius-like function across the laminar flame front. The model constants β_2 and β_1 control the activation threshold and the width around the reaction zone, where the sensor \mathcal{S} is active. β_3 controls the efficiency function \mathcal{E} and thus directly acts on the propagation speed of the thickened flame front. As β_3 is in the exponential of Eq. (5.7), it weakly influences \mathcal{E} for reasonably small values of \mathcal{F} . However, if \mathcal{F} is large (if the flame is resolved on a coarse grid), the influence of β_3 also becomes large. Charlette *et al.* [123] proposes a dynamic adjustment of β_3 , depending on resolved fields. This dynamic formulation is not implemented, but the information provided in [123] is used to set a constant (but case dependent) β_3 . In the present case, the model coefficients are $\beta_1 = 200$, $\beta_2 = 0.6$, and $\beta_3 = 0.5$.

5.2 Generic Laminar 4-Burner System

5.2.1 Case Setup

The generic laminar can-combustor RBK4 depicted in Fig. 3.2 comprises four cans coupled via an upstream plenum. The burner/flame zone in the individual cans was investigated in numerous previous studies, although in a different context, e.g., see [47, 58, 124]. A fixed pressure is imposed at the downstream termination of the cans, which yields a fully reflecting $R_d = -1$ boundary condition. A fixed velocity is imposed at the plenum's upstream termination, which yields a fully reflecting $R = 1$ boundary condition. The computational domain is pseudo-2D. The plenum is “closed” using periodic boundary conditions.

The can-can coupling and the acoustic characteristics of the downstream termination of the cans are quite different compared to applied can-annular combustors (see Sec. 3.2.1). This specific choice is because the CFD setup of the entire configuration is relatively simple for this particular setup, allowing standard Dirichlet boundary conditions at the in- and outlet. However, the

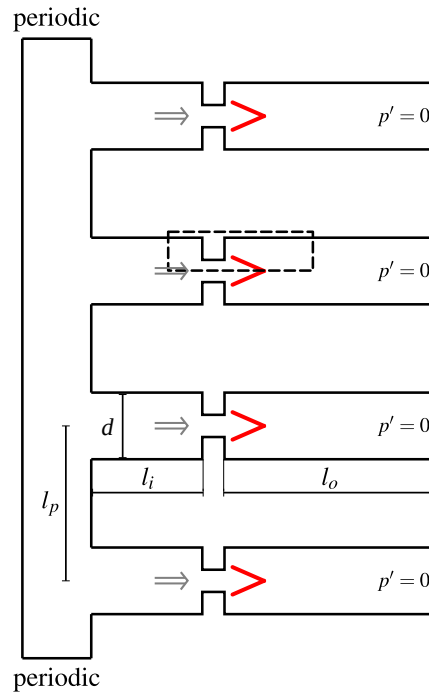


Figure 5.1: Sketch of the RBK4 configuration used to develop and validate the proposed hybrid strategies. The dashed box indicates the CFD domain of the hybrid model.

Table 5.2: Geometrical measures of RBK4.

l_i (m)	l_o (m)	l_p (m)	d (m)
0.05	0.1	0.1	0.005

RBK4 system still yields the same symmetry properties and Bloch-symmetric thermoacoustic modes as a real can-annular combustor, which qualifies it as a first validation case for the hybrid models developed. The dimensions of the RBK4 configuration are tuned to yield a thermoacoustically unstable system with realistic modal growth rates and non-trivial mode shapes. Table 5.2 summarizes the geometrical measures of the RBK4 configuration.

The entire RBK4 configuration is resolved in a fully compressible CFD simulation to generate reference data to validate the proposed hybrid approaches. The structured grid contains 596K hex-cells. In the region of burner-plate and flame, the mesh is uniform with a cell size of $25\ \mu\text{m}$, corresponding to an average of 18 cells within the reaction zone (similar to the mesh used by [58] and [125]). The mesh is significantly coarser in the remaining parts of the domain, where mainly acoustic wave propagation has to be modeled. A fixed velocity boundary condition at the inlet and fixed pressure boundary condition of 1 atm at the outlet are used. Adiabatic slip conditions are imposed at the walls, except at the burner plate, for which a no-slip condition with a fixed temperature of 373 K is set.

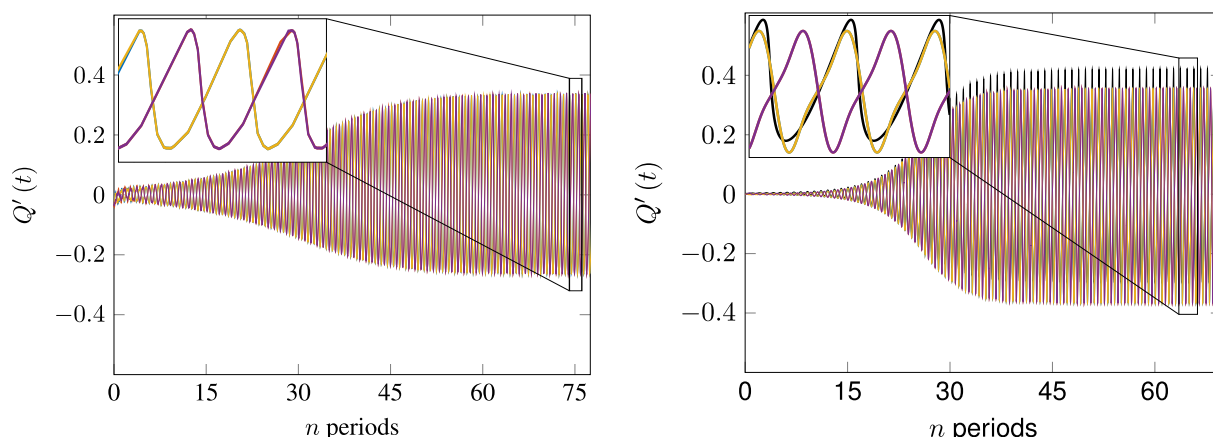


Figure 5.2: Normalized heat release rate fluctuation in the individual cans. Left: compressible CFD of full configuration. Right: low-Mach symmetry preserving ROLEX model. Black line shows the heat release rate fluctuation recorded in the CFD domain, serving as “clone model”.

5.2.2 Hybrid Model Results

The RBK4 configuration is investigated using four different model setups:

1. Compressible CFD of entire configuration as reference (see PAPER_BLOCH and PAPER_ROLEX)
2. Compressible time domain Bloch-wave approach (see PAPER_BLOCH)
3. Compressible ROLEX model (see PAPER_ROLEX)
4. Low-Mach, symmetry preserving ROLEX model (see present section)

Using the compressible, symmetry-preserving setup in the present configuration is impossible, as the burner/flame studied exhibits an unstable ITA mode [126]. Therefore, the original compressible setup of Fig. 3.11a) was used in PAPER_ROLEX.

The low-Mach, symmetry-preserving setup results are compared with the monolithic CFD results in the following. The RBK4 configuration exhibits an unstable “push-pull” mode of ITA origin. Such a mode is characterized by fluctuations of opposite sign in adjacent cans (see Sec. 3.2.2). Figure 5.2 shows the normalized heat release fluctuations in the individual cans for the monolithic CFD (left) and the low-Mach, symmetry-preserving ROLEX model on the right. The amplitude and signal shape of the heat release rates, as well as the “push-pull” mode structure predicted by the LOM, agree reasonably well with the results of the full CFD. The CFD part of the hybrid model plotted in black shows a slightly different signal shape, which the Wiener-type flame models can not entirely reproduce. Note that in this model setup, the CFD domain is not part of the self-excited system but only serves as a “clone model” for identifying the flame model parameters.

Figure 5.3 analyses the results in frequency domain. Here, the frequency \mathfrak{F} is normalized by the first “pure” plenum eigenfrequency defined as $f = c/U$, where c denotes the speed of sound

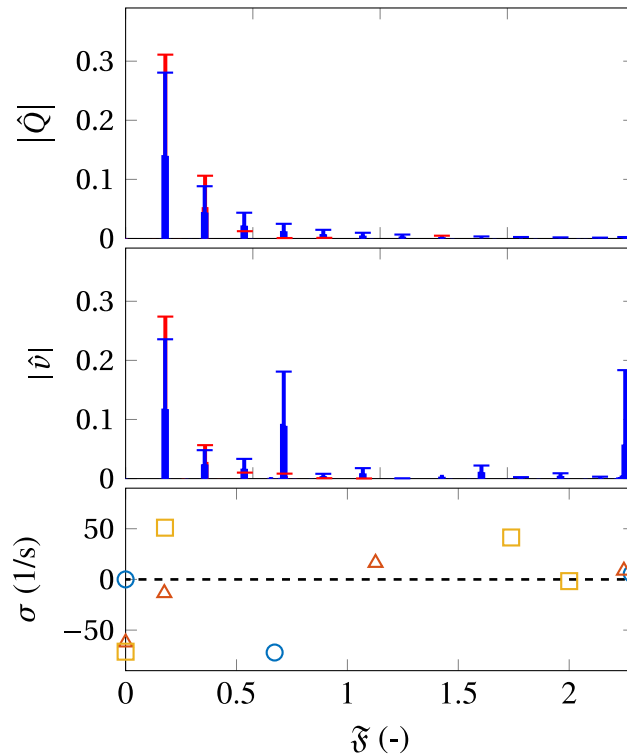


Figure 5.3: LC spectrum of heat release rate (top) and reference velocity (middle). Hybrid approach in red, monolithic CFD in blue. Result of linear stability analysis (bottom) shows eigenmodes of azimuthal order $m = 0$ (blue circles), $m = 1$ (red triangles), and $m = 2$ (orange squares).

in the fresh gas, and U is the circumference of the plenum. The top plot and the middle plot of 5.3 show the amplitude spectrum of heat release rate and velocity fluctuation at the flame reference position exemplary for one can. Due to the symmetry of the present “push-pull” mode, the amplitude spectra of the other cans are identical and thus not shown. The results from the monolithic CFD are plotted in blue. Those from the hybrid model are plotted in red. For reference, the bottom plot shows the eigenfrequencies of the configuration obtained from linear stability analysis (see PAPER_BLOCH).

The hybrid model captures the amplitude and frequency of the fundamental unstable mode very well. Also, the acoustic resonance of a higher harmonic with the axial mode at $\tilde{\mathfrak{F}} \approx 0.7$ is captured, although with lower amplitude. Due to the limitations of the nonlinear flame model employed, further higher harmonics are not resolved properly, which is not considered relevant for applied configurations. Overall, the hybrid model and the monolithic CFD agree well, validating the proposed approach. At the same time, the computational cost of the hybrid model is about ten times smaller than that of full CFD. In realistic setups, which typically have much more than four cans, the reduction of computational cost will be significantly higher.

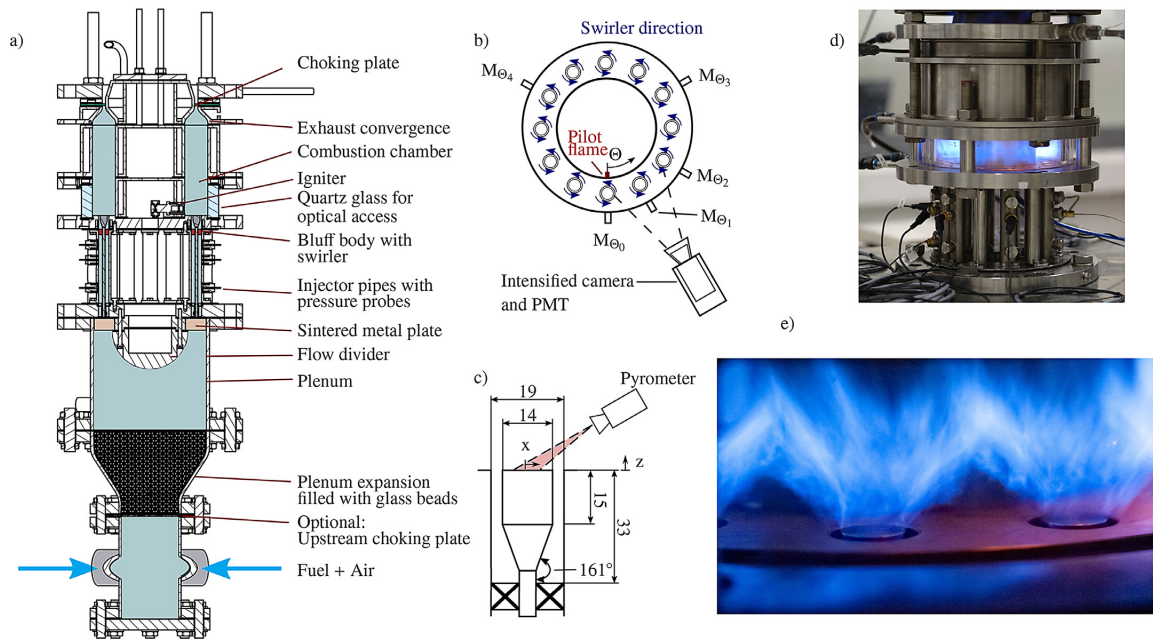


Figure 5.4: Intermediate pressure annular combustor operated at NTNU. Reproduced from [113].

5.3 NTNU Annular Rig

5.3.1 Case Setup

The intermediate pressure annular test-rig [113, 116] operated at NTNU was selected as an annular validation case for the hybrid models developed. Figure 5.4 gives an overview of the design of the test-rig.

The test-rig comprises 12 swirl-stabilized flames in a common annular chamber. The chamber is terminated with a choked nozzle at the downstream side, allowing the rig to operate at pressures up to 3.5 bar. The chamber is fed by 12 injector tubes, each containing the swirler and a bluff body to avoid flame flashback. The injector tubes are fed by a large plenum, which is acoustically separated by a sinter plate. A $H_2 - CH_4$ fuel/air mixture is supplied at the plenum inlet. Due to the long residence time in the plenum, perfectly premixed conditions can be assumed at the flame. The metal walls of the chamber are water-cooled, and their steady-state temperature was determined experimentally. The flames are optically accessible through a quartz-glass window in the lower part of the outer chamber wall. Five injector tubes contain two pressure conductors each, which can be used to reconstruct the acoustic field within the injector tubes and the chamber.

For the present purpose, an operating point that exhibits an intermediate amplitude LC of a strongly spinning first-order azimuthal mode in the experiment was chosen. For this operating point, the chamber pressure is $p = 2.16 \text{ bar}$, and the rig is fueled with a volume ratio of 57% CH_4 and 43% H_2 at an equivalence ratio of $\phi = 0.8$. The total mass flow rate through the rig is $\dot{m} = 97 \text{ g/s}$. For further details on this operating point, in particular the measured LC oscillations,

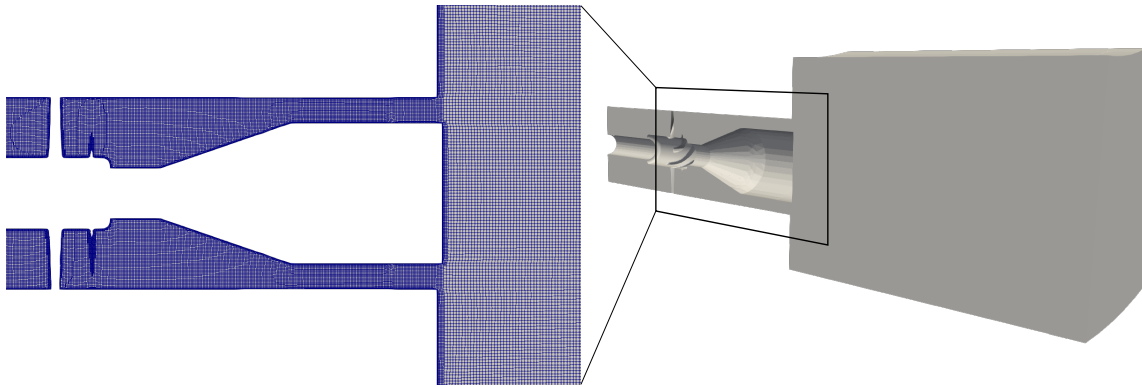


Figure 5.5: Cut through the single-sector CFD domain of the NTNU annular rig (right). Mesh in the swirler and flame anchoring region is shown on the left.

the reader is referred to [113]².

According to Fig. 3.15 and Fig. 3.16, the first step in the proposed modeling strategies is to set up the single-flame LES. Here, the LES domain comprises one injector tube, cut shortly upstream of the swirler and a sector of the chamber, cut at approximately twice the steady flame height. The domain and the mesh are visualized in Fig. 5.5. The domain is discretized with a hex-dominant mesh of approx. 10M cells.

The mesh cells have an edge length of 0.15 mm in the swirler region and at the walls and a uniform edge length of 0.3 mm in the flame region. Resolving the flame with $n = 7$ grid points leads to a maximum thickening factor $\mathcal{F} < 10$. As the configuration is perfectly premixed, the laminar flame properties $s_L = 0.2882$ m/s, $\delta_L = 0.244$ mm and $\Omega_0 = 9.07 \cdot 10^{-6}$ needed as input for the thickened flame model, have to be provided for one single equivalence ratio $\phi = 0.8$ only. The velocity is fixed at the inlet and the pressure at the outlet. No-slip conditions with the experimentally obtained temperatures are imposed on the walls. A periodic condition is set at the azimuthal cutting interfaces of the chamber.

5.3.2 Results

5.3.2.1 Single-Sector LES

The test-rig is thermoacoustically unstable for the operating point considered. Therefore, no mean flame images or other mean-field measurements, which could be used to validate the single-sector LES results, are available for this operating point. Instead, phase-averaged flame images recorded during the LC oscillation serve as reference data. In order to compare the LES results with the experimental LC measurements, the LES is externally forced by imposing the LC velocity fluctuation at the inlet. The velocity fluctuation is reconstructed from the pressure measurements in one of the injector tubes using the two-microphone method.

The resulting heat release field in the LES is phase-averaged at the same phase angles as in the experiment and line-of-sight integrated to reproduce the images obtained experimentally.

²In [113], the considered operating point is denoted “ $\dot{m}_a = 91.87$ gs⁻¹, $P_H = 0.2$, $\Phi = 0.8$ ”

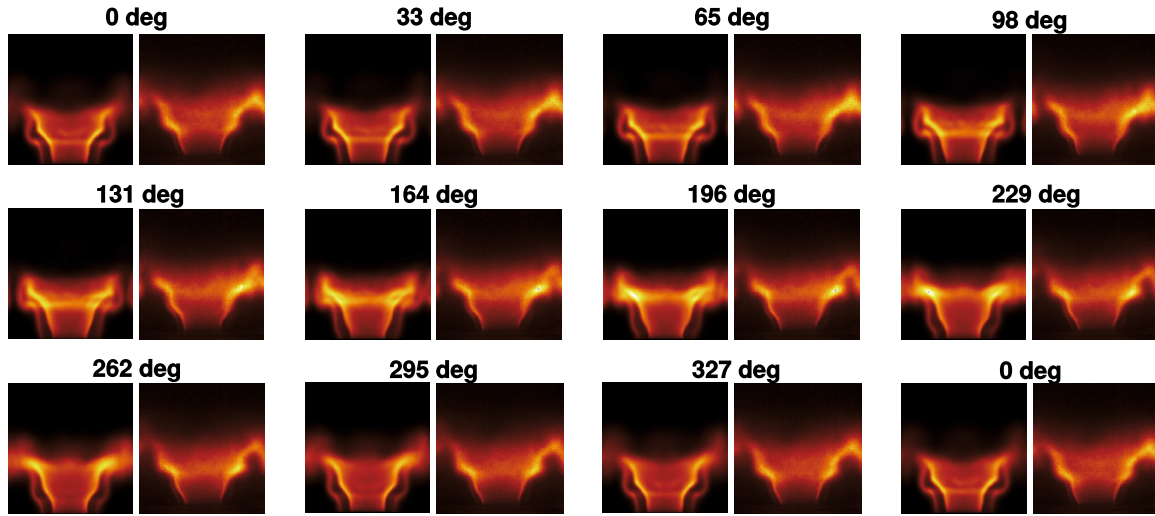


Figure 5.6: Phase-averaged line-of-sight integrated heat release distribution during LC oscillation. LES results in respective left plots, experimental measurements in right plots.

Unfortunately, the resulting flame shapes show some deviation w.r.t. the experiment, and flame anchoring is mispredicted. Instead of the V-flame shape observed in the experiment, the flame in the LES simulation also burns in the outer shear layer, forming an M-like flame shape.

Discrepancies of measured and actual wall temperatures in the experiment were identified as a possible reason for this mismatch. The temperatures of the diabatic walls were reduced to 300K to test this hypothesis. The resulting phase averaged, and line-of-sight integrated heat release rates are compared to the experimental OH* chemiluminescence measurements in Fig. 5.6. Despite the reduced wall temperatures, the LES shows noticeable deviations from the experiment. While the flame height and the flame center of gravity are approximately correct for all phase instants, the reaction rate in the outer shear layer is still over-predicted in the LES.

The most probable reason for the discrepancies is a misprediction of wall heat fluxes. Fully resolving the turbulent boundary layer is not feasible. The employed WALE turbulence model [120] is designed to adopt the turbulent viscosity - and by assuming a constant $Pr_T = 0.6$ also the thermal diffusivity - in the wall region. Wall functions thus should not be used [65]. However, it is yet unclear how well the WALE model with the present grid resolution at the wall represents the turbulent thermal boundary layer. Additionally, the thickened flame model alters the diffusion coefficients in the vicinity of the flame. According to Eq. (5.3), in the region where the sensor is active $\mathcal{S} = 1$, turbulent heat diffusion is disabled, and the laminar heat diffusion is augmented by the factor \mathcal{F} . This may increase or decrease the overall wall heat flux in this region. The effects on burner-anchored flames such as the considered ones, where the anchoring strongly depends on the wall heat fluxes, need further investigation. However, this is not the focus of this thesis and will be continued in a follow-up study. Here, the setup of the hybrid models was continued according to Figs. 3.16 and 3.15, though the single-sector LES leaves room for improvement. Due to the better agreement with the experimental flame shape, the cold-wall LES was employed in the following steps.

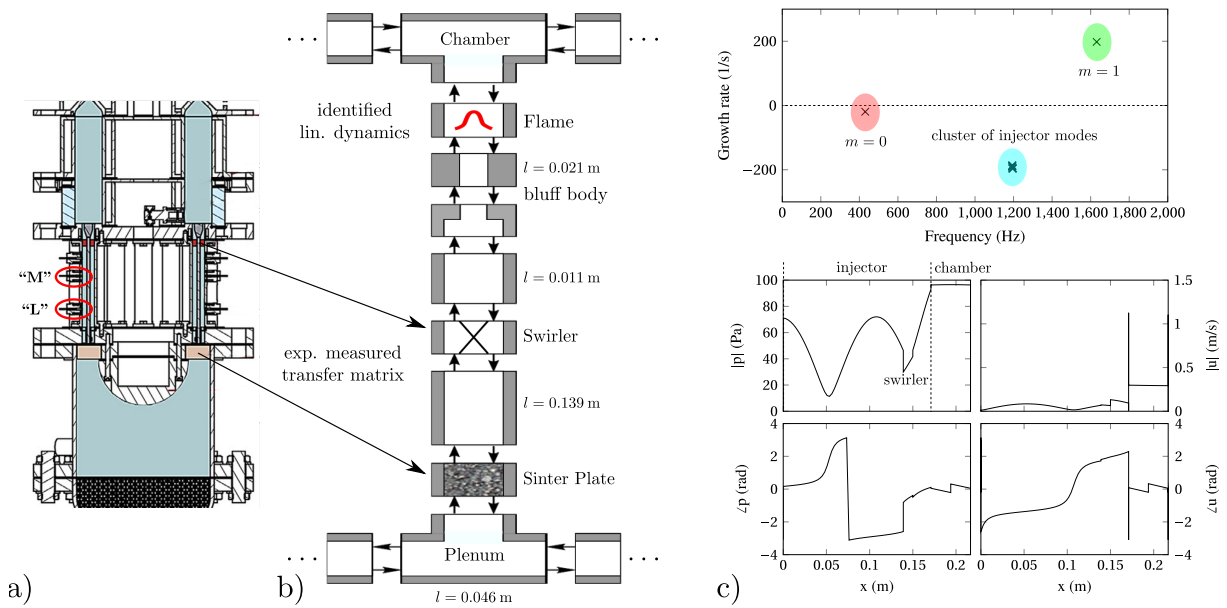


Figure 5.7: a) Cross section of the experimental test-rig (adopted from [113]). Microphone positions “M” and “L” marked with red ellipses. b) One sector of the 1D network model. c) Result of linear stability analysis of the 1D network model. The four plots at the bottom show the distribution of acoustic pressure and velocity for the dominant $m = 1$ mode shown in the pole map at the top.

5.3.2.2 Low-Order Model

The considered annular test-rig features a large plenum and chamber and thus is, at first glance, not representable with 1D network modeling tools. However, modeling the considered rig with an acoustic Helmholtz solver reveals that the relevant first-order azimuthal chamber mode, which is unstable in the experiment, features an essentially 1D acoustic field within the chamber and the injector tubes (see Fig. 3.3). Due to the sinter-plate at the injector tube inlets, the plenum is acoustically almost decoupled and plays a minor role.

This suggests that at least the relevant azimuthal modes can be represented in a quasi-1D network model using the in-house code taX [72]. The advantage of this modeling approach compared to, e.g., an acoustic Helmholtz solver is the drastically reduced number of states in the exported acoustic state-space model (3.5), making the overall hybrid model more efficient. Figure 5.7 illustrates one sector of the network model representing the annular rig. The duct lengths and area ratios of the injector are directly taken from the 3D configuration. The length of the ducts representing the plenum and the chamber is the azimuthal distance between two burners taken at the area-weighted center line of the chamber circumference. The area ratio between the injector and the plenum/chamber is the ratio of the injector cross-section to the azimuthal cross-section of the plenum/chamber, respectively. The measured acoustic characteristics of the sinter-plate and the swirler are included in the network model. The FTF representing linear flame dynamics was determined numerically (see Sec. 5.3.2.3). Note that the network model does not represent the axial extent of the chamber and plenum and can thus not correctly model axial modes $m = 0$ and higher-order azimuthal modes, which feature a non-uniform axial distribution in the chamber.

Linear stability analysis reveals a dominant unstable mode of order $m = 1$. The predicted frequency of $f_{lin} = 1620\text{Hz}$ is reasonably close to the LC frequency of $f_{exp} = 1588\text{Hz}$ measured in the experiment. The acoustic pressure associated with this mode well agrees with the result of the Helmholtz-solver shown in Fig. 3.3. Both points suggest that the presented network model can well represent the relevant acoustic characteristics of the annular rig.

5.3.2.3 Identification of Linear Flame Dynamics

The proposed ROLEX model requires a linear flame model (e.g., a FTF) as input. To compute the FTF according to the CFD/SI methodology [103], the single-flame LES was forced with a broadband velocity fluctuation at the inlet. The imposed broadband signal has a uniform power spectral density up to a frequency of $\approx 4000\text{Hz}$, a maximal amplitude of 10% of the mean flow velocity, and a signal length of 150 ms.

The linear flame model structure employed has to include a noise model to correctly represent the effect of turbulent combustion noise [114]. The *Autoregressive Exogenous Model* (ARX) is the most simple rational polynomial model providing a noise model. It reads

$$\dot{Q}'(t, \Theta) = \frac{B(q, \Theta)}{A(q, \Theta)} u'(t) + \frac{1}{A(q, \Theta)} e(t), \quad (5.9)$$

where $q^{-i} u'(t) = u'(t - i\Delta t)$ is the time shift operator,

$$\begin{aligned} A(q, \Theta) &= 1 + a_1 q^{-1} + a_2 q^{-2} \dots a_{n_a} q^{-n_a} \\ B(q, \Theta) &= 1 + b_1 q^{-1} + b_2 q^{-2} \dots b_{n_b} q^{-n_b} \end{aligned} \quad (5.10)$$

are polynomial filters, Θ contains the model parameters a_i, b_i , and $e(t)$ is a white noise term. It requires fewer model parameters than the more general *Box-Jenkins* model type. Consequently, the required time series length is shorter, at the cost that the identified noise model is not independent of the deterministic model part, as seen in Eq. (5.9) [114]. For the present purpose, the ARX model is the best compromise between accuracy and computational effort.

Figure 5.8 shows the gain and phase of the deterministic model part (the FTF) on the left side and the gain and phase of the identified noise model on the right side. The order of the polynomial filters shown in Eq. (5.10) is $n_a = 20$ and $n_b = 90$ at a sample time step of $\Delta t = 5 \cdot 10^{-5}\text{s}$. Note that the present linear flame model relies on a fairly large number of coefficients and a small sampling time step. This is related to the relatively high LC frequency $f \approx 1600\text{Hz}$, which has to be properly resolved, and the length of the impulse response $\Delta T \stackrel{!}{<} n_b \Delta t$, which has to be covered by the polynomial filter.

5.3.2.4 Hybrid Model Results

The NTNU annular rig is investigated using two different hybrid model setups:

1. Low-Mach, symmetry-preserving ROLEX model

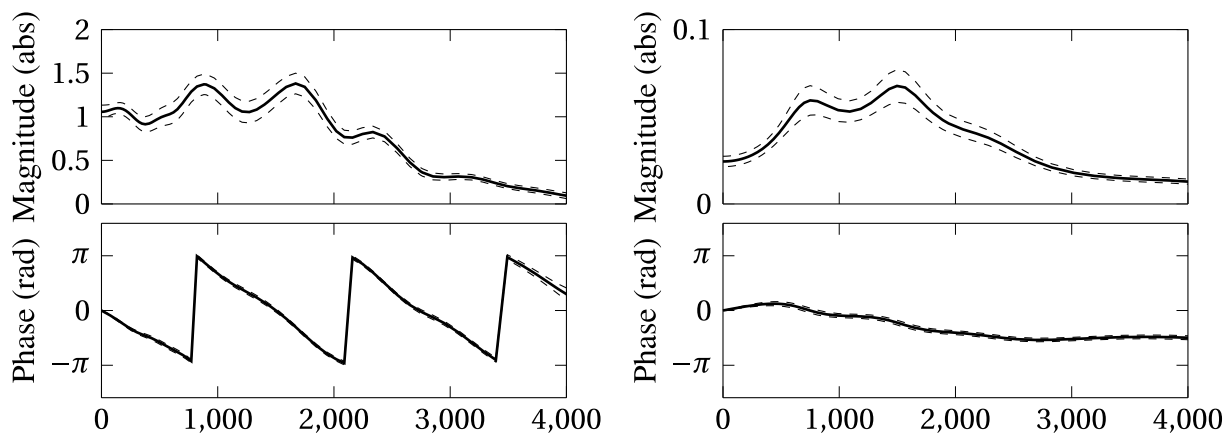


Figure 5.8: Gain and phase of the FTF on the left, gain and phase of the noise model on the right side. The dashed lines mark the 95% confidence interval.

2. Low-Mach time domain Bloch-wave approach

The results are compared to the experimental measurements of Indlekofer *et al.* [113]. The chosen operating point showing a strongly spinning $m = 1$ mode at moderate LC amplitudes is considered a realistic yet challenging test case for the developed hybrid models. The focus of the comparison between the hybrid model and experiment is on LC amplitudes and frequencies, as well as on the emerging wave pattern. Due to the symmetry-preserving nature of the observed LC wave pattern, the time domain Bloch-wave approach is applicable.

Unfortunately, the time-resolved integrated heat release rate fluctuation, which is easily accessible from the LES, was not measured during the LC oscillations. Nevertheless, the heat release fluctuations \dot{Q}' computed by the ROLEX model reveal the predicted wave pattern and mode symmetry. Figure 5.9 shows \dot{Q}'_n of all $N = 12$ flames computed with the ROLEX model, together with \dot{Q}'_{CFD} on which the online adaption of the flame model relies. The ROLEX model predicts a stable LC oscillation evolving from a noisy initial state. While the amplitudes are still growing (see Zoom 1 in Fig. 5.9), the oscillation pattern is rather erratic, with some flames being in sync while others oscillating at different amplitude and phase. Once a stable LC is reached (see Zoom 2 in Fig. 5.9), the individual flames oscillate at identical amplitudes and with a phase shift of $\pi/6$ relative to the neighboring flame, a pattern characteristic for a spinning $m = 1$ mode. Once formed, this pattern is stable for the entire simulation time. This demonstrates that the ROLEX model can correctly predict the emerging wave pattern of a degenerate mode, even if the initial state is different. The stable LC oscillation in Zoom 2 of Fig. 5.9 also shows an underlying modulation of lower frequency, the cause of which is yet unclear. The flame resolved by LES serves as “clone model”. Its response is shown with a black line in Fig. 5.9. Its amplitude matches that of the flame LOM fed with the same input, while the signal shape differs. This can be attributed to an incomplete representation of higher harmonics due to the limitations of the flame LOM employed.

In comparison, Fig 5.10 shows \dot{Q}' predicted by the Bloch-wave approach. Here, only the heat release rate in the LES is shown. The \dot{Q}'_n in the remaining sectors have equal amplitude and are phase-shifted according to

$$\hat{Q}'_n(t) = \hat{Q}'_{CFD}(t) e^{imn\frac{2\pi}{N}}, \quad (5.11)$$

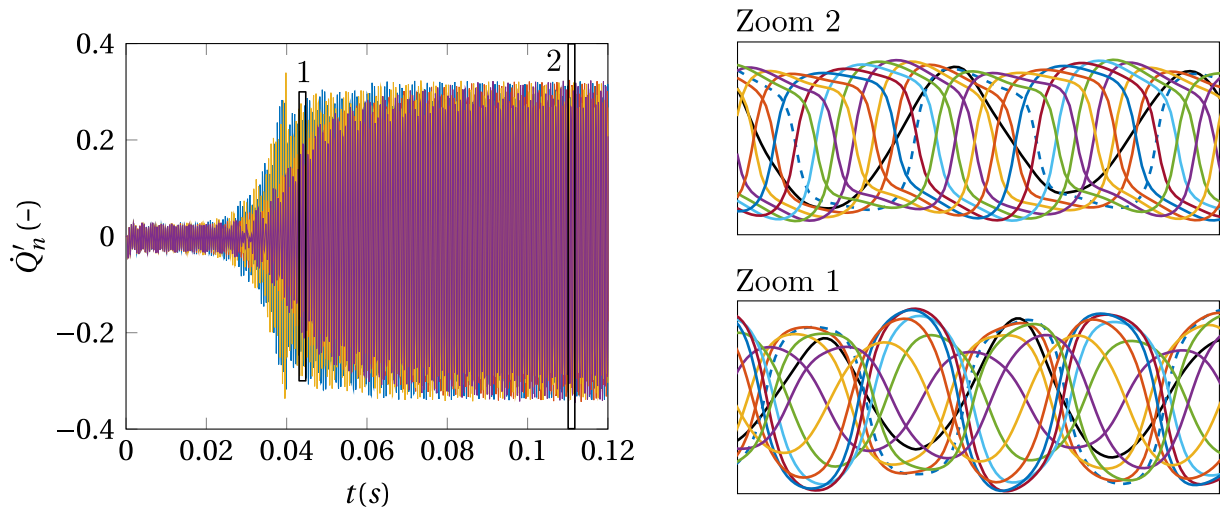


Figure 5.9: Normalized heat release rate fluctuation of the individual flames in the ROLEX model. Black line shows the heat release rate fluctuation recorded in the CFD domain, serving as “clone model”. The dashed line shows the flame model fed with the same input as the CFD. The zooms each show approx. two oscillation periods.

with $m = 1$ in the present case. The Bloch-wave approach also predicts a stable LC oscillation evolving from a noisy initial state. Compared to the ROLEX model prediction, the amplitude grows faster and saturates at a slightly lower level. Overall, the signal is more noisy, indicating that the noise model employed in the ROLEX model may underpredict the noise level. The faster growth can be addressed to the symmetry assumption of the Bloch approach. The noisy initial state is assumed to be perfectly synchronized in an $m = 1$ pattern. Consequently, the $m = 1$ mode starts at a non-zero initial amplitude in the Bloch approach. In contrast, in the ROLEX model, the individual sectors only synchronize noticeably at an intermediate amplitude level (see Zoom 1 in Fig. 5.9).

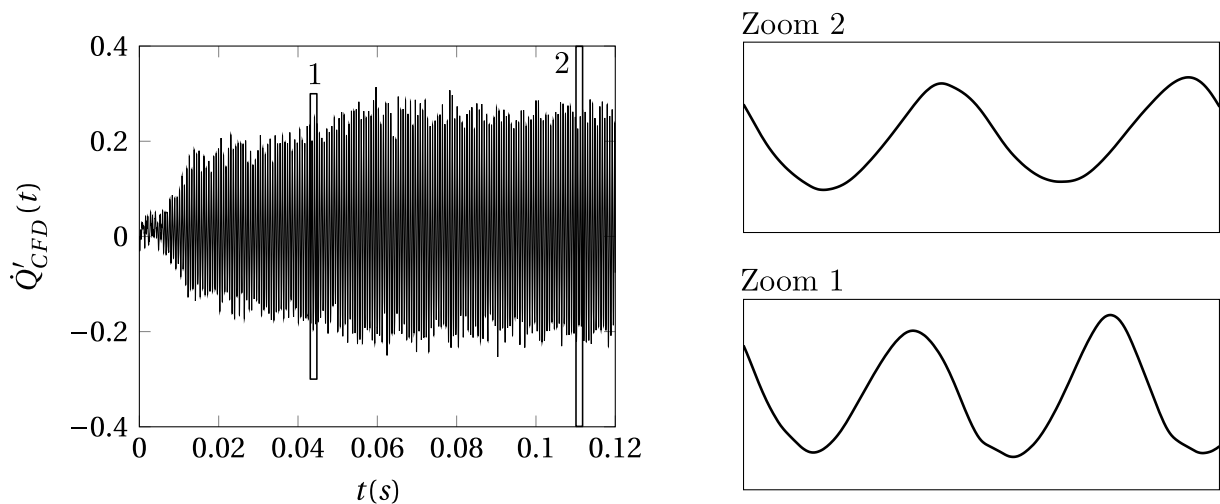


Figure 5.10: Normalized heat release rate fluctuation computed with the time domain Bloch-wave approach. The zooms each show approx. two oscillation periods.

The hybrid model results are compared to the experimental measurements of the LC pressure

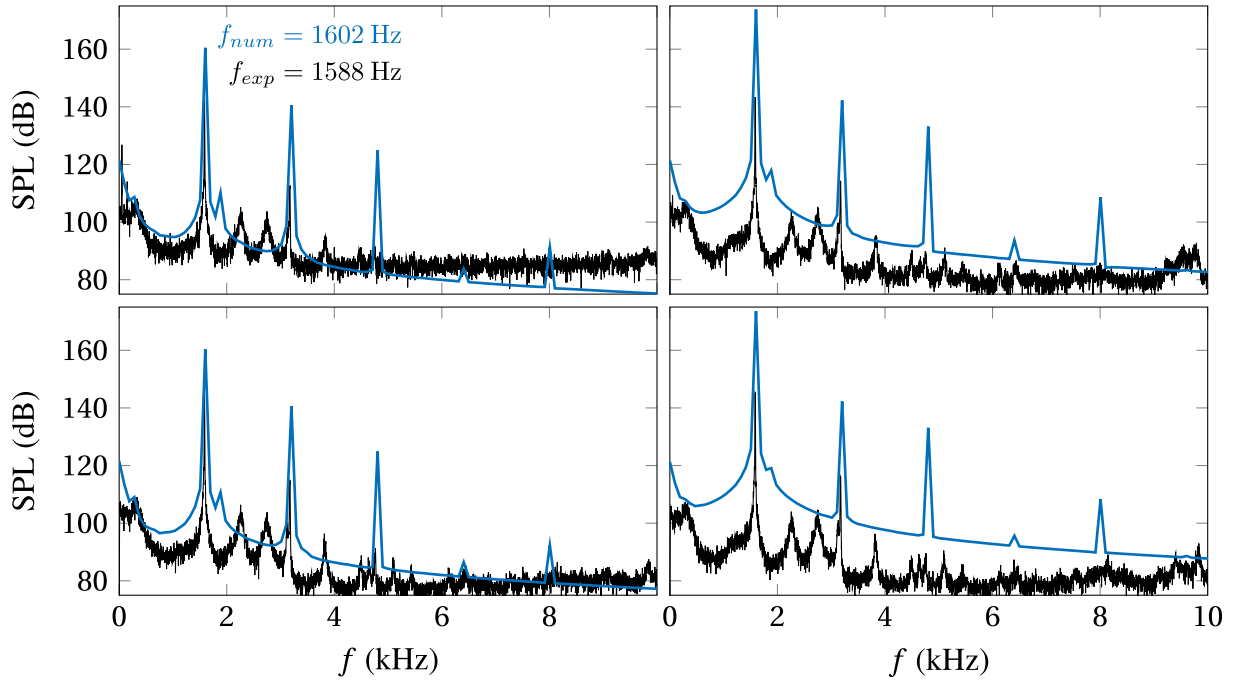


Figure 5.11: Sound pressure level measured in experiment vs. computed by ROLEX model. Left side shows microphone position “L”, right side position “M”. Top row shows injector 1, bottom row injector 2.

oscillations at the two microphone positions “M” and “L” (see Fig. 5.7) at two neighboring injectors. Note that the microphone positions are outside the CFD domain. The pressure oscillations predicted by the hybrid models are reconstructed from the state-vector x of the coupled acoustic state-space model. Figure 5.11 shows the sound pressure level (SPL) from the experiment and the ROLEX model at the four positions considered. The SPL is computed from the power spectrum $P_{xx}(f)$ of the recorded pressure fluctuations according to

$$\text{SPL}(f) = 10 \log_{10} \left(\frac{P_{xx}(f)}{P_0} \right), \quad (5.12)$$

where the reference sound power is set to the common value $P_0 = (2 \cdot 10^{-5} \text{ Pa})^{23}$. The ROLEX model accurately predicts the measured LC frequency but overestimates the amplitudes. For microphone position “L”, a SPL ≈ 142 dB is measured, compared to SPL ≈ 160 dB predicted by the ROLEX model. In the ROLEX model, the second and third harmonics clearly stand out against the background noise level. In the experiment, only the second harmonic is clearly differentiable. This indicates that the flame model employed does not accurately predict all higher harmonics, as already discussed with Fig. 5.9. According to a spinning $m = 1$ mode structure, both the measured and computed SPL are almost identical in both injectors. The SPL at microphone position “M” and “L” are also almost identical in the experiment. In contrast, the ROLEX model predicts a significantly lower SPL at position “L”. This indicates a misprediction of the mode shape inside the injector.

Figure 5.12 shows the SPL predicted by the Bloch-approach. Only injector 1 is shown, as the

²³Strictly speaking, P_0 is the reference signal power, not the reference sound power, as Pa^2 is not the correct unit of sound power

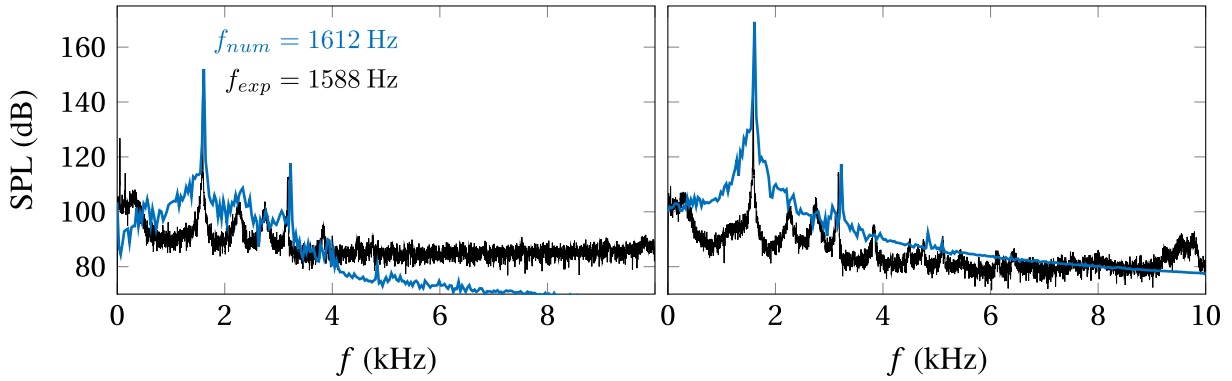


Figure 5.12: Sound pressure level measured in experiment vs. computed by Bloch-wave approach. Left side shows microphone position “L”, right side position “M”.

Bloch-wave approach assumes equal amplitudes in every sector. The predicted LC frequency is close to the experimental observation and the prediction of the ROLEX model. The amplitude at microphone position “L” $\text{SPL} \approx 152$ dB is lower than in the ROLEX model but still much larger than the $\text{SPL} \approx 140$ dB measured in the experiment. The second harmonic observed in the experimental spectrum is well captured. Like in the experiment, no further harmonics can be differentiated from the noise background. Similar to the ROLEX model, the predicted SPL at microphone position “M” is much larger, which is not observed in the experiment.

Figure 5.13 shows the magnitude and phase of the dominant frequency component at $f = 1602$ Hz (ROLEX) resp. $f = 1612$ Hz (Bloch) along the injector, reconstructed from the state vector x of the acoustic LOM. Both approaches employ the same acoustic model and thus predict a very similar mode shape, although the amplitudes in the ROLEX model are much higher. Due to an unfortunate coincidence, the pressure measurements are positioned in a minimum (“L”) and a maximum (“M”) of the pressure magnitude. This explains the large difference in predicted SPL for the two microphone positions. In the experiment, the mode shape seems to be shifted, resulting in almost equal amplitudes at “L” and “M”. The different mode shapes in the experiment and the simulations can be addressed to deficiencies of the acoustic model employed. Possible sources of error are the (measured) scattering matrices of the swirler and the sinter-plate and the transition from injector to chamber, characterized by a very large area ratio combined with the temperature jump caused by the flame. The 0D jump conditions employed in the acoustic network model may be overly simplifying.

Overall, the two hybrid models capture important characteristics of the experimental measurements but show quantitative differences in amplitudes, which can be addressed to the deficiencies of the LES sector model employed (see 5.3.2.1) and the simple acoustic model. The results are expected to improve if these two crucial model ingredients are improved. The ROLEX model and the Bloch approach yield very similar results, thereby cross-validating each other. The slight differences in the results are addressed to the limitations of the flame LOMs employed in the ROLEX model.

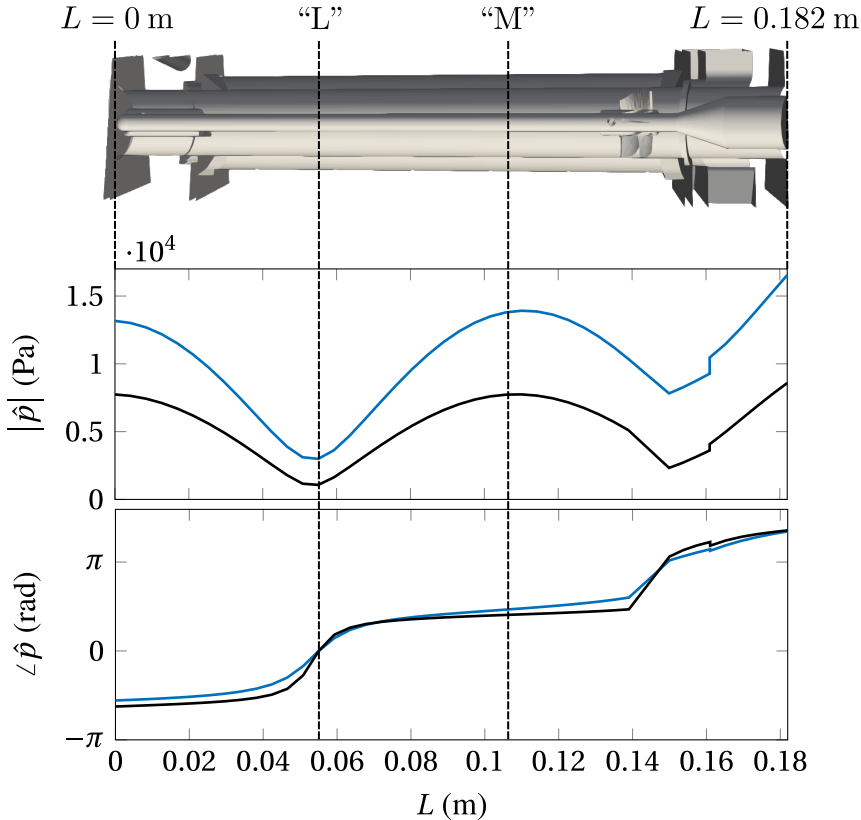


Figure 5.13: Magnitude (top) and phase (bottom) of the dominant frequency component of \hat{p} . ROLEX model shown in blue, Bloch approach in black. The dashed lines indicate from left to right: sinter plate, microphone positions “L” and “M”, and chamber back plate.

6 Contextualization and Discussion of Publications

The present section discusses and contextualizes the four publications attached in the appendix. The papers *Time Domain Bloch Boundary Conditions for Efficient Simulation of Thermoacoustic Limit-Cycles in (Can-)Annular Combustors* (PAPER_BLOCH) and *Hybrid CFD/low-order modeling of thermoacoustic limit cycle oscillations in can-annular configurations* (PAPER_ROLEX) develop and demonstrate nonlinear time domain models for LC prediction in (can-)annular combustors. The paper *A Strategy to Tune Acoustic Terminations of Single-Can Test-Rigs to Mimic Thermoacoustic Behavior of a Full Engine* (PAPER_TESTRIG) adapts the numerical model developed in PAPER_BLOCH to apply it to experimental LC prediction utilizing single-can test-rigs. Finally, the paper *Large eddy simulation of the dynamics of lean premixed flames using global reaction mechanisms calibrated for CH₄-H₂ fuel blends* (PAPER_MECH) demonstrates the calibration of a global reaction mechanism needed to simulate the validation case of the proposed hybrid models.

In the following, the connections between the papers and the relevant literature are discussed, starting with an overview of nonlinear thermoacoustic models focusing on LC prediction of (can-)annular configurations. Afterward, the link to single-can testing is discussed. This chapter concludes with a discussion of the global chemical mechanisms calibrated using the method of PAPER_MECH.

6.1 Numerical Limit Cycle Prediction in (Can-)Annular Configurations

The flame is the most essential element with nonlinear characteristics in thermoacoustic systems. Other elements that may also feature nonlinear dynamics in the relevant amplitude range, for example, damping devices [127], are less central and not considered here. The remaining elements constituting a thermoacoustic system can be well represented by linear dynamics in the relevant amplitude range. Thus, the overview of nonlinear thermoacoustic models of (can-)annular combustors essentially boils down to discussing the available nonlinear flame model types and their arrangement within the global thermoacoustic model.

6.1.1 Overview of Nonlinear Flame Models

Here, the focus is on models that aim for quantitative accuracy. Simplified analytical models, which are typically employed for fundamental investigations, are excluded from the following

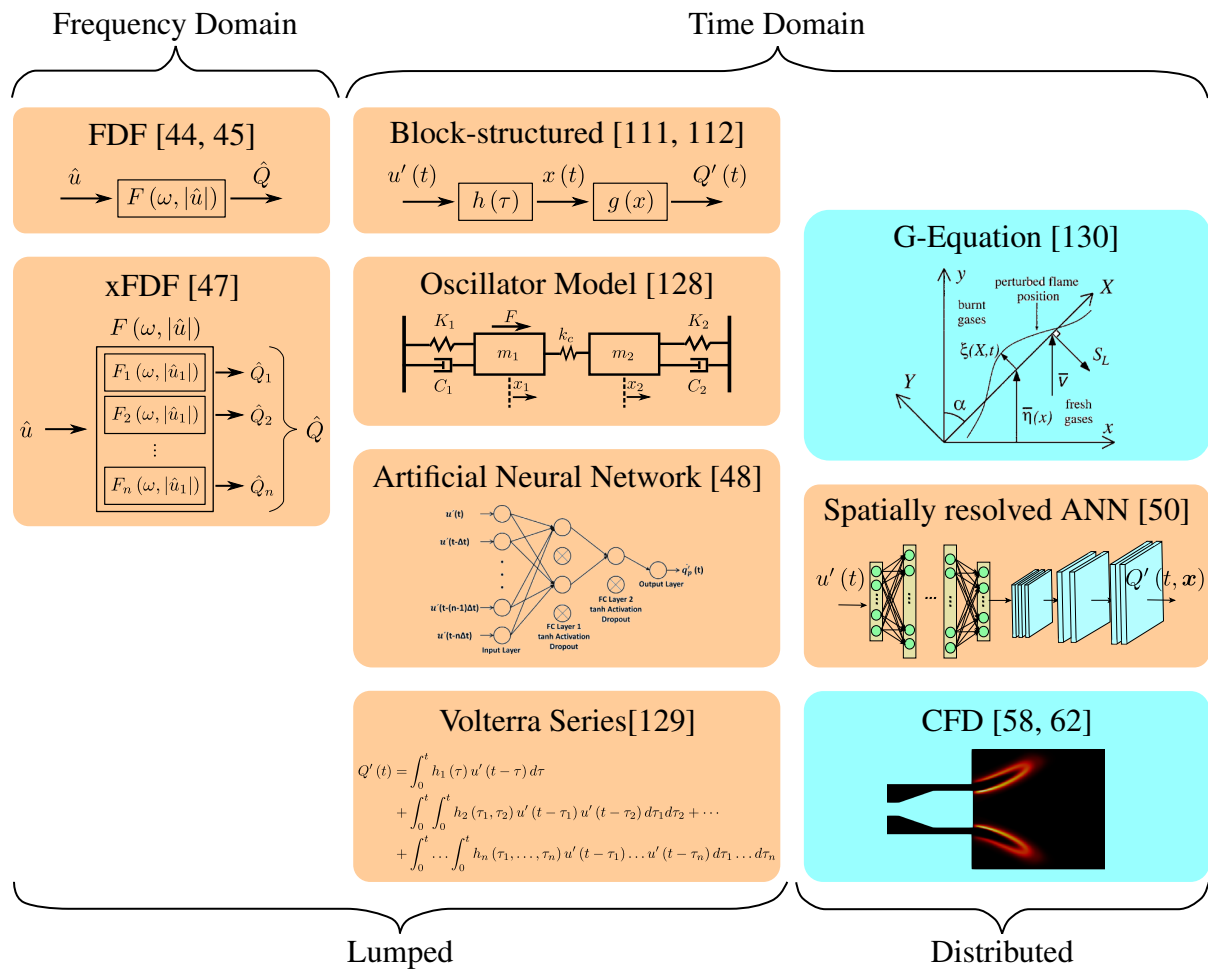


Figure 6.1: Common types of nonlinear flame models with exemplary references. The turquoise color indicates physics-based, and the other color indicates data-driven modeling. Lumped models yield the integral heat release rate fluctuation, while distributed models resolve its spatial distribution.

discussion. Figure 6.1 gives an overview of common types of nonlinear flame models and aims to classify them based on various aspects. Overall, the models' predictive capability, accuracy, and generality increase from top left to bottom right. The opposite is true for the computational effort to identify and/or solve the model. However, this is only the general trend. In detail, the computational effort and the achievable accuracy depend, among other aspects, on the degrees of freedom of the particular model. For the data-driven models highlighted in other in Fig. 6.1, the vast majority of the computational effort is required to identify the model parameters prior to the actual simulation of the self-excited system. Physics-based models highlighted in turquoise in Fig. 6.1 do not require this identification step, but instead, the simulation of the self-excited system is costly.

Starting with the left column in Fig. 6.1, the only commonly used frequency domain models are the *Flame Describing Function* (FDF) [44, 45] and its variant, the *extended FDF* (xFDF) [47]. Both model types are “*weakly nonlinear*”, meaning they are essentially an amplitude-dependent version of the linear FTF. Their gain and phase depend on the input amplitude. The xFDF additionally accounts for the generation of higher harmonics. Other typical nonlinear phenomena,

such as the interaction of multiple frequencies, are neglected, which limits the predictive capabilities and the generality. The numerical identification of an (x)FDF involves harmonic forcing of the considered flame at many frequencies and amplitudes and, therefore, means a considerable computational effort. Orchini and Juniper [131] attempted to relax some of the assumptions of the FDF by defining multi-input describing functions. However, their advantages generally do not seem to justify the drastically increased computational effort. Heckl *et al.* [132, 133] and Gopinathan *et al.* [134] provided time domain formulations of an FDF based on amplitude-dependent distributed time-lag models. However, the main drawback of these formulations is their explicit dependence on the instantaneous amplitude, which is difficult to obtain in during simulation time of the self-excited system [135]. In spite of their limitations, the (x)FDF is widely used, and several studies (see e.g. [45, 47, 60, 136–138]) demonstrate their capabilities in predicting LC amplitudes and also hysteresis behavior for both single- and multi-burner configurations.

Time domain models are principally better suited to describe nonlinear dynamics and are more numerous. The middle column of Fig. 6.1 shows “lumped” time domain models. As the (x)FDF discussed previously, these models output the global (or integral) heat release rate fluctuation, distinguishing them from the spatially resolved models in the right column. *Block-structured models* [111, 112] are the simplest dynamic nonlinear time domain models. They assume a separability of linear dynamic and nonlinear static model parts. Various arrangements of linear and nonlinear blocks are common: the most popular types are the Wiener-type (nonlinear block at the output), the Hammerstein-type (nonlinear block at the input), as well as numerous combinations of the aforementioned, including more than one linear or nonlinear element [111]. The separation of linear dynamics and nonlinearity eases the identification of the individual building blocks because all intermediate in- and outputs are directly accessible, and the individual blocks can be computed separately. However, this separation is not generally justified if not based on actual system characteristics. This limits the generality of these models and their applicability as a nonlinear flame model valid for a wide range of amplitudes and frequencies. Attempts in these directions are not overall convincing [112]. For the model proposed in PAPER_ROLEX, this model structure is advantageous. It allows the use of a pre-identified FTF, which ensures the correct linear stability and enables the separate identification of the nonlinear model parameters. The main drawback of Block-structured models, their limited generality, is of minor importance in the ROLEX approach since the flame models have to reproduce the correct dynamics only near the system states encountered.

The *Volterra Series* is located on the other side of the spectrum of lumped time domain models. Comprising an infinite number of terms, the Volterra Series completely describes any nonlinear time-invariant system, similar to the *Impulse Response* for linear systems. In fact, the kernels of the Volterra Series are the n -th order impulse responses. The data-driven identification of the kernels of a truncated Volterra Series is difficult because the individual terms are not orthogonal. In the context of nonlinear flame modeling, it is exclusively used for deductive purposes [85, 129, 139].

In the last decade, *Artificial Neural Networks* (ANN) have gained increasing interest as general nonlinear flame model [43, 48, 49, 140]. The predictive capabilities of these models have significantly improved since their first use in the context of nonlinear flame modeling [43]. Recent studies [49, 140] demonstrate that ANN can be trained with high-amplitude broadband forcing flame response data of reasonable signal length and can well match the transfer behavior of

an FDF, although yet demonstrated for laminar flames only. However, as the ANN is a purely data-driven black-box model, it performs poorly outside the range of training data. This may lead to unexpected results when simulating LC oscillations in a self-excited context [43].

The *Oscillator Model* in Fig. 6.1 completes the collection of lumped time domain models. Doehner *et al.* [128] proposed this set of parsimonious nonlinear ODEs to bridge the gap between the common “weakly nonlinear” frequency domain models and the very sophisticated ANNs. The ODEs constituting the model can be interpreted as a system of coupled nonlinear oscillators, where the positions of the point masses and the force acting on them represent the model in- and output. Compared to an ANN, the Oscillator Model relies on much fewer parameters and can be identified from broadband forcing data with a smaller signal length. On the other hand, the predefined model structure limits the achievable accuracy. Though promising, this model type has yet to be applied in a self-excited system.

The right column in Fig. 6.1 shows the class of time domain models with spatial distribution. In contrast to the aforementioned models, they yield the spatial distribution of the local heat release rate at each time instant, making them more versatile and applicable for non-compact flames. The global heat release rate fluctuation can be easily obtained by integrating the local heat release rate. Traditionally, this has been the domain of physics-based models relying on fundamental governing equations. However, the recent progress in ANNs makes this domain also accessible to data-driven model types [50], denoted as “*Spatially resolved ANN*” in Fig. 6.1.

The *G-Equation*, or *Level-Set Method*, is a kinematic description of a (flame) front that is convected by a background flow and propagates normal to itself at a given (flame) speed. The G-Equation can accurately track the flame motion but requires a velocity model, which governs the background flow field [130]. Commonly employed model formulations neglect important mechanisms such as flame flow feedback, which play a crucial role in flame movement. Instead, they rely on ad-hoc models for convective velocity perturbations, whose parameters must be adjusted to yield the correct behavior [141]. The G-Equation is mainly used for phenomenological studies (e.g., see [90] in the context of can-annular combustors). Yu *et al.* demonstrate that the G-Equation may achieve quantitative prediction accuracy by learning the model parameters based on a parallel CFD simulation [142, 143] or an experiment [144].

A fully compressible, reactive CFD simulation directly solves Eqs. (2.1)-(2.5) and is thus the most general flame model available. As the governing equations include every relevant physical mechanism, the model is, in principle, capable of exactly representing the actual flame dynamics. In the case of acoustically compact velocity-sensitive flames, a low-Mach CFD simulation describes nonlinear flame dynamics equally well [105]. The CFD simulation often serves as a reference on which the identification of the aforementioned models is based. Alternatively, a monolithic, fully compressible CFD can be used to resolve the entire self-excited system [38, 40, 42]. Lastly, the CFD can also be coupled with an acoustic solver as proposed by Jaensch *et al.* [58] to study a self-excited system.

6.1.2 Discussion of Available Thermoacoustic Model Setups

Except for the fully compressible, reactive CFD simulation, which inherently accounts for all relevant mechanisms, all thermoacoustic models implementing one of the flame models dis-

Table 6.1: Assessment of different classes of nonlinear thermoacoustic models.

	Model Type	Achievable Accuracy	Generality/Reliability	Comp. Cost Identification	Comp. Cost Self-excited system
1	Lumped Flame+ Acoustic Model	- / 0	-	-	+
2	(Hybrid) CFD	+	+	+	-
				(no Identification)	
3	Time domain Bloch approach	+	-	+	0
				(no Identification)	
4	ROLEX Model	0	+	0	0

cussed in Sec. 6.1.1 are hybrid in nature. A separate model part accounts for acoustics (and possibly other relevant phenomena such as propagation of entropy and mixture fraction waves), and the flame model is coupled via jump conditions. Essentially all acoustic solvers ranging from 1D network models [31, 32, 69–72] to 3D Helmholtz [37, 73] and LEE/LNSE solvers [74, 77] can be combined with the flame models above. The individual choice depends on the complexity of the system considered and the required accuracy. Following the approach of Jaensch *et al.* [58], these acoustic solvers can also be combined with a compressible or low-Mach CFD simulation resolving flame dynamics.

The model setup of the time domain Bloch approach proposed in PAPER_BLOCH is very similar to the hybrid CFD/LOM model developed by Jaensch *et al.* [58]. The distinguishing feature is the use of Bloch-BC in the acoustic solver, which reduces the symmetric multi-burner setup to a single-burner system for a given mode order.

The ROLEX model proposed in PAPER_ROLEX implements data-driven, lumped flame models coupled to an acoustic solver (Block-structured Wiener-type flame models coupled to a network model in the present case). Here, the feature distinguishing from existing models in literature is the online identification of the flame model parameters based on the CFD simulation solved parallel to the self-excited system. The principal idea of identifying flame model parameters from a parallel high-fidelity simulation is similarly found in Yu *et al.* [142, 143]. However, the objectives and the employed method differ significantly. Yu *et al.* applies combined state and parameter estimation to match the flame dynamics observed in a CFD simulation with a parallel G-Equation solver of the same flame. In PAPER_ROLEX, the nonlinear flame models represent *identical flames but not the same flame* as the parallel CFD simulation. The state of the flame resolved with CFD generally differs from the states of the flames represented by the nonlinear LOMs. Consequently, in PAPER_ROLEX we apply parameter estimation only. The identified parameters are transferred to the remaining flame models of the (can-)annular system, which do not have a parallel CFD simulation.

All mentioned combinations of flame model and acoustic solver are, in principle, capable of predicting LC oscillations in (can-)annular configurations. The approaches differ by the achievable accuracy, robustness/reliability, and computational cost. Table 6.1 assesses the different model classes based on these categories. The models of category 1 in Tbl. 6.1, which implement data-driven, lumped flame models, are very efficient in solving the self-excited system. However,

depending on the exact model used, the identification step may be very costly, while the achievable accuracy is moderate (again heavily dependent on the exact model used). As these model types are not based on physical principles, they do not perform well outside the training data range and are thus not overall reliable. The opposite is true for category 2, the hybrid CFD model structure proposed by Jaensch *et al.* [58]. No prior identification step is necessary; instead, the simulation of the self-excited system is very costly, as all flames have to be explicitly resolved in CFD. The time domain Bloch approach proposed in PAPER_BLOCH can achieve comparable accuracy at a lower computational cost due to the symmetry condition employed. This comes at the expense of reduced reliability and generality because the model can neither predict the occurrence nor the effects of symmetry breaking. The ROLEX model proposed in PAPER_ROLEX does not explicitly rely on symmetry and is thus more general. However, the achievable accuracy is limited by the data-driven flame models employed, even though they are being updated to best fit the CFD results. The computational cost of simulating the self-excited system is comparable to that of the time domain Bloch approach. Nevertheless, the ROLEX model additionally requires the prior identification of an FTF.

According to the discussion above, no favorite model structure is the best choice under all circumstances. Models of category 1 in Tbl. 6.1 are preferable if the costly identification step is not a major factor and if limited accuracy is tolerable. This is, for example, the case when a large number of (acoustic) setups with the same flame are investigated. In this case, the identification step is necessary only once, and the low computational cost of simulating the self-excited system comes into play. The category 2 models in Tbl. 6.1 are preferable if accuracy and reliability are the paramount goals. However, one has to keep in mind that applying this approach to a realistic (can-)annular configuration means tremendous computational cost, as discussed in Sec. 3.1.

The two symmetry-enhanced models proposed in PAPER_BLOCH and PAPER_ROLEX are preferable in all remaining circumstances. Again, the focus of the particular study decides which of the two modeling approaches should be selected. If the operability of a specific configuration is the focus of the investigation, the Bloch approach is the model of choice, as it requires less preparation than the ROLEX model. Often, only one or a few azimuthal mode orders are expected to be dominant in a specific system (often known from practical or experimental experience with the system). The Bloch approach can be run for only those mode orders. Suppose the model predicts a high amplitude LC oscillation for only one mode order. This rules out the considered design and/or operating point, regardless of whether the other mode orders are stable. In contrast, if the focus is on a detailed analysis of the system, for example, on the effect of small damping devices that break the symmetry or on the azimuthal orientation of the nodal line of a degenerate mode pair, then the ROLEX approach is the method of choice. The ROLEX approach is also preferable for getting a global overview of a system without previous knowledge of dominant mode orders. Lastly, the ROLEX approach not only predicts LC oscillations but also yields a nonlinear flame LOM, which - although only valid in the vicinity of the observed amplitudes and frequencies - can be re-used for further studies. For example, the effect of small modifications of the acoustic properties can be quickly estimated without rerunning a CFD simulation.

Finally, the strengths of both approaches can be combined. Running the ROLEX model will yield a good overview of the system, although not the best possible accuracy of the predicted LC amplitudes due to the limitations of the employed flame LOMs. The result of the ROLEX model will reveal the system's dominant mode order and whether the Bloch approach is applicable. If

symmetry is maintained, the ROLEX results can be backed up with the Bloch approach run at the obtained dominant mode order. Due to its accurate representation of flame dynamics, this will yield the best possible accuracy.

6.2 Thermoacoustic Tuning of Single-Can Test-Rigs

In PAPER_BLOCH we developed a numerical tool to predict LC oscillation in an entire can-annular configuration based on a single-can (or single-flame) simulation. The principal idea behind this model is highly relevant also for experimental test facilities. As explained in Sec. 3.2.1, thermoacoustics of an entire can-annular configuration can not be represented by one single can without further measures. Nevertheless, gas turbine manufacturers strive to use their existing single-can test-rigs (which are mainly built for investigating emissions and flame stability against blow-off and flashback) for thermoacoustic characterization of the full engine by adapting the single-can acoustics with passive devices to mimic the influence of the remaining parts of the engine [6, 145, 146]. Hitherto, this adaption of single-can test-rigs lacked a solid theoretical foundation. In PAPER_TESTRIG we develop a strategy to tune single-can test-rigs based on the Bloch-wave theorem. First, equivalent reflection coefficients \mathcal{R}_m at the upstream and downstream termination of a single can are computed for the given engine configuration. In a second step, passive acoustic elements, here Helmholtz-resonators, are installed at the upstream and downstream termination of the can and are tuned to mimic the equivalent reflection coefficients.

The use of equivalent reflection coefficients \mathcal{R}_m closely connects this approach to the numerical model from PAPER_BLOCH. These reflection coefficients are also employed in related numerical studies [28, 87, 88]. To the author's knowledge, the strategy developed in PAPER_TESTRIG is the first time that the equivalent reflection coefficient \mathcal{R}_m is used in an experimental context. The main difference to the Bloch approach from PAPER_BLOCH is, that \mathcal{R}_m can not be imposed exactly in an experimental test-rig but must be emulated with passive acoustic elements. In principal, active control methods [147–149] could be used to approximate \mathcal{R}_m at the can terminations. However, this approach seems difficult to implement in high-pressure single-can test-rigs of applied can-annular combustors because of generally limited access and the hot gas environment.

The strategy developed in PAPER_TESTRIG offers a theoretically sound approach for studying thermoacoustic properties of a full can-annular combustion system based on a single-can test rig. As the alternative to this strategy is to build and run a pressurized full can-annular test combustor, the developed strategy has the potential to greatly reduce experimental efforts in the design phase of can-annular combustors.

6.3 Calibrating Global Reaction Mechanisms

The global energy transition necessitates the use of renewable fuels such as hydrogen. Gas turbines with state-of-the-art combustor technologies are often not ready for a complete replacement of natural gas with hydrogen. Therefore, the deployment of hydrogen / natural gas fuel

blends becomes increasingly important [7]. This poses a challenge for the numerical simulation of these combustors. Detailed reaction mechanisms (DM) are capable of handling fuel blends if they include all fuel species. However, due to their large number of species and reactions, using DM would drastically increase the computational cost of the numerical methods developed in PAPER_BLOCH and PAPER_ROLEX. In contrast, global reaction mechanisms (GM) are computationally efficient but are usually calibrated for a relatively narrow operating window. Their accuracy deteriorates if used at off-design points. Most of the readily available GM are developed for pure natural gas or pure hydrogen [150]. As they typically do not include one or the other fuel species, they cannot be used for a hydrogen / natural gas fuel blend.

In PAPER_MECH we extend the method proposed by Polifke *et al.* [115] to calibrate global reaction mechanisms focusing on the correct representation of flame dynamics. The accurate prediction of flame dynamics by the CFD simulation employed is the foundation of the numerical methods developed in PAPER_BLOCH and PAPER_ROLEX. When applying the ROLEX model or the Bloch approach at an operating point for which no global reaction mechanism is available, a necessary step in the setup of the single-sector LES is the calibration of a suitable reaction mechanism following the approach from PAPER_MECH. This step was also essential for the simulation of the NTNU annular rig discussed in Sec. 5.3, which is operated with a volume ratio of 57% CH₄ and 43% H₂.

7 Summary of Papers

This chapter summarizes the four publications that constitute this thesis. For each publication, the original abstract and the individual contributions of each author are presented. Note that the individual publications are ordered thematically, not chronologically.

During this PhD project, the present author additionally contributed to eight peer-reviewed publications, one of them as the first author. These publications do not directly contribute to the framework developed within this thesis but are nevertheless thematically more or less closely linked. These publications are briefly summarized below.

The paper [47] (first author) proposes the xFDF (see 6.1.1), which extends the FDF by including the flame response at higher harmonics of the input. The xFDF yields more accurate LC predictions than the classical FDF, particularly in configurations where higher harmonics play a significant role. In [151], we investigate various Machine Learning algorithms to interpolate and extrapolate an FDF. The algorithms studied allow for a reduction in the number of data points required for identifying an FDF. The paper [88] uses the equivalent reflection coefficient to explain the clustering of intrinsic thermoacoustic (ITA) modes in annular combustors. This study contributes to understanding the various types of thermoacoustic modes found in an annular combustor setup. In [85], we analyze the response of a symmetrical flame to transverse excitation, for example, caused by azimuthal modes in an annular combustion chamber. We demonstrate that the flame primarily responds at twice the forcing frequency, which can trigger higher-order modes and may lead to modal coupling. The paper [152] studies the interplay of clustered ITA and acoustic modes in can-annular combustors. It demonstrates how an exceptional point shapes the eigenvalue spectrum of a can-annular configuration and in which circumstances modes drift away from their original cluster. In [128], we propose the Oscillator Flame Model (see 6.1.1). This new type of nonlinear flame model aims to fill the gap between frequency domain models such as the FDF and sophisticated, data-driven models like ANN. In [105], we compare the fully compressible and low-Mach CFD formulation for identifying the FTF. We demonstrate that the dynamics of acoustically compact, velocity-sensitive flames are equally well described by the low-Mach formulation, which is preferable due to the simpler numerical setup. The paper [153] addresses model order reduction for complex moving fronts, which are transported by advection or a reaction-diffusion process. It proposes a new approach similar to autoencoder ANNs but with additional insights into the system, which can be used for efficient reduced-order models.

7.1 Time Domain Bloch Boundary Conditions for Efficient Simulation of Thermoacoustic Limit-Cycles in (Can-)Annular Combustors

This paper presents and validates the time domain Bloch-wave approach, which directly exploits the symmetry of (can-)annular configurations. If the inherent assumptions about the mode symmetry are fulfilled, the proposed approach proves to be very efficient and accurate.

Original Abstract: Thermo-acoustic eigenmodes of annular or can-annular combustion chambers, which typically feature a discrete rotational symmetry, may be computed in an efficient manner by utilizing the Bloch-wave theory. Unfortunately, the application of the Bloch-wave theory to combustion dynamics has hitherto been limited to the frequency domain. In this study we present a time domain formulation of Bloch boundary conditions (BBC), which allows to employ them in time domain simulations, e.g. CFD simulations. The BBCs are expressed as acoustic scattering matrices and translated to complex-valued state-space systems. In a hybrid approach an unsteady, compressible CFD simulation of the burner-flame zone is coupled via characteristic-based state-space boundary-conditions to a reduced order model of the combustor acoustics that includes BBCs. The acoustic model with BBC accounts for cross-can acoustic coupling and the discrete rotational symmetry of the configuration, while the CFD simulation accounts for the nonlinear flow-flame-acoustic interactions. This approach makes it possible to model limit cycle oscillations of (can-)annular combustors at drastically reduced computational cost compared to CFD simulations of the full configuration, and without the limitations of weakly nonlinear approaches that utilize a flame describing function. In the current study the suggested approach is applied to a generic multi-can combustor. Results agree well with a fully compressible CFD simulation of the complete configuration.

Contribution according to Contributor Role Taxonomy scheme (CRediT):

Contribution	Author
Conceptualization	M. Haeringer
Methodology	M. Haeringer
Software	M. Haeringer
Validation	M. Haeringer
Formal analysis	M. Haeringer, W. Polifke
Data Curation	M. Haeringer
Writing - Original Draft	M. Haeringer
Writing - Review Editing	M. Haeringer, W. Polifke
Visualization	M. Haeringer
Supervision	W. Polifke

Status: Published in *Journal of Engineering for Gas Turbines and Power*.

Review Process: Peer-reviewed, Scopus-listed.

Reference: M. Haeringer and W. Polifke. Time Domain Bloch Boundary Conditions for Efficient Simulation of Thermoacoustic Limit-Cycles in (Can-)Annular Combustors. *Journal of Engineering for Gas Turbines and Power*, 141(12):121005, 2019. doi: 10.1115/1.4044869

7.2 Hybrid CFD/Low-Order Modeling of Thermoacoustic Limit Cycle Oscillations in Can-Annular Configurations

This paper presents and validates the ROLEX model. Though slightly less accurate and efficient than the time domain Bloch-wave approach, the ROLEX model is generally applicable and does not rely on assumptions about mode symmetry.

Original Abstract: We propose a hybrid strategy for modeling non-linear thermoacoustic phenomena, e.g. limit-cycle (LC) oscillations, in can-annular combustion systems. The suggested model structure comprises a compressible CFD simulation limited to the burner/flame zone of one single can, coupled to a low-order model (LOM) representing the remaining combustor. In order to employ the suggested strategy for modeling non-linear phenomena such as LC oscillations, the LOM must capture non-linear flame dynamics in the cans, which are not resolved by CFD. Instead of identifying such non-linear flame models in preliminary simulations, we aim at learning the non-linear dynamics “on-the-fly”, while simulating the self-excited system under consideration. Based on the observation of flame dynamics in the CFD domain, the parameters of the employed non-linear models are estimated during run time. The present study reveals that block-oriented models, which comprise a linear dynamic part followed by a static non-linear function, are well suited for this purpose. The proposed hybrid model is applied to a laminar can-annular combustor. Results agree well with the monolithic CFD simulation of the entire combustor, while the computational cost is drastically reduced. The employed flame models, whose parameters are identified during the simulation of the self-excited LC oscillation, represent well the relevant non-linear dynamics of the considered flame.

Contribution according to Contributor Role Taxonomy scheme (CRediT):

Contribution	Author
Conceptualization	M. Haeringer, W. Polifke
Methodology	M. Haeringer
Software	M. Haeringer
Validation	M. Haeringer
Formal analysis	M. Haeringer
Data Curation	M. Haeringer
Writing - Original Draft	M. Haeringer
Writing - Review Editing	M. Haeringer, W. Polifke
Visualization	M. Haeringer
Supervision	W. Polifke

Status: Published in *International Journal of Spray and Combustion Dynamics*.

Review Process: Peer-reviewed, Scopus-listed.

Reference: M. Haeringer and W. Polifke. Hybrid CFD/Low-Order Modeling of Thermoacoustic Limit Cycle Oscillations in Can-Annular Configurations. *Int. J. Spray Comb. Dynamics*, 14(1-2): 143–152, 2022. doi: 10.1177/17568277221085953.

7.3 A Strategy to Tune Acoustic Terminations of Single-Can Test-Rigs to Mimic Thermoacoustic Behavior of a Full Engine

In this paper, the consequences of the Bloch-wave theorem are used to gain insight into the transferability of results obtained with a single-can test-rig to the entire engine. It transfers knowledge gained from the development of numerical models to experimental test-rigs.

Original Abstract: Thermoacoustic properties of can-annular combustors are commonly investigated by means of single-can test-rigs. To obtain representative results, it is crucial to mimic can-can coupling present in the full engine. However, current approaches either lack a solid theoretical foundation or are not practicable for high-pressure rigs. In the present study we employ Bloch-wave theory to derive reflection coefficients that correctly represent can-can coupling. We propose a strategy to impose such reflection coefficients at the acoustic terminations of a single-can test-rig by installing passive acoustic elements, namely straight ducts or Helmholtz resonators. In an iterative process, these elements are adapted to match the reflection coefficients for the dominant frequencies of the full engine. The strategy is demonstrated with a network model of a generic can-annular combustor and a 3D model of a realistic can-annular combustor configuration. For the latter we show that can-can coupling via the compressor exit plenum is negligible for frequencies sufficiently far away from plenum eigenfrequencies. Without utilizing previous knowledge of relevant frequencies or flame dynamics, the test-rig models are adapted within a few iterations and match the full engine with good accuracy. Using Helmholtz resonators for test-rig adaption turns out to be more viable than using straight ducts.

Contribution according to Contributor Role Taxonomy scheme (CRediT):

Contribution	Author
Conceptualization	M. Haeringer, W. Polifke
Methodology	M. Haeringer, G. J. J. Fournier
Software	M. Haeringer, M. Meindl
Validation	M. Haeringer
Formal analysis	M. Haeringer
Data Curation	M. Haeringer
Writing - Original Draft	M. Haeringer
Writing - Review Editing	M. Haeringer, G. J. J. Fournier, W. Polifke
Visualization	M. Haeringer
Supervision	W. Polifke

Status: Published in *Journal of Engineering for Gas Turbines and Power*.

Review Process: Peer-reviewed, Scopus-listed.

Reference: M. Haeringer, G. J. J. Fournier, M. Meindl, and W. Polifke. A Strategy to Tune Acoustic Terminations of Single-Can Test-Rigs to Mimic Thermoacoustic Behavior of a Full Engine. *Journal of Engineering for Gas Turbines and Power*, 143(7):710029, 2021. doi: 10.1115/1.4048642

7.4 Large Eddy Simulation of the Dynamics of Lean Premixed Flames Using Global Reaction Mechanisms Calibrated for CH₄-H₂ Fuel Blends

This paper extends an existing method to calibrate a global reaction mechanism. The focus of the calibration is the correct prediction of flame dynamics. This is particularly relevant due to the increased use of fuel blends, for which no global mechanisms are available in the literature.

Original Abstract: The effects of hydrogen addition on the flame dynamics of a bluff-body stabilized methane–hydrogen turbulent flame are studied with large eddy simulation (LES). The LES is carried out with the thickened flame model and global kinetic mechanisms calibrated for the methane–hydrogen mixtures. Conjugate heat transfer is included in the LES to consider a proper wall temperature while the flame shape changes with hydrogen addition. A data-based calibration of the global mechanisms is done with a methodology based on reproducing the net species production rates computed with a detailed kinetic mechanism. An improvement in this methodology is proposed to increase its accuracy and reliability. The calibrated mechanisms accurately describe the variation of the laminar flame speed and the thermal flame thickness with hydrogen addition and equivalence ratio in a freely propagating premixed flame. The variations of the consumption speed and the thermal flame thickness with the strain rate in a symmetric counterflow premixed flame are also well predicted. The numerical simulations reproduce the transition from V- to M-shape flame induced by hydrogen addition, and the axial distribution of the heat release agrees with the experimental measurements of OH chemiluminescence. The unit impulse response and the flame transfer function are computed from the LES data using system identification (SysID). The flame transfer functions show a remarkable agreement with the experimental data, demonstrating that the LES-SysID approach using properly calibrated global mechanisms can predict the response of turbulent methane–hydrogen flames to velocity fluctuations. A comparison of the unit impulse response for the various hydrogen additions is presented, and the effect of hydrogen in the flow–flame interaction of the burner evaluated is discussed.

Contribution according to Contributor Role Taxonomy scheme (CRediT):

Contribution	Author
Conceptualization	A. M. Garcia, W. Polifke, M. Haeringer
Methodology	A. M. Garcia, W. Polifke, M. Haeringer
Software	A. M. Garcia, J. Prager
Validation	A. M. Garcia
Formal analysis	A. M. Garcia
Data Curation	A. M. Garcia
Writing - Original Draft	A. M. Garcia, S. Le Bras, W. Polifke
Writing - Review Editing	A. M. Garcia, S. Le Bras, J. Prager, M. Haeringer, W. Polifke
Visualization	A. M. Garcia
Supervision	W. Polifke

Status: Published in *Physics of Fluids*.

Review Process: Peer-reviewed, Scopus-listed.

Reference: A. M. Garcia, S. Le Bras, J. Prager, M. Haeringer, and W. Polifke. Large Eddy Simulation of the Dynamics of Lean Premixed Flames Using Global Reaction Mechanisms Calibrated for CH₄-H₂ Fuel Blends. *Physics of Fluids*, 34(9):095105, 2022. doi: 10.1063/5.0098898.

8 Conclusion and Outlook

Within this thesis, two hybrid, symmetry-enhanced modeling strategies for annular and can-annular combustion systems were developed: the time domain Bloch-wave approach and the ROLEX model. The Bloch approach relies on relatively strict assumptions about mode symmetry and includes only one azimuthal mode order at a time. However, it is simple to set up and if its assumptions are met, the achievable accuracy is comparable with that of a monolithic compressible large-eddy simulation (LES) of the entire system. The ROLEX model, on the other hand, includes more model ingredients, particularly a Flame Transfer Function (FTF) that must be identified in a prior simulation. The flame model limits its achievable accuracy, which is thus generally lower than that of the Bloch approach. However, the ROLEX model yields a complete picture of the system considered, including all mode orders, possible interactions of individual mode orders, and the occurrence and effects of symmetry breaking. In a way, the two modeling frameworks are complementary to each other. The ROLEX model can indicate which azimuthal mode orders are relevant and whether the Bloch approach is applicable. The Bloch approach may then be used to obtain highly accurate results of the relevant mode order.

Both model types come at significantly lower computational cost than a monolithic compressible LES of the entire configuration because their LES domains are limited to one single burner/flame zone. At the same time, both models can represent rich nonlinear dynamics, in contrast to the widely used “weakly nonlinear” frequency domain models that rely on the Flame Describing Function (FDF). Also, a tedious identification of a nonlinear model for a wide range of frequencies and amplitudes is not required. These features qualify the two models developed for use in the design process of a new combustion system. Their moderate computational cost allows repeated application to design iterations, and their accuracy is sufficient for reliable predictions.

The accuracy of the models proposed within this thesis crucially depends on their ingredients: the single-flame LES, the acoustic low-order model (LOM), and, in the case of the ROLEX approach, the flame model. The reaction mechanism is a decisive factor for the accuracy and efficiency of the LES. Within this thesis, a tool to calibrate a global reaction mechanism for an arbitrary fuel and operating point was developed. Due to the widespread introduction of new fuels such as ammonia, fuel blends, particularly mixtures of fossil fuels and hydrogen, and dilution of the reactants with steam or exhaust gas, for which no global mechanisms are readily available, such a tool becomes increasingly important.

Within this thesis, the underlying idea of the Bloch approach, the representation of the entire system as a single sector plus symmetry condition, was transferred to experimental single-can test-rigs. The strategy developed enables the use of single-can test-rigs for thermoacoustic investigations of an entire can-annular combustion system. It may thus reduce the need for testing on full can-annular rigs, which are very complex and expensive facilities.

Future work may focus on extending the numerical models developed within this thesis. Currently, the ROLEX model employs a Wiener-type flame model, which is relatively simple and relies only on a few parameters, making the identification process very efficient. However, its prediction capabilities are limited, though sufficient for the application cases studied in this thesis. Using a parsimonious set of nonlinear ordinary differential equations (see [128]) or a G-equation solver with online parameter identification (see [142]) could be a promising alternative to Wiener-type models. Furthermore, additional physical mechanisms of the flame response can be implemented without requiring major changes to the model structure. Only velocity-sensitive, premixed flames responding to axial velocity perturbations are currently considered. Models representing the response to equivalence ratio fluctuations or transverse velocity perturbations can be included without essential difficulty. Moreover, the coupling of acoustic LOM and LES can be generalized. Right now, only acoustic waves are passed through the interface. However, the present framework can be easily extended to other wave types, such as entropy and mixture fraction waves.

Bibliography

- [1] United Nations. Framework Convention on Climate Change. In *Adoption of the Paris Agreement*, 21st Conference of the Parties, Paris: United Nations, 2015.
- [2] S. C. Gülen and M. Curtis. Gas Turbine's Role in Energy Transition. In *Volume 5: Education; Electric Power; Fans and Blowers*, page V005T09A002, Rotterdam, Netherlands, 2022. American Society of Mechanical Engineers. doi: 10.1115/GT2022-81802.
- [3] M. Götz, J. Lefebvre, F. Mörs, A. McDaniel Koch, F. Graf, S. Bajohr, R. Reimert, and T. Kolb. Renewable Power-to-Gas: A Technological and Economic Review. *Renewable Energy*, 85:1371–1390, 2016. doi: 10.1016/j.renene.2015.07.066.
- [4] S. Öberg, M. Odenberger, and F. Johnsson. Exploring the Competitiveness of Hydrogen-Fueled Gas Turbines in Future Energy Systems. *International Journal of Hydrogen Energy*, 47(1):624–644, 2022. doi: 10.1016/j.ijhydene.2021.10.035.
- [5] L. B. Davis. Dry Low NO_x Combustion Systems for GE Heavy-Duty Gas Turbines. In *Volume 3: Coal, Biomass and Alternative Fuels; Combustion and Fuels; Oil and Gas Applications; Cycle Innovations*, page V003T06A003, Birmingham, UK, 1996. American Society of Mechanical Engineers. doi: 10.1115/96-GT-027.
- [6] U. Gruschka, B. Janus, J. Meisl, M. Huth, and S. Wasif. ULN System for the New SGT5-8000H Gas Turbine: Design and High Pressure Rig Test Results. In *ASME Turbo Expo 2008: Power for Land, Sea, and Air*, pages 913–919. American Society of Mechanical Engineers, 2008.
- [7] M. J. Hughes and J. D. Berry. DLN Evo Combustion Technology Development for a High-Hydrogen Flexible F-Class Retrofit. In *ASME Turbo Expo 2023 Turbomachinery Technical Conference and Exposition*, 2023.
- [8] T. Poinso. Prediction and Control of Combustion Instabilities in Real Engines. *Proceedings of the Combustion Institute*, 36(1):1–28, 2017. doi: 10.1016/j.proci.2016.05.007.
- [9] K. Venkatesan, A. Cross, C. Yoon, F. Han, and S. Bethke. Heavy Duty Gas Turbine Combustion Dynamics Study Using a Two-Can Combustion System. In *ASME Turbo Expo 2019: Turbomachinery Technical Conference & Exposition*, Phoenix, USA, 2019.
- [10] K. Moon, H. Jegal, C. Yoon, and K. T. Kim. Cross-Talk-Interaction-Induced Combustion Instabilities in a Can-Annular Lean-Premixed Combustor Configuration. *Combustion and Flame*, 220:178–188, 2020. doi: 10.1016/j.combustflame.2020.06.041.

- [11] P. E. Buschmann, N. A. Worth, and J. P. Moeck. Experimental Study of Thermoacoustic Modes in a Can-Annular Model Combustor. In *SoTiC 2021 - Symposium on Thermoacoustics in Combustion: Industry Meets Academia (2021)*, Virtual, 2021.
- [12] K. Moon, Y. Choi, and K. T. Kim. Experimental Investigation of Lean-Premixed Hydrogen Combustion Instabilities in a Can-Annular Combustion System. *Combustion and Flame*, 235:111697, 2022. doi: 10.1016/j.combustflame.2021.111697.
- [13] K. Moon, D. Bae, and K. T. Kim. Modal Dynamics of Self-Excited Thermoacoustic Instabilities in Even and Odd Numbered Networks of Lean-Premixed Combustors. *Combustion and Flame*, 255:112928, 2023. doi: 10.1016/j.combustflame.2023.112928.
- [14] S. C. Humbert and A. Orchini. Acoustics of Can-Annular Combustors: Experimental Characterisation and Modelling of a Lab-Scale Multi-Can Setup with Adjustable Geometry. *Journal of Sound and Vibration*, 564:117864, 2023. doi: 10.1016/j.jsv.2023.117864.
- [15] J. Beita, M. Talibi, N. Rocha, C. Ezenwajiaku, S. Sadasivuni, and R. Balachandran. Experimental Investigation of Combustion Instabilities in a Laboratory-Scale, Multi-Can Gas Turbine Combustor. In *Volume 3B: Combustion, Fuels, and Emissions*, page V03BT04A030, Boston, Massachusetts, USA, 2023. American Society of Mechanical Engineers. doi: 10.1115/GT2023-103206.
- [16] P. E. Buschmann, N. A. Worth, and J. P. Moeck. Thermoacoustic Oscillations in a Can-Annular Model Combustor with Asymmetries in the Can-to-Can Coupling. *Proceedings of the Combustion Institute*, 39(4):5707–5715, 2023. doi: 10.1016/j.proci.2022.07.060.
- [17] K. Kunze. *Untersuchung des Thermoakustischen Flammenübertragungsverhaltens in einer Ringbrennkammer*. PhD thesis, Universität München, 2004.
- [18] J.-F. Bourgouin, D. Durox, J. P. Moeck, T. Schuller, and S. Candel. Self-Sustained Instabilities in an Annular Combustor Coupled by Azimuthal and Longitudinal Acoustic Modes. page V01BT04A007, 2013. doi: 10.1115/GT2013-95010.
- [19] J. R. Dawson and N. A. Worth. Flame Dynamics and Unsteady Heat Release Rate of Self-Excited Azimuthal Modes in an Annular Combustor. *Combustion and Flame*, 161(10):2565–2578, 2014. doi: 10.1016/j.combustflame.2014.03.021.
- [20] M. Betz, M. Wagner, M. Zahn, N. V. Stadlmair, M. Schulze, C. Hirsch, and T. Sattelmayer. Impact of Damper Parameters on the Stability Margin of an Annular Combustor Test Rig. In *Volume 4B: Combustion, Fuels and Emissions*, page V04BT04A001, Charlotte, North Carolina, USA, 2017. American Society of Mechanical Engineers. doi: 10.1115/GT2017-64239.
- [21] M. Mazur, H. T. Nygård, J. R. Dawson, and N. A. Worth. Characteristics of Self-Excited Spinning Azimuthal Modes in an Annular Combustor with Turbulent Premixed Bluff-Body Flames. *Proceedings of the Combustion Institute*, 2018. doi: 10.1016/j.proci.2018.07.080.
- [22] T. Indlekofer, A. Faure-Beaulieu, N. Noiray, and J. Dawson. The Effect of Dynamic Operating Conditions on the Thermoacoustic Response of Hydrogen Rich

- Flames in an Annular Combustor. *Combustion and Flame*, 223:284–294, 2021. doi: 10.1016/j.combustflame.2020.10.013.
- [23] F. Farisco, L. Panek, and J. B. Kok. Thermo-Acoustic Cross-Talk between Cans in a Can-Annular Combustor. *International Journal of Spray and Combustion Dynamics*, 9(4):452–469, 2017. doi: 10.1177/1756827717716373.
- [24] K. Moon, H. Jegal, J. Gu, and K. T. Kim. Combustion-Acoustic Interactions through Cross-Talk Area between Adjacent Model Gas Turbine Combustors. *Combustion and Flame*, 202:405–416, 2019. doi: 10.1016/j.combustflame.2019.01.027.
- [25] J. Brind. Acoustic Boundary Conditions for Can-Annular Combustors. *International Journal of Turbomachinery, Propulsion and Power*, 8(3):32, 2023. doi: 10.3390/ijtp8030032.
- [26] S. Bethke, W. Krebs, P. Flohr, and B. Prade. Thermoacoustic Properties of Can Annular Combustors. In *8th AIAA/CEAS Aeroacoustics Conference & Exhibit*, Breckenridge, CO, USA, 2002. American Institute of Aeronautics and Astronautics. doi: 10.2514/6.2002-2570.
- [27] M. Yoon. Thermoacoustics and Combustion Instability Analysis for Multi-Burner Combustors. *Journal of Sound and Vibration*, 492:115774, 2021. doi: 10.1016/j.jsv.2020.115774.
- [28] G. Ghirardo, C. Di Giovine, J. P. Moeck, and M. R. Bothien. Thermoacoustics of Can-Annular Combustors. *Journal of Engineering for Gas Turbines and Power*, 141(1):011007, 2019. doi: 10.1115/1.4040743.
- [29] M. Haeringer and W. Polifke. Time Domain Bloch Boundary Conditions for Efficient Simulation of Thermoacoustic Limit-Cycles in (Can-)Annular Combustors. *Journal of Engineering for Gas Turbines and Power*, 141(12):121005, 2019. doi: 10.1115/1.4044869.
- [30] M. Haeringer, G. J. J. Fournier, M. Meindl, and W. Polifke. A Strategy to Tune Acoustic Terminations of Single-Can Test-Rigs to Mimic Thermoacoustic Behavior of a Full Engine. *Journal of Engineering for Gas Turbines and Power*, 143(7):710029, 2021. doi: 10.1115/1.4048642.
- [31] J.-F. Parmentier, P. Salas, P. Wolf, G. Staffelbach, F. Nicoud, and T. Poinsot. A Simple Analytical Model to Study and Control Azimuthal Instabilities in Annular Combustion Chambers. *Combustion and Flame*, 159(7):2374–2387, 2012. doi: 10.1016/j.combustflame.2012.02.007.
- [32] M. Bauerheim, J.-F. Parmentier, P. Salas, F. Nicoud, and T. Poinsot. An Analytical Model for Azimuthal Thermoacoustic Modes in an Annular Chamber Fed by an Annular Plenum. *Combustion and Flame*, 161(5):1374–1389, 2014. doi: 10.1016/j.combustflame.2013.11.014.
- [33] M. Bauerheim, F. Nicoud, and T. Poinsot. Progress in Analytical Methods to Predict and Control Azimuthal Combustion Instability Modes in Annular Chambers. *Physics of Fluids*, 28(2):021303, 2016. doi: 10.1063/1.4940039.

- [34] S. Evesque and W. Polifke. Low-Order Acoustic Modelling for Annular Combustors: Validation and Inclusion of Modal Coupling. In *ASME Turbo Expo 2002: Power for Land, Sea, and Air*, volume 1: Turbo Expo 2002, pages 321–331, Amsterdam, The Netherlands, 2002. ASMEDC. doi: 10.1115/GT2002-30064.
- [35] W. Polifke, C. O. Paschereit, and K. Döbbeling. Constructive and Destructive Interference of Acoustic and Entropy Waves in a Premixed Combustor with a Choked Exit. *International Journal of Acoustics and Vibration*, 6(3):135–146, 2001. doi: 10.20855/IJAV.2001.6.382.
- [36] D. Yang and A. S. Morgans. Low-Order Network Modeling for Annular Combustors Exhibiting Longitudinal and Circumferential Modes. In *ASME Turbo Expo 2018: Turbomachinery Technical Conference and Exposition*, GT2018-76506, Lillestrom, Norway, 2018. ASME. doi: 10.1115/GT2018-76506.
- [37] G. Campa and S. M. Camporeale. Prediction of the Thermoacoustic Combustion Instabilities in Practical Annular Combustors. *J. Eng. Gas Turbines and Power*, 136(9): 091504–091504, 2014. doi: 10.1115/1.4027067.
- [38] G. Staffelbach, L. Y. M. Gicquel, G. Boudier, and T. Poinsot. Large Eddy Simulation of Self Excited Azimuthal Modes in Annular Combustors. *Proceedings of the Combustion Institute*, 32(2):2909–2916, 2009. doi: 10.1016/j.proci.2008.05.033.
- [39] P. Wolf, R. Balakrishnan, G. Staffelbach, L. Gicquel, and T. Poinsot. Using LES to Study Reacting Flows and Instabilities in Annular Combustion Chambers. *Flow, Turbulence and Combustion*, 88:191–206, 2012. doi: 10.1007/s10494-011-9367-7.
- [40] P. Wolf, G. Staffelbach, L. Y. M. Gicquel, J.-D. Müller, and T. Poinsot. Acoustic and Large Eddy Simulation Studies of Azimuthal Modes in Annular Combustion Chambers. *Combustion and Flame*, 159(11):3398–3413, 2012. doi: 10.1016/j.combustflame.2012.06.016.
- [41] R. Meloni, G. Ceccherini, V. Michelassi, and G. Riccio. Analysis of the Self-Excited Dynamics of a Heavy-Duty Annular Combustion Chamber by Large-Eddy Simulation. *Journal of Engineering for Gas Turbines and Power*, 141(11), 2019. doi: 10.1115/1.4044929.
- [42] J. Z. Ho, S. Jella, M. Talei, G. Bourque, T. Indlekofer, and J. Dawson. Assessment of the LES-FGM Framework for Capturing Stable and Unstable Modes in a Hydrogen / Methane Fuelled Premixed Combustor. *Combustion and Flame*, 255:112904, 2023. doi: 10.1016/j.combustflame.2023.112904.
- [43] S. Jaensch and W. Polifke. Uncertainty Encountered When Modelling Self-Excited Thermoacoustic Oscillations with Artificial Neural Networks. *Int. J. Spray Combust. Dyn.*, 9(4):367–379, 2017. doi: 10.1177/1756827716687583.
- [44] A. P. Dowling. A Kinematic Model of a Ducted Flame. *Journal of Fluid Mechanics*, 394:51–72, 1999. doi: 10.1017/S0022112099005686.

- [45] N. Noiray, D. Durox, T. Schuller, and S. Candel. A Unified Framework for Nonlinear Combustion Instability Analysis Based on the Flame Describing Function. *Journal of Fluid Mechanics*, 615:139–167, 2008. doi: 10.1017/S0022112008003613.
- [46] X. Han and A. S. Morgans. Simulation of the Flame Describing Function of a Turbulent Premixed Flame Using an Open-Source LES Solver. *Combustion and Flame*, 162(5): 1778–1792, 2015. doi: 10.1016/j.combustflame.2014.11.039.
- [47] M. Haeringer, M. Merk, and W. Polifke. Inclusion of Higher Harmonics in the Flame Describing Function for Predicting Limit Cycles of Self-Excited Combustion Instabilities. *Proceedings of the Combustion Institute*, 37(4):5255–5262, 2019. doi: 10.1016/j.proci.2018.06.150.
- [48] N. Tathawadekar, A. K. Doan, C. F. Silva, and N. Thuerey. Modelling of the Nonlinear Flame Response of a Bunsen-type Flame via Multi-Layer Perceptron. *Proceedings of the Combustion Institute*, 38(4):6261–6269, 2021. doi: 10.1016/j.proci.2020.07.115.
- [49] V. Yadav, M. Casel, and A. Ghani. Physics-Informed Recurrent Neural Networks for Linear and Nonlinear Flame Dynamics. *Proceedings of the Combustion Institute*, page S1540748922003145, 2022. doi: 10.1016/j.proci.2022.08.036.
- [50] M. Rywik, A. Zimmermann, A. J. Eder, E. Scoletta, and W. Polifke. Spatially Resolved Modeling of the Nonlinear Dynamics of a Laminar Premixed Flame with a Multilayer Perceptron - Convolution Autoencoder Network. *Journal of Engineering for Gas Turbines and Power*, 146:061009–1,10, 2024. doi: 10.1115/1.4063788.
- [51] B. Schuermans, H. Luebecke, D. Bajusz, and P. Flohr. Thermoacoustic Analysis of Gas Turbine Combustion Systems Using Unsteady CFD. In *Proceedings of ASME Turbo Expo*, GT2005-68393, Reno, Nevada, USA, 2005. ASME. doi: 10.1115/GT2005-68393.
- [52] C. T. Wall. *Numerical Methods for Large Eddy Simulation of Acoustic Combustion Instabilities*. PhD thesis, Stanford University, 2005.
- [53] J. Moeck, C. Scharfenberg, O. Paschereit, and R. Klein. A Zero-Mach Solver and Reduced Order Acoustic Representations for Modeling and Control of Combustion Instabilities. In *Active Flow Control II*, volume 108 of *Notes on Numerical Fluid Mechanics and Multidisciplinary Design*, pages 291–306. Springer, 2010. ISBN 978-3-642-11735-0.
- [54] S. R. Chakravarthy, C. Balaji, R. K. R. Katreddy, and A. Nath. A Framework for Numerical Simulation of Turbulent Incompressible Unsteady Flame Dynamics Coupled with Acoustic Calculations in Time and Frequency Domains. In *N31 - Int'l Summer School and Workshop on Non-Normal and Nonlinear Effects In Aero- and Thermoacoustics*, page 12, Munich, Germany, 2013. ISBN ,.
- [55] T. Klenke, F. Lo Presti, K. Lackhove, F. di Mare, A. Sadiki, and J. Janicka. Two-Way Hybrid LES/CAA Approach Including Acoustic Feedback Loop for the Prediction of Thermoacoustic Instabilities in Technical Combustors. In *Volume 4A: Combustion, Fuels and Emissions*, page V04AT04A019, Charlotte, North Carolina, USA, 2017. American Society of Mechanical Engineers. doi: 10.1115/GT2017-63271.

- [56] P. Tudisco, R. Ranjan, S. Menon, S. Jaensch, and W. Polifke. Application of the Time-Domain Impedance Boundary Condition to Large-Eddy Simulation of Combustion Instability in a Shear-Coaxial, High Pressure Combustor. *Flow, Turbulence and Combustion*, 99(1):185–207, 2017. doi: 10.1007/s10494-017-9804-3.
- [57] P. Tudisco, R. Ranjan, and S. Menon. Simulation of Transverse Combustion Instability in a Multi-Injector Combustor Using the Time-Domain Impedance Boundary Conditions. *Flow, Turbulence and Combustion*, 101(1):55–76, 2018. doi: 10.1007/s10494-017-9885-z.
- [58] S. Jaensch, M. Merk, E. Gopalakrishnan, S. Bomberg, T. Emmert, R. Sujith, and W. Polifke. Hybrid CFD/Low-Order Modeling of Nonlinear Thermoacoustic Oscillations. *Proceedings of the Combustion Institute*, 36(3):3827–3834, 2017. doi: 10.1016/j.proci.2016.08.006.
- [59] G. A. Mensah, G. Campa, and J. P. Moeck. Efficient Computation of Thermoacoustic Modes in Industrial Annular Combustion Chambers Based on Bloch-Wave Theory. *Journal of Engineering for Gas Turbines and Power*, 138(8):081502, 2016. doi: 10.1115/1.4032335.
- [60] G. A. Mensah and J. P. Moeck. Limit Cycles of Spinning Thermoacoustic Modes in Annular Combustors: A Bloch-Wave and Adjoint-Perturbation Approach. In *ASME Turbo Expo 2017: Turbine Technical Conference and Exposition*, GT2017-64817, 2017. doi: 10.1115/GT2017-64817.
- [61] F. Bloch. Über die Quantenmechanik der Elektronen in Kristallgittern. *Zeitschrift für Physik*, 52(7-8):555–600, 1929. doi: 10.1007/BF01339455.
- [62] M. Haeringer and W. Polifke. Hybrid CFD/Low-Order Modeling of Thermoacoustic Limit Cycle Oscillations in Can-Annular Configurations. *Int. J. Spray Comb. Dynamics*, 14(1-2):143–152, 2022. doi: 10.1177/17568277221085953.
- [63] A. M. Garcia, S. Le Bras, J. Prager, M. Haeringer, and W. Polifke. Large Eddy Simulation of the Dynamics of Lean Premixed Flames Using Global Reaction Mechanisms Calibrated for CH₄-H₂ Fuel Blends. *Physics of Fluids*, 34(9):095105, 2022. doi: 10.1063/5.0098898.
- [64] C. J. Greenshields and H. G. Weller. *Notes on Computational Fluid Dynamics: General Principles*. CFD Direct Limited, Reading, UK, 2022. ISBN 978-1-399-92078-0.
- [65] K. Oberleithner and A. Albayrak. Vorhersage von Flammentransferfunktionen: Abschätzung der Flammentransferfunktion aus stationären Strömungsfeldern. Abschlussbericht 1151, FVV / Informationstagung Turbomaschinen, Frühjahr 2018, Bad Neuenahr, 2018.
- [66] T. Poinso and S. K. Lele. Boundary Conditions for Direct Simulation of Compressible Viscous Flows. *Journal of Computational Physics*, 101(1):104–129, 1992. doi: 10.1016/0021-9991(92)90046-2.

-
- [67] S. van Buren. *Acoustic and Thermal Characterization of Quarter-Wave Resonators*. PhD thesis, TU München, München, Germany, 2021.
- [68] S. W. Rienstra and A. Hirschberg. *An Introduction to Acoustics*. Technical report, 2004.
- [69] J. Li, D. Wang, A. S. Morgans, and L. Yang. Analytical Solutions of Acoustic Field in Annular Combustion Chambers with Non-Uniform Cross-Sectional Surface Area and Mean Flow. *Journal of Sound and Vibration*, 506:116175, 2021. doi: 10.1016/j.jsv.2021.116175.
- [70] J. Li, D. Yang, C. M. Luzzato, and A. S. Morgans. Open Source Combustion Instability Low Order Simulator (OSCILOS–Long). Technical report, Imperial College of Science, Technology and Medicine / Thermo-Fluids Section, London, UK, 2017.
- [71] B. Schuermans, V. Bellucci, and C. O. Paschereit. Thermoacoustic Modeling and Control of Multi-Burner Combustion Systems. In *Volume 2: Turbo Expo 2003*, pages 509–519, Atlanta, GA, USA, 2003. ASMEDC. doi: 10.1115/GT2003-38688.
- [72] T. Emmert, S. Jaensch, C. Sovardi, and W. Polifke. taX - a Flexible Tool for Low-Order Duct Acoustic Simulation in Time and Frequency Domain. In *7th Forum Acusticum*, Krakow, 2014. DEGA.
- [73] G. Heilmann and T. Sattelmayer. On the Convective Wave Equation for the Investigation of Combustor Stability Using FEM-methods. *International Journal of Spray and Combustion Dynamics*, page 175682772210844, 2022. doi: 10.1177/17568277221084470.
- [74] T. Hofmeister, T. Hummel, F. Berger, N. Klarmann, and T. Sattelmayer. Elimination of Numerical Damping in the Stability Analysis of Noncompact Thermoacoustic Systems With Linearized Euler Equations. *Journal of Engineering for Gas Turbines and Power*, 143(3):031013, 2021. doi: 10.1115/1.4049651.
- [75] A. Kierkegaard, S. Boij, and G. Efraimsson. A Frequency Domain Linearized Navier-Stokes Equations Approach to Acoustic Propagation in Flow Ducts with Sharp Edges. *The Journal of the Acoustical Society of America*, 127(2):710–719, 2010. doi: 10.1121/1.3273899.
- [76] J. Gikadi, S. Föllner, and T. Sattelmayer. Impact of Turbulence on the Prediction of Linear Aeroacoustic Interactions: Acoustic Response of a Turbulent Shear Layer. *Journal of Sound and Vibration*, 333(24):6548–6559, 2014. doi: 10.1016/j.jsv.2014.06.033.
- [77] M. Meindl, A. Albayrak, and W. Polifke. A State-Space Formulation of a Discontinuous Galerkin Method for Thermoacoustic Stability Analysis. *Journal of Sound and Vibration*, 481:115431, 2020. doi: 10.1016/j.jsv.2020.115431.
- [78] A. Gentemann, A. Fischer, S. Evesque, and W. Polifke. Acoustic Transfer Matrix Reconstruction and Analysis for Ducts with Sudden Change of Area. In *9th AIAA/CEAS Aeroacoustics Conference and Exhibit*, page 3142, 2003.
- [79] T. Sattelmayer, A. Eroglu, M. Koenig, W. Krebs, and G. Myers. Industrial Combustors: Conventional, Non-premixed, and Dry Low Emissions (DLN). In T. C. Lieuwen and

- V. Yang, editors, *Gas Turbine Emissions*, pages 290–362. Cambridge University Press, 1 edition, 2013. doi: 10.1017/CBO9781139015462.015.
- [80] F. E. Marble and S. M. Candel. Acoustic Disturbance from Gas Non-Uniformities Convected Through a Nozzle. *Journal of Sound and Vibration*, 55(2):225–243, 1977. doi: 10.1016/0022-460X(77)90596-X.
- [81] N. Lamarque and T. Poinso. Boundary Conditions for Acoustic Eigenmodes Computation in Gas Turbine Combustion Chambers. *AIAA Journal*, 46(9):2282–2292, 2008. doi: 10.2514/1.35388.
- [82] N. A. Worth and J. R. Dawson. Cinematographic OH-PLIF Measurements of Two Interacting Turbulent Premixed Flames with and without Acoustic Forcing. *Combustion and Flame*, 159(3):1109–1126, 2012. doi: 10.1016/j.combustflame.2011.09.006.
- [83] J. O’Connor, V. Acharya, and T. Lieuwen. Transverse Combustion Instabilities: Acoustic, Fluid Mechanic, and Flame Processes. *Progress in Energy and Combustion Science*, 49: 1–39, 2015. doi: 10.1016/j.pecs.2015.01.001.
- [84] A. Saurabh and C. O. Paschereit. Dynamics of Premixed Swirl Flames under the Influence of Transverse Acoustic Fluctuations. *Combustion and Flame*, 182:298–312, 2017. doi: 10.1016/j.combustflame.2017.04.014.
- [85] N. Purwar, M. Haeringer, B. Schuermans, and W. Polifke. Flame Response to Transverse Velocity Excitation Leading to Frequency Doubling and Modal Coupling. *Combustion and Flame*, 230:111412, 2021. doi: 10.1016/j.combustflame.2021.111412.
- [86] J. von Saldern, A. Orchini, and J. Moeck. Analysis of Thermoacoustic Modes in Can-Annular Combustors Using Effective Bloch-Type Boundary Conditions. *Journal of Engineering for Gas Turbines and Power*, 143(7):071019, 2021. doi: 10.1115/1.4049162.
- [87] G. J. J. Fournier, M. Meindl, C. F. Silva, G. Ghirardo, M. R. Bothien, and W. Polifke. Low-Order Modeling of Can-Annular Combustors. *Journal of Engineering for Gas Turbines and Power*, 143(12):121004, 2021. doi: 10.1115/1.4051954.
- [88] G. J. J. Fournier, M. Haeringer, C. F. Silva, and W. Polifke. Low-Order Modeling to Investigate Clusters of Intrinsic Thermoacoustic Modes in Annular Combustors. *Journal of Engineering for Gas Turbines and Power*, 143(4):041025, 2021. doi: 10.1115/1.4049356.
- [89] G. Ghirardo, J. P. Moeck, and M. R. Bothien. Effect of Noise and Nonlinearities on Thermoacoustics of Can-Annular Combustors. *Journal of Engineering for Gas Turbines and Power*, 142(4):041005, 2020. doi: 10.1115/1.4044487.
- [90] J. G. R. von Saldern, J. P. Moeck, and A. Orchini. Nonlinear Interaction between Clustered Unstable Thermoacoustic Modes in Can-Annular Combustors. *Proceedings of the Combustion Institute*, 38(4):6145–6153, 2021. doi: 10.1016/j.proci.2020.06.236.
- [91] K. Moon, C. Yoon, and K. T. Kim. Influence of Rotational Asymmetry on Thermoacoustic Instabilities in a Can-Annular Lean-Premixed Combustor. *Combustion and Flame*, 223:295–306, 2021. doi: 10.1016/j.combustflame.2020.10.012.

-
- [92] N. A. Worth and J. R. Dawson. Modal Dynamics of Self-Excited Azimuthal Instabilities in an Annular Combustion Chamber. *Combustion and Flame*, 160(11):2476–2489, 2013. doi: 10.1016/j.combustflame.2013.04.031.
- [93] A. Faure-Beaulieu and N. Noiray. Symmetry Breaking of Azimuthal Waves: Slow-flow Dynamics on the Bloch Sphere. *Physical Review Fluids*, 5(2):023201, 2020. doi: 10.1103/PhysRevFluids.5.023201.
- [94] A. Faure-Beaulieu, T. Indlekofer, J. R. Dawson, and N. Noiray. Experiments and Low-Order Modelling of Intermittent Transitions between Clockwise and Anticlockwise Spinning Thermoacoustic Modes in Annular Combustors. *Proceedings of the Combustion Institute*, 38(4):5943–5951, 2021. doi: 10.1016/j.proci.2020.05.008.
- [95] A. Faure-Beaulieu, T. Indlekofer, J. R. Dawson, and N. Noiray. Imperfect Symmetry of Real Annular Combustors: Beating Thermoacoustic Modes and Heteroclinic Orbits. *Journal of Fluid Mechanics*, 925:R1, 2021. doi: 10.1017/jfm.2021.649.
- [96] T. Indlekofer, A. Faure-Beaulieu, J. R. Dawson, and N. Noiray. Spontaneous and Explicit Symmetry Breaking of Thermoacoustic Eigenmodes in Imperfect Annular Geometries. *Journal of Fluid Mechanics*, 944:A15, 2022. doi: 10.1017/jfm.2022.468.
- [97] N. Noiray and B. Schuermans. On the Dynamic Nature of Azimuthal Thermoacoustic Modes in Annular Gas Turbine Combustion Chambers. *Proceedings of the Royal Society A: Mathematical, Physical and Engineering Sciences*, 469(2151):20120535–20120535, 2013. doi: 10.1098/rspa.2012.0535.
- [98] S. Jaensch, C. Sovardi, and W. Polifke. On the Robust, Flexible and Consistent Implementation of Time Domain Impedance Boundary Conditions for Compressible Flow Simulations. *Journal of Computational Physics*, 314:145–159, 2016. doi: 10.1016/j.jcp.2016.03.010.
- [99] H. Weller, G. Tabor, H. Jasak, and C. Fureby. A Tensorial Approach to Computational Continuum Mechanics Using Object-Oriented Techniques. *Computers in physics*, 12: 620–631, 1998. doi: 10.1063/1.168744.
- [100] J. Lunze. *Regelungstechnik. 1: Systemtheoretische Grundlagen, Analyse und Entwurf einschleifiger Regelungen: mit 64 Beispielen, 166 Übungsaufgaben sowie einer Einführung in das Programmsystem MATLAB*. Springer-Lehrbuch. Springer, Berlin, 5., neu bearb. und erw. Aufl edition, 2006. ISBN 978-3-540-28326-3.
- [101] T. Emmert, M. Meindl, S. Jaensch, and W. Polifke. Linear State Space Interconnect Modeling of Acoustic Systems. *Acta Acustica united with Acustica*, 102(5):824–833, 2016. doi: 10.3813/AAA.918997.
- [102] W. Polifke, C. Wall, and P. Moin. Partially Reflecting and Non-Reflecting Boundary Conditions for Simulation of Compressible Viscous Flow. *Journal of Computational Physics*, 213:437–449, 2006. doi: doi:10.1016/j.jcp.2005.08.016.
- [103] W. Polifke. Black-Box System Identification for Reduced Order Model Construction. *Annals of Nuclear Energy*, 67C:109–128, 2014. doi: 10.1016/j.anucene.2013.10.037.

- [104] T. Lieuwen. Modeling Premixed Combustion - Acoustic Wave Interactions: A Review. *Journal of Propulsion and Power*, 19(5):765–781, 2003. doi: 10.2514/2.6193.
- [105] A. J. Eder, C. F. Silva, M. Haeringer, J. Kuhlmann, and W. Polifke. Incompressible versus Compressible Large Eddy Simulation for the Identification of Premixed Flame Dynamics. *International Journal of Spray and Combustion Dynamics*, 15(1):16–32, 2023. doi: 10.1177/17568277231154204.
- [106] B.-T. Chu. On the Generation of Pressure Waves at a Plane Flame Front. *Symposium (International) on Combustion*, 4(1):603–612, 1953. doi: 10.1016/S0082-0784(53)80081-0.
- [107] M. Hoeijmakers, V. Kornilov, I. Lopez Arteaga, P. de Goey, and H. Nijmeijer. Intrinsic Instability of Flame-Acoustic Coupling. *Combustion and Flame*, 161(11):2860–2867, 2014. doi: 10.1016/j.combustflame.2014.05.009.
- [108] T. Emmert, S. Bomberg, and W. Polifke. Intrinsic Thermoacoustic Instability of Premixed Flames. *Combustion and Flame*, 162(1):75–85, 2015. doi: 10.1016/j.combustflame.2014.06.008.
- [109] P. Brokof, G. J. J. Fournier, and W. Polifke. Linear Time-Continuous State-Space Realization of Flame Transfer Functions by Means of a Propagation Equation. In *INTER-NOISE and NOISE-CON Congress and Conference Proceedings*, pages 3490–3501, Glasgow, Scotland, 2023. Institute of Noise Control Engineering. doi: 10.3397/IN_2022_0496.
- [110] T. Wigren. Recursive Prediction Error Identification Using the Nonlinear Wiener Model. *Automatica*, 29(4):1011–1025, 1993. doi: 10.1016/0005-1098(93)90103-Z.
- [111] M. Schoukens and K. Tiels. Identification of Block-Oriented Nonlinear Systems Starting from Linear Approximations: A Survey. *Automatica*, 85:272–292, 2017. doi: 10.1016/j.automatica.2017.06.044.
- [112] Z. Zhang, D. Guan, Y. Zheng, and G. Li. Characterizing Premixed Laminar Flame–Acoustics Nonlinear Interaction. *Energy Conversion and Management*, 98:331–339, 2015. doi: 10.1016/j.enconman.2015.03.095.
- [113] T. Indlekofer, B. Ahn, Y. H. Kwah, S. Wiseman, M. Mazur, J. R. Dawson, and N. A. Worth. The Effect of Hydrogen Addition on the Amplitude and Harmonic Response of Azimuthal Instabilities in a Pressurized Annular Combustor. *Combustion and Flame*, 228:375–387, 2021. doi: 10.1016/j.combustflame.2021.02.015.
- [114] M. Merk, R. Gaudron, C. Silva, M. Gatti, C. Mirat, T. Schuller, and W. Polifke. Prediction of Combustion Noise of an Enclosed Flame by Simultaneous Identification of Noise Source and Flame Dynamics. *Proceedings of the Combustion Institute*, 37:5263–5270, 2019. doi: 10.1016/j.proci.2018.05.124.
- [115] W. Polifke, W. Geng, and K. Döbbeling. Optimization of Rate Coefficients for Simplified Reaction Mechanisms with Genetic Algorithms. *Combust. and Flame*, 113(1-2):119–134, 1998. doi: 10.1016/S0010-2180(97)00212-5.

- [116] M. Mazur, Y. H. Kwah, T. Indlekofer, J. R. Dawson, and N. A. Worth. Self-Excited Longitudinal and Azimuthal Modes in a Pressurised Annular Combustor. *Proceedings of the Combustion Institute*, 38(4):5997–6004, 2021. doi: 10.1016/j.proci.2020.05.033.
- [117] S. Jaensch and W. Polifke. *CFD-basierte, Niedrigdimensionale Modellierung Der Nicht-linearen Dynamik von Vormischflammen*, volume FVV-Heft Nr. 1098. 2016.
- [118] B. Franzelli, E. Riber, L. Y. Gicquel, and T. Poinso. Large Eddy Simulation of Combustion Instabilities in a Lean Partially Premixed Swirled Flame. *Combustion and Flame*, 159(2):621–637, 2012. doi: 10.1016/j.combustflame.2011.08.004.
- [119] H. Jasak. *Error Analysis and Estimation for the Finite Volume Method with Applications to Fluid Flows*. PhD thesis, Imperial College, London, UK, 1996.
- [120] F. Nicoud and F. Ducros. Subgrid-Scale Stress Modelling Based on the Square of the Velocity Gradient Tensor. *Flow Turbulence and Combustion*, 62(3):183–200, 1999. doi: 10.1023/A:1009995426001.
- [121] O. Colin, F. Ducros, D. Veynante, and T. Poinso. A Thickened Flame Model for Large Eddy Simulation of Turbulent Premixed Combustion. *Physics of Fluids*, 12(7):1843–1863, 2000. doi: 10.1063/1.870436.
- [122] F. Charlette, C. Meneveau, and D. Veynante. A Power-Law Flame Wrinkling Model for LES of Premixed Turbulent Combustion Part I: Non-Dynamic Formulation and Initial Tests. *Combustion and Flame*, 131(1):159–180, 2002. doi: 10.1016/S0010-2180(02)00400-5.
- [123] F. Charlette, C. Meneveau, and D. Veynante. A Power-Law Flame Wrinkling Model for LES of Premixed Turbulent Combustion Part II: Dynamic Formulation. *Combustion and Flame*, 131(1-2):181–197, 2002. doi: 10.1016/S0010-2180(02)00401-7.
- [124] V. N. Kornilov, R. Rook, J. H. M. ten Thije Boonkkamp, and L. P. H. de Goey. Experimental and Numerical Investigation of the Acoustic Response of Multi-Slit Bunsen Burners. *Combustion and Flame*, 156(10):1957–1970, 2009. doi: 10.1016/j.combustflame.2009.07.017.
- [125] F. Duchaine, F. Boudy, D. Durox, and T. Poinso. Sensitivity Analysis of Transfer Functions of Laminar Flames. *Combustion and Flame*, 158(12):2384–2394, 2011. doi: 10.1016/j.combustflame.2011.05.013.
- [126] C. F. Silva, T. Emmert, S. Jaensch, and W. Polifke. Numerical Study on Intrinsic Thermoacoustic Instability of a Laminar Premixed Flame. *Combustion and Flame*, 162(9):3370–3378, 2015. doi: 10.1016/j.combustflame.2015.06.003.
- [127] K. Förner and W. Polifke. Nonlinear Aeroacoustic Identification of Helmholtz Resonators Based on a Local-Linear Neuro-Fuzzy Network Model. *J. Sound Vibration*, 407:170–190, 2017. doi: 10.1016/j.jsv.2017.07.002.
- [128] G. Doehner, M. Haeringer, and C. F. Silva. Nonlinear Flame Response Modelling by a Parsimonious Set of Ordinary Differential Equations. *International Journal of Spray and Combustion Dynamics*, 14(1-2):17–29, 2022. doi: 10.1177/17568277221094760.

- [129] F. Selimefendigil. *Identification and Analysis of Nonlinear Heat Sources in Thermo-Acoustic Systems*. Doctoral Thesis, TU München, 2010.
- [130] T. Schuller, D. Durox, and S. Candel. A Unified Model for the Prediction of Laminar Flame Transfer Functions: Comparisons Between Conical and V-Flame Dynamics. *Combustion and Flame*, 134(1-2):21–34, 2003. doi: 10.1016/S0010-2180(03)00042-7.
- [131] A. Orchini and M. Juniper. Flame Double Input Describing Function Analysis. *Combustion and Flame*, 171:87–102, 2016.
- [132] M. A. Heckl. Analytical Model of Nonlinear Thermo-Acoustic Effects in a Matrix Burner. *J. Sound Vib.*, 332(17):4021–4036, 2013. doi: 10.1016/j.jsv.2012.11.010.
- [133] M. Heckl. A New Perspective on the Flame Describing Function of a Matrix Flame. *International Journal of Spray and Combustion Dynamics*, 7(2):91–112, 2015. doi: 10.1260/1756-8277.7.2.91.
- [134] S. M. Gopinathan, D. Iurashev, A. Bigongiari, and M. Heckl. Nonlinear Analytical Flame Models with Amplitude-Dependent Time-Lag Distributions. *Int. J. Spray and Combustion Dynamics*, 10:264–276, 2017. doi: 10.1177/1756827717728056.
- [135] B. Boashash. Estimating and Interpreting the Instantaneous Frequency of a Signal. I. Fundamentals. *Proceedings of the IEEE*, 80(4):520–538, 1992. doi: 10.1109/5.135376.
- [136] A. P. Dowling and S. R. Stow. Acoustic Analysis of Gas Turbine Combustors. *Journal of Propulsion and Power*, 19(5):751–764, 2003. doi: 10.2514/2.6192.
- [137] P. Palies, D. Durox, T. Schuller, and S. Candel. Nonlinear Combustion Instability Analysis Based on the Flame Describing Function Applied to Turbulent Premixed Swirling Flames. *Combustion and Flame*, 158(10):1980–1991, 2011. doi: 10.1016/j.combustflame.2011.02.012.
- [138] D. Laera, T. Schuller, K. Prieur, D. Durox, S. M. Camporeale, and S. Candel. Flame Describing Function Analysis of Spinning and Standing Modes in an Annular Combustor and Comparison with Experiments. *Combustion and Flame*, 184:136–152, 2017. doi: 10.1016/j.combustflame.2017.05.021.
- [139] F. Selimefendigil and W. Polifke. A Nonlinear Frequency Domain Model for Limit Cycles in Thermoacoustic Systems with Modal Coupling. *Int. J. Spray Comb. Dynamics*, 3:303–330, 2011. doi: 10.1260/1756-8277.3.4.303.
- [140] N. Tathawadkar, A. Ösün, A. J. Eder, C. F. Silva, and N. Thuerey. Linear and Nonlinear Flame Response Prediction of Turbulent Flames Using Neural Network Models. In *Symposium on Thermoacoustics in Combustion*, Zurich, Switzerland, 2023.
- [141] T. Steinbacher and W. Polifke. Convective Velocity Perturbations and Excess Gain in Flame Response as a Result of Flame-Flow Feedback. *Fluids*, 7(2):61, 2022. doi: 10.3390/fluids7020061.

-
- [142] H. Yu, T. Jaravel, M. Ihme, M. P. Juniper, and L. Magri. Data Assimilation and Optimal Calibration in Nonlinear Models of Flame Dynamics. *Journal of Engineering for Gas Turbines and Power*, 141(12), 2019. doi: 10.1115/1.4044378.
- [143] H. Yu, M. P. Juniper, and L. Magri. Combined State and Parameter Estimation in Level-Set Methods. *Journal of Computational Physics*, 399:108950, 2019. doi: 10.1016/j.jcp.2019.108950.
- [144] H. Yu, M. P. Juniper, and L. Magri. A Data-Driven Kinematic Model of a Ducted Premixed Flame. *Proceedings of the Combustion Institute*, page S1540748920302170, 2020. doi: 10.1016/j.proci.2020.06.137.
- [145] P. Kaufmann, W. Krebs, R. Valdes, and U. Wever. 3D Thermoacoustic Properties of Single Can and Multi Can Combustor Configurations. In *Volume 3: Combustion, Fuels and Emissions, Parts A and B*, pages 527–538, Berlin, Germany, 2008. ASMEDC. doi: 10.1115/GT2008-50755.
- [146] H. Mongia, T. Held, G. Hsiao, and R. P. Pandalai. Challenges and Progress in Controlling Dynamics in Gas Turbine Combustors. *Journal of Propulsion and Power*, 19(5):ab Seite 822, 2003.
- [147] M. R. Bothien, J. P. Moeck, and C. Oliver Paschereit. Active Control of the Acoustic Boundary Conditions of Combustion Test Rigs. *J. Sound Vib.*, 318(4-5):678–701, 2008. doi: 10.1016/j.jsv.2008.04.046.
- [148] M. R. Bothien and C. O. Paschereit. Tuning of the Acoustic Boundary Conditions of Combustion Test Rigs With Active Control: Extension to Actuators With Nonlinear Response. *J. Eng. Gas Turbines Power*, 132(9), 2010. doi: 10.1115/1.4000599.
- [149] S. Niether. *Modification of a High Pressure Test Rig for Thermoacoustic Measurements*. PhD thesis, TU Berlin, Berlin, 2018.
- [150] N. Zettervall, C. Fureby, and E. J. K. Nilsson. Evaluation of Chemical Kinetic Mechanisms for Methane Combustion: A Review from a CFD Perspective. *Fuels*, 2(2):210–240, 2021. doi: 10.3390/fuels2020013.
- [151] M. McCartney, M. Haeringer, and W. Polifke. Comparison of Machine Learning Algorithms in the Interpolation and Extrapolation of Flame Describing Functions. *J. Eng. Gas Turbines and Power*, 142:14, 2020. doi: 10.1115/1.4045516.
- [152] G. J. J. Fournier, F. Schaefer, M. Haeringer, C. F. Silva, and W. Polifke. Interplay of Clusters of Acoustic and Intrinsic Thermoacoustic Modes in Can-Annular Combustors. *Journal of Engineering for Gas Turbines and Power*, 144(12):121015, 2022. doi: 10.1115/1.4055381.
- [153] P. Krah, S. Büchholz, M. Häring, and J. Reiss. Front Transport Reduction for Complex Moving Fronts: Nonlinear Model Reduction for an Advection–Reaction–Diffusion Equation with a Kolmogorov–Petrovsky–Piskunov Reaction Term. *Journal of Scientific Computing*, 96(1):28, 2023. doi: 10.1007/s10915-023-02210-9.

List of Figures

1.1	Hybrid models developed within this thesis	3
3.1	Dimensions of an applied can-annular combustor	10
3.2	Sketch of a can-annular and annular configuration	11
3.3	Acoustic pressure field for the first order azimuthal chamber mode of the annular test-rig considered within this thesis	12
3.4	Acoustic pressure field for the first order azimuthal mode of a can-annular configuration	13
3.5	Equivalent reflection coefficient of a can-annular system	16
3.6	Strategies employed to couple CFD and LOM	17
3.7	Subsonic in- and outlet boundary with characteristic waves traveling normal to boundaries.	20
3.8	Characteristic-based filtering to obtain the acoustic waves leaving the domain.	23
3.9	CBSBC for an outlet boundary. The state-space model in the green box represents the imposed reflection coefficient.	24
3.10	Developed time domain BBC model setups	26
3.11	Developed ROLEX model setup. a) coupling via CBSBC, b) low-Mach $v' - Q'$ coupling.	27
3.12	Developed symmetry preserving ROLEX model setup. a) coupling via CBSBC, b) low-Mach $v' - Q'$ coupling	29
3.13	Wiener-type flame model comprising a linear time-invariant dynamic part (FTF) and a static nonlinear function correcting the linear model output \tilde{Q}'	31
3.14	Output of static non-linear function Eq. (3.34) (red) with exemplary s and sinusoidal input signal (black).	32
3.15	Individual steps necessary to set up and simulate LC of (can-)annular configurations with the proposed ROLEX model.	33

3.16	Individual steps necessary to set up and simulate LC of (can-)annular configurations with the proposed time domain Bloch-wave approach.	34
5.1	Sketch of the RBK4 configuration used to develop and validate the proposed hybrid strategies	44
5.2	Normalized heat release rate fluctuation in the individual cans computed by full CFD and ROLEX model	45
5.3	LC spectrum of heat release rate (top) and reference velocity (middle). Result of linear stability analysis (bottom).	46
5.4	Intermediate pressure annular combustor operated at NTNU	47
5.5	Cut through the single-sector CFD domain of the NTNU annular rig (right). Mesh in the swirler and flame anchoring region is shown on the left.	48
5.6	Phase-averaged line-of-sight integrated heat release distribution during LC oscillation. LES results in respective left plots, experimental measurements in right plots.	49
5.7	1D network model and result of linear stability analysis of the experimental test-rig	50
5.8	Gain and phase of the FTF on the left, gain and phase of the noise model on the right side. The dashed lines mark the 95% confidence interval.	52
5.9	Normalized heat release rate fluctuation of the individual flames in the ROLEX model.	53
5.10	Normalized heat release rate fluctuation computed with the time domain Bloch-wave approach.	53
5.11	Sound pressure level measured in experiment vs. computed by ROLEX model. Left side shows microphone position “L”, right side position “M”. Top row shows injector 1, bottom row injector 2.	54
5.12	Sound pressure level measured in experiment vs. computed by Bloch-wave approach. Left side shows microphone position “L”, right side position “M”.	55
5.13	Magnitude (top) and phase (bottom) of the dominant frequency component of \hat{p}	56
6.1	Common types of nonlinear flame models with exemplary references	58

List of Tables

5.1	Parameters of the global 3-step mechanism calibrated for the operating point of the NTNU annular rig. SI units.	42
5.2	Geometrical measures of RBK4.	44
6.1	Assessment of different classes of nonlinear thermoacoustic models.	61

Appendices

Time-Domain Bloch Boundary Conditions for Efficient Simulation of Thermoacoustic Limit Cycles in (Can-)Annular Combustors

Matthias Haeringer¹

Department of Mechanical Engineering,
Technical University of Munich,
Garching D-85747, Germany
e-mail: haeringer@fd.mw.tum.de

Wolfgang Polifke

Department of Mechanical Engineering,
Technical University of Munich,
Garching, D-85747, Germany

Thermo-acoustic eigenmodes of annular or can-annular combustion chambers, which typically feature a discrete rotational symmetry, may be computed in an efficient manner by utilizing the Bloch-wave theory. Unfortunately, the application of the Bloch-wave theory to combustion dynamics has hitherto been limited to the frequency domain. In this study, we present a time-domain formulation of Bloch boundary conditions (BBC), which allows to employ them in time domain simulations, e.g., computational fluid dynamics (CFD) simulations. The BBCs are expressed as acoustic scattering matrices and translated to complex-valued state-space systems. In a hybrid approach an unsteady, compressible CFD simulation of the burner-flame zone is coupled via characteristic-based state-space boundary conditions to a reduced order model of the combustor acoustics that includes BBCs. The acoustic model with BBC accounts for cross-can acoustic coupling and the discrete rotational symmetry of the configuration, while the CFD simulation accounts for the nonlinear flow-flame acoustic interactions. This approach makes it possible to model limit cycle oscillations of (can-)annular combustors at drastically reduced computational cost compared to CFD simulations of the full configuration and without the limitations of weakly nonlinear approaches that utilize a flame describing function. In this study, the suggested approach is applied to a generic multican combustor. Results agree well with a fully compressible CFD simulation of the complete configuration. [DOI: 10.1115/1.4044869]

Introduction

With the introduction of low-emission, lean-premixed gas turbine combustion systems, thermo-acoustic combustion instabilities (TCI) have become a major concern in the development of new combustors. Arising from constructive feedback between flame dynamics and acoustics, TCIs can lead to large-scale pressure oscillations, which significantly limit the operational range and may even cause structural damage [1].

Nowadays, the majority of gas turbine combustion systems are of annular or can-annular type. Although the basic configuration of these two types differs in some respects, they have two important things in common. First, both types typically feature a discrete rotational symmetry, i.e., they comprise a number of N identical sectors—in the following denoted as “unit cells”—arranged equidistantly around the circumference of the engine. Second, the individual unit cells—each containing a burner—are coupled acoustically [2] and therefore interact with each other. This gives rise to azimuthal modes, which extend over all burners around the circumference. Such azimuthal modes, which differ fundamentally from axial modes in isolated burners, are often the dominant unstable modes in real engines [1].

In order to predict the occurrence of TCIs in such systems, the model used has to account for the interaction of individual burners. In principle, a large eddy simulation of the whole combustion system including all unit cells captures the relevant physics [3–5]. As this approach directly solves the nonlinear governing equations, it inherently accounts for nonlinear effects such as nonlinear saturation of the flame response. However, the tremendous computational effort of this approach has prevented its application in

the industrial development process. Alternatives with reduced levels of accuracy and computational effort are frequency domain methods, based on simplified analytical models [6–8], network model approaches [9–11], or linearized conservation equations as the inhomogeneous Helmholtz equation [12].

Mensah et al. [13] utilized the Bloch-wave theory [14] in combination with the Helmholtz equation to determine thermo-acoustic eigenmodes of an annular combustor. For discrete symmetric systems, the Bloch-wave theory allows to consider just one unit cell by imposing special periodic boundary conditions—also called Bloch-boundary conditions (BBC). This drastically reduces computational cost. While the Bloch-wave theory is well established in aero-acoustics (e.g., see Refs. [15] and [16]), there are just a few pertinent studies in the field of thermo-acoustics. Ghirardo et al. [17] applied the Bloch-wave theory to compute eigenmodes of a generic can-annular combustor. Mensah et al. [18] assessed the effects of asymmetry by combining the Bloch-wave theory with an adjoint-based perturbation method. Important in the context of this work is the study of Mensah and Moeck [19] who combined the Bloch-wave approach with the weakly nonlinear flame describing function framework [20] to compute limit cycles of azimuthally spinning modes in annular combustors.

All of these studies cited apply the Bloch-wave theory in combination with frequency domain methods. These methods rely on the availability of an accurate model for the flame dynamics. This is especially the case, if nonlinear phenomena such as limit cycle oscillations are considered. The required nonlinear flame model, e.g., a flame describing function, is costly to determine or even not available. In contrast, time-domain methods like large eddy simulations inherently include nonlinear flame dynamics and are therefore better suited to account for nonlinear phenomena.

However, in other fields of physics the application of Bloch-wave theory with time-domain methods is already established (see, e.g., Refs. [21] and [22]). This study is intended to fill this

¹Corresponding author.

Manuscript received July 29, 2019; final manuscript received August 1, 2019; published online November 8, 2019. Editor: Jerzy T. Sawicki.

gap in the field of thermo-acoustics. It presents a time-domain formulation of BBC, which may be coupled to other time-domain models, e.g., a CFD simulation, in a straightforward manner. The proposed approach follows the hybrid strategy suggested by Jaensch et al. [23], who coupled a compressible CFD simulation of the burner-flame zone, which represents nonlinear flame–flow interactions, to a reduced order model of the system acoustics. In this study, the reduced order acoustic model includes a BBC, which accounts for discrete rotational symmetry of the considered system. The proposed approach therefore combines the advantages of time-domain models—in particular the incorporation of nonlinear effects—with a significant reduction in computational cost that is offered by Bloch-wave theory.

The paper is structured as follows: In the Bloch-Wave Theory section, Bloch-wave theory and its application to the calculation of thermo-acoustic eigenmodes of discrete rotational systems are recapitulated. The Time-Domain State-Space Representation section introduces the formulation of BBCs as acoustic scattering matrices, their translation into complex-valued time-domain state-space models, and the interconnection with other acoustic elements. This section also presents the hybrid approach, which couples the state-space model including the time-domain BBC to a fully compressible CFD simulation representing the flame–flow interactions. The CFD With Bloch-Boundary Conditions section discusses the complications that arise from the coupling of a complex-valued state-space system with a CFD simulation that can only handle real-valued signals, then the proposed approach is applied to compute limit cycle oscillation of individual azimuthal modes of a generic multi-can combustor in the application to a generic multican combustor section. Results are compared to a fully compressible CFD simulation of the complete configuration. In the Conclusion section a short conclusion is drawn.

Bloch-Wave Theory

This section recalls the Bloch-wave theory in the context of thermo-acoustics. The structure follows the presentation of Ghirardo et al. [17]. It is assumed that the full combustion system consists of N identical sectors (denoted as “unit cells”) that are equidistantly spaced around the circumference. This system exhibits a discrete rotational symmetry of N th order, i.e., the geometry is invariant under rotation by an angle of $\phi = 2\pi/N$. Figure 1 shows an example of such a system with $N = 4$.

According to the Bloch-wave theorem [14], the solution of the acoustic pressure field in such discrete rotational symmetric systems can be written as

$$\hat{p}(\mathbf{x}) = \Psi(\mathbf{x})e^{im\phi}, \text{ with} \quad (1)$$

$$m = -(N/2 - 1), \dots, -1, 0, 1, \dots, N/2 - 1, N/2.$$

Here, \hat{p} denotes the Fourier transform of acoustic pressure and $\mathbf{x} = (r, \phi, z)$ is the position vector comprised of the radial, circumferential, and axial coordinate. Ψ is a function that is identical in all N unit cells, m is called the Bloch-wave number, and its absolute value $|m|$ is the azimuthal mode order. Equation (1) implies that the solution in the full configuration is mapped from the solution in one unit cell by changing its complex phase according to the Bloch-wave number m .

Depending on the Bloch-wave number m , the appearing modes can be classified into three types, i.e., spinning modes, purely axial modes, and “push–pull” modes. Bloch-wave numbers of $m = \pm 1, \dots, \pm(N/2 - 1)$ designate modes spinning in the (anti-)clockwise direction [17]. In the following, we assume that the full configuration also exhibits reflectional symmetry, i.e., azimuthal mean flow is negligible. In this case, the modes with Bloch-wave numbers $\pm m$ are degenerate pairs that share the same eigenfrequency. The corresponding modes merely differ by the direction of rotation.

In contrast to the spinning modes, modes with $m = 0$ and $m = N/2$ do not occur in pairs. The former are purely axial modes

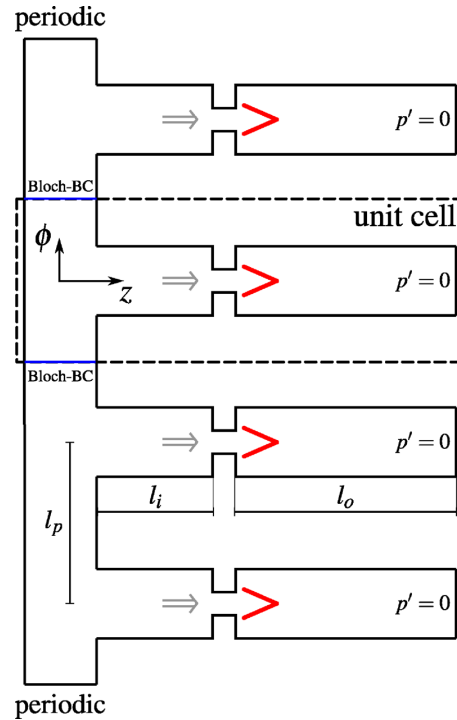


Fig. 1 Generic pseudo-2D plenum-burner configuration with $N = 4$ burners. Unit cell marked by dashed box. BBC at unit cell interfaces are marked in blue and indicated by “Bloch-BC”. Gray arrows indicate the mean flow direction.

with identical pressure fields in each unit cell, i.e., all unit cells oscillate in phase. The latter only exist for even N and are called “push–pull” modes. They are characterized by pressure and velocity fields with alternating signs in adjacent unit cells [17], i.e., all unit cells are perfectly out of phase with their respective neighbors.

With the assumption of reflection symmetry introduced previously, the mode pair with Bloch-wave numbers of opposite sign shares the same eigenfrequency ω . Therefore, the time-domain pressure field for a certain azimuthal mode order $|m|$ can be formulated as

$$p(\mathbf{x}, t) = \text{Re}\{\Psi(\mathbf{x})e^{i\omega t}(c_1e^{im\phi} + c_2e^{-im\phi})\} \quad (2)$$

where the coefficients c_1 and c_2 are the respective amplitudes of the anticlockwise and clockwise spinning waves. The amplitudes are in general not fixed a priori, but are part of the solution and may in general evolve in time. For the two types of standing modes—, i.e., axial and “push–pull” modes—this superposition is actually superfluous, as both c_1 and c_2 components have the same structure. However, to avoid case distinctions also those mode types are in the following expressed as superposition of two components.

In order to facilitate a time-domain formulation of BBCs and in particular the coupling with a transient CFD simulation, we represent in this study the pressure field for a certain azimuthal mode order m with the less common, but mathematically equivalent ansatz²

$$p(\mathbf{x}, t) = \text{Re}\{\Psi(\mathbf{x})e^{im\phi}(c_1e^{i\omega t} + c_2e^{-i\omega t})\} \quad (3)$$

²With this ansatz Bloch-wave number and azimuthal mode order are identical.

with positive Bloch-wave numbers $m = 0, \dots, N/2$ and the complex conjugate $\bar{\omega}$ of the angular frequency.

The solution for the full configuration is obtained by mapping the solution from one unit cell to the others according to Eq. (1). In order to obtain the solution in the unit cell, appropriate boundary conditions have to be set at the interfaces to the adjacent cells. Therefore, we consider the unit cell centered at the azimuthal position $\phi = \phi_0$ and extended over $\phi = [\phi_0 - \pi/N, \phi_0 + \pi/N]$. The conditions that the function $\Psi(\mathbf{x})$ is identical in each unit cell and that the pressure is continuous across the interfaces between adjacent cells demand that Ψ has to be equal at both interfaces

$$\Psi\left(r, \phi = \phi_0 - \frac{\pi}{N}, z\right) = \Psi\left(r, \phi = \phi_0 + \frac{\pi}{N}, z\right) \quad (4)$$

Inserting this relation in Eq. (1) yields a pseudo-periodic boundary condition for the pressure

$$\hat{p}\left(r, \phi = \phi_0 + \frac{\pi}{N}, z\right) = \hat{p}\left(r, \phi = \phi_0 - \frac{\pi}{N}, z\right) e^{im\frac{2\pi}{N}} \quad (5)$$

The same considerations apply for the azimuthal acoustic velocity \hat{u}_ϕ , yielding the identical pseudo-periodic condition

$$\hat{u}_\phi\left(r, \phi = \phi_0 + \frac{\pi}{N}, z\right) = \hat{u}_\phi\left(r, \phi = \phi_0 - \frac{\pi}{N}, z\right) e^{im\frac{2\pi}{N}} \quad (6)$$

These pseudo-periodic boundary conditions, Eqs. (5) and (6), for the acoustic variables are also called BBCs. For each azimuthal mode order, they impose a certain phase shift between the two interfaces. Using these boundary conditions, the eigenmodes of different azimuthal mode orders m may be obtained by solving acoustic governing equations in one unit cell. One possibility is to represent the unit cell as a network model, i.e., as a connection of basic acoustic elements. The hybrid approach proposed in this paper adopts this network model approach, but it is important to note that the Bloch-wave theory is a physical condition and therefore not restricted to a specific acoustic solver.

The Bloch-wave approach is applicable as long as the system is composed of identical unit cells. Provided that the geometry features discrete rotational symmetry, Bloch-wave theory is thus valid for axial modes ($m=0$), “push–pull” modes ($m=N/2$), and azimuthally spinning modes ($m = 1, \dots, N/2 - 1$). In the linear regime, standing waves that result from superposition of two counter-rotating spinning modes of same mode order m and equal amplitudes ($c_1=c_2$) may also be represented by Bloch waves. However, in the nonlinear regime a standing wave will expose individual burners to nonidentical amplitude levels, which in general leads to nonidentical flame dynamics due to nonlinear saturation [24]. This effect breaks the discrete rotational symmetry, which is the prerequisite for applying Bloch-wave theory [19].

Time-Domain State-Space Representation

Scattering Matrix Representation. In a network model approach, an acoustic system is split into basic elements that are connected to each other at the ports of these elements [25]. Each acoustic element can be characterized by its scattering matrix, which relates in- and outgoing acoustic waves expressed in terms of the Riemann-invariants $\hat{f} = \hat{p}/\rho c + \hat{u}$ and $\hat{g} = \hat{p}/\rho c - \hat{u}$ where ρ is the mean density and c the mean speed of sound.

Figure 2 shows the unit cell marked in Fig. 1 by the dashed box, with BBC imposed at the interface to the adjacent unit cells. The right and left interfaces are denoted with indices “R” and “L,” respectively. As indicated in Fig. 2, these pseudo-periodic boundary conditions may be considered as an acoustic element that connects the two interfaces. The scattering matrix of this element can be deduced from relations Eqs. (5) and (6) and reads

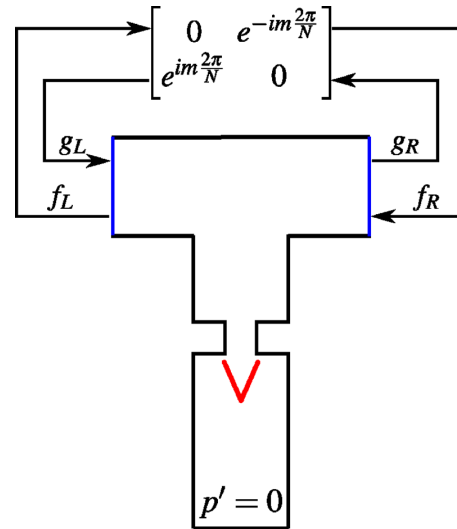


Fig. 2 Scattering-matrix representation of BBC

$$\begin{bmatrix} \hat{g}_L \\ \hat{f}_R \end{bmatrix} = \begin{bmatrix} 0 & e^{-im\frac{2\pi}{N}} \\ e^{im\frac{2\pi}{N}} & 0 \end{bmatrix} \begin{bmatrix} \hat{f}_L \\ \hat{g}_R \end{bmatrix} \quad (7)$$

The scattering matrix representing the BBC is a frequency independent and memoryless phase shift condition.

State-Space Representation. Thermo-acoustic network models are conveniently formulated as linear state-space models. The thermo-acoustic network tool tax [25] used in this study is based on state-space representation. Those state-space models may be obtained from analytical solutions, modal expansion [26], or a spatial discretization of linearized conservation equations in the considered element [27,28]. Advantages of this representation are the simple interconnection of individual elements [26] and the direct access to eigenmodes by solving a linear eigenvalue problem [28]. The general form of a state-space model reads

$$\begin{aligned} \dot{x} &= Ax + Bu \\ y &= Cx + Du \end{aligned} \quad (8)$$

where u are the inputs and y the outputs of the system. The state vector x describes the internal state of the system and \dot{x} denotes the time derivative of the state vector. The matrix A characterizes internal dynamics, B the influence of the inputs on the internal state, C projects the states onto the outputs, and D describes any direct influence of inputs on outputs.

The scattering matrix in Eq. (7) describes a system with no internal dynamics. Consequently, the system has no internal states and its state-space representation has empty matrices A , B , C . If $g_L(t)$ and $f_R(t)$ are chosen as outputs and $f_L(t)$ and $g_R(t)$ as inputs of the system, the BBC represented as state-space model is written as

$$\begin{bmatrix} g_L(t) \\ f_R(t) \end{bmatrix} = D \cdot \begin{bmatrix} f_L(t) \\ g_R(t) \end{bmatrix} = \begin{bmatrix} 0 & e^{-im\frac{2\pi}{N}} \\ e^{im\frac{2\pi}{N}} & 0 \end{bmatrix} \cdot \begin{bmatrix} f_L(t) \\ g_R(t) \end{bmatrix} \quad (9)$$

Here, the D matrix is identical to the scattering matrix in Eq. (7), but formally the model in Eq. (9) is formulated in time domain while Eq. (7) is formulated in frequency domain. The matrices are identical due to the linearity of the Fourier transform: the constant

(complex-valued) coefficient $e^{\pm im\frac{2\pi}{N}}$ both appears in time and frequency domain.

Unlike the vast majority of common state-space models, the present model representing BBC has complex-valued coefficients. In general, this results in complex-valued output signals. According to Eq. (3), the physically relevant quantity is the real part of the signals. Further implications resulting from these complex-valued coefficients are discussed in the section CFD With Bloch-Boundary Conditions.

The time-domain state-space formulation of BBC in Eq. (9) offers great flexibility in coupling them with other time-domain models. They may be interconnected with state-space models of other acoustic elements in order to represent more complex acoustic systems [25,29]. Connecting a network model of one unit cell of the combustor shown in Fig. 1 with the Bloch-element in Eq. (9) yields a network model for the full combustor, valid for a certain azimuthal mode order m . Figure 2 illustrates this approach. Note that the state-space representation of this interconnected model now in general has also complex-valued coefficients, because the Bloch-element is complex-valued. The time-evolution of acoustic pressure and velocity together with the heat release rate fluctuation is obtained by solving this interconnected model, which has the form Eq. (8), for a given initial condition x_0 . The solution can then be mapped from the computed unit cell to the remaining combustor according to Eq. (1). The physical quantities are described by the real part of the solution.

Hybrid Approaches: Coupling to CFD. If the approach described previously is used to simulate limit cycle oscillations, the network model has to include an accurate flame model that accounts for nonlinear dynamics. As for frequency domain methods mentioned in the introduction, the bottleneck of the above-mentioned approach is therefore the availability of such a flame model. An appealing alternative was suggested by Jaensch et al. [23], where a fully compressible CFD simulation of the burner-flame zone serves as a nonlinear time-domain flame model. The compressible simulation is coupled to a low-order state-space model of the acoustics via the characteristic variables f and g by characteristic-based state-space boundary conditions (CBSBC) [27]. In this study, this hybrid approach is followed to couple a reduced order model including BBC to a CFD simulation, as illustrated in Fig. 3. We will call this approach Bloch-CBSBC/CFD. The gist of the method is that a compressible simulation of the burner-flame zone is coupled at the up- and downstream side to state-space models representing the remaining acoustic elements of one unit cell and the BBCs. This interconnected system forms a nonlinear time-domain model of the complete combustor, which is valid for a certain azimuthal mode order m . If the modeled system is unstable, solving this model in time will yield limit cycle oscillations of the considered azimuthal mode order. Again, the results in the computed unit cell can be mapped to the remaining combustor.

In this study, we consider a combustor as sketched in Fig. 1 where the individual chambers are connected only via an upstream plenum. In reality in can-annular combustors, the individual chambers are connected at both up- and downstream side or even sit in the same chamber as in annular combustors. There is no essential difficulty to account for such two-side coupling in the present approach. In that case, both state-space models at the in- and outlet have to include the Bloch-element in Eq. (9). Note that the approach is not limited to network-models for the acoustics, because the considered state-space models generally can be interpreted as a representation of an acoustic solver [27]. If the unit cell has a more complex geometry, the acoustics (including the BBC) may be modeled by Helmholtz-equation or linearized Euler-equations and exported as a state-space model [28], which can be coupled to CFD in the same manner as described in this study.

The present approach considers only axial acoustic forcing of the flame, because the reduced order model is coupled to the CFD simulation of the flame zone by means of plane waves traveling in

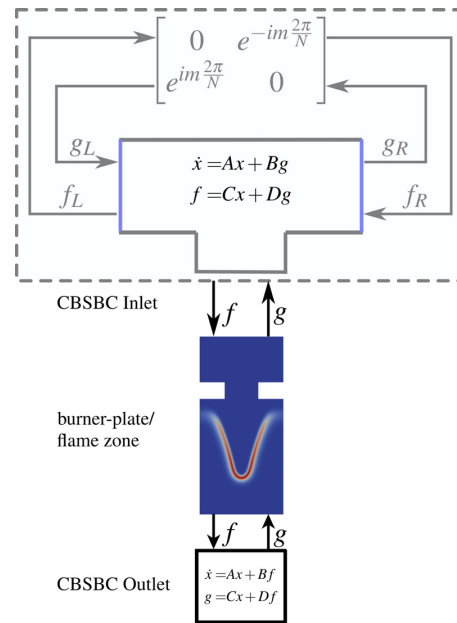


Fig. 3 Hybrid approach of coupling compressible CFD to state-space models including Bloch elements

axial direction. If in annular combustors the flame significantly responds to transverse velocity fluctuations, the present approach will fail to model this interaction. However, recent studies argue that, compared to axial forcing, the flame response on transversal forcing is negligible, e.g., see Refs. [30] and [31].

One conceptual problem inhibits the direct application of the proposed approach: While common CFD codes can only handle real-valued signals, the coupled state-space system including the Bloch-element has complex-valued coefficients and in general returns complex-valued signals. In principle, it is conceivable to implement a CFD code capable of handling complex-valued variables. However, the section CFD With Bloch-Boundary Conditions focuses on utilizing the Bloch-CBSBC with standard CFD codes and presents a strategy to resolve the problem of complex-valued outputs.

CFD With Bloch-Boundary Conditions

We consider a compressible CFD coupled with Bloch-CBSBC as illustrated in Fig. 3. As the CFD simulation can handle only real-valued signals, $f(t)$ and $g(t)$ at the interface to the Bloch-CBSBC have to be purely real-valued, which results in a purely real-valued acoustic pressure and axial velocity at this location. The wave $g(t)$ traveling outward the CFD domain is purely real-valued anyway. Thus, we have to restrict the solutions computed by the Bloch-CBSBC to those that yield purely real-valued outputs $f(t)$ imposed at the interface to the CFD domain. From the perspective of CFD simulation, this is reasonable, because the physical pressure and velocity is governed by the real part of the signals. But what is the azimuthal pressure and velocity distribution for those special solutions, which yield purely real-valued outputs? As outlined in the following, restricting the solutions to purely real-valued outputs will fix the amplitudes of the counter-rotating waves to $c_1 = c_2$.

The azimuthal pressure distribution is governed by Eq. (3). For simplicity, we omit the radial and axial dependence of Ψ and we neglect the modal growth rate. These assumptions abbreviate the following expressions but they are not required for the validity of the results. We omit the Re operator in Eq. (3) and directly

Downloaded from https://asmelibrarycollection.asme.org/gasurbinespower/article-pdf/64/194/191/141_12_121005.pdf by Technische Universitat Muenchen user on 14 November 2019

consider the complex-valued pressure $\tilde{p}(\phi, t)$, which is solved for in the Bloch-CBSBC. Hence, Eq. (3) can be written as

$$\begin{aligned} \tilde{p}(\phi, t) = & \Psi(\phi) [(c_1 + c_2)\cos(\omega t)\cos(m\phi) \\ & + (c_2 - c_1)\sin(\omega t)\sin(m\phi)] \\ & + i[(c_1 - c_2)\sin(\omega t)\cos(m\phi) \\ & + (c_1 + c_2)\cos(\omega t)\sin(m\phi)] \end{aligned} \quad (10)$$

At the interface to the CFD simulation, which is located at the azimuthal position $\phi = \phi_0$, the pressure has to be purely real-valued for all times t . According to Eq. (10), for positive wave amplitudes c_i only

$$c_1 = c_2, \quad \phi_0 = \frac{n\pi}{m}, \quad \text{for } n = 0, 1, 2, \dots \quad (11)$$

satisfies this requirement. Equation (11) shows that restricting the solution to purely real-valued signals at the interface to the CFD simulation results in an azimuthally standing wave inside the reduced order model, as the two waves of one mode order have equal amplitude $c_1 = c_2$. The condition $\phi_0 = (n\pi/m)$ requires the CFD simulation be located in a pressure antinode. The same result is deduced for the axial velocity in Appendix. Note that the imaginary part of pressure is zero only at the azimuthal angles $\phi_0 = (n\pi/m)$, not over the entire circumference.

The azimuthal distribution of pressure and azimuthal velocity inside the reduced order model is that of a standing wave. For axial and “push-pull” modes, this result is trivial, as they always feature a standing mode structure no matter what amplitudes c_1

and c_2 . For those mode types both the obtained limit cycle amplitude and the mode shape computed by the reduced order model will be that observed in the full configuration.

For the other mode types $m = 1, \dots, N/2 - 1$ the result shown in Eq. (11) is at the first glance contradictory: At the end of the second section, it was stated that exactly this mode structure breaks discrete rotational symmetry and inhibits the application of Bloch-wave theory. However, the standing wave structure occurs inside the reduced order model, which is linear and thus independent of amplitude. The CFD simulation, which is the only nonlinear (and therefore amplitude-dependent) element in the entire model, is located in a pressure antinode and hence faces the same amplitudes of axial velocity and pressure as for a spinning wave. By recalling that the applied BBC assure discrete rotational symmetry, i.e., identical nonlinear saturation of all flames, it becomes apparent that for mode orders $m = 1, \dots, N/2 - 1$ the entire formulation actually accounts for spinning waves with either $c_1 = 0$ or $c_2 = 0$. The limit cycle amplitude obtained is that of a spinning mode. During postprocessing, the corresponding spinning wave structure may be reconstructed from the standing wave pressure distribution computed by the reduced order model by doubling one wave component and setting the other one to zero, e.g., $c_{1,sp} = 2 \cdot c_1$ and $c_{2,sp} = 0$.

In order to confirm the theoretical results, the state-space model of the unit cell sketched in Fig. 2 with $N = 4$ and $m = 1$ is considered. The system is solved once in original form and once with purely real-valued signals $\text{Im}\{\tilde{p}(\phi = 0, t)\} = 0$ and $\text{Im}\{\tilde{u}_z(t)\} = 0$ at the interface, as if it were coupled to a CFD simulation at $\phi = 0$. Figure 4 shows the resulting acoustic plenum pressure and azimuthal velocity over the azimuthal angle ϕ for four different phase instants in one oscillation period. For the specific

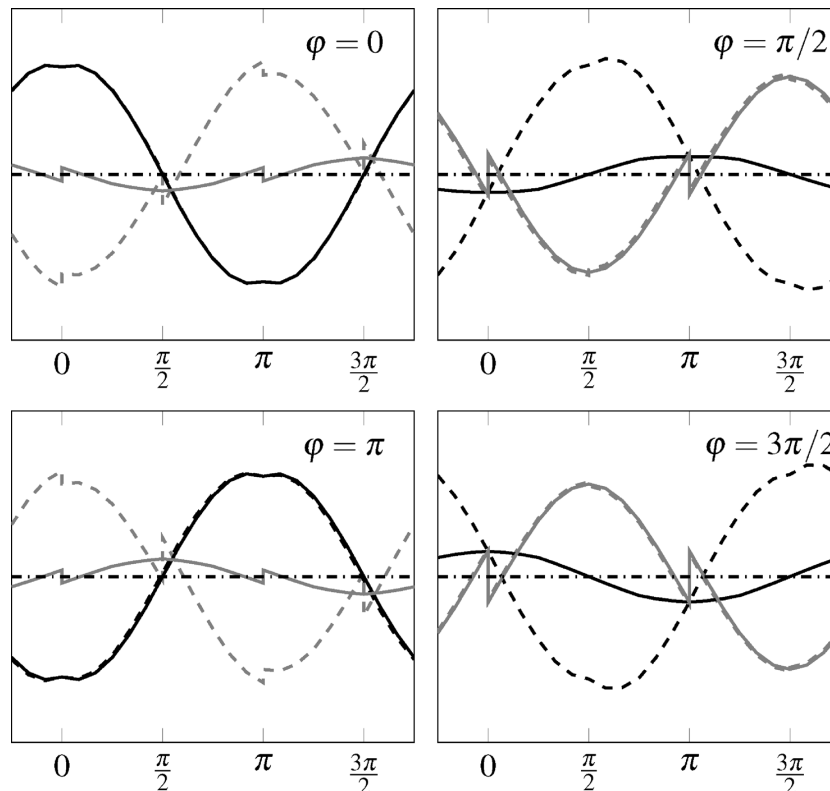


Fig. 4 Normalized acoustic pressure (black) and azimuthal velocity (gray) of original system (dashed line) and suppressed imaginary part (solid line) over azimuthal angle at four different phase instants. Unit cell is centered at $\phi = 0$.

initialization chosen, the original system (dashed lines) features an azimuthally spinning wave, while the system with purely real-valued signals at $\phi = 0$ (solid lines) shows a standing wave. It is important to note that at $\phi = 0$, where the interface to the CFD in the Bloch-CBSBC/CFD framework is located, the pressure is identical for both versions at all times. Also, the axial velocity, which is equal to the jump in azimuthal velocity, is identical for both versions.

To summarize the considerations above: While purely real-valued signals at the interface to the CFD require a standing mode structure inside the Bloch-CBSBC, the complete model always accounts for modes that maintain the discrete rotational symmetry. These may be (standing) axial or “push-pull” modes or degenerate modes that form azimuthally spinning waves. The restriction of the latter mode type to spinning waves is not physical. If degenerate modes in the considered full configuration develop a standing wave in the limit cycle, its amplitude will differ from that obtained by the Bloch-CBSBC/CFD approach [32].

The analysis above reveals important limitations of the proposed Bloch-CBSBC/CFD approach: According to Eq. (10), for nonzero wave amplitudes c_i it is only possible to have vanishing imaginary parts at one distinct azimuthal angle and only for the pressure and the axial velocity. Thus, the coupling interface has to be located at one distinct azimuthal angle and the CFD has to be coupled axially, i.e., via plane waves in axial direction z , as shown in Fig. 3. This, for example, inhibits an extension of the CFD domain over the complete unit cell, as this would require to couple the BBC at two different azimuthal angles and in azimuthal direction. Furthermore, the above-mentioned analysis relies on reflection symmetry of the considered configuration. If this is not fulfilled, the limit cycle obtained by the present approach will deviate from the limit cycle of the full configuration.

Application to a Generic Multican Combustor

The suggested Bloch-CBSBC/CFD approach is applied to the generic laminar multican combustor configuration sketched in Fig. 1. The system features reflection symmetry and a discrete rotational symmetry with $N = 4$. Results are compared to a fully compressible CFD simulation of the complete configuration. Unlike most configurations investigated in literature (for example, see Refs. [6], [7], [17], [24], and [33]), where individual burners are coupled on the downstream side or on both sides, here the burners are coupled on the upstream side only. The reason for this choice is that the present configuration allows us to test the proposed Bloch-CBSBC/CFD approach, while it is relatively simple to model in CFD. This configuration allows us to use standard Dirichlet boundary conditions at the inlet and outlet, while including downstream coupling would require more sophisticated boundary conditions.

In order to limit the computational effort, only the pseudo-2D configuration in Fig. 1 is considered in this study. The geometry is characterized by a plenum-length of $l_p = 0.1$ m, an inlet-length of $l_i = 0.05$ m and an outlet-length of $l_o = 0.1$ m (see Fig. 1). The individual burners and the plenum have a width of $d = 5$ mm. The burner-flame zone of the individual chambers was investigated in numerous previous studies regarding various aspects, e.g., see Refs. [23], [34], and [35]. The burner plates feature a length of 1 mm and an area ratio of 2.5. Their temperature is fixed to 373 K while all other walls are adiabatic. At the left side of the plenum perfectly premixed methane–air fuel with an equivalence ratio of 0.8 and a temperature of 293 K enters with a fixed velocity (acoustic reflection factor $R = 1$). The inlet velocity is chosen such that the mean velocity at the chamber inlets equals $\bar{u} = 0.4$ m/s. At the burner outlets a fixed atmospheric pressure is imposed (reflection factor $R = -1$). All other boundaries are acoustically hard walls, except the periodic faces shown in Fig. 1. Note that these boundary conditions are acoustically lossless (except the diabatic burner-plate), which has some implications on the stability properties of the system.

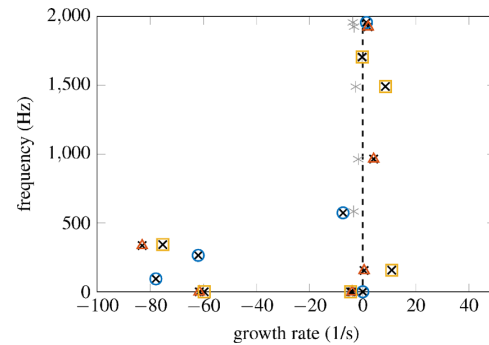


Fig. 5 Eigenfrequencies of the full configuration (cross) compared with eigenfrequencies of the unit cell with BBC with $m = 0$ (circle), $m = 1$ (triangle) and $m = 2$ (square). Gray asterisk markers indicate pure acoustic modes without flame dynamics.

Linear Stability Analysis. In order to access the eigenmodes and linear stability properties, a network model of the considered configuration was built. The flame model required to link the flame responses in the individual chambers to the acoustics was taken from a previous study [36]. Eigenfrequencies of the system are determined from the network model of the complete configuration and from a network model of one unit cell following the Bloch-wave approach. As shown in Fig. 5, the results of those two approaches agree very well, which is in accordance with the result of Mensah et al. [13].

The obtained eigenmodes may be classified as acoustic or intrinsic thermo-acoustic (ITA) modes. They may be distinguished by “switching off” flame dynamics in the network model: While the ITA modes disappear in the absence of flame dynamics, the acoustic modes are only weakly affected (see the corresponding pure acoustic modes indicated with gray asterisk markers). All eigenmodes shown in Fig. 5 with frequencies below 500 Hz are of ITA type and well below the first acoustic eigenfrequency, while all other eigenmodes visible are of acoustic type. It is noteworthy that the ITA modes occur with the same principal structure as the acoustic modes: There are ITA modes with azimuthal mode order $m = 0$ (axial modes), $m = 1$ (degenerate mode pairs), and $m = 2$ (push-pull modes).

The most dominant eigenmode of the system is the first ITA push-pull mode at a frequency of 158 Hz. This is the only mode in the low frequency regime with a positive growth rate. For frequencies above 600 Hz, the gain of the flame transfer function is essentially zero (see Ref. [36]); therefore, the positive growth rate of modes at these frequencies can be considered to be an artifact of the ideal acoustic elements and boundary conditions of the present system. The growth rates of these modes are not reliable, as they are very sensitive to uncertainties in the flame model. Thus, from the results of linear stability analysis one may conclude that the azimuthal mode order $m = 2$ should be linearly unstable, while the other mode orders $m = 0$ and $m = 1$ should be stable.

However, for the limit cycle simulations presented in the section “Results”, other (stable) modes are important as well, as they add resonances to the system. Especially of interest are the first acoustic axial mode at 572 Hz, the first acoustic azimuthal mode at 964 Hz, the first acoustic push-pull mode at 1490 Hz, and the second acoustic axial mode at 1956 Hz. The marginal stable mode at 1704 Hz is a pure plenum mode that will not play a role, because it cannot interact with the burners.

Numerical Setup. For the compressible CFD simulation of the full configuration, the domain sketched in Fig. 1 was discretized using a structured mesh with a total number of 569,000 cells. In the region of burner-plate and flame, the mesh is uniform with a

cell size of $25\ \mu\text{m}$, corresponding to an average of 18 cells within the reaction zone (similar to the mesh used by Jaensch et al. [23] and Duchaine et al. [37]). In the remaining parts of the domain, where mainly acoustic wave propagation has to be modeled, the mesh is significantly coarser. Reactions are modeled by a two-step mechanism including six species [37]. Second-order accurate discretization schemes are used both in space and time. A customized version of rhoReactingFoam from the OpenFOAM[®] package, accounting for different Schmidt numbers of the individual species, is employed as solver. The simulation is started from simultaneous ignition of all flames. It was performed until the build-up of a stable limit cycle oscillation.

For the Bloch-CBSBC/CFD approach, the domain resolved by CFD is restricted to the burner-plate/flame zone, as sketched in Fig. 3. Exploiting the symmetry of this zone, only half of it has to be considered. This leads to a total number of 61,600 cells, which drastically reduces computational cost compared to the CFD of full configuration. Otherwise, exactly the same numerical setup was used for this approach. Both inlet and outlet conditions are imposed by CBSBC. As illustrated in Fig. 3, the inlet state-space model represents the upstream elements of the unit cell and the Bloch-element with the considered mode order m . The outlet state-space model accounts for the duct and the open end downstream of the flame. Without any essential difficulty, the outlet model could also include a Bloch-element, if the considered chambers are connected at the downstream side, too. For the Bloch-CBSBC/CFD approach, the CFD is initialized with a nearly converged steady-state field and the state-space models at the in- and outlet are initialized with $x_0 = 0$. The configurations with $m = 0$ and $m = 1$ that are predicted to be stable in the low frequency regime (see Fig. 5) are excited at the inlet with Gaussian impulse at the beginning of the simulation in order to observe the decay of the stable modes. The unstable configuration $m = 2$ is not excited externally.

Results

Full Configuration. The simultaneous ignition of all flames initially excites the axial modes of the system. The initial excitation of these stable modes decay, while the ITA push-pull mode, which is not excited by the simultaneous ignition, grows until it reaches a limit cycle as observed in Fig. 6, which shows the normalized heat release rate oscillation $Q'(t)$ in one chamber. The time-trace of $Q'(t)$ in the other chambers is phase-shifted by π but otherwise identical. $Q'(t)$ is dominated by the low frequency push-pull mode; therefore, the decay of the axial modes at higher frequencies is not observable there.

Figure 7 shows for the same chamber the magnitude of the Fourier-transform of heat release rate $|\hat{Q}|$ and axial velocity at the burner plate $|\hat{u}_z|$ during the limit cycle. The dominant peak in the spectrum with a magnitude of $|\hat{Q}| = 0.28$ at a frequency of

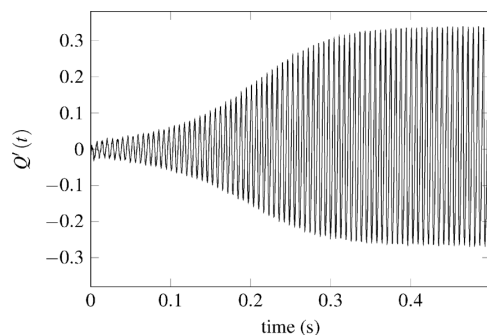


Fig. 6 Normalized heat release rate of full configuration. First transient after the ignition is excluded from the view.

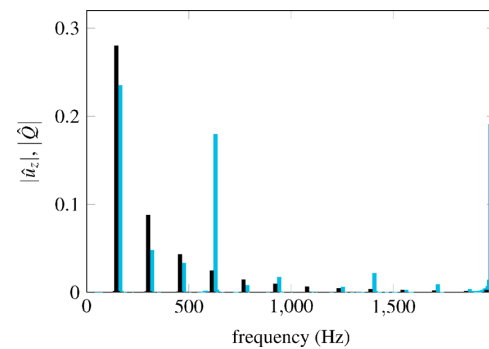


Fig. 7 Spectrum of normalized heat release rate (black) and axial velocity at burner plate (blue) of full system

155 Hz is related to the ITA push-pull mode. This frequency is quite close to the prediction of linear stability analysis.

The further peaks of $|\hat{Q}|$ are the higher harmonics of this mode. Where these higher harmonics are close to other modes of the system, they get amplified [34], which is reflected in the peaks of $|\hat{u}_z|$ at 621 Hz (fourth harmonic) and 1400 Hz (ninth harmonic). Even harmonics feature axial and odd harmonics push-pull structure; thus, they get amplified by modes with corresponding structure in their vicinity, i.e., the fourth harmonic is amplified by the axial mode at 572 Hz, while the third harmonic is not, because it has push-pull structure. None of the harmonics is of first azimuthal mode order ($m = 1$); therefore, the azimuthal mode at 963 Hz does not amplify any harmonics.

In addition to the harmonics, $|\hat{u}_z|$ shows a peak at the second acoustic axial mode at 1965 Hz. As mentioned previously, this is an artifact of the acoustically ideal boundary conditions; thus, this mode is not considered further.

Bloch Characteristic-Based State-Space Boundary Conditions/CFD Approach. The time-trace of $Q'(t)$ obtained by the proposed Bloch-CBSBC/CFD approach with azimuthal mode order $m = 2$ is shown in Fig. 8. Starting from a small deviation of the initial field from steady-state, the push-pull mode grows until it eventually reaches a limit cycle. The finally reached amplitude level is almost identical to the one of the full configuration. However, a stationary limit cycle is reached significantly earlier. One reason is that the initial excitation of the push-pull mode due to deviations of the initial field from steady-state is larger than in the full configuration, where it is essentially zero because of completely symmetric initialization. Another reason might be the presence of axial modes in the full configuration, which have large amplitudes at the beginning and might inhibit the initial growth of the push-pull mode.

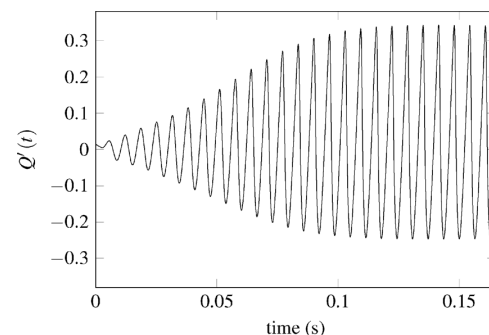


Fig. 8 Normalized heat release rate for $m = 2$

The spectrum of $|\hat{Q}|$ and $|\hat{u}_z|$ while the limit cycle is shown in Fig. 9. The dominant peak of $|\hat{Q}|$ again corresponds to the push-pull mode. The frequency of 155 Hz and magnitude of 0.265 is very close to the result of full configuration. As in the spectrum of the full configuration, the further peaks of $|\hat{Q}|$ are related to the higher harmonics of this mode. In contrast to the full system, there is no axial mode present in the considered unit cell with $m=2$; therefore, the fourth harmonic is not amplified by this resonance. Likewise, the second acoustic axial mode is not present in the limit cycle. However, the amplification of the ninth harmonic at 1400 Hz by the first acoustic push-pull mode is reproduced correctly. To summarize, the Bloch-CBSBC/CFD approach with $m=2$ reproduces correctly the limit cycle frequency and amplitude level of the full system while just one burner-flame zone has to be explicitly resolved by CFD.

As already mentioned, the two remaining systems with $m=0$ and $m=1$ are linearly stable. Therefore, the initial perturbation provided by a Gaussian impulse at the inlet decays. The configuration with $m=0$ corresponding to axial modes features a decaying oscillation at 563 Hz, close to the result of linear stability analysis for the first acoustic axial mode. The configuration modeling the azimuthal mode order $m=1$ shows decaying oscillations at frequencies of 152 Hz and 936 Hz. While the first one corresponds to the first azimuthal ITA mode, the second one is close to the first azimuthal acoustic mode.

Comparison of Mode Structures. This section is devoted to compare the mode shapes in the plenum obtained by the different approaches. The previous subsection Bloch Characteristic-Based State-Space Boundary Conditions/CFD Approach dealt with quantities at the burner plate that are directly observable in the CFD simulation in both approaches. In contrast to that, the plenum is represented by the inlet state-space model in the Bloch-CBSBC/CFD approach. The acoustic pressure and azimuthal velocity in the plenum of one unit-cell is accessed by evaluating the state vector x of the inlet state-space model. The mode shape in the remaining unit cells is obtained by mapping the quantities according to Eq. (1). In the full CFD, the acoustic pressure and azimuthal velocity is recorded at 40 equidistantly spaced locations in the plenum.

The mode shapes are recovered from these pressure and velocity signals by taking the real part of their Fourier transform $\text{Re}\{\hat{p}\}$, $\text{Re}\{\hat{u}_\phi\}$ at the dominant frequencies for each azimuthal mode order m . Figures 10–12 compare the shapes of the dominant modes with azimuthal order $m=2$, $m=0$, and $m=1$, respectively.

For $m=2$, the shapes of the ITA push-pull mode obtained from full CFD and Bloch-CBSBC/CFD approach can be directly compared in the limit cycle. The results plotted in Fig. 10 show excellent agreement between both approaches. As expected, the mode has a second-order azimuthal structure. At the locations of the chamber entries, the azimuthal velocity jumps. The height of the jumps corresponds to the axial velocity in the chambers. Corresponding to the structure of the push-pull mode, the axial velocity changes sign in adjacent chambers.

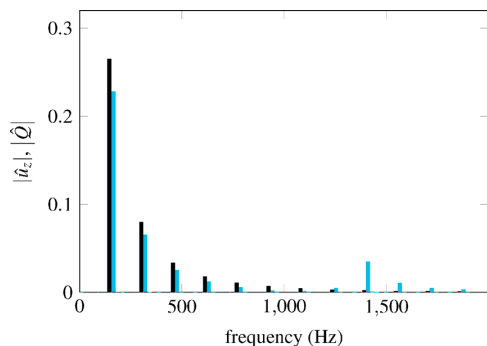


Fig. 9 Spectrum of normalized heat release rate (black) and axial velocity at burner plate (blue) for $m=2$

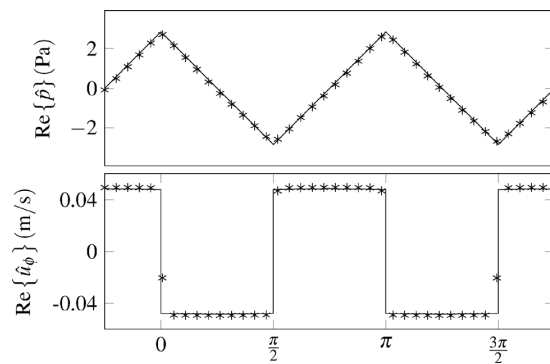


Fig. 10 Plenum mode shape of intrinsic push-pull mode ($m=2$) in limit cycle plotted over azimuthal angle. Result of Bloch-CBSBC approach (solid line) compared with recordings in full CFD (asterisk markers).

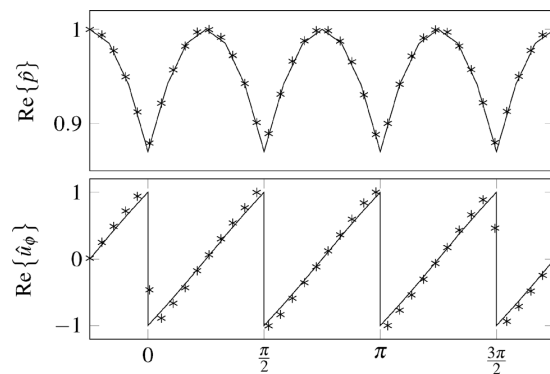


Fig. 11 Plenum mode shape of first acoustic axial mode ($m=0$). Bloch-CBSBC approach (solid line) compared with full CFD (asterisk markers). Both are normalized by their maximum.

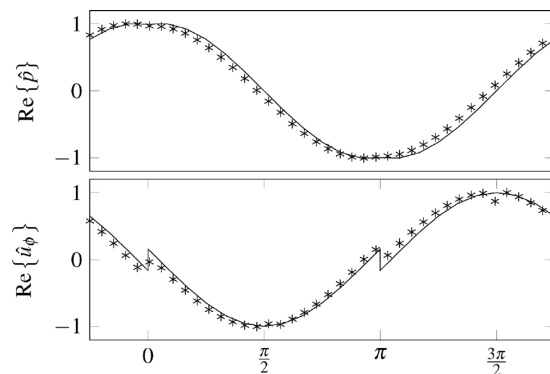


Fig. 12 Plenum mode shape of first acoustic azimuthal mode ($m=1$). Bloch-CBSBC approach (solid line) compared with full CFD (asterisk markers). Both are normalized by their maximum.

As the configurations with $m=0$ and $m=1$ do not develop a limit cycle, a direct comparison of the shapes of dominant modes as for $m=2$ is not possible. Instead, the dominant modes of the Bloch-CBSBC/CFD approaches are compared to their equivalent observed in the full CFD. As the amplitudes of these stable modes depend on their initial excitation, for both approaches they are

normalized by their maximal value in order to allow qualitative comparison.

The dominant mode of the system $m=0$ is the first acoustic axial mode, shown in Fig. 11 together with its equivalent from full CFD. Also, for this mode order, both approaches agree very well. The jumps of azimuthal velocity have equal height and sign, indicating identical axial velocities in each chamber, as expected for an axial mode.

The dominant mode of the system $m=1$ is the first acoustic azimuthal mode, shown in Fig. 12 together with its equivalent from full CFD. Again, both approaches agree very well. As illustrated in the section CFD with Bloch-Boundary Conditions, the mode shape of Bloch-CBSBC/CFD approach will be that of a standing wave, because imaginary parts of the signals at $\phi=0$ are suppressed by coupling to CFD. This is exactly what can be observed in Fig. 12. The azimuthal velocity features jump at $\phi=0$ and $\phi=\pi$ with equal height but opposite sign, while it is continuous at $\phi=\pi/2$ and $\phi=3\pi/2$. This corresponds to opposite axial velocities in two opposite chambers and zero axial velocity in the other chambers. It seems that also in the full CFD, this mode develops as an azimuthally standing wave, as it shows the same structure. However, the absolute amplitude of that mode is very small; therefore, the impact of its standing wave character on the discrete rotational symmetry of the system is considered negligible.

Conclusion

We formulated BBC as a complex-valued time-domain state-space model. This formulation offers great flexibility to couple BBC with other time-domain models. We propose a hybrid approach called Bloch-CBSBC/CFD, where the burner-flame zone of a (can-) annular combustor is resolved by compressible CFD and coupled via characteristic-based state-space boundary conditions to a state-space model representing the remaining acoustic elements of the unit cell together with BBC. This yields a nonlinear time-domain model of the complete (can-)annular combustor, which is valid for the considered azimuthal mode order.

The proposed approach relies on two important assumptions. First, the present formulation requires *axial* coupling of CFD and Bloch-CBSBC. Thus, flame response to *transversal* acoustic forcing is not accounted for and assumed to be negligible. For can-annular systems, this assumption is perfectly justified for the low-frequency instabilities considered in this study. For annular systems, recent studies confirm that compared to axial forcing, transversal forcing plays a secondary role [30,31]. Second, the Bloch-wave theory is only valid for discrete rotational symmetric systems; it assumes that the appearing modes do not break this symmetry. This is fulfilled for axial and “push-pull” modes and for degenerate modes that develop as spinning waves. Degenerate modes, however, may develop as spinning or standing waves. At large amplitudes, the latter induce nonidentical nonlinear saturation for the individual flames and hence break the symmetry. The proposed approach is not able to predict whether a degenerate mode develops as a spinning or standing wave, but instead will always represent the former.

The suggested approach is applied to compute limit cycle oscillations of a generic multican combustor configuration with laminar flames. Results are validated with a fully compressible CFD simulation of the complete combustor. The Bloch-CBSBC/CFD approach accurately predicts the stability properties and finally reached limit cycle amplitude and frequency, while compared to the CFD of the full configuration the computational effort is significantly lower. Also, the mode shapes are reproduced correctly. In contrast, the amplification of some higher harmonics due to the interaction with different azimuthal mode orders is not accounted for.

This study deals with a very generic geometry that is easily represented as a network model and allows at the same time a CFD of the full configuration at moderate cost. If more realistic combustors are considered, the state-space model representing the

remaining acoustic elements of the unit cell and the BBC may be obtained with a more sophisticated acoustic solver.

Acknowledgment

The authors gratefully acknowledge the Research Association for Combustion Engines (Forschungsvereinigung Verbrennungskraftmaschinen e.V. FVV) for the financial support to Matthias Haeringer and the compute and data resources provided by the Leibniz Supercomputing Centre.³

Funding Data

- Research Association for Combustion Engines (Forschungsvereinigung Verbrennungskraftmaschinen e.V. FVV, project number: 6012700).

Nomenclature

- A, B, C, D = matrices of state-space model
- BBC = Bloch boundary condition
- c = speed of sound
- c_i = amplitudes of counter-rotating waves
- f, g = acoustic Riemann invariants
- FDF = flame describing function
- i = imaginary unit
- m = Bloch-wave number
- N = degree of discrete rotational symmetry
- p = acoustic pressure
- Q' = heat release rate fluctuation
- R = acoustic reflection factor
- r, ϕ, z = radial, azimuthal, axial coordinate
- t = time
- u = input state-space model
- u_ϕ, u_z = azimuthal/axial acoustic velocity
- x = state vector
- \mathbf{x} = position vector
- y = output state-space model
- ρ = density
- Ψ = periodic part of Bloch wave

Appendix: Acoustic Velocity of a Bloch Mode

The linearized inviscid one-dimensional momentum equation in cylindrical coordinates

$$\rho \frac{\partial \tilde{u}_\phi}{\partial t} = -\frac{1}{r} \frac{\partial \tilde{p}}{\partial \phi} \quad (\text{A1})$$

links the azimuthal acoustic velocity \tilde{u}_ϕ to the pressure. Inserting Eq. (3) and integrating Eq. (A1) in time yields an expression for the azimuthal acoustic velocity. With the simplifications introduced before Eq. (10), it is written as

$$\tilde{u}_\phi(\phi, t) = i\Psi_u(\phi)e^{im\phi}(c_1e^{i\omega t} - c_2e^{-i\omega t}), \text{ with} \quad (\text{A2})$$

$$\Psi_u(\phi) = \frac{1}{r\rho\omega} \frac{\partial \Psi(\phi)}{\partial \phi} + i\frac{m}{r\rho\omega} \Psi(\phi) \quad (\text{A3})$$

The axial velocity $u_z(t)$ at the interface to the CFD located at $\phi_0=0$ is calculated by applying mass conservation $\tilde{u}_z(t) = \tilde{u}_\phi|_L(t) - \tilde{u}_\phi|_R(t)$ at the T junction shown in Fig. 13, where L and R correspond to azimuthal positions $\phi=0^-$ and $\phi=0^+$, respectively. With the result $c_1=c_2$ from Eq. (11), the axial velocity is written as

³www.lrz.de

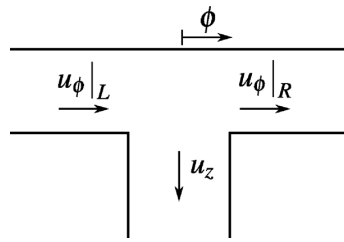


Fig. 13 Acoustic velocities at a T junction

$$\begin{aligned} \tilde{u}_z(t) &= i \left[\Psi_u|_L - \Psi_u|_R \right] [2c_1 i \sin(\omega t)] \\ &= 2c_1 \sin(\omega t) \left[\frac{1}{r\rho\omega} \left(\frac{\partial\Psi}{\partial\phi} \Big|_R - \frac{\partial\Psi}{\partial\phi} \Big|_L \right) + i \frac{m}{r\rho\omega} \left(\Psi \Big|_R - \Psi \Big|_L \right) \right] \end{aligned} \quad (A4)$$

Continuity of pressure across the T junction requires that $\Psi|_L = \Psi|_R$. It follows that the axial acoustic velocity is written as

$$\tilde{u}_z(t) = 2c_1 \sin(\omega t) \left[\frac{1}{r\rho\omega} \left(\frac{\partial\Psi}{\partial\phi} \Big|_R - \frac{\partial\Psi}{\partial\phi} \Big|_L \right) \right] \quad (A5)$$

thus the axial velocity at the interface to CFD ($\phi = 0$) is indeed purely real-valued, provided that $c_1 = c_2$.

References

[1] Poinso, T., 2017, "Prediction and Control of Combustion Instabilities in Real Engines," *Proc. Combust. Inst.*, **36**(1), pp. 1–28.
 [2] Farisco, F., Panek, L., and Kok, J. B., 2017, "Thermo-Acoustic Cross-Talk Between Cans in a Can-Annular Combustor," *Int. J. Spray Combust. Dyn.*, **9**(4), pp. 452–469.
 [3] Staffebach, G., Gicquel, L. Y. M., Boudier, G., and Poinso, T., 2009, "Large Eddy Simulation of Self Excited Azimuthal Modes in Annular Combustors," *Proc. Combust. Inst.*, **32**(2), pp. 2909–2916.
 [4] Wolf, P., Balakrishnan, R., Staffebach, G., Gicquel, L., and Poinso, T., 2012, "Using LES to Study Reacting Flows and Instabilities in Annular Combustion Chambers," *Flow, Turbul. Combust.*, **88**(1–2), pp. 191–206.
 [5] Wolf, P., Staffebach, G., Gicquel, L. Y. M., Müller, J.-D., and Poinso, T., 2012, "Acoustic and Large Eddy Simulation Studies of Azimuthal Modes in Annular Combustion Chambers," *Combust. Flame*, **159**(11), pp. 3398–3413.
 [6] Parmentier, J.-F., Salas, P., Wolf, P., Staffebach, G., Nicoud, F., and Poinso, T., 2012, "A Simple Analytical Model to Study and Control Azimuthal Instabilities in Annular Combustion Chambers," *Combust. Flame*, **159**(7), pp. 2374–2387.
 [7] Bauerheim, M., Parmentier, J.-F., Salas, P., Nicoud, F., and Poinso, T., 2014, "An Analytical Model for Azimuthal Thermoacoustic Modes in an Annular Chamber Fed by an Annular Plenum," *Combust. Flame*, **161**(5), pp. 1374–1389.
 [8] Bauerheim, M., Nicoud, F., and Poinso, T., 2016, "Progress in Analytical Methods to Predict and Control Azimuthal Combustion Instability Modes in Annular Chambers," *Phys. Fluids (1994-Present)*, **28**(2), p. 021303.
 [9] Evesque, S., and Polifke, W., 2002, "Low-Order Acoustic Modelling for Annular Combustors: Validation and Inclusion of Modal Coupling," *ASME Paper No. GT-2002-30064*.
 [10] Polifke, W., Paschereit, C. O., and Döbbling, K., 2001, "Constructive and Destructive Interference of Acoustic and Entropy Waves in a Premixed Combustor With a Choked Exit," *Int. J. Acoust. Vib.*, **6**(3), pp. 135–146.
 [11] Yang, D., and Morgans, A. S., 2018, "Low-Order Network Modeling for Annular Combustors Exhibiting Longitudinal and Circumferential Modes," *ASME Paper No. GT2018-76506*.
 [12] Campa, G., and Camporeale, S. M., 2014, "Prediction of the Thermoacoustic Combustion Instabilities in Practical Annular Combustors," *ASME J. Eng. Gas Turbines Power*, **136**(9), p. 091504.

[13] Mensah, G. A., Campa, G., and Moeck, J. P., 2016, "Efficient Computation of Thermoacoustic Modes in Industrial Annular Combustion Chambers Based on Bloch-Wave Theory," *ASME J. Eng. Gas Turbines Power*, **138**(8), p. 081502.
 [14] Bloch, F., 1929, "Über Die Quantenmechanik Der Elektronen in Kristallgittern," *Z. Für Phys.*, **52**(7–8), pp. 555–600.
 [15] Bradley, C. E., 1994, "Time Harmonic Acoustic Bloch Wave Propagation in Periodic Waveguides—Part I: Theory," *J. Acoust. Soc. Am.*, **96**(3), pp. 1844–1853.
 [16] Dai, X., and Aurégan, Y., 2018, "A Cavity-by-Cavity Description of the Aeroacoustic Instability Over a Liner With a Grazing Flow," *J. Fluid Mech.*, **852**, pp. 126–145.
 [17] Ghirardo, G., Di Giovine, C., Moeck, J. P., and Bothien, M. R., 2019, "Thermoacoustics of Can-Annular Combustors," *ASME J. Eng. Gas Turbines Power*, **141**(1), p. 011007.
 [18] Mensah, G. A., Magri, L., Orchini, A., and Moeck, J. P., 2019, "Effects of Asymmetry on Thermoacoustic Modes in Annular Combustors: A Higher-Order Perturbation Study," *ASME J. Eng. Gas Turbines Power*, **141**(4), p. 041030.
 [19] Mensah, G. A., and Moeck, J. P., 2017, "Limit Cycles of Spinning Thermoacoustic Modes in Annular Combustors: A Bloch-Wave and Adjoint-Perturbation Approach," *ASME Paper No. GT2017-64817*.
 [20] Noiray, N., Durox, D., Schuller, T., and Candel, S., 2008, "A Unified Framework for Nonlinear Combustion Instability Analysis Based on the Flame Describing Function," *J. Fluid Mech.*, **615**, pp. 139–167.
 [21] Tanaka, Y., Tomoyasu, Y., and Tamura, S.-I., 2000, "Band Structure of Acoustic Waves in Phononic Lattices: Two-Dimensional Composites With Large Acoustic Mismatch," *Phys. Rev. B*, **62**(11), pp. 7387–7392.
 [22] Gazalet, J., Dupont, S., Kastelik, J., Rolland, Q., and Djafari-Rouhani, B., 2013, "A Tutorial Survey on Waves Propagating in Periodic Media: Electronic, Photonic and Phononic Crystals. Perception of the Bloch Theorem in Both Real and Fourier Domains," *Wave Motion*, **50**(3), pp. 619–654.
 [23] Jaensch, S., Merk, M., Gopalakrishnan, E., Bomberg, S., Emmert, T., Sujith, R., and Polifke, W., 2017, "Hybrid CFD/Low-Order Modeling of Nonlinear Thermoacoustic Oscillations," *Proc. Combust. Inst.*, **36**(3), pp. 3827–3834.
 [24] Laera, D., Schuller, T., Prieur, K., Durox, D., Camporeale, S. M., and Candel, S., 2017, "Flame Describing Function Analysis of Spinning and Standing Modes in an Annular Combustor and Comparison With Experiments," *Combust. Flame*, **184**, pp. 136–152.
 [25] Emmert, T., Meindl, M., Jaensch, S., and Polifke, W., 2016, "Linear State Space Interconnect Modeling of Acoustic Systems," *Acta Acust. United Acust.*, **102**(5), pp. 824–833.
 [26] Schuermans, B., Bellucci, V., and Paschereit, C. O., 2003, "Thermoacoustic Modeling and Control of Multi-Burner Combustion Systems," *ASME Paper No. GT2003-38688*.
 [27] Jaensch, S., Sovardi, C., and Polifke, W., 2016, "On the Robust, Flexible and Consistent Implementation of Time Domain Impedance Boundary Conditions for Compressible Flow Simulations," *J. Comput. Phys.*, **314**, pp. 145–159.
 [28] Meindl, M., Emmert, T., and Polifke, W., 2016, "Efficient Calculation of Thermoacoustic Modes Utilizing State-Space Models," 23rd International Congress on Sound and Vibration (ICSV23), Athens, Greece, July 10–14.
 [29] Schuermans, B., 2003, "Modeling and Control of Thermoacoustic Instabilities," Ph.D. thesis, École Polytechnique Fédérale de Lausanne, Lausanne, Switzerland.
 [30] Dawson, J. R., and Worth, N. A., 2014, "Flame Dynamics and Unsteady Heat Release Rate of Self-Excited Azimuthal Modes in an Annular Combustor," *Combust. Flame*, **161**(10), pp. 2565–2578.
 [31] O'Connor, J., Acharya, V., and Lieuwen, T., 2015, "Transverse Combustion Instabilities: Acoustic, Fluid Mechanic, and Flame Processes," *Prog. Energy Combust. Sci.*, **49**, pp. 1–39.
 [32] Ghirardo, G., Juniper, M., and Moeck, J., 2016, "Weakly Nonlinear Analysis of Thermoacoustic Instabilities in Annular Combustors," *J. Fluid Mech.*, **805**, pp. 52–87.
 [33] Worth, N. A., and Dawson, J. R., 2013, "Self-Excited Circumferential Instabilities in a Model Annular Gas Turbine Combustor: Global Flame Dynamics," *Proc. Combust. Inst.*, **34**(2), pp. 3127–3134.
 [34] Haeringer, M., Merk, M., and Polifke, W., 2018, "Inclusion of Higher Harmonics in the Flame Describing Function for Predicting Limit Cycles of Self-Excited Combustion Instabilities," *Proc. Combust. Inst.*, **37**(4), pp. 5255–5262.
 [35] Kornilov, V. N., Rook, R., ten Thije Boonkkamp, J. H. M., and de Goey, L. P. H., 2009, "Experimental and Numerical Investigation of the Acoustic Response of Multi-Slit Bunsen Burners," *Combust. Flame*, **156**(10), pp. 1957–1970.
 [36] Silva, C. F., Emmert, T., Jaensch, S., and Polifke, W., 2015, "Numerical Study on Intrinsic Thermoacoustic Instability of a Laminar Premixed Flame," *Combust. Flame*, **162**(9), pp. 3370–3378.
 [37] Duchaine, F., Boudy, F., Durox, D., and Poinso, T., 2011, "Sensitivity Analysis of Transfer Functions of Laminar Flames," *Combust. Flame*, **158**(12), pp. 2384–2394.

Downloaded from https://asmedigitalcollection.asme.org/gasturbinespower/article-pdf/GT2019-141_12_121005.pdf by Technische Universitat Munchen user on 14 November 2019



Original Research Article

*International journal of
spray and
combustion
dynamics*

Hybrid CFD/low-order modeling of thermoacoustic limit cycle oscillations in can-annular configurations

International Journal of Spray and Combustion Dynamics
2022, Vol. 14(1-2) 143–152
© The Author(s) 2022
Article reuse guidelines:
sagepub.com/journals-permissions
DOI: 10.1177/17568277221085953
journals.sagepub.com/home/scdMatthias Haeringer  and Wolfgang Polifke

Abstract

We propose a hybrid strategy for modeling non-linear thermoacoustic phenomena, e.g. limit-cycle (LC) oscillations, in can-annular combustion systems. The suggested model structure comprises a compressible CFD simulation limited to the burner/flame zone of one single can, coupled to a low-order model (LOM) representing the remaining combustor. In order to employ the suggested strategy for modeling non-linear phenomena like LC oscillations, the LOM must capture non-linear flame dynamics in the cans, which are not resolved by CFD. Instead of identifying such non-linear flame models in preliminary simulations, we aim at learning the non-linear dynamics “on-the-fly”, while simulating the self-excited system under consideration. Based on the observation of flame dynamics in the CFD domain, the parameters of the employed non-linear models are estimated during run time. The present study reveals that block-oriented models, which comprise a linear dynamic part followed by a static non-linear function, are well suited for this purpose.

The proposed hybrid model is applied to a laminar can-annular combustor. Results agree well with the monolithic CFD simulation of the entire combustor, while the computational cost is drastically reduced. The employed flame models, whose parameters are identified during the simulation of the self-excited LC oscillation, represent well the relevant non-linear dynamics of the considered flame.

Keywords

Thermoacoustics, can-annular, limit-cycle oscillations, hybrid modeling, online parameter identification

Date received: 6 November 2021; accepted: 4 February 2022

Introduction

Thermoacoustic combustion instabilities pose a major threat for modern low-emission gas turbine combustion systems. Emerging from constructive feedback of acoustics and flame dynamics they cause oscillations of flow variables, which limit the operational range and may even cause structural damage. It is thus of utmost importance to address thermoacoustic instabilities already in the design phase of a new combustion system.¹ Modern land-based gas turbines are often equipped with can-annular combustion systems. Those configurations feature separate flames in nominally identical cans, which are arranged equidistantly around the circumference of the engine. The individual cans are connected acoustically, e.g. via the so-called annular gap in front of the first turbine stage at the downstream side, and via the compressor exit plenum at the upstream side.² This coupling gives rise to azimuthal thermoacoustic modes, which involve all cans simultaneously.^{3–5} It is thus not possible to model

thermoacoustics of can-annular configurations by considering only one can without any further means.^{6–8} While a fully compressible, reactive LES captures all relevant physical phenomena, the computational cost of resolving an entire applied combustion system is very high, even for a relatively small (annular) configuration^{9–11} or a two-can setup.¹² During the design process, which is characterized by repeated modifications of the setup, the computational cost of such an approach is prohibitive.

In order to reduce the computational cost, strategies based on Bloch-wave theory¹³ have been developed recently. By exploiting the discrete rotational symmetry

TU München, DE

Corresponding author:

Matthias Haeringer, TU München Fakultät für Maschinenwesen, Professur für Thermofluidynamik, Boltzmannstr. 15, D-85747 Garching.
Email: haeringer@tfd.mw.tum.de

Creative Commons Non Commercial CC BY-NC: This article is distributed under the terms of the Creative Commons Attribution-NonCommercial 4.0 License (<https://creativecommons.org/licenses/by-nc/4.0/>) which permits non-commercial use, reproduction and distribution of the work without further permission provided the original work is attributed as specified on the SAGE and Open Access page (<https://us.sagepub.com/en-us/nam/open-access-at-sage>).

of typical (can-)annular configurations, the computational domain can be limited to only one can or one sector. Mensah et al.¹⁴ utilized Bloch-wave theory to efficiently calculate the eigenfrequencies of an annular test-rig. Combined with a flame describing function (FDF) this approach was also used to predict the limit-cycle (LC) amplitude with frequency domain methods.¹⁵ Haeringer and Polifke⁷ proposed a strategy to utilize Bloch-wave theory in time domain. There, a CFD simulation of one burner/flame zone (or one can) is coupled to a low-order model (LOM), which includes Bloch boundary conditions and thus accounts for the discrete rotational symmetry of the system. This allows the direct and efficient simulation of LC oscillations in (can-)annular configurations, circumventing the costly computation of an FDF and not relying on the assumptions associated with the FDF.

These approaches generally assume that discrete rotational symmetry holds, even for high-amplitude LC oscillations. However, in particular for azimuthally standing waves emerging from degenerate modes, the individual flames are exposed to different amplitude levels causing different levels of non-linear saturation, which breaks the symmetry among the respective cans or sectors.¹⁶ Additionally, only modes of one single azimuthal order can be represented in a single simulation that relies on Bloch-wave theory. On the one hand, this means that multiple simulations are required to assess the stability and to model the LC of all mode orders. On the other hand, possible non-linear interactions of modes of different azimuthal order can not be captured.

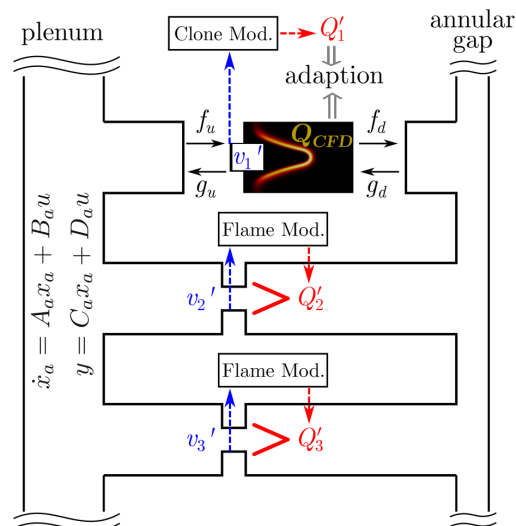


Figure 1. Schematic of the proposed hybrid approach. Compressible CFD coupled to linear acoustic model via CBSBC. Flame models are connected with acoustic model and adapted according to the observation in CFD and “clone model”.

In the present study, we propose a hybrid approach similar to that of Haeringer and Polifke⁷, but now the CFD simulation of one can is coupled to a LOM, which explicitly models the remaining combustor. This removes the above mentioned restrictions of the Bloch-wave approach by dropping its central assumption that the acoustic field in the combustor features a certain symmetry.

In order to simulate LC oscillations, the proposed approach has to account for the non-linear dynamics of the flames. While this is inherently the case for the flame resolved by CFD, the LOM must also include non-linear flame models representing the dynamics of all remaining flames. However, non-linear flame models, which are valid for a wide range of frequencies and amplitudes - the relevant frequencies and amplitudes are typically not known in advance - are generally very costly to determine¹⁷⁻¹⁹ or are only of qualitative nature.²⁰ Instead, here we propose to identify the non-linear flame models “on-the-fly”, based on a linear model of flame dynamics plus observations of non-linear flame dynamics in CFD during the simulation of the self-excited configuration. The resulting flame model will in general only be valid for the frequencies observed in the respective simulation. This, however, allows the use of relatively simple model structures and limits the amount of data needed for identification.

Recently, Yu et al.²¹⁻²³ investigated a related approach. Yu et al. employed data assimilation techniques for online identification of state and parameters of a level-set based flame model, in order to match the dynamics of the identical flame resolved in CFD. Although there are similarities to the present approach, note that Yu et al. aim to match the dynamics of the *same* flame resolved in CFD, while our goal is to learn the dynamics of a different flame, which has only the same characteristics as the resolved one but is in general subjected to a different input. Instead of achieving an exact one-to-one match with the CFD observation, which requires parameter *and* state identification, the goal of the present approach is to constantly improve the model by merely online parameter identification.

The structure of the paper is as follows: In Sec. “*Hybrid modeling approach*”, the proposed hybrid strategy is introduced in detail. Afterwards, Sec. “*Flame model structure...*” deals with the non-linear flame model structure chosen in this study and the online identification of its parameters. In Sec. “*Application to generic can-annular combustor*” the results of the proposed strategy applied to a “toy model” are presented and compared to results from monolithic CFD of the entire combustor. A conclusion and a short outlook are presented in Sec. “*Conclusion*”.

Hybrid modeling approach

The general strategy is depicted in Figure 1. A fully compressible, reactive CFD simulation of the burner/flame zone in one can is coupled to a LOM of the remaining

combustor, which represents acoustics and flame dynamics of all components not resolved by the CFD. To abbreviate the notation in the following, the parts resolved in the CFD domain are denoted “resolved”, while all remaining parts of the combustor are denoted “modeled”.

The present strategy can be seen as an extension of the hybrid modeling approach proposed by Jaensch et al.²⁴. By employing characteristic-based state-space boundary conditions (CBSBC),²⁵ Jaensch et al. coupled a compressible CFD simulation of a laminar slit flame¹ to an acoustic LOM of the remaining single-burner combustor. The resulting hybrid model could well represent non-linear thermoacoustic oscillations of the considered single burner combustor. In the present study, we again employ CBSBC to couple compressible CFD and LOM. What distinguishes the present work from the study of Jaensch et al., is that in the present work the hybrid model represents a multi-burner configuration and thus the LOM comprises not only linear acoustic elements but also non-linear flame models.

The CBSBCs couple a compressible CFD simulation with general linear acoustic models via the plane acoustic waves f and g crossing the interface between CFD and LOM as illustrated in Figure 1. The acoustic system is represented as state-space model of the form

$$\begin{aligned} \dot{x}_a &= A_a x_a + B_a u \\ y &= C_a x_a + D_a u. \end{aligned} \quad (1)$$

The matrix A_a governs the internal dynamics of the acoustic system. B_a represent the effect of inputs u on the internal system state x_a . C_a and D_a map the state and inputs onto the outputs y . Such an acoustic state-space model may be obtained either from measured impedances, acoustic network models, or may be derived from a discretization of linearized governing equations.²⁵ In the present context, the coupled LOM is non-linear, because it contains non-linear flame models and can thus not be represented as linear state-space model in the form of Eq. (1). To resolve this issue, the non-linear flame models are separated from the linear acoustic model as indicated in Figure 1. The in- and outputs of the separately solved flame models are connected to the acoustic state-space model by appending the in- and outputs of the latter according to

$$u = [g_u, f_d, Q'_2, Q'_3, \dots, Q'_N] \quad (2)$$

$$y = [f_u, g_d, v'_2, v'_3, \dots, v'_N]. \quad (3)$$

The first two entries in Eq. (2) and (3) are the characteristic acoustic waves at the in- and outlet boundary of the CFD domain, which couple CFD and acoustic LOM as shown in Figure 1. The remaining entries are the in- and outputs of the non-linear flame models. The input of flame model i is the velocity fluctuation v'_i at a reference position upstream of flame i . The output is the fluctuation of the integrated heat release rate Q'_i of flame i . Both, v' and Q' denote fluctuations

w.r.t. their mean and are normalized by their respective mean. By appending the in- and outputs as shown in Eq. (2) and (3), the linear part of the LOM - the acoustic model - can be coupled to CFD via CBSBC as usual. The additional advantage of this separation is that the in- and outputs and the parameters of the flame models are easily accessible and not hidden in a monolithic LOM.

The non-linear flame models are adapted “on-the-fly”, based on the observation of the resolved flame dynamics. Generally, we assume nominally identical flames within each can. However, this does neither imply identical current states of all flame models, nor identical in-/output behavior of all flames. This is a result of the nature of azimuthal modes present in can-annular combustors. They generally result in non-identical acoustic states in the individual cans. If degenerate modes form azimuthally standing waves, they even cause different amplitude levels in the individual cans, which affects the amplitude dependent in-/output behavior of the non-linear flame models.¹⁶ Thus, the parameter adaption is based on a “clone model” (see Figure 1), which is fed with the same input as the resolved flame, thus ensuring that the model is exposed to the same amplitude level and the same acoustic state as the resolved flame. Based on the output of the “clone model” and the resolved flame, the model parameters are estimated and applied to all other flame models.

The identified non-linear dynamics will in general only be valid in the vicinity of the simulated trajectory of the self-excited system and the proposed approach will not yield a general non-linear flame model, which is valid for all frequencies, amplitudes, and operating conditions. This, however, is not the goal of the proposed strategy, as we only want to find the stable LC of the considered system.

Due to the coupling of CFD and LOM via CBSBC, the considered modeling strategy is limited to plane acoustic waves at the interface between CFD and LOM. While this is not a severe restriction for typical can-annular combustors,⁸ this limitation will inhibit the application of the present strategy to annular combustors. Note that this limitation is only caused by the coupling framework employed here and is not a general limitation of the proposed hybrid strategy. Using a different coupling framework based on heat release rate Q' and reference velocity v' , also proposed in Jaensch et al.²⁴, may resolve this limitation and make the approach applicable to annular combustors as well. This, however, is not part of the present study, where we demonstrate the approach based on a generic can-annular system.

Flame model structure and online parameter adaption

The flame models employed for the present purpose must meet the following requirements. They must

- feature non-linear dynamics, in particular saturation of gain (and possibly change in phase) for high input amplitudes. Other non-linear effects like the generation of higher harmonics and cross-frequency coupling are desired as well.
- accurately represent linear dynamics (in the limit of zero input amplitude) for a wide frequency range. This ensures the correct stability properties of the considered system.
- depend only on a few free parameters because the amount of training data available during identification “on-the-fly” is limited.
- allow training of the free model parameters without heavy computations, as this would slow down the entire simulation.

Among all available model structures, block-oriented non-linear models meet the above requirements best (see e.g. Schoukens and Tiels²⁶ for an overview of block-oriented models and their identification). Commonly, block-oriented non-linear models are applied for systems with separable linear and non-linear dynamics, e.g. to account for non-linear sensor or actuator characteristics.²⁷ This is clearly not the case here. The separation has no physical motivation, but is convenient for the present purpose and captures the essential features of non-linear flame dynamics, as shown in Sec. “Application to...”.

We choose a so-called “Wiener-model” structure,²⁸ where a linear dynamic model part is followed by a static non-linear function as illustrated in Fig 2. Here, the dynamic linear model is denoted as flame transfer function (FTF) and represents linear flame dynamics for a large frequency range. It thus governs the linear stability properties of the considered configuration. The FTF is measured or identified in advance using established system identification techniques²⁹ and it is not modified during the simulation. Instead, only the parameters s of the algebraic non-linear function, which acts on the output of the FTF, are identified based on observations of resolved flame dynamics.

We consider perfectly premixed velocity sensitive flames. In frequency domain (\hat{q} denoting the Laplace transform of q), the FTF $F(\omega)$ is defined as²

$$\hat{Q} = F(\omega)\hat{v}. \quad (4)$$

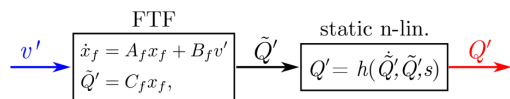


Figure 2. Wiener-type flame model comprising a linear time-invariant dynamic part (FTF) and a static non-linear function correcting the linear model output \tilde{Q} .

It relates - in the limit of zero amplitude, but for a wide range of frequencies ω - the normalized heat release rate response \tilde{Q}' to the normalized upstream reference velocity fluctuation v' .

The transfer function $F(\omega)$ can be equivalently represented in time-domain as linear state-space model

$$\begin{aligned} \dot{x}_f &= A_f x_f + B_f v' \\ \tilde{Q}' &= C_f x_f, \end{aligned} \quad (5)$$

where the matrices A_f, B_f, C_f have the same meaning as in the state-space representation Eq. (1) of the acoustic system. x_f again represents the internal state of the system - here of the flame - but the individual states do not necessarily have immediate physical meaning. Note that for a realistic flame transfer function, the matrix D_f is zero, otherwise the corresponding impulse response at time $t = 0$ would be infinite.

For the static non-linear part of the model, a variety of different functional forms are conceivable, but they have to meet the requirements stated above. According to our observations the algebraic function $h(\tilde{Q}', \dot{\tilde{Q}}', s)$

$$Q' = h(\tilde{Q}', \dot{\tilde{Q}}', s) = \frac{2}{s_1 \pi} \arctan\left(\frac{s_1 \pi}{2} \tilde{Q}'\right) + s_2 \tilde{Q}' \dot{\tilde{Q}}' \quad (6)$$

parametrized by $s = [s_1, s_2]$ works well. It converts the linear model output \tilde{Q}' and its time derivative $\dot{\tilde{Q}}'$ into the non-linear flame model output Q' . The time derivative of the linear model $\dot{\tilde{Q}}'$ is directly accessible from the state-space model Eq. (5) according to

$$\dot{\tilde{Q}}' = C_f \dot{x}_f = C_f (A_f x_f + B_f v') \quad (7)$$

The static non-linear function in Eq. (6) is an ad-hoc model with two terms that serve different purposes: The first term causes saturation for high input amplitudes and generates odd harmonics. The second term was originally proposed by Purwar et al.³⁰ in the context of non-linear flame response to transverse excitation. It generates second harmonics without causing an offset of the mean and creates a sawtooth-shaped signal, like it is often observed for high-

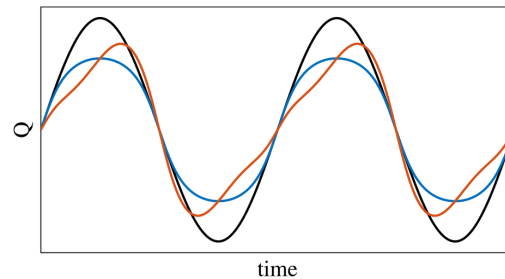


Figure 3. Output of static non-linear function (red) with exemplary $s = [1, -0.4]$ and sinusoidal input signal (black). Blue curve shows saturation term only.

amplitude thermoacoustic oscillations, e.g. see Indlekofer et al.³¹. Figure 3 illustrates the effect of the two terms on a sinusoidal input signal for exemplary values of the tuning parameters s_1 and s_2 .

The drawback of the considered static non-linear function is, that it can not modify the phase of the linear model output. This could be achieved by choosing a different model structure. However, as shown in Sec. “*Analysis of adapted flame model*”, this does not seem to be necessary for the considered configuration, because there the phase of the flame response changes only slightly with amplitude.³² Linearizing the static non-linear function yields the relation

$$\lim_{\tilde{Q}' \rightarrow 0} h(\tilde{Q}', \dot{\tilde{Q}}', s) = \tilde{Q}'. \quad (8)$$

In the zero-amplitude limit, the output of the FTF is thus not affected by the static non-linear function. It therefore has no influence on the linear stability properties of the considered configuration. The limit of the saturation term³ at infinite amplitude is

$$\lim_{\tilde{Q}' \rightarrow \pm\infty} \frac{2}{s_1\pi} \arctan\left(\frac{s_1\pi}{2}\tilde{Q}'\right) = \pm \frac{1}{s_1}. \quad (9)$$

Thus, the maximum and minimum heat release rate response at the fundamental frequency is strictly bounded by s_1^{-1} . This limitation is physically meaningful because the minimal normalized heat release rate response of a real flame is also strictly bounded by flame extinction ($\min Q' = -1$). If the considered configuration is linearly unstable, the limit in Eq. (9) ensures that a LC oscillation develops, because it essentially reduces the flame response gain to zero as the amplitude goes to infinity.

The output of the static non-linear function is controlled by the tuning parameters s_1 and s_2 . These parameters are identified “on-the-fly” by solving the non-linear least squares problem

$$s = \arg \min \left(h(\tilde{Q}'|_{0 \rightarrow t}, \dot{\tilde{Q}}'|_{0 \rightarrow t}, s) - Q'_{CFD}|_{0 \rightarrow t} \right)^2. \quad (10)$$

Here, $\tilde{Q}'|_{0 \rightarrow t}$, $\dot{\tilde{Q}}'|_{0 \rightarrow t}$ and $Q'_{CFD}|_{0 \rightarrow t}$ denote the time-series of linear “clone-model” output, its time derivative and of the normalized fluctuation of the volume integrated heat release rate observed from CFD recorded from initial time zero to current time t (c.f. Figure 1). The least-squares problem in Eq. (10) is solved repeatedly after a prescribed update period τ using the Levenberg-Marquardt algorithm of the Eigen[®] library.³³ The solution of Eq (10) is considered converged if either the norm of the residual or its gradient or the relative change of parameter s is below a prescribed threshold (here the square root of machine precision). This constantly improves the estimation of the model parameters s_1 and s_2 as the amplitude in the CFD simulation grows. After identifying the parameters for the “clone-model”, s_1 and s_2 are applied to all flame models.

Equation (10) demonstrates the advantage of a block-oriented non-linear model structure for the present purpose. The optimization routine relies on stored time-series from CFD and linear model output, which are independent of the parameters s_1 and s_2 . Thus, within the optimization loop, only the algebraic function Eq. (6) has to be evaluated and no dynamical model has to be solved, which makes the parameter identification step very efficient.

Application to a generic can-annular combustor

Setup

The proposed hybrid approach is applied to a quasi-2D laminar premixed can-annular combustor with 4 cans and is validated with the results from a compressible CFD simulation of the entire configuration, hereafter referred to as “monolithic” CFD simulation. The considered combustor can be seen as a “toy model”, for which a CFD simulation of the entire combustor is feasible.

We consider the exact same configuration as in Haeringer and Polifke⁷. This allows a direct comparison of the results from the hybrid time-domain Bloch-wave approach of Haeringer and Polifke with the present results. The configuration investigated in Haeringer and Polifke and in the present study is similar to that illustrated in Figure 1. The 4 cans of the combustor contain laminar slit flames and are coupled by an upstream plenum. Instead of the annular gap in the generic setup shown in Figure 1, the cans are terminated with acoustically open ends at the downstream side.

For the monolithic CFD simulation, the entire combustor is discretized with 569000 cells. For the hybrid approach, the CFD domain is limited to the immediate vicinity of the burner plate and the flame in one can and is discretized with 61600 cells, which leads to a significant reduction in computational cost compared to the monolithic CFD. For both, hybrid model and monolithic CFD, a customized version of the compressible solver rhoReactingFoam from the OpenFOAM[®] package is employed. The reactions are modeled with a two-step scheme of methane-air combustion involving 6 species.³⁴ The flame front is resolved by 18 grid points. Second-order accurate discretization schemes in space and time are used. The acoustic LOM of the hybrid approach is built with the thermoacoustic network modeling tool taX⁴.³⁵ For further details about the configuration and the numerical setup we refer to Haeringer and Polifke⁷.

The FTF needed for the flame model structure illustrated in Figure 2 is taken from a previous study,³⁶ which investigated the same burner/flame zone. The parameters of the static non-linear function are initialized with $s_1 = 1$ and $s_2 = 0$. Different initializations for s_1 were tested and yielded the same result in terms of model parameters s

and LC frequency and amplitude. The update period τ , after which Eq. (10) is evaluated to renew the values of s is set to approximately 1.5 oscillation periods of the most unstable eigenmode. Using lower or higher values for τ changes the results during exponential growth, but does not significantly alter the final LC oscillations. Generally, τ should be roughly in the order of the oscillation period of the most dominant frequency in order to achieve a reasonable fit quality and to allow fast tracking of changes in flame dynamics.

Comparison with monolithic CFD

Figure 4 shows the time traces of heat release rate in all individual cans obtained from monolithic CFD. The simulation starts with the simultaneous ignition of all flames. The initial transient resulting from ignition is excluded from this view. Figure 5 shows the same results obtained with the proposed hybrid approach. Here the simulation starts from a nearly converged mean-field and zero acoustic x_a and flame states x_f . All shown quantities, in particular v' and Q' , denote fluctuations w.r.t. their mean and are normalized by their respective mean. Time \mathcal{T} is normalized by the oscillation period of the dominant eigenmode. Frequency \mathcal{F} is normalized by the first “pure” plenum eigenfrequency defined as $F = c/U$, where c denotes the speed of sound in the fresh gas and U is the circumference of the plenum.

For both approaches, the configuration is linearly unstable, which leads to exponential growth of oscillation amplitudes and the formation of a stable LC oscillation. The heat release time-series are characteristic of a so-called “push-pull” mode, which is in the present 4-can configuration a mode of azimuthal order $m = 2$. This is consistent with the results from linear stability analysis of the configuration (see Haeringer and Polifke⁷ for details) shown in the bottom plot of Figure 6. It reveals a dominant low-

frequency mode of azimuthal order $m = 2$. The heat release rate oscillations in adjacent cans are phase-shifted by π , but otherwise identical. Consequently, as observed in the zoomed view in Figure 4, the time traces of the opposing cans Q'_1 and Q'_3 as well as Q'_2 and Q'_4 are exactly aligned with each other.

Considering Figure 5, the hybrid approach reproduces the oscillation pattern well. The time traces of the two opposing modeled flames Q'_2 and Q'_4 are identical and phase-shifted by π with respect to the adjacent modeled flame Q'_3 and the resolved flame Q'_{CFD} . The “clone model” heat release rate Q'_1 also shown in Figure 5 reproduces Q'_{CFD} reasonably well, given the relatively simple flame model structure employed. The shape of the heat release rate signals matches reasonably well with monolithic CFD results, indicating that generation and amplification of higher harmonics are correctly captured.

The hybrid model clearly overestimates the LC amplitude level. Possible reasons are discussed in Sec. “Analysis of the adapted flame model”. Additionally, it features a higher growth rate σ at small amplitudes. This is related to the “on-the-fly” identification strategy, which constantly improves the flame models. Consequently, during the initial phase of the simulation, when only a small amount of data is available for the parameter estimation step in Eq. (10), the models are not yet quantitatively accurate.

The spectral analysis of the LC oscillations in the monolithic CFD and the hybrid model shown in Figure 6 is in line with the outcome of the previous analysis. The top plot in Figure 6 compares the LC spectrum of heat release rate Q'_{CFD} from the hybrid approach (red) with Q'_1 from monolithic CFD (blue). The middle plot compares the LC spectra of v'_1 . For the monolithic CFD, the spectra of Q' and v' in the other cans are identical to the one shown. For the hybrid model, they are very similar.

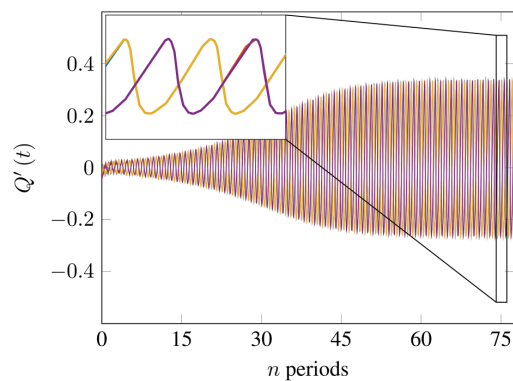


Figure 4. Heat release rate fluctuations in all cans obtained with monolithic CFD. Q'_1 in blue, Q'_2 in red, Q'_3 in orange, Q'_4 in magenta.

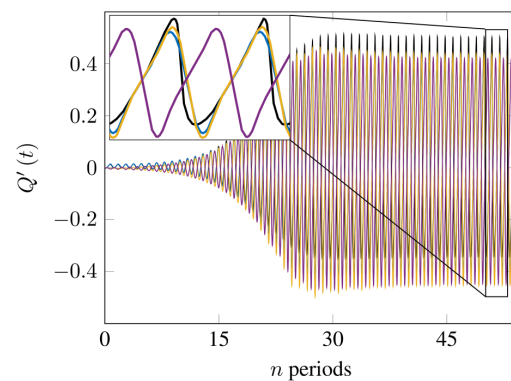


Figure 5. Heat release rate fluctuations in all cans obtained with hybrid model (c.f. Figure 1). Q'_{CFD} in black, Q'_1 (“clone model”) in blue, Q'_2 in red, Q'_3 in orange, Q'_4 in magenta.

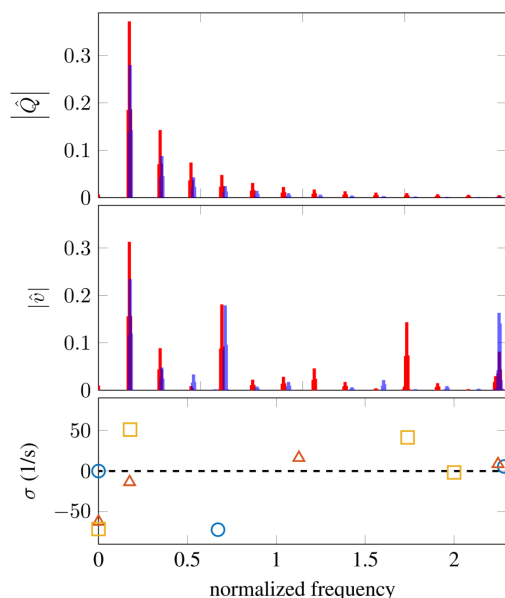


Figure 6. LC spectrum of heat release rate (top) and reference velocity (middle). Hybrid approach in red, monolithic CFD in blue. Result of linear stability analysis (bottom) shows eigenmodes of azimuthal order $m = 0$ (blue circles), $m = 1$ (red triangles) and $m = 2$ (orange squares).

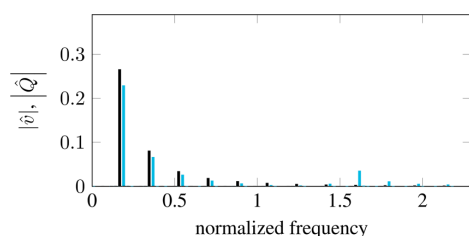


Figure 7. LC spectrum of heat release rate (black) and reference velocity (blue) obtained from Bloch-wave approach with $m = 2$. Reproduced from⁷.

The bottom plot of Figure 6 shows the eigenfrequencies of the configuration obtained from linear stability analysis. The dominant unstable mode is a $m = 2$ low-frequency “push-pull” mode of intrinsic thermo-acoustic (ITA) origin (see Haeringer and Polifke⁷). The positive σ of the modes at $\mathcal{F} > 1$ is an artifact of the acoustically ideal boundary conditions and, due to the small mean flow velocity, only minimal acoustic losses at the burner plate. As a result, the growth rates of these modes are very sensitive to uncertainties in the FTF, whereas the gain of the FTF is essentially zero for $\mathcal{F} > 0.5$.³⁶ As observed in Figure 6, the

low-frequency “push-pull” mode dominates the LC spectrum in both the monolithic CFD and the hybrid model. While the LC frequency obtained from both approaches matches very well, the hybrid model overestimates the LC amplitude of Q' and v' of this mode by approximately 30%.

The further peaks observed in the top and middle plot of Figure 6 are higher harmonics of the unstable “push-pull” mode. Due to resonance, the harmonics are amplified in the vicinity of other eigenfrequencies.³² The LC obtained from monolithic CFD shows distinct resonances only with the axial $m = 1$ modes at $\mathcal{F} \approx 0.7$ and $\mathcal{F} \approx 2.2$. Due to the azimuthal symmetry of the higher harmonics of the nearly perfectly symmetric “push-pull” mode, other modes can not be excited. The hybrid model correctly captures the resonances with the axial modes, but also shows resonance with the $m = 1$ mode at $\mathcal{F} \approx 1$ (weak) and the $m = 2$ mode at $\mathcal{F} \approx 1.7$. These resonances are possible due to the asymmetry of the hybrid model (three identical modeled cans connected to one resolved can) and the resulting asymmetry of the “push-pull” mode. Due to the low-pass behavior of the flame response, no resonances are observed in the heat release spectrum during LC oscillation.

Comparison with Bloch-wave approach

Here we compare the present results with those of the hybrid time-domain Bloch-wave approach of Haeringer and Polifke⁷. As the CFD domain is identical in both approaches, the computational cost of one simulation is comparable. Note, however, that if the dominant azimuthal mode order is not known in advance, multiple simulations are necessary to investigate all mode orders m with the Bloch-wave approach. For the present 4-can setup, 3 simulations are necessary.

Figure 7 shows the LC amplitude spectrum of heat release rate and reference velocity obtained with the Bloch-wave approach at $m = 2$. The fundamental of \hat{Q} and \hat{v} are predicted accurately. However, in contrast to the present approach, resonances of the higher harmonics in the vicinity of axial eigenmodes $m = 0$ are not captured, because these are not present in the simulation for $m = 2$. Additionally, the Bloch-wave approach relies on discrete rotational symmetry. It would thus fail to capture the effects of symmetry breaking due to non-identical non-linear saturation of the individual flames. This, however, is only relevant if the LC is dominated by a degenerate mode ($m = 1$ here).¹⁶

To summarize, compared to the Bloch-wave approach, the present approach is less accurate in predicting the LC amplitude of an isolated azimuthal mode, which does not break the symmetry of the system. On the other hand, it is more general and computationally more efficient.

Analysis of adapted flame model

The parameters identified “on-the-fly” converge smoothly to final values of $s_1 = 1.325$ and $s_2 = -1.368 \cdot 10^{-3}$. In order to assess the quality of the flame model with these parameter values, we compare it with the extended flame describing function (xFDF) of the same flame.³² The xFDF comprises multiple describing functions, which relate the fundamental and the higher harmonics of the flame response \hat{Q} to the fundamental of the input \hat{v} .

As stated in Sec. “Hybrid modeling approach”, the identified flame model will in general only be valid in the vicinity of the system trajectory observed in the simulation. Thus, comparing the model frequency response with the xFDF for a large frequency range is pointless. Instead we compare in Figure 8 the in-/output relation of adapted model and xFDF only for the observed dominant frequency $\mathcal{F} = 0.178$. The first order describing function xFDF₁ (blue dashed), which relates the fundamental of \hat{v} and \hat{Q} is in good agreement with the in-/output relation of the saturation term in Eq. (6) (blue solid). Also, the second order describing function xFDF₂ (red dashed), which relates the fundamental of \hat{v} and the second harmonic of \hat{Q} , is well matched by the second term of Eq. (6) (red solid), at least for small amplitudes. For higher amplitudes, which are not reached in the simulated LC, the agreement decreases due to the influence of higher order non-linearities not present in Eq. (6). As a reference, the linear in-/output relation of the FTF is shown as black dashed line.

Overall, the results shown in Figure 8 confirm that the “on-the-fly” parameter identification works as intended. However, the question remains why the LC amplitude is overestimated by the hybrid model, especially because the non-linear saturation of the adapted flame model is even slightly bigger than that of the xFDF.

We identify two possible reasons for the over-estimation of the LC amplitude. First, the employed model structure can not adapt to changes in the flame response phase. However, as the unstable mode is of ITA origin, any

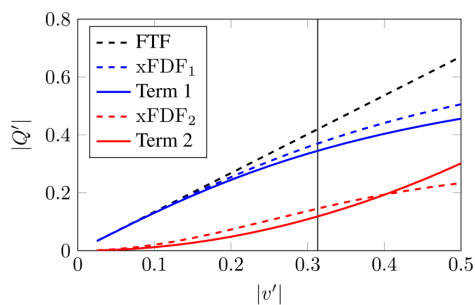


Figure 8. In-/output relation of adapted flame model, first two xFDF describing functions and FTF at LC frequency $\mathcal{F} = 0.178$. The vertical black line indicates the LC amplitude.

changes in phase would directly reflect to the oscillation frequency. But as the LC frequency is almost identical to the linear eigenfrequency, changes of phase with amplitude seem to be negligible. Second, the employed LOM only includes linear acoustic losses at the burner plate, which are very small for the considered configuration. During the LC, non-linear acoustic losses at the burner plate may, however, play a significant role, especially in relation to the negligible linear losses. To address this problem in future work, one might include a model for these non-linear losses and identify its parameters “on-the-fly”, just like it is done for the flame model.

Conclusion

We propose a hybrid approach for the efficient simulation of limit-cycle (LC) oscillations in can-annular combustors. The suggested hybrid model couples a CFD simulation of the burner/flame zone of one can with a low-order model (LOM) of the remaining combustor.

In order to account for non-linear thermoacoustic phenomena, for example the formation of LC oscillations, the LOM must include non-linear flame models. The tedious and costly identification of such models in preceding simulations is avoided by identifying them “on-the-fly” during the simulation of the self-excited system under consideration. Due to the much smaller CFD domain, the computational cost is massively reduced compared to a monolithic CFD simulation of the entire combustion system. This allows the application of the proposed approach for predicting thermoacoustic LC oscillations already in the design phase of a new combustion system.


The presented hybrid model shares similarities with the time-domain Bloch-wave approach proposed by Haeringer and Polifke⁷, especially regarding the reduction of the CFD domain to one burner/flame zone. While the Bloch-wave approach assumes perfect symmetry of the considered system and yields more accurate predictions if this assumption applies, the present approach is more generally applicable.

The capabilities of the suggested hybrid approach are demonstrated by applying it to a laminar 4-can “toy model” combustor and by validating it with monolithic CFD. A possible next step for future work is to apply the modeling framework to a realistic turbulent can-annular combustor. This requires incorporating a noise model in the flame model structure in order to capture resonances of turbulent combustion noise.³⁷ The present study focuses on can-annular combustors. However, while following the same general strategy, one may simply replace the coupling of CFD and LOM via CBSBC with a coupling based on reference velocity and heat release rate, which does not rely on plane acoustic waves at the CFD boundaries.²⁴ This would make the proposed strategy also applicable to annular configurations.

Acknowledgements

We appreciate Stefan Jaensch's valuable contributions to the development of the general idea. The authors gratefully acknowledge the Research Association for Combustion Engines (Forschungsvereinigung Verbrennungskraftmaschinen e.V. FVV, project number 6012700) for the financial support to Matthias Haeringer and the compute and data resources provided by the Leibniz Supercomputing Centre (www.lrz.de).

ORCID iD

Matthias Haeringer  <https://orcid.org/0000-0001-5286-0756>

Notes

1. the same flame is considered in the present study
2. Note that the approach can be easily extended to technically premixed configurations by employing a multiple-input FTF
3. only this term creates response at the input frequency and thus closes the thermoacoustic feedback loop³²
4. Code available at <https://gitlab.lrz.de/tfd/tax>

References

1. Poinso T. Prediction and Control of Combustion Instabilities in Real Engines. *Proc Combust Inst* 2017; 36: 1–28. DOI: 10.1016/j.proci.2016.05.007.
2. Farisco F, Panek L and Kok JB. Thermo-acoustic Cross-talk Between Cans in a Can-annular Combustor. *International Journal of Spray and Combustion Dynamics* 2017; 9(4): 452–469. DOI: 10.1177/1756827717716373.
3. Moon K, Jegal H, Gu J et al. Combustion-acoustic Interactions Through Cross-talk Area Between Adjacent Model Gas Turbine Combustors. *Combust Flame* 2019; 202: 405–416. DOI: 10.1016/j.combustflame.2019.01.027.
4. Moon K, Jegal H, Yoon C et al. Cross-talk-interaction-induced Combustion Instabilities in a Can-annular Lean-premixed Combustor Configuration. *Combust Flame* 2020; 220: 178–188. DOI: 10.1016/j.combustflame.2020.06.041.
5. Yoon M. Thermoacoustics and Combustion Instability Analysis for Multi-burner Combustors. *J Sound Vib* 2021; 492: 115774. DOI: 10.1016/j.jsv.2020.115774.
6. Ghirardo G, Di Giovine C, Moeck JP et al. Thermoacoustics of Can-Annular Combustors. *J Eng Gas Turbine Power* 2019; 141(1): 011007. DOI: 10.1115/1.4040743.
7. Haeringer M and Polifke W. Time Domain Bloch Boundary Conditions for Efficient Simulation of Thermoacoustic Limit-Cycles in (Can-)Annular Combustors. *J Eng Gas Turbine Power* 2019; 141(12): 121005. DOI: 10.1115/1.4044869.
8. Haeringer M, Fournier GJJ, Meindl M et al. A Strategy to Tune Acoustic Terminations of Single-Can Test-Rigs to Mimic Thermoacoustic Behavior of a Full Engine. *J Eng Gas Turbine Power* 2021; 143(7): 710029. DOI: 10.1115/1.4048642.
9. Staffelbach G, Gicquel LYM, Boudier G et al. Large Eddy Simulation of Self Excited Azimuthal Modes in Annular Combustors. *Proc Combust Inst* 2009; 32(2): 2909–2916. DOI: 10.1016/j.proci.2008.05.033.
10. Wolf P, Balakrishnan R, Staffelbach G et al. Using LES to Study Reacting Flows and Instabilities in Annular Combustion Chambers. *Flow, Turbul Combust* 2012; 88: 191–206. DOI: 10.1007/s10494-011-9367-7.
11. Wolf P, Staffelbach G, Gicquel LYM et al. Acoustic and Large Eddy Simulation Studies of Azimuthal Modes in Annular Combustion Chambers. *Combust Flame* 2012; 159(11): 3398–3413. DOI: 10.1016/j.combustflame.2012.06.016.
12. Venkatesan K, Cross A, Yoon C et al. Heavy Duty Gas Turbine Combustion Dynamics Study using a Two-Can Combustion System. In *ASME Turbo Expo 2019: Turbomachinery Technical Conference & Exposition*. Phoenix, USA.
13. Bloch F. Über Die Quantenmechanik Der Elektronen in Kristallgittern. *Zeitschrift für Physik* 1929; 52(7-8): 555–600. DOI: 10.1007/BF01339455.
14. Mensah GA, Campa G and Moeck JP. Efficient Computation of Thermoacoustic Modes in Industrial Annular Combustion Chambers Based on Bloch-Wave Theory. *J Eng Gas Turbine Power* 2016; 138(8): 081502. DOI: 10.1115/1.4032335.
15. Mensah GA and Moeck JP. Limit Cycles of Spinning Thermoacoustic Modes in Annular Combustors: A Bloch-Wave and Adjoint-Perturbation Approach. In *ASME Turbo Expo 2017: Turbine Technical Conference and Exposition*. GT2017-64817. ISBN 978-0-7918-5085-5. doi:10.1115/GT2017-64817.
16. Laera D, Schuller T, Prieur K et al. Flame Describing Function Analysis of Spinning and Standing Modes in An Annular Combustor and Comparison with Experiments. *Combust Flame* 2017; 184: 136–152. DOI: 10.1016/j.combustflame.2017.05.021.
17. Selimefendigil F and Polifke W. A Nonlinear Frequency Domain Model for Limit Cycles in Thermoacoustic Systems with Modal Coupling. *Int J Spray Comb Dynamics* 2011; 3: 303–330. DOI: 10.1260/1756-8277.3.4.303.
18. Jaensch S and Polifke W. Uncertainty Encountered When Modelling Self-Excited Thermoacoustic Oscillations with Artificial Neural Networks. *Int J Spray Combust Dyn* 2017; 9(4): 367–379. DOI: 10.1177/1756827716687583.
19. Tathawadekar N, Doan AK, Silva CF et al. Modelling of the nonlinear flame response of a Bunsen-type flame via multi-layer perceptron. *38th Symposium on Combustion* January 24th to 29th, 2021; doi:10.1016/j.proci.2020.07.115.
20. Bonciolini G, Faure-Beaulieu A, Bourquard C et al. Low Order Modelling of Thermoacoustic Instabilities and Intermittency: Flame Response Delay and Nonlinearity. *Combust Flame* 2021; 226: 396–411. DOI: 10.1016/j.combustflame.2020.12.034.
21. Yu H, Jaravel T, Ihme M et al. Data Assimilation and Optimal Calibration in Nonlinear Models of Flame Dynamics. *J Eng Gas Turbine Power* 2019; 141(12): 121010. DOI: 10.1115/1.4044378.
22. Yu H, Juniper MP and Magri L. Combined State and Parameter Estimation in Level-set Methods. *J Comput Phys* 2019; 399: 108950. DOI: 10.1016/j.jcp.2019.108950.
23. Yu H, Juniper MP and Magri L. A Data-driven Kinematic Model of a Ducted Premixed Flame. *Proc Combust Inst* 2020; 38(4): 6231–6239. DOI: 10.1016/j.proci.2020.06.137.
24. Jaensch S, Merk M, Gopalakrishnan E et al. Hybrid CFD/ Low-Order Modeling of Nonlinear Thermoacoustic

- Oscillations. *Proc Combust Inst* 2017; 36(3): 3827–3834. DOI: 10.1016/j.proci.2016.08.006.
25. Jaensch S, Sovardi C and Polifke W. On the Robust, Flexible and Consistent Implementation of Time Domain Impedance Boundary Conditions for Compressible Flow Simulations. *J Comput Phys* 2016; 314: 145–159. DOI: 10.1016/j.jcp.2016.03.010.
26. Schoukens M and Tiels K. Identification of Block-oriented Nonlinear Systems Starting From Linear Approximations: A Survey. *Automatica* 2017; 85: 272–292. DOI: 10.1016/j.automatica.2017.06.044.
27. Ljung L. *System Identification: Theory for the User*. Second ed. New Jersey: Prentice Hall PTR, 1999. ISBN 0-13-656695-2.
28. Wigren T. Recursive Prediction Error Identification Using the Nonlinear Wiener Model. *Automatica* 1993; 29(4): 1011–1025. DOI: 10.1016/0005-1098(93)90103-Z.
29. Polifke W. Black-Box System Identification for Reduced Order Model Construction. *Ann Nucl Energy* 2014; 67C: 109–128. DOI: 10.1016/j.anucene.2013.10.037.
30. Purwar N, Haeringer M, Schuermans B et al. Flame Response to Transverse Velocity Excitation Leading to Frequency Doubling and Modal Coupling. *Combust Flame* 2021; 230: 111412. DOI: 10.1016/j.combustflame.2021.111412.
31. Indlekofer T, Ahn B, Kwah YH et al. The Effect of Hydrogen Addition on the Amplitude and Harmonic Response of Azimuthal Instabilities in a Pressurized Annular Combustor. *Combust Flame* 2021; 228: 375–387. DOI: 10.1016/j.combustflame.2021.02.015.
32. Haeringer M, Merk M and Polifke W. Inclusion of Higher Harmonics in the Flame Describing Function for Predicting Limit Cycles of Self-excited Combustion Instabilities. *Proc Combust Inst* 2018; 37(4): 5255–5262. DOI: 10.1016/j.proci.2018.06.150.
33. Guennebaud G and Jacob B. Eigen v3, 2010.
34. Selle L, Lartigue G, Poinso T et al. Compressible Large Eddy Simulation of Turbulent Combustion in Complex Geometry on Unstructured Meshes. *Combust Flame* 2004; 137(4): 489–505. DOI: 10.1016/j.combustflame.2004.03.008.
35. Emmert T, Jaensch S, Sovardi C et al. taX - a Flexible Tool for Low-Order Duct Acoustic Simulation in Time and Frequency Domain. In *7th Forum Acusticum*. Krakow: DEGA.
36. Silva CF, Emmert T, Jaensch S et al. Numerical Study on Intrinsic Thermoacoustic Instability of a Laminar Premixed Flame. *Combust Flame* 2015; 162(9): 3370–3378. DOI: 10.1016/j.combustflame.2015.06.003.
37. Merk M, Gaudron R, Silva C et al. Prediction of Combustion Noise of An Enclosed Flame by Simultaneous Identification of Noise Source and Flame Dynamics. *Proc Combust Inst* 2019; 37: 5263–5270. DOI: 10.1016/j.proci.2018.05.124.

A Strategy to Tune Acoustic Terminations of Single-Can Test-Rigs to Mimic Thermoacoustic Behavior of a Full Engine

Matthias Haeringer¹

Department of Mechanical Engineering,
Technical University of Munich,
Garching D-85747, Germany
e-mail: haeringer@td.mw.tum.de

Guillaume J. J. Fournier

Department of Mechanical Engineering,
Technical University of Munich,
Garching D-85747, Germany
e-mail: fournier@td.mw.tum.de

Max Meindl

Department of Mechanical Engineering,
Technical University of Munich,
Garching D-85747, Germany
e-mail: meindl@td.mw.tum.de

Wolfgang Polifke

Department of Mechanical Engineering,
Technical University of Munich,
Garching D-85747, Germany
e-mail: polifke@tum.de

Thermoacoustic properties of can-annular combustors are commonly investigated by means of single-can test-rigs. To obtain representative results, it is crucial to mimic can-can coupling present in the full engine. However, current approaches either lack a solid theoretical foundation or are not practicable for high-pressure rigs. In this study, we employ Bloch-wave theory to derive reflection coefficients that correctly represent can-can coupling. We propose a strategy to impose such reflection coefficients at the acoustic terminations of a single-can test-rig by installing passive acoustic elements, namely straight ducts or Helmholtz resonators. In an iterative process, these elements are adapted to match the reflection coefficients for the dominant frequencies of the full engine. The strategy is demonstrated with a network model of a generic can-annular combustor and a three-dimensional (3D) model of a realistic can-annular combustor configuration. For the latter, we show that can-can coupling via the compressor exit plenum is negligible for frequencies sufficiently far away from plenum eigenfrequencies. Without utilizing previous knowledge of relevant frequencies or flame dynamics, the test-rig models are adapted within a few iterations and match the full engine with good accuracy. Using Helmholtz resonators for test-rig adaption turns out to be more viable than using straight ducts. [DOI: 10.1115/1.4048642]

Introduction

Thermoacoustic combustion instabilities are a major concern in the development of new low emission gas turbine combustors. Arising from constructive feedback between unsteady heat release and acoustics, these instabilities may result in large-amplitude oscillations of acoustic quantities, which can cause increased emission levels or even structural damage [1].

Latest generation land-based gas turbines are often equipped with a can-annular combustion system. In this combustor type, a number of cans are arranged equidistantly around the circumference of the engine. The individual cans are coupled acoustically by a large upstream plenum that is fed by the gas turbine compressor and thus called compressor exit plenum. On the downstream side, the cans are coupled via a small annular gap in front of the first turbine stator [2].

From a thermoacoustic point of view, this coupling is of particular interest although it is weak. It gives rise to azimuthal modes, which involve multiple cans and extend over the entire circumference of the engine. Several studies have characterized this coupling [2–4] and its importance regarding thermoacoustics of the entire engine [5–9]. Generally, due to the coupling of the individual cans, the thermoacoustic properties of an entire can-annular combustor cannot be directly represented by a single-can system.

However, full-scale numerical or experimental investigations of the thermoacoustic properties of an entire can-annular combustion system are extremely expensive and thus not feasible in the design phase of a new combustor. Typically in the late design phase, the thermoacoustic properties of the full engine are explored by means of single-can or single-sector test-rigs [5,6,10]. A variety

of approaches are used to mimic can-can coupling in such single-can test-rigs. A commonly applied method is to extend the up- and downstream termination of the test-rig by straight ducts [6,10,11]. This, however, should be seen as an ad hoc approach without solid theoretical foundation. Another possibility to at least account for some modes resulting from can-can coupling is to employ two-can test-rigs [12], which obviously implies high effort.

More elaborate numerical approaches take into account the equivalent reflection coefficients that a single can is exposed to in the full can-annular system [13]. If these reflection coefficients can be imposed at the up- and downstream end of a single-can test-rig, it mimics the thermoacoustics of the entire engine. In numerical simulations, this has already been exploited to simulate an entire can-annular combustor by resolving only one single can [14].

In experimental test-rigs, active control methods could in principle be used to impose the appropriate reflection coefficients [15–17]. However, in high-pressure single-can test-rigs of applied can-annular combustors this approach seems difficult to implement, because of generally limited access and the hot gas environment.

This study instead focuses on test-rig adaption by passive acoustic elements. We critically assess the common practice of accounting for can-can coupling by extending the up- and downstream termination of test-rigs by straight ducts. In order to refine the current approach we propose and scrutinize an iterative adaption strategy to match the theoretically derived equivalent reflection coefficients with passive acoustic elements. We finally discuss two acoustic element types—straight ducts and Helmholtz resonators—that might be employed within the proposed strategy and apply them to adapt thermoacoustic models of single-can test-rigs. This study reveals that test-rig adaption using duct extensions is not practical.

¹Corresponding author.

Manuscript received September 3, 2020; final manuscript received September 14, 2020; published online March 31, 2021. Editor: Jerzy T. Sawicki.

The paper is structured as follows: In the section Equivalent Reflection Coefficients Computed From Bloch-Wave Theory, we recall the application of Bloch-wave theory in the context of thermoacoustics. We employ it to derive the equivalent reflection coefficients for a single can at a given azimuthal mode order. In the section Passive Acoustic Elements to Approximate Equivalent Reflection Coefficient, we discuss appropriate passive acoustic elements to mimic the equivalent reflection coefficients and propose an iterative adaption strategy. In the sections Application to Network Model of a Generic Can-Annular Combustor and Validation With a Configuration of Applied Relevance, the proposed strategy is applied to a network model of a generic can-annular combustor adapted using straight ducts and a three-dimensional (3D) model of a realistic can-annular combustor adapted using Helmholtz resonators. After a discussion of the expected importance of effects that are neglected in the present thermoacoustic models, a conclusion is drawn in the section Conclusion.

Equivalent Reflection Coefficients Computed From Bloch-Wave Theory

Within this section, we present the reflection coefficients up- and downstream of a single can in a can-annular combustor for a given azimuthal mode order m . These reflection coefficients lump the acoustic response of all remaining cans of the engine. The situation is sketched in Fig. 1 for a generic multican combustor. The considered single can is marked by the inner (red) dashed box, the equivalent reflection coefficients $\mathcal{R}_{m,u}$ and $\mathcal{R}_{m,d}$ are defined at its up- and downstream termination. Provided plane acoustic waves, the reflection coefficients are defined as the ratio of the down- and upstream traveling acoustic Riemann invariants $f = \hat{p}/\rho c + \hat{u}$ and $g = \hat{p}/\rho c - \hat{u}$ and are related to the acoustic impedance Z at the respective positions by

$$\mathcal{R}_{m,u} = \frac{f_u}{g_u} = \frac{Z_u + 1}{Z_u - 1}, \quad \mathcal{R}_{m,d} = \frac{g_d}{f_d} = \frac{Z_d - 1}{Z_d + 1} \quad (1)$$

In general, $\mathcal{R}_{m,x}$ (with $\hat{x}u/d$) in Fig. 1 depend on the thermoacoustic properties of the remaining cans. Therefore, in the most general case, the acoustic properties and especially flame dynamics of all individual cans have to be known in order to compute $\mathcal{R}_{m,x}$.

However, typical can-annular combustors feature a discrete rotational symmetry, where the whole combustor consists of a number of N identical sectors arranged equidistantly around the

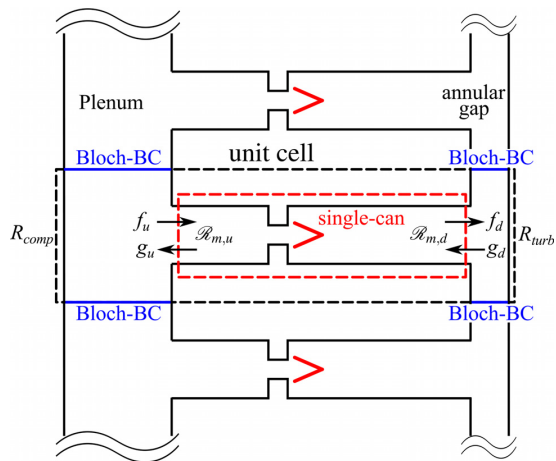


Fig. 1 Generic can-annular combustor. Cans are coupled at up- and downstream side via compressor exit plenum and annular gap. R_{turb} and R_{comp} denote reflection coefficients of turbine inlet and compressor exit.

circumference of the engine. These sectors—marked with the black dashed box in Fig. 1 and in the following denoted as “unit cells”—comprise one single can and the corresponding sector of the compressor exit plenum and the annular gap in front of the first turbine stage. For such a rotationally symmetric configuration, the equivalent reflection coefficients for a given azimuthal mode order m can be computed by utilizing Bloch-wave theory [18,19]. As shown in the following, in this case $\mathcal{R}_{m,x}$ are only dependent on the elements coupling the individual cans and the degree of symmetry N and are independent of the thermoacoustics of the individual cans.

Mensah et al. [19] showed that the (thermo-)acoustic eigenmodes of discrete rotationally symmetric systems can be computed efficiently by utilizing Bloch-wave theory [18]. The eigenmodes \hat{p} of a can-annular combustor can thus be written as

$$\hat{p}(\mathbf{x}) = \Psi(\mathbf{x})e^{im\phi}, \quad \text{with} \\ m = -(N/2 - 1), \dots, -1, 0, 1, \dots, N/2 - 1, N/2 \quad (2)$$

Here, $\mathbf{x} = (r, \phi, z)$ is the position vector comprised of the radial, circumferential, and axial coordinate, Ψ is a function that—for a given eigenmode—is identical in all N unit cells, and m is called the Bloch-wave number. For low frequencies relevant in the present context, the absolute value $|m|$ of the Bloch-wave number is equivalent to the azimuthal mode order [19] and both terms are used synonymously in the following.

The (thermo-)acoustic eigenmodes expressed by Eq. (2) can be classified into three types: azimuthally spinning modes with Bloch-wave numbers of $m = \pm 1, \dots, \pm(N/2 - 1)$, purely axial modes with $m = 0$, and so-called “push-pull” modes with $m = N/2$. The latter only exist for combustors with an even number of cans and are characterized by an acoustic pressure and velocity field of alternating signs in adjacent cans [13,14]. Except for axial modes with $m = 0$, which feature identical pressure fields in all sectors, all other mode types result from coupling of the individual unit cells. Thus, a single-can test-rig, where this coupling is not accounted for will only show modes of azimuthal order $m = 0$.

For applied can-annular combustors, the mean flow in azimuthal direction is negligible. Provided discrete rotational symmetry, such a system features also reflection symmetry. In this case, the azimuthally spinning modes appear as degenerate pairs, where modes with Bloch-wave numbers of opposite sign merely differ by their direction of rotation. For the following derivations, we can therefore limit our considerations to non-negative m [14,19].

Without loss of generality, we consider a unit cell centered at $\phi = 0$ and extended over an azimuthal angle $\phi = [-\pi/N, \pi/N]$. By definition, $\Psi(\mathbf{x})$ is identical in each unit cell. As the pressure is continuous across the interfaces connecting two unit cells (marked blue in Fig. 1), $\Psi(\mathbf{x})$ at the left and right boundary of the unit cell has to be equal [13]

$$\Psi\left(r, \phi = -\frac{\pi}{N}, z\right) = \Psi\left(r, \phi = \frac{\pi}{N}, z\right) \quad (3)$$

Combining Eq. (3) with Eq. (2) leads to a quasi-periodic boundary condition—called Bloch boundary condition (BBC)—for the acoustic pressure [19]

$$\hat{p}\left(r, \phi = \frac{\pi}{N}, z\right) = \hat{p}\left(r, \phi = -\frac{\pi}{N}, z\right)e^{im\frac{2\pi}{N}} \quad (4)$$

Assuming that discrete rotational symmetry holds, a given azimuthal mode order m of the full can-annular combustor is completely represented by a single unit cell with BBC at the coupling interfaces, as sketched in Fig. 2. The equivalent reflection coefficients $\mathcal{R}_{m,x}$ defined at the in-/outlet of a single can are in this case independent of the remaining cans. They only depend on the

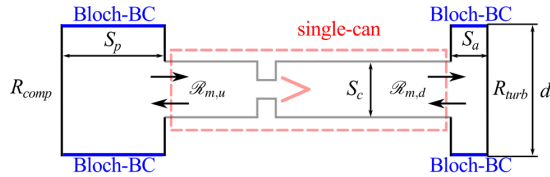


Fig. 2 Definition of $\mathcal{R}_{m,x}$ at the in-/outlet of a single can. $\mathcal{R}_{m,x}$ are dependent on the azimuthal distance d of two cans and the cross sections of can S_c , annular gap S_a and compressor exit plenum S_p .

acoustics of the coupling parts, i.e., the annular gap and the compressor exit plenum, the acoustic termination toward turbine R_{turb} and compressor R_{comp} , and the azimuthal mode order m and the number of cans N . $\mathcal{R}_{m,x}$ can thus be computed from an acoustic model that comprises these coupling parts and BBC. This strategy has already been applied by Ghirardo et al. [13] to compute the equivalent reflection coefficient of a generic can outlet section.

The equivalent reflection coefficients defined in this way are valid for a given mode order m . They may be interpreted as the cumulative acoustic response of all remaining cans for a given azimuthal mode order, i.e., they represent the response of a certain synchronization pattern across all cans.

Equivalent Reflection Coefficients of a Generic Can-Annular Combustor. In order to discuss the general features of the equivalent reflection coefficients, Fig. 3 shows $\mathcal{R}_{m,x}$ of a generic can-annular system with $N=16$ cans for all azimuthal mode orders m . The shown $\mathcal{R}_{m,x}$ was computed using an acoustic network model similar as shown in Fig. 4. For simplicity, the acoustic termination toward turbine and compressor is assumed to be ideal sound hard walls with $R_{turb} = R_{comp} = 1$. $\mathcal{R}_{m,x}$ crucially depend on the area ratio A of annular gap and can ($A = S_a/S_c$) or plenum and can ($A = S_p/S_c$), respectively. Figure 3 shows the phase of the reflection coefficients for $A=20$ (top) and $A=0.06$ (bottom). The former is representative of the plenum/can transition (corresponds to $\mathcal{R}_{m,u}$), and the latter is typical for the transition can/annular gap (corresponds to $\mathcal{R}_{m,d}$). Due to rotational and reflectional symmetry, no acoustic energy is exchanged between individual cans. Thus, the gain of $\mathcal{R}_{m,x}$ only depends on the gain of R_{turb} and R_{comp} . In the present case, the gain $|\mathcal{R}_{m,x}|$ is thus uniformly unity for all mode orders and therefore not shown.

The phase of \mathcal{R}_m of all azimuthal mode orders m is plotted versus the Helmholtz number $He = \omega d/c$, where ω is the angular frequency, c is the speed of sound, and d is the azimuthal distance of

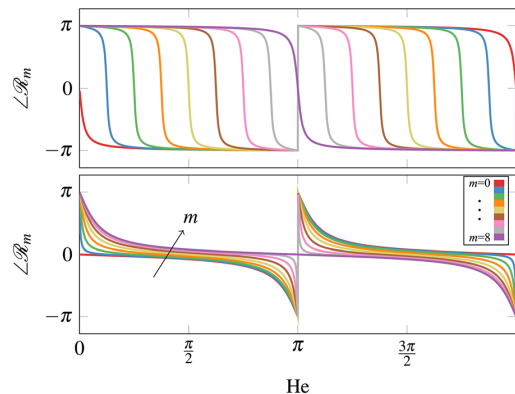


Fig. 3 $\angle \mathcal{R}_m$ of generic 16-can combustor with two different area ratios $A=20$ (top) and $A=0.06$ (bottom) plotted versus Helmholtz-number He

the individual cans. In the zero-frequency limit, the equivalent reflection coefficient behaves like a wall $\mathcal{R}_{m=0} = 1$ for $m=0$ and like an ideal open end $\mathcal{R}_{m \neq 0} = -1$ for all other mode orders [13]. For $He = 2\pi \frac{m}{N}$, which correspond to purely azimuthal modes of order m that are only active in the plenum or the annular gap, the corresponding equivalent reflection coefficient equals $\mathcal{R}_m = 1$. For $He = \pi$, at which the distance d of two cans equals half a wavelength, Bloch-symmetry necessitates pressure nodes at the can centers for $m \neq N/2$, corresponding to an equivalent reflection coefficient $\mathcal{R}_{m \neq N/2} = -1$ [20]. In typical can-annular systems, $He = \pi$ is the cut-on frequency of transversal modes inside the cans. The validity of the 1D model employed here is thus questionable for $He > \pi$. However, the frequency range of interest in the present context is $He < \pi/4$.

For large area ratios A (top plot of Fig. 3), typical for the transition compressor-plenum/can, the equivalent reflection coefficient essentially represents an ideal open end with $\mathcal{R}_m \approx -1$ for a wide frequency range. Only in the vicinity of pure plenum modes of the respective azimuthal order \mathcal{R}_m deviates from the ideal open end. This indicates that for typical area ratios and for frequencies sufficiently far away from pure plenum modes, the compressor exit plenum is essentially decoupled from the individual cans. \mathcal{R}_m of higher azimuthal mode orders may thus be approximated with $\mathcal{R}_{m=0}$.

For small area ratios A (bottom plot of Fig. 3), typical for the transition can/annular gap, the general behavior of the equivalent reflection coefficients is similar. However, especially for frequencies $He < \pi/4$, the individual \mathcal{R}_m are more distinct from each other, compared to \mathcal{R}_m for large A . This indicates that for this frequency range, the coupling of individual cans via the annular gap with small A is more important than the coupling via the compressor exit plenum with large A . This preliminary result will be confirmed later by considering a realistic 3D configuration.

Overall, the phase of the equivalent reflection coefficients of individual mode orders m is closely spaced for both large and small A . This is a consequence of the weak coupling of individual cans for extreme values of A characteristic of can-annular combustors. It leads to clustering of eigenmodes with different m , because the reflection coefficient at the can entry and exit are similar for all m [8,13]. For intermediate values of $A \sim 1$, $\angle \mathcal{R}_m$ of individual mode orders would be more distinct, resulting from stronger coupling.

The objective of this work is to provide a strategy to investigate the thermoacoustics of a can-annular combustor by means of a single-can test-rig. If the equivalent reflection coefficients $\mathcal{R}_{m,x}$ can be imposed at the up- and downstream termination of the single-can test-rig, it will represent a given mode order m of the full engine and will have identical thermoacoustic properties. In the Passive Acoustic Elements to Approximate Equivalent Reflection Coefficient section, we discuss two types of passive acoustic elements that might be used to approximate $\mathcal{R}_{m,x}$.

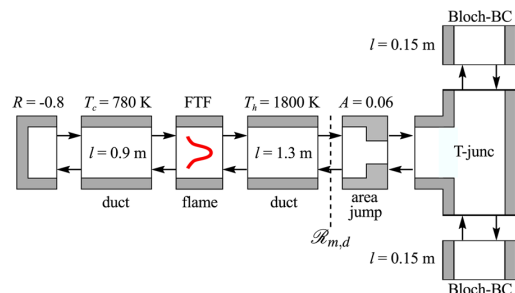


Fig. 4 Network model of considered generic can-annular combustor

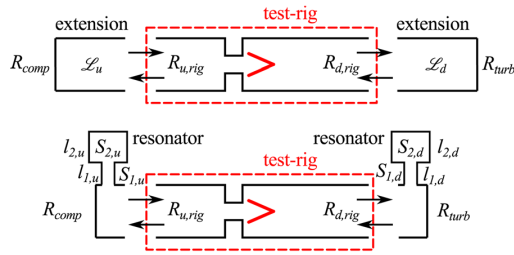


Fig. 5 Matching $\mathcal{R}_{m,x}$ of the full engine by extending the single-can test-rig with straight ducts (top) and by installing Helmholtz-resonators at the in-/outlet (bottom)

Passive Acoustic Elements to Approximate Equivalent Reflection Coefficient

As shown in Fig. 3, the ensemble of cans reflects acoustic waves with a certain phase shift, which depends on frequency ω and azimuthal mode order m . The general idea of this work is to approximate this phase shift for a given azimuthal mode order m with passive acoustic elements. A common practice to account for can–can coupling in single-can test-rigs is to extend the (up- and) downstream termination of the test-rig by straight ducts. In order to critically assess—and improve—this current practice, we investigate how a straight duct extension can be used to approximate the equivalent reflection coefficients. The second element we consider is a Helmholtz-type resonator.

Figure 5 shows schematically how the two considered elements should be installed in a test-rig. The passive acoustic elements have to be adapted such that the phase of test-rig and equivalent reflection coefficient

$$\angle R_{x,rig}(\omega_d) \stackrel{!}{=} \angle \mathcal{R}_{m,x}(\omega_d) \quad (5)$$

match for the design frequency ω_d . As mentioned in the Equivalent Reflection Coefficients of a Generic Can-Annular Combustor section, the gain $|\mathcal{R}_{m,x}|$ depends on the gain $|R_{comp/turb}|$ and is identical for all mode orders m . It is thus crucial that the considered elements do not affect the gain of the test-rig reflection coefficient $R_{x,rig}$. As the gain of R_{turb} is determined by the mean flow through the first turbine stator vanes [21], the duct extension used to shift the outlet termination $R_{comp,turb}$ must have a constant cross section. The Helmholtz resonator in turn must be designed for a minimum damping rate, i.e., it should be operated sufficiently far away from its eigenfrequency [22].

The only design parameter of the straight duct extensions with constant cross section is their length \mathcal{L}_x . Neglecting the effect of mean flow,² the phase shift induced by shifting the in-/outlet termination by the distance \mathcal{L}_x depends linearly on the frequency ω

$$\angle R_{x,rig} = -\frac{2\omega\mathcal{L}_x}{c} \quad (6)$$

In order to shape the frequency response of the Helmholtz resonator, four main design parameters are available: lengths l_1 and l_2 and cross sections S_1 and S_2 of the resonator neck and volume, respectively. Additional design parameters that are not considered here could be the purge mass flow rate and temperature.

Computing the exact frequency response of Helmholtz resonators depending on the mentioned design parameters requires sophisticated numerical or experimental methods [22]. However, in practice the same type of acoustic model will be used to obtain $\angle R_{x,rig}$ and $\angle \mathcal{R}_{m,x}$. In case the employed acoustic model does not include certain effects that might be relevant in practice, they are

²Axial mean flow can be accounted for by changing the propagation speed of f to $\bar{u} + c$ and g to $\bar{u} - c$.

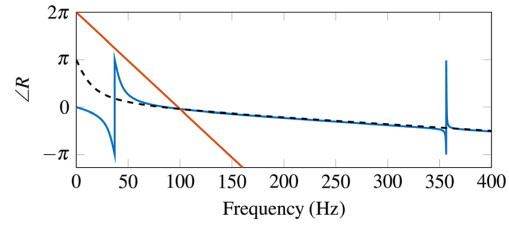


Fig. 6 $\angle \mathcal{R}_{m=1,d}$ from Fig. 7 (dashed black) compared to $\angle R_{d,rig}$ adapted by straight duct extension (red) and Helmholtz resonator (blue). Both elements are designed for $\nu_d = 100$ Hz.

neglected in both computed $\angle R_{x,rig}$ and $\angle \mathcal{R}_{m,x}$. Thus, for the present purpose, comparably crude modeling approaches such as the Helmholtz equation employed in this study might be sufficient to compute $\mathcal{R}_{m,x}$ and to design the passive acoustic elements. In the section Influence of Effects Neglected in Combustor Model, we discuss how effects neglected in the employed acoustic models may compromise the proposed strategy.

Figure 6 exemplarily shows $\angle R_{d,rig}$ adapted by duct extension (blue line) and Helmholtz resonator (red line) to match $\angle \mathcal{R}_{m=1,d}$ taken from Fig. 7 at a design frequency of $\nu_d = \omega_d/2\pi = 100$ Hz. From Fig. 6, it becomes apparent that the Helmholtz resonator is more appropriate to match the equivalent reflection coefficient shown. Due to its four degrees-of-freedom, it can be designed to well approximate \mathcal{R}_m in a quite large frequency range around ν_d . In contrast, the straight duct extension matches \mathcal{R}_m only directly at ν_d .

In order to use a single-can test-rig to study the thermoacoustic stability properties and possibly the limit cycle (LC) of mode order m of a full can-annular combustor, $R_{x,rig}$ has to be designed to match $\mathcal{R}_{m,x}$ at the dominant (respectively, most unstable) frequencies of the full engine. However, these design frequencies are normally not known a priori. Even if the pure acoustic eigenfrequencies might be known from an acoustic model, the (generally unknown) flame dynamics may alter these frequencies. Furthermore, intrinsic thermoacoustic (ITA) modes may play an important role [23–25]. Their frequencies are not predictable without knowledge of the flame dynamics. Therefore, the passive acoustic elements in general have to be adapted in an iterative procedure, which ensures that the dominant frequency observed in the single-can test-rig converges to the dominant frequency of the full engine of a given azimuthal mode order m . A strategy is presented in the Iterative Adaption of Passive Elements section.

If the initial design of the Helmholtz resonator is good enough to approximate the relevant frequency range sufficiently well, as shown in Fig. 6, iterative adaption may not be necessary. However, the large number of degrees-of-freedom complicates the search for an optimal design, while this is straightforward for the duct extension. In the present case, the parameters of the resonator were chosen such that the design frequency is well above the Helmholtz mode and below the first axial mode, which coincide with the abrupt phase transitions at 40 Hz and 355 Hz, respectively. Sufficiently far away from the resonator eigenfrequencies, its damping rates are expected to be comparably small [22]. While the design works properly for the present case, a general design guideline is not immediately obvious and the set of parameters has to be optimized from case to case. In the following, we therefore investigate the capabilities of both element types based on numerical models of single-can test-rig and full can-annular combustor.

Iterative Adaption of Passive Elements. As discussed previously, the frequency ν_d for which the Helmholtz resonator or the straight duct extension is initially designed to fulfill Eq. (5) does in general not coincide with the dominant frequencies of the full

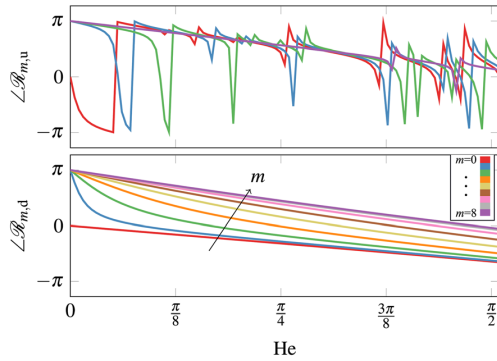


Fig. 7 Equivalent reflection coefficient of 3D configuration. $\angle \mathcal{R}_{m,u}$ for $m=0,1,2,8$ (top) and $\angle \mathcal{R}_{m,d}$ (bottom) versus Helmholtz-number He.

engine. We therefore propose a fixed point iteration strategy with the objective that the dominant frequency observed in the single-can test-rig approaches the dominant frequency of the full engine for a given mode order m .

At this point, the terminology *dominant frequency* has to be defined more clearly. In case of an unstable system, the dominant frequency is clearly visible as a narrow peak in the measured pressure spectrum (corresponds to LC frequency). For a stable system, the peaks in the pressure spectrum are broadened. However, the eigenmodes of the stable system still show up as maxima in the measured pressure spectrum. The peaks result from resonances of broad-band combustion noise emitted by the turbulent flame with stable eigenmodes of the system [26]. Thus, we define dominant frequency generally as the position of maxima in the sound pressure spectrum, no matter whether they appear as narrow or broad peaks.

Step zero of the proposed strategy is to compute the equivalent reflection coefficients $\mathcal{R}_{m,x}$ of the full can-annular combustor as defined in the Equivalent Reflection Coefficients of a Generic Can-Annular Combustor section. If Helmholtz resonators are employed for the test-rig adaption, the initial parameters for a given m are selected to optimally approximate $\mathcal{R}_{m,x}$ in the relevant frequency range. The passive acoustic elements installed at the test-rig are designed to fulfill Eq. (5) at an initial guess ν^0 of the dominant frequency of the full engine. For both computing $\mathcal{R}_{m,x}$ and designing the elements, an acoustic solver based on the Helmholtz equation is employed.

The following steps of the proposed approach are:

- (1) Run the adapted test-rig and measure the dominant frequency ν^n .
- (2) Adapt the installed passive acoustic elements to fulfill Eq. (5) at the measured frequency ν^n .
- (3) Iterate until the dominant frequency ν^n measured in the test-rig stays constant. Repeat with different m .

Unconditional convergence of the proposed iterative algorithm cannot be proven, as in practice a comprehensive mathematical description of all subsystems is not available. However, for all setups investigated in this study, the algorithm converged even for initial frequencies ν^0 far away from the final value. This suggests that the algorithm will converge for practically relevant cases.

In order to minimize the number of iterations necessary to adapt the passive elements, the initial frequency guess ν^0 should be as close to the dominant frequency for mode order m of the full system as possible. Due to the clustering of eigenmodes in typical can-annular combustors (see Fig. 8), the dominant frequencies of the individual azimuthal mode orders are generally close to each other [13]. Thus, the dominant frequency obtained for a certain m may serve as ν^0 for the next higher m . In case the single-can test-

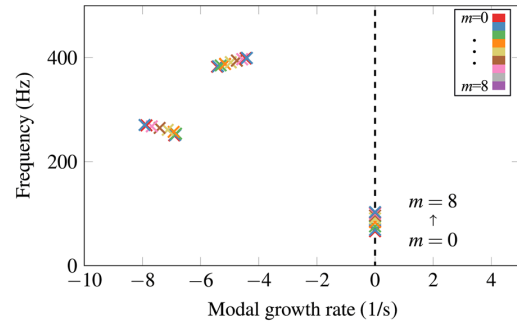


Fig. 8 Eigenfrequencies for all azimuthal mode orders m of full can-annular combustor at a_{LC} . The corresponding amplitude levels are in the range $a_{LC} = 0.59-0.65$.

rig comprises an entire sector of the considered can-annular combustor (including part of the compressor plenum and the annular gap), it represents mode order $m=0$ of the full engine and can be used to obtain the dominant frequency for $m=0$. Alternatively, if known from an acoustic model, the pure acoustic eigenfrequency of the considered m can be used as initial guess ν^0 . In many cases, flame dynamics do not affect the acoustic eigenmode drastically and it can thus be considered as good approximation of the thermoacoustic eigenmode. This however is not the case if the dominant mode is of ITA origin [24].

The relative change of dominant frequency $\Delta\nu^n$ between iteration $n-1$ and n may be used to define a convergence criterion

$$\Delta\nu^n = \frac{|\nu^n - \nu^{n-1}|}{\nu^n} < \epsilon \quad (7)$$

If $\Delta\nu^n$ is smaller than a predefined threshold ϵ , the iterations are stopped. An additional criterion based on the relative change of design parameters of the adapted elements may be used to distinguish slow progress from actual convergence of the algorithm. Although we cannot strictly prove that meeting these criteria is always sufficient for convergence of the algorithm, in all cases investigated in this study criterion (7) correctly indicated convergence.

If the test-rig is adapted by means of straight duct extensions, only the lengths \mathcal{L}_x are available to fulfill Eq. (5) at the observed dominant frequency. If Helmholtz resonators are used, at least the four geometrical parameters illustrated in Fig. 4 are available for the adaption process. In this work, we only modify one single parameter during the iteration process. In general, more sophisticated adaption strategies that modify multiple parameters at once in order to optimally approximate $\angle \mathcal{R}_{m,x}$ around ν^n are conceivable. Deriving such strategies could be part of a follow-up study.

Application to Network Model of a Generic Can-Annular Combustor

Within this section, we demonstrate test-rig adaption for a generic can-annular combustor using straight duct extensions. Both full configuration and adapted test-rig are modeled by a quasi-1D thermo-acoustic network model. The results of the full configuration serve as a benchmark for the adapted test-rig. For the adaption using Helmholtz resonators, 3D effects might play a role. Consequently, this strategy is discussed in the section Validation With a Configuration of Applied Relevance, where a full 3D configuration is considered.

Setup. Figure 4 shows the network model of one unit cell of the generic can-annular combustor considered in the present section. The network model contains only 1D elements. The

extension of the combustor in azimuthal direction is taken into account by a T-junction at the outlet. For simplicity we focus on matching only the downstream reflection coefficient $\mathcal{R}_{m,d}$, but the approach could equally be applied to adapt both up- and downstream termination simultaneously. The upstream reflection coefficient of the individual cans is set to $R_u = -0.8$ in order to take into account acoustic losses present in realistic systems. The dimensions and physical conditions of the system (cf. Fig. 4) are set in accordance with typical can-annular combustors. Fluid properties of air are used. The transition toward the turbine, which is often a choked nozzle in actuality, is represented by $R_{\text{turb}} = 1$ [21].

Flame dynamics are modeled by a flame transfer function (FTF) of a swirl burner test-rig taken from [27]. The dimensions of the flame and the mean flow speed in this test-rig are comparable to realistic can-annular combustors, although the employed FTF was measured at atmospheric conditions. Full engine and adapted test-rig model are compared based on their LC frequency and amplitude, because these are the most relevant quantities in practice. The iterative algorithm to adapt the test-rig model is also based on LC frequencies, as these correspond to the dominant frequencies measured experimentally. In order to capture the formation of LC oscillations, we introduce a generic saturation factor s that models the amplitude dependence of the flame response F [28]

$$F(\omega, a) = \frac{\hat{Q}(\omega, a)}{\hat{u}} = s(a)\text{FTF}(\omega), \quad s(a) = \frac{1}{1 + e^{16(a-0.5)}} \quad (8)$$

Here, \hat{Q} and \hat{u} denote the Fourier transform of the heat release rate and acoustic velocity at the reference position of the FTF and a is a measure of the amplitude level. The network models of the full can-annular combustor and the adapted single-can system are built and solved using the tool *taX*³ [29]. The LC amplitude level a_{LC} , which corresponds to a growth rate $\sigma = 0$ of the most unstable system eigenmode, is calculated using a gradient-based root search algorithm. The corresponding LC frequency is obtained by computing the eigenfrequencies of the network model with a saturation factor of $s(a_{\text{LC}})$.

Results of the Full Configuration. Figure 8 shows the eigenfrequencies of the full can-annular combustor with saturation factor $s(a_{\text{LC}})$ for all azimuthal mode orders m . The clustering of eigenmodes of different m is clearly visible [13]. Among the clusters shown, one can identify an axial quarter-wave, three-quarter-wave, and five-quarter-wave mode. All modes in the quarter-wave cluster are unstable. The LC amplitude level a_{LC} and frequency is determined separately for each mode order m .

As a_{LC} is calculated separately for each m , any nonlinear interaction of individual mode orders m is neglected. Furthermore, the proposed approach of identifying equivalent reflection coefficients for the individual azimuthal mode orders assumes that those can be studied separately. In reality, at finite amplitude levels different azimuthal mode orders can interact, which may result in one dominant mode with LC frequency and amplitude level different from the values computed here. Additionally, the computed a_{LC} relies on Bloch-symmetry, which assumes that discrete rotational symmetry is retained even for finite amplitude levels [28]. This is not necessarily the case in practice. However, for the proposed approach, it is not crucial to exactly predict the LC amplitude and frequency that results from the interaction of multiple unstable modes and that is potentially influenced by a symmetry break. In case the proposed approach indicates a thermoacoustic instability at only *one single* azimuthal mode order, the combustor has to be redesigned anyway. Thus, it is not necessary to correctly represent the case of multiple unstable mode orders and accurately predict the exact amplitude level a_{LC} .

³Code available at <https://gitlab.lrz.de/tfd/taX>

The equivalent reflection coefficient $\mathcal{R}_{m,d}$ of the considered can-annular combustor is defined at the location indicated in Fig. 4 and shown in the bottom plot of Fig. 3.

Iterative Adaption of the Test-Rig Model. In the following, we illustrate the adaption procedure for the “push-pull” mode $m = 8$. For all other mode orders, the procedure is exactly equivalent and we just show the final results. We use the LC frequency $\nu_1^0 = 66$ Hz of $m = 0$ as initial frequency guess. This is the dominant frequency that would be measured in the single-can test-rig without any extensions. In order to demonstrate the robustness of the proposed approach, we repeat the procedure with an initial frequency of $\nu_2^0 = 300$ Hz which is quite far away from the dominant frequency for $m = 8$. According to Eq. (6), the corresponding initial extension lengths are $\mathcal{L}_{d,1}^0 = 4.33$ m for ν_1^0 and $\mathcal{L}_{d,2}^0 = 1.26$ m for ν_2^0 .

Figure 9 shows $\angle \mathcal{R}_{m,d}$ for the considered azimuthal mode order $m = 8$ together with the phase of the outlet reflection coefficient of the test-rig $\angle \mathcal{R}_{d,\text{rig}}$ for the individual iterations. Starting the iterations at $\nu_1^0 = 66$ Hz, the process takes five steps until a prescribed $\Delta\nu < 0.5\%$ is reached. This is a very strict criterion that could probably be weakened in practice. However, here we want to demonstrate the accuracy that can be achieved by the proposed approach.

Figure 10 shows the corresponding LC frequencies ν^n observed in the test-rig model for the individual iterations. Within five iterations, the LC frequency $\nu^5 = 103.0$ Hz matches the LC frequency of $m = 8$ of the full engine with a relative error below 0.2%. The obtained LC amplitude level after convergence is $a_{\text{LC}} = 0.594$, which is the same value as for the full can-annular combustor. The final extension length is $\mathcal{L}_d^5 = 3.06$ m.

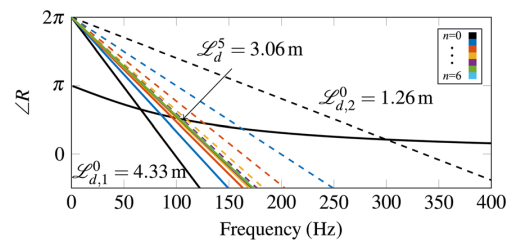


Fig. 9 $\angle \mathcal{R}_{m=8,d}$ (black curve) together with $\angle \mathcal{R}_{d,\text{rig}}$ for the individual iterations. Phase for initial lengths shown in black, solid lines indicate iterations for $\nu^0 = 66$ Hz dashed lines for $\nu^0 = 300$ Hz.

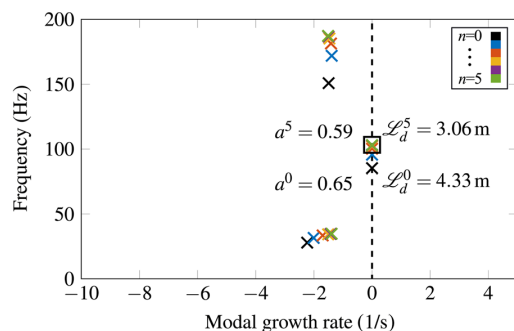


Fig. 10 LC frequencies of the test-rig for individual iterations with $\nu^0 = 66$ Hz (colored crosses), LC frequency for initial extension length marked with black crosses. Black square indicates LC frequency of the full engine for $m = 8$.

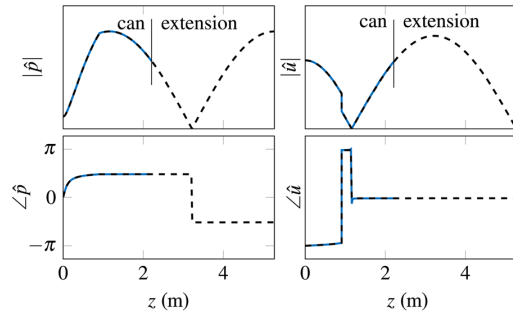


Fig. 11 Normalized absolute value and phase of acoustic pressure and axial velocity in test-rig can with extension (dashed black) and in can of full engine (solid blue) for $m = 8$ plotted over the axial coordinate z

Table 1 Extension lengths for individual azimuthal mode orders m

m	1	2	3	4	5	6	7	8
\mathcal{L}_d (m)	6.12	5.31	4.51	3.89	3.49	3.24	3.10	3.06

Note that if the criterion in Eq. (7) is weakened to $\Delta\nu < 5\%$, which is more a realistic value due to limited measurement accuracy, the approach converges already after two iterations. In this case, the relative error of the test-rig LC frequency is below 3%, while the relative error in LC amplitude level is approx. 2%.

If $\nu_2^0 = 300$ Hz, which is far away from the actual LC frequency of the full engine, is used as initial frequency guess, the process converges after six iterations for $\Delta\nu < 0.5\%$ and after three iterations for $\Delta\nu < 5\%$, while the achieved accuracy is comparable to that of ν_1^0 .

Figure 11 compares the mode shapes in one can predicted by the respective network model of the full engine and the adapted test-rig. Inside the can, the acoustic pressure and velocity of the full engine and the single-can test-rig agree well.

The procedure illustrated for $m = 8$ is completely analogous for all other azimuthal mode orders. The dominant frequency $\nu = 66$ Hz of $m = 0$ is used as an initial guess for all mode orders. For each m , the approach converges within a maximum of five iterations, while the relative errors in LC frequency and amplitude levels are below 1%. If a weakened convergence criterion $\Delta\nu < 5\%$ is used, the approach converges within two iterations for each mode order m . Table 1 shows the resulting extension lengths for each mode order m .

Stability Properties of the Adapted Test-Rig. In the section Iterative Adaption of the Test-Rig Model, we pointed out that a single-can test-rig model can be adapted iteratively to show the same LC as the full configuration at a given azimuthal mode order.⁴ So far, we have not discussed the stability properties of the adapted test-rig model. A LC is characterized by $\sigma = 0$, while the (linear) stability of the system is determined by the sign of σ in the zero-amplitude limit $a = 0$. The passive acoustic elements are designed such that Eq. (5) holds for *purely real-valued* design frequencies ω_d ($\sigma = 0$). For $\sigma \neq 0$, Eq. (5) does not hold in general. Thus, even if the LC frequencies of test-rig and full engine match, the eigenfrequencies in the zero-amplitude limit are generally not identical.

⁴Provided that Bloch-symmetry holds and nonlinear interaction of individual mode orders is negligible.

We can however argue that for a unique, stable LC to develop, the modal growth rate must be $\sigma > 0$ in the zero-amplitude limit. Provided that both systems develop an identical LC, both systems must be linearly unstable with $\sigma > 0$ in the zero-amplitude limit. To conclude, both adapted test-rig and full engine will have the same stability properties, although their eigenmodes do not necessarily have the same frequency and growth rate in the zero-amplitude limit.

Critical Assessment of the Adaption Strategy. The converged extension lengths for the individual mode orders shown in Table 1 are quite large compared to the length of the can. This will cause problems for the practical implementation of this strategy if the evaluated extension length cannot be realized in the high-pressure test-bench.

Figure 11 illustrates exemplarily for $m = 8$, why the extension has to be that long. $\mathcal{R}_{m=8,d}$ could be approximated by an acoustically soft termination at axial position $z = 3.2$ m in Fig. 11 (pressure node). In this case, the mode in the full engine would be approximated by a half-wave mode in the test-rig. However, as $R_{\text{turb}} = 1$ at the end of the extension is fixed, the full engine mode has to be approximated by a three-quarter-wave mode, which results in large \mathcal{L}_d . It is apparent that in this case there exists also a lower frequency quarter-wave mode in the test-rig. This mode is observed in Fig. 10 at frequency $\nu = 34$ Hz. It has no counterpart in the full engine and can be seen as an artifact of the proposed method (in the following also called “spurious mode”).

This mode may become dominant in the test-rig, which causes ambiguity on which measured frequency the iterations should be based on. However, a general criterion can be formulated. We define the phase being wrapped in the interval $[-\pi, \pi]$: If $\angle\mathcal{R}_{m,d} > 0$, the full engine mode is approximated by a three-quarter-wave mode, i.e., the iterations must be based on the second mode of the test-rig. If $\angle\mathcal{R}_{m,d} \leq 0$, the full engine mode is approximated by a quarter-wave mode and the iterations must be based on the first mode of the test-rig. However, if for $\angle\mathcal{R}_{m,d} > 0$ the spurious mode is unstable in the test-rig, it will be difficult or even impossible to identify the frequency of the second mode on which the iterations have to be based on. Additionally, if the spurious mode is unstable and dominates for the final extension length, the stability of the full engine mode cannot be assessed with the adapted test-rig.

The final extension lengths in Table 1 are not directly related to any characteristic length of the combustor. Thus, they cannot be deduced from geometrical consideration, as it is current practice. Instead, iterative adjustment according to the proposed strategy is necessary. This, however, would be very costly in high-pressure test-rigs. The high-pressure cell has to be opened for each iteration step and for each mode order. If instead of a single operating condition with a fixed dominant frequency, an entire operating window with variable dominant frequencies is investigated, the effort of implementing such an iterative strategy will be prohibitive.

In summary, the iterative test-rig adaption demonstrated within this section is most likely impractical, but when using straight duct extensions there is no obvious alternative to the proposed iterative strategy.

Validation With a Configuration of Applied Relevance

Within this section, we demonstrate test-rig adaption using Helmholtz resonators for a can-annular combustor with 16 cans modeled by the 3D inhomogeneous Helmholtz equation. The objective is to demonstrate the proposed test-rig adaption for a configuration that could similarly be found in practice (e.g., see Ref. [6]). Again, results from the adapted single-can system are compared to the full can-annular combustor model.

Setup. Figure 12 shows a slice through one sector of the considered setup along the axial direction. Flame dynamics are

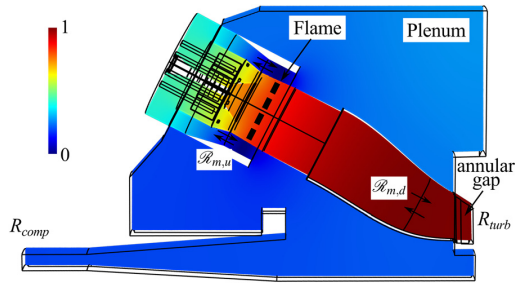


Fig. 12 3D model of realistic can-annular combustor. Individual cans are coupled via plenum and annular gap. Colors show normalized $|R|$ for the dominant mode of azimuthal order $m = 1$.

represented by the flame model shown in Eq. (8) [27]. They are coupled to the acoustics by a source term that is active in the flame region indicated in Fig. 12. The flame divides the domain into a cold ($T_c = 780$ K) and hot ($T_h = 1800$ K) region. Fluid properties of air are used. BBCs are imposed at the cutting interface of plenum and annular gap. The acoustic terminations toward compressor and turbine are set to $R_{comp} = R_{turb} = 1$. To account for acoustic damping, which is not included in the Helmholtz equation, we assume that a LC is established at a positive modal growth rate of $\sigma = 2$ s⁻¹ [30]. The model is built and solved using the finite element software COMSOL MULTIPHYSICS [31].

Equivalent Reflection Coefficient. Due to nonplanar acoustic waves in the vicinity of the annular gap and the plenum-can transition, the equivalent reflection coefficients $\mathcal{R}_{m,x}$ are defined in some axial distance to the azimuthal coupling interfaces (see Fig. 12). They are obtained by computing the forced response of the plenum and annular gap section at discrete frequencies for individual m .

Figure 7 shows $\angle \mathcal{R}_{m,u}$ of the plenum (top) and $\angle \mathcal{R}_{m,d}$ of the annular gap (bottom) versus $He = \omega d/c$. For better visibility, only $m = 0, 1, 2, 8$ of $\angle \mathcal{R}_{m,u}$ is shown. The characteristic length d is set to the can-can distance at the annular gap, i.e., 1/16th of the total annular gap perimeter. The relevant frequencies of the first axial mode order are in the range $He \approx \pi/14 \dots \pi/6$.

The equivalent reflection coefficient of the annular gap $\mathcal{R}_{m,d}$ is in good agreement with that obtained from the network model shown in Fig. 3. Compared to the network model case, the individual values of $\angle \mathcal{R}_{m,d}$ are more distinct from each other (due to a larger A in the present configuration), which indicates that the cluster of first axial mode order is not as closely spaced as in Fig. 8. The overall linear decrease of $\angle \mathcal{R}_{m,d}$ with frequency reflects the axial distance of $\mathcal{R}_{m,d}$ to the annular gap.

At first glance, $\angle \mathcal{R}_{m,u}$ looks notably different from that in Fig. 3 and its behavior seems quite chaotic. The abrupt phase changes observed in Fig. 7 are related to eigenfrequencies of the plenum. As explained for Fig. 3, at these eigenfrequencies, the equivalent reflection coefficient equals $\mathcal{R}_{m,u} = 1$. In case of the quasi-1D network model, the plenum eigenfrequencies are regularly spaced, resulting in a regular behavior of $\angle \mathcal{R}_{m,u}$ as shown in Fig. 3. In the present configuration, the plenum is a large volume of complex shape, which features irregularly spaced eigenfrequencies with complex 3D mode shapes. In particular for higher frequencies ($He > 3\pi/8$) the eigenfrequencies are closely spaced. However, except for the immediate vicinity of these plenum eigenfrequencies, $\angle \mathcal{R}_{m,u}$ for all m closely follow a common trend, which linearly decreases from π . This linear decrease results from the axial distance of $\mathcal{R}_{m,u}$ to the can-plenum transition. Thus, except for very low frequencies $He < \pi/16$ and the immediate vicinity of plenum eigenfrequencies, all mode orders impose an almost ideal open end at the can inlet.

Importance of Upstream Coupling. Except for the immediate vicinity of plenum eigenfrequencies, the individual $\angle \mathcal{R}_{m,u}$ are closely spaced in the frequency range $He \approx \pi/16 \dots 3\pi/8$ that is relevant to the first axial mode order. In particular, $\angle \mathcal{R}_{m,u}$ are much closer together than the individual $\angle \mathcal{R}_{m,d}$ in the same frequency range. The phase $\angle \mathcal{R}_{m=0,u}$ of the uncoupled $m = 0$ configuration is thus a good approximation for all other azimuthal mode orders, except near plenum eigenfrequencies. This indicates that for most of the relevant frequency range, the coupling via the annular gap is much more important than the coupling via the plenum.

To substantiate this argumentation, we compare LC amplitude levels and frequencies of the full system and a system coupled at the downstream side only ($m = 0$ set at the plenum interfaces) in Table 2. All frequencies are normalized by the LC frequency of the $m = 0$ system. The azimuthal mode order $m = 5$ is stable, thus a_{LC} is undefined there. As observed in Table 2, the relative difference of the two configurations in terms of LC amplitude level and frequency is below 5% for all mode orders, except for ν of $m = 2$ and a_{LC} of $m = 6$. The LC frequency of azimuthal mode order $m = 2$ is close to a plenum eigenfrequency visible in Fig. 7 at $He \approx \pi/10$. This explains the differences between fully coupled and downstream-only coupled systems for this mode order m . To conclude, for the present configuration can-can coupling via the plenum is negligible for frequencies that are not in the immediate vicinity of plenum eigenfrequencies. In the following, we will therefore only consider adaption of the downstream termination. The error of representing the upstream termination by the uncoupled plenum ($m = 0$) is considered to be small compared to other possible error sources.

However, this finding cannot be generalized for all practical relevant systems. The investigated setup does not have cross-fire tubes, which would directly connect the cans upstream of the flame. These could drastically increase the upstream coupling of the individual cans, which would have to be accounted for in the same manner as shown for the downstream termination.

Matching Downstream Termination. The initial design of the Helmholtz resonator with the considered four degrees-of-freedom (cf. Fig. 5) is nontrivial. However, the four parameters allow approximating $\angle \mathcal{R}_{m,d}$ well for a wide frequency range. Due to the high computational effort when searching a four-dimensional parameter space for an optimal design, we only consider $m = 1$ and $m = 8$. However, the strategy can be applied accordingly to all other mode orders.

As indicated in Fig. 6 and discussed below, for a good match with $\angle \mathcal{R}_{m,d}$ the Helmholtz mode of the resonator should be well below the relevant frequency range, while the first axial mode should be well above. To shift the Helmholtz mode to low frequencies, the resonator volume should be as large as the limitations of the high-pressure cell allow. However, the length of the volume l_2 is bounded by the lower frequency limit of the axial mode. The above guidelines are common for all mode orders m . The two remaining design parameters l_1 and S_1 are used to optimally approximate $\angle \mathcal{R}_{m,d}$ for the given m .

Figure 13 shows $\angle \mathcal{R}_{rig,d}$ adapted with Helmholtz resonators designed for $m = 8$ (top) and $m = 1$ (bottom) compared to $\angle \mathcal{R}_{m,d}$ of the respective mode orders. The resonators are mounted at the

Table 2 Normalized LC frequencies ν and amplitudes a_{LC} of individual m for fully coupled “u/d” and downstream-only coupled “d” configuration

m	1	2	3	4	5	6	7	8
$\nu, u/d$	1.14	1.17	1.40	1.49	1.74	1.81	1.85	1.86
ν, d	1.09	1.28	1.44	1.49	1.76	1.82	1.85	1.86
$a_{LC, u/d}$	0.66	0.63	0.56	0.42	—	0.47	0.50	0.51
$a_{LC, d}$	0.68	0.64	0.56	0.44	—	0.36	0.49	0.50

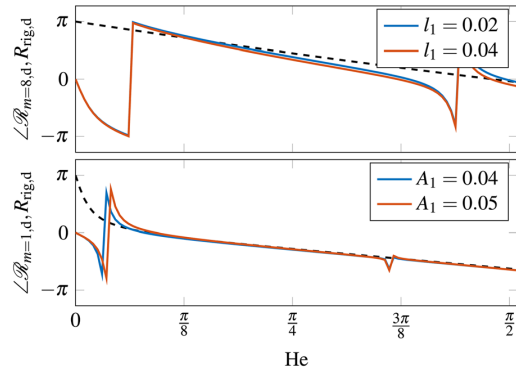


Fig. 13 $\angle \mathcal{R}_{\text{rig,d}}$ adapted with Helmholtz resonator for $m=8$ (top) and $m=1$ (bottom) together with $\angle \mathcal{R}_{m,d}$ of respective m (black dashed)

azimuthal interfaces of the annular gap. The parameters chosen for $m=1$ and $m=8$ are summarized in Table 3. The parameters l_1 and A_1 (respectively, for $m=8$ and $m=1$), for which a range is specified, are employed for the iterative adaption. For $m=1$ $\angle \mathcal{R}_{m,d}$ can be approximated very well for a wide frequency range. To achieve comparable accuracy for $m=8$, the necessary resonator volume would have to be even larger than the present one, which is not considered to be realistic. In general, the achievable accuracy crucially depends on the set of parameters that is realizable in the available test-bench.

The resonators are initially designed to exactly represent $\angle \mathcal{R}_{m,d}$ at the LC frequency of the respective lower mode order. This results in initial parameters $A_1 = 0.04$ for $m=1$ and $l_1 = 0.03$ m for $m=8$. With a convergence criterion $\Delta\nu < 0.5\%$ the adaption algorithm immediately converges with the initial resonator design for $m=8$. For $m=1$ convergence is reached after the first iteration with an updated $A_1 = 0.045$. The normalized LC frequencies and amplitude levels obtained with the adapted test-rig models are $\nu = 1.09$ and $a_{\text{LC}} = 0.67$ for $m=1$ and $\nu = 1.86$ and $a_{\text{LC}} = 0.48$ for $m=8$. Thus, the relative error compared to the downstream only coupled system is below 1% regarding LC frequency and below 5% regarding amplitude level. The relative error in LC frequency compared to the fully coupled configuration is below 5% (cf. Table 2). The normalized LC $|\hat{p}|$ obtained from the test-rig model adapted for $m=1$ is shown in Fig. 14 and agrees well with $|\hat{p}|$ of $m=1$ of the full configuration shown in Fig. 12. The outline of the adapted resonator is also visible in Fig. 14.

Critical Assessment of Adaption Strategy. Test-rig adaption by means of Helmholtz resonators seems much more practicable than using duct extensions. Due to the good initial agreement of $\angle \mathcal{R}_{\text{rig,d}}$ and $\angle \mathcal{R}_{m,d}$ over a wide frequency range, the number of iterations necessary to adapt the resonator is very small, iterations might even be avoided altogether. At the same time, it is possible to investigate entire operating windows with variable dominant frequencies without having to redesign the up-/downstream terminations for each operating condition.

The design parameters of the considered resonator appear to be much easier accessible than the length of duct extensions. It

Table 3 Parameters of Helmholtz resonators fitted for $m=1$ and $m=8$

	S_2/S_1	l_2 (m)	$A_1 = S_1/S_c$	l_1 (m)
$m=1$	20	1.2	0.04 – 0.05	0.43
$m=8$	20	1	0.4	0.02 – 0.04

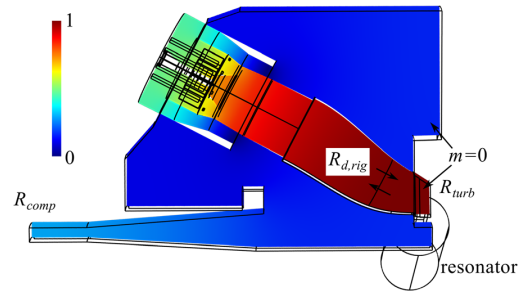


Fig. 14 Normalized $|\hat{p}|$ of dominant mode in single-can test-rig model adapted with Helmholtz resonator for $m=1$

should be possible to change the neck length and cross section remotely, without opening the high-pressure cell. Other design parameters not considered here, like the purge flow temperature, should be easily accessible, too.

The Helmholtz resonators will also introduce “spurious” modes that are not present in the full combustor. However, as their eigenfrequencies are related to the Helmholtz-mode of the resonator, they will be strongly damped and are expected to play a minor role.

A main drawback of this element type is that there is no generalized design guideline yet. The initial design and the iteration strategy have to be adjusted from case to case. Part of future work might be to develop an optimal iteration strategy that changes multiple parameters at once. Another drawback is the large size of the adapted resonators. In case the optimized initial resonator design does not fit in the high-pressure cell, the test-rig adaption will again rely more on the iterative algorithm. Furthermore, it is not yet clear how strong the damping of the resonator (which is designed to be small in the relevant frequency range) will affect the thermoacoustic properties of the test-rig.

Influence of Effects Neglected in Combustor Model

The strategy proposed in this work is only demonstrated with thermoacoustic models. The models used do not account for non-acoustic effects like heat transfer, entropy waves, and mean flow (in the Helmholtz solver). Furthermore, acoustic damping is only modeled in a simplistic way, i.e., by means of nonideal boundary conditions in the network model and by assuming uniformly distributed damping in the 3D configuration (which is equivalent to setting the LC growth-rate to $\sigma > 0$ [30]). Acoustic boundary conditions toward turbine and compressor are idealized.

These effects neglected in the present models will generally affect the thermoacoustic properties of the considered systems. However, it is important to note that in this study these effects are neglected in both the test-rig model and the model of the full configuration. In reality, those effects will in turn be present in both configurations. We do not aim to accurately model a real combustor configuration. Instead, we demonstrate the correspondence between adapted test-rig and full configuration.

To assess the importance of effects neglected in the thermoacoustic models of this study, we thus have to focus on the parts where test-rig and full configuration differ, i.e., the up-/downstream terminations of the can. In particular at the downstream termination, neglected effects related to entropy fluctuations, mean flow, and localized acoustic damping might have different influences on the thermoacoustic properties of test-rig and full engine.

In case duct extensions are used for test-rig adaption, the convective time delay relevant to entropy waves is drastically increased. Also, the Helmholtz resonator might be affected by entropy waves. However, due to the generally large convective

time delays in realistic combustor configurations, effects caused by entropy waves typically occur at very low frequencies and are thus well separable from purely acoustic effects considered in this study.

The elements installed upstream the first turbine stator vanes may change the nonacoustic flow properties, which in turn affects R_{turb} . For example, the cooling of the duct extension or the purge flow through the Helmholtz resonator may change mean flow temperature and velocity. However, the expected changes of the mean flow are very small and so is the influence on R_{turb} .

Acoustic damping localized at the annular gap in the full engine and at the Helmholtz resonator in the adapted test-rig is only taken into account in the simplistic way mentioned above. With the methods employed in this study, we cannot quantify the influence of this localized acoustic damping on the thermoacoustics of test-rig and full engine. This has to be addressed by more sophisticated numerical models and/or by experimental validation of the proposed strategy.

Conclusion

This study discusses the strategies to adapt single-can combustion test-rigs to reproduce the thermoacoustic properties of a full can-annular combustor. The coupling of the individual cans inside the can-annular combustor can be lumped into equivalent reflection coefficients $\mathcal{R}_{m,x}$ (with \dot{x}/d) up- and downstream of a single can. If correct values of $\mathcal{R}_{m,x}$ can be imposed at the up-/downstream terminations of a single-can test-rig, the rig mimics the thermoacoustic properties of the full engine.

We exploit the discrete rotational symmetry of typical can-annular combustors and employ Bloch-wave theory to obtain $\mathcal{R}_{m,x}$. These reflection coefficients induce a frequency dependent phase shift, which generally depends on the coupling interfaces, the azimuthal mode order m and the number of cans, but not on the thermoacoustic properties of the individual cans.

Two types of passive acoustic elements, namely duct extensions of constant cross section and Helmholtz resonators, are employed to match the phase shift induced by $\mathcal{R}_{m,x}$ for given design frequencies. For both computing $\mathcal{R}_{m,x}$ and designing the passive elements, an acoustic solver based on the Helmholtz equation is employed. We propose an iterative strategy, which ensures that the design frequency converges to the dominant frequency of the given mode order of the full system. Following that approach, the single-can test-rig can be used to investigate each azimuthal mode order m of the full can-annular combustor in terms of stability, limit cycle frequencies, and amplitude levels without a priori knowledge of relevant frequencies of the full engine.

The proposed strategy is applied to a network model of a generic can-annular combustor and to a 3D applied configuration modeled by the Helmholtz equation. For the latter, we show that the coupling via the compressor exit plenum is negligible for frequencies that are not in the immediate vicinity of plenum eigenfrequencies. The test-rig models adapted following the proposed strategy mimic the full engine with comparably good accuracy for both considered element types. However, using Helmholtz resonators seems much more practical. Their design parameters are easier to access remotely and the geometrical dimensions of the adapted resonators are more reasonable than those of the duct extension. Most importantly, the up-/downstream reflection coefficient tuned by a Helmholtz resonator matches $\mathcal{R}_{m,x}$ for a wide frequency range. Thus, fewer or no iterations are necessary to adapt the resonator and one single resonator design may be employed to investigate an entire operating window.

The proposed strategy has been demonstrated only with numerical models and has yet to be validated experimentally.

Acknowledgment

The authors gratefully acknowledge the Research Association for Combustion Engines (Forschungsvereinigung

Verbrennungskraftmaschinen e.V. FVV) for the financial support to Matthias Haeringer. This project has received funding from the European Union's Horizon 2020 research and innovation program *Annular Instabilities and Transient Phenomena in Gas Turbine Combustors* (ANNULIGH).

Funding Data

- Forschungsvereinigung Verbrennungskraftmaschinen (Project No. 6012700; Funder ID: 10.13039/501100003162).
- Horizon 2020 (Grant Agreement No. 765998; Funder ID: 10.13039/100010661).

Nomenclature

a	= amplitude level
A	= cross section area ratio
BBC	= Bloch boundary condition
c	= speed of sound
d	= characteristic length
f, g	= acoustic Riemann invariants
F	= flame response
FTF	= flame transfer function
He	= Helmholtz number
ITA	= intrinsic thermoacoustic
l	= length
\mathcal{L}	= extension length
LC	= limit cycle
m	= Bloch-wave number/azimuthal mode order
n	= iteration number
N	= number of cans
p	= acoustic pressure
Q	= heat release rate
r, ϕ, z	= radial, azimuthal, and axial coordinate
R	= reflection coefficient
\mathcal{R}	= equivalent reflection coefficient
s	= saturation factor
S	= cross section area
u	= acoustic velocity
x	= position vector
Z	= acoustic impedance
Δ	= relative difference
ν	= frequency
ρ	= density
σ	= modal growth rate
Ω	= angular frequency

References

- [1] Poinset, T., 2017, "Prediction and Control of Combustion Instabilities in Real Engines," *Proc. Combust. Inst.*, **36**(1), pp. 1–28.
- [2] Farisco, F., Panek, L., and Kok, J. B., 2017, "Thermo-Acoustic Cross-Talk Between Cans in a Can-Annular Combustor," *Int. J. Spray Combust. Dyn.*, **9**(4), pp. 452–469.
- [3] Farisco, F., Panek, L., Kok, J. B. W., Pent, J., and Rajaram, R., 2015, "Thermo-Acoustic Coupling in Can-Annular Combustors—A Numerical Investigation," *International Congress of Sound and Vibration (ICSV22)*, Florence, Italy, July 12–16, Vol. 23, p. 9.
- [4] Panek, L., Farisco, F., and Huth, M., 2017, "Thermo-Acoustic Characterization of Can-Can Interaction of a Can-Annular Combustion System Based on Unsteady CFD LES Simulation," *Proceedings of the First Global Power and Propulsion Forum*, Zurich, Switzerland, Paper No. GPPF-2017-81.
- [5] Bethke, S., Krebs, W., Flohr, P., and Prade, B., 2002, "Thermoacoustic Properties of Can Annular Combustors," *AIAA Paper No. 2002-2570*.
- [6] Kaufmann, P., Krebs, W., Valdes, R., and Wever, U., 2008, "3D Thermoacoustic Properties of Single Can and Multi Can Combustor Configurations," *ASME Paper No. GT2008-50755*.
- [7] Moon, K., Jegal, H., Gu, J., and Kim, K. T., 2019, "Combustion-Acoustic Interactions Through Cross-Talk Area Between Adjacent Model Gas Turbine Combustors," *Combust. Flame*, **202**, pp. 405–416.
- [8] Ghirardo, G., Moeck, J. P., and Bothien, M. R., 2020, "Effect of Noise and Nonlinearities on Thermoacoustics of Can-Annular Combustors," *ASME J. Eng. Gas Turbines Power*, **142**(4), p. 041005.

- [9] Jegal, H., Moon, K., Gu, J., Li, L. K., and Kim, K. T., 2019, "Mutual Synchronization of Two Lean-Premixed Gas Turbine Combustors: Phase Locking and Amplitude Death," *Combust. Flame*, **206**, pp. 424–437.
- [10] Gruschka, U., Janus, B., Meisl, J., Huth, M., and Wasif, S., 2008, "ULN System for the New SGT5-8000H Gas Turbine: Design and High Pressure Rig Test Results," *ASME Paper No. GT2008-51208*.
- [11] Mongia, H. C., Held, T. J., Hsiao, G. C., and Pandalai, R. P., 2003, "Challenges and Progress in Controlling Dynamics in Gas Turbine Combustors," *J. Propul. Power*, **19**(5), pp. 822–829.
- [12] Venkatesan, K., Cross, A., Yoon, C., Han, F., and Bethke, S., 2019, "Heavy Duty Gas Turbine Combustion Dynamics Study Using a Two-Can Combustion System," *ASME Paper No. GT2019-90327*.
- [13] Ghirardo, G., Di Giovine, C., Moeck, J. P., and Bothien, M. R., 2018, "Thermoacoustics of Can-Annular Combustors," *ASME J. Eng. Gas Turbines Power*, **141**(1), p. 011007.
- [14] Haeringer, M., and Polifke, W., 2019, "Time Domain Bloch Boundary Conditions for Efficient Simulation of Thermoacoustic Limit-Cycles in (Can-)Annular Combustors," *ASME J. Eng. Gas Turbines Power*, **141**(12), p. 121005.
- [15] Bothien, M. R., Moeck, J. P., and Oliver Paschereit, C., 2008, "Active Control of the Acoustic Boundary Conditions of Combustion Test Rigs," *J. Sound Vib.*, **318**(4–5), pp. 678–701.
- [16] Bothien, M. R., and Paschereit, C. O., 2010, "Tuning of the Acoustic Boundary Conditions of Combustion Test Rigs With Active Control: Extension to Actuators With Nonlinear Response," *ASME J. Eng. Gas Turbines Power*, **132**(9), p. 091503.
- [17] Niether, S., 2018, "Modification of a High Pressure Test Rig for Thermoacoustic Measurements," *Empirical dissertation*, TU Berlin, Berlin.
- [18] Bloch, F., 1929, "Über Die Quantenmechanik Der Elektronen in Kristallgittern," *Z. Phys.*, **52**(7–8), pp. 555–600.
- [19] Mensah, G. A., Campa, G., and Moeck, J. P., 2016, "Efficient Computation of Thermoacoustic Modes in Industrial Annular Combustion Chambers Based on Bloch-Wave Theory," *ASME J. Eng. Gas Turbines Power*, **138**(8), p. 081502.
- [20] Fournier, G. J. J., Haeringer, M., Silva, C. F., and Polifke, W., 2020, "Low-Order Modeling to Investigate Clusters of Intrinsic Thermoacoustic Modes in Annular Combustors," *ASME J. Eng. Gas Turbines Power*, Epub.
- [21] Marble, F. E., and Candel, S. M., 1977, "Acoustic Disturbance From Gas Non-Uniformities Convected Through a Nozzle," *J. Sound Vib.*, **55**(2), pp. 225–243.
- [22] Förner, K., and Polifke, W., 2017, "Nonlinear Aeroacoustic Identification of Helmholtz Resonators Based on a Local-Linear Neuro-Fuzzy Network Model," *J. Sound Vib.*, **407**, pp. 170–190.
- [23] Hoeijmakers, M., Kornilov, V., Lopez Arteaga, I., de Goey, P., and Nijmeijer, H., 2014, "Intrinsic Instability of Flame-Acoustic Coupling," *Combust. Flame*, **161**(11), pp. 2860–2867.
- [24] Bomberg, S., Emmert, T., and Polifke, W., 2015, "Thermal Versus Acoustic Response of Velocity Sensitive Premixed Flames," *Proc. Combust. Inst.*, **35**(3), pp. 3185–3192.
- [25] Albayrak, A., Steinbacher, T., Komarek, T., and Polifke, W., 2017, "Convective Scaling of Intrinsic Thermo-Acoustic Eigenfrequencies of a Premixed Swirl Combustor," *ASME J. Eng. Gas Turbines Power*, **140**(4), p. 041510.
- [26] Merk, M., Gaudron, R., Silva, C., Gatti, M., Mirat, C., Schuller, T., and Polifke, W., 2019, "Prediction of Combustion Noise of an Enclosed Flame by Simultaneous Identification of Noise Source and Flame Dynamics," *Proc. Combust. Inst.*, **37**(4), pp. 5263–5270.
- [27] Tay-Wo-Chong, L., Bomberg, S., Ulhaq, A., Komarek, T., and Polifke, W., 2012, "Comparative Validation Study on Identification of Premixed Flame Transfer Function," *ASME J. Eng. Gas Turbines Power*, **134**(2), p. 021502.
- [28] Mensah, G. A., and Moeck, J. P., 2017, "Limit Cycles of Spinning Thermoacoustic Modes in Annular Combustors: A Bloch-Wave and Adjoint-Perturbation Approach," *ASME Paper No. GT2017-64817*.
- [29] Emmert, T., Meindl, M., Jaensch, S., and Polifke, W., 2016, "Linear State Space Interconnect Modeling of Acoustic Systems," *Acta Acust. Acust.*, **102**(5), pp. 824–833.
- [30] Silva, C. F., Nicoud, F., Schuller, T., Durox, D., and Candel, S., 2013, "Combining a Helmholtz Solver With the Flame Describing Function to Assess Combustion Instability in a Premixed Swirled Combustor," *Combust. Flame*, **160**(9), pp. 1743–1754.
- [31] COMSOL, Inc., 2014, "COMSOL Multiphysics Reference Manual, Version 4.4," COMSOL, Burlington, MA.

Large eddy simulation of the dynamics of lean premixed flames using global reaction mechanisms calibrated for CH₄-H₂ fuel blends

Cite as: Phys. Fluids **34**, 095105 (2022); <https://doi.org/10.1063/5.0098898>

Submitted: 13 May 2022 • Accepted: 04 August 2022 • Accepted Manuscript Online: 06 August 2022 • Published Online: 07 September 2022

 Alex M. Garcia,  Sophie Le Bras,  Jens Prager, et al.

COLLECTIONS

Paper published as part of the special topic on [Development and Validation of Models for Turbulent Reacting Flows](#)



View Online



Export Citation



CrossMark

ARTICLES YOU MAY BE INTERESTED IN

[Assessing accuracy, reliability and efficiency of combustion models for prediction of flame dynamics with large eddy simulation](#)

Physics of Fluids (2022); <https://doi.org/10.1063/5.0098975>

[LES-based prediction of technically premixed flame dynamics and comparison with perfectly premixed mode](#)

Physics of Fluids **34**, 085125 (2022); <https://doi.org/10.1063/5.0098962>

[Large-eddy simulations of self-excited thermoacoustic instability in a premixed swirling combustor with an outlet nozzle](#)

Physics of Fluids **34**, 044112 (2022); <https://doi.org/10.1063/5.0087055>

Physics of Fluids

Submit Today!

Special Topic: Hydrogen Flame and Detonation Physics



Phys. Fluids **34**, 095105 (2022); <https://doi.org/10.1063/5.0098898>

34, 095105

© 2022 Author(s).

Large eddy simulation of the dynamics of lean premixed flames using global reaction mechanisms calibrated for CH₄-H₂ fuel blends

Cite as: Phys. Fluids **34**, 095105 (2022); doi: 10.1063/5.0098898

Submitted: 13 May 2022 · Accepted: 4 August 2022 ·

Published Online: 7 September 2022



Alex M. Garcia,^{1,2,a)}  Sophie Le Bras,²  Jens Prager,³  Matthias Häring,¹ and Wolfgang Polifke¹ 

AFFILIATIONS

¹Technical University of Munich, School of Engineering and Design, D-85747 Garching, Germany

²Siemens Digital Industries Software, 3001 Leuven, Belgium

³Siemens Digital Industries Software, 90411 Nuremberg, Germany

Note: This paper is part of the special topic, Development and Validation of Models for Turbulent Reacting Flows.

a) Author to whom correspondence should be addressed: alex.garcia@tum.de

ABSTRACT

The effects of hydrogen addition on the flame dynamics of a bluff-body stabilized methane–hydrogen turbulent flame are studied with large eddy simulation (LES). The LES is carried out with the thickened flame model and global kinetic mechanisms calibrated for the methane–hydrogen mixtures. Conjugate heat transfer is included in the LES to consider a proper wall temperature while the flame shape changes with hydrogen addition. A data-based calibration of the global mechanisms is done with a methodology based on reproducing the net species production rates computed with a detailed kinetic mechanism. An improvement in this methodology is proposed to increase its accuracy and reliability. The calibrated mechanisms accurately describe the variation of the laminar flame speed and the thermal flame thickness with hydrogen addition and equivalence ratio in a freely propagating premixed flame. The variations of the consumption speed and the thermal flame thickness with the strain rate in a symmetric counterflow premixed flame are also well predicted. The numerical simulations reproduce the transition from V- to M-shape flame induced by hydrogen addition, and the axial distribution of the heat release agrees with the experimental measurements of OH chemiluminescence. The unit impulse response and the flame transfer function are computed from the LES data using system identification (SysID). The flame transfer functions show a remarkable agreement with the experimental data, demonstrating that the LES-SysID approach using properly calibrated global mechanisms can predict the response of turbulent methane–hydrogen flames to velocity fluctuations. A comparison of the unit impulse response for the various hydrogen additions is presented, and the effect of hydrogen in the flow–flame interaction of the burner evaluated is discussed.

Published under an exclusive license by AIP Publishing. <https://doi.org/10.1063/5.0098898>

I. INTRODUCTION

The blending of hydrogen with conventional hydrocarbon gaseous fuels has received increased attention for its potential to contribute to CO₂ reduction.¹ The effect of hydrogen blending on the thermoacoustic response of a lean premixed combustion system depends on the combustion system and its operating conditions.^{2,3} Most experimental studies show that thermoacoustic instability may be induced by adding hydrogen to methane–air flames.^{4–6} Conversely, hydrogen addition may also suppress thermoacoustic instability.^{2,7} The effect of hydrogen on thermoacoustic instabilities is highly related to the impact of hydrogen on flame shape and length.^{5,6,8} Hydrogen addition reduces the flame length and may

trigger a transition from V- to M-shape in non-adiabatic turbulent flames,^{6,9–11} even if the unstretched laminar flame speed remains constant.^{9,10}

Numerical simulation can be used to determine the frequency response of turbulent flames to study their thermoacoustic behavior.^{12,13} However, numerical simulation of turbulent combustion of hydrogen blends is challenging due to the properties of hydrogen. Direct numerical simulations of hydrogen-enriched methane–air turbulent flames expose that considering accurate chemistry and diffusion are necessary to correctly describe the flame behavior.^{14,15} These requirements can be met by performing large eddy simulation using a combustion model based on transported chemistry, where the

transport and reaction of the species consider effects, such as heat loss, stretch, and preferential diffusion (non-unity Lewis number and differential diffusion).

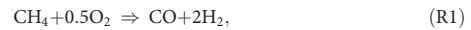
The accuracy of any model based on transported chemistry lies, among other aspects, on the chemical kinetic mechanism used to describe the reaction process. Detailed kinetic mechanisms (DM) are impractical in LES due to the large number of species and reaction steps to be considered. Alternatively, reduced versions of these mechanisms (the so-called skeletal mechanisms) can be used in LES,¹⁶ but still with a relatively high computational cost. Analytically reduced mechanism (ARM)^{17,18} allows reducing the computational cost by identifying the species that do not need to be transported with the flow. However, different from a skeletal mechanism, the production rate of the transported species in an ARM is not expressed as a combination of elementary reaction in the Arrhenius form but rather as a combination of complex analytical relations.¹⁷ This complexity, together with the number of transported species that could still be more than twenty, makes ARM not the first option for applications where lower computational cost is needed due to computational power limitations or a high number of conditions required to be simulated. In such cases, global mechanisms are an alternative that reduces the computational cost.

A global mechanism (GM) is an empirical scheme that only considers the major species involved in the combustion process, now described by a reduced number of global reaction steps. Global mechanisms are calibrated by adjusting the rate parameters in the Arrhenius equation of each reaction step to match some of the main physical properties of the flame, such as laminar flame speed, auto-ignition delay time, or species production rates, obtained from experiments or using a detailed kinetic mechanism for given operation conditions. The calibration is then formulated as an optimization problem, where various methods exist to find a proper set of parameters.^{19–22} The use of global mechanisms in LES has reproduced important aspects of turbulent combustion.^{23–26} Although some aspects of the turbulence-chemistry-diffusion interactions are lost if intermediate species are not considered,^{22,27} the study of global mechanism capabilities to describe different aspects of combustion is still an ongoing task.^{28–30}

Given that thermoacoustic instabilities represent an important challenge in the design of combustion systems, comprehensive validation of LES models should include the prediction of flame dynamics. Therefore, the present work further tests the capabilities of global mechanisms by considering methane–hydrogen mixtures with highly different chemical-diffusion properties and focusing on the prediction of flame dynamics. Both hydrogen combustion and thermoacoustic are two major research topics on present combustion. Global mechanisms are calibrated for various lean methane–hydrogen–air mixtures based on the methodology proposed by Polifke *et al.*¹⁹ This methodology is improved in the present work to make it more accurate. Canonical 1D laminar flames are used to validate the global mechanisms compared with detailed and skeletal kinetic mechanisms. Then, the global mechanisms are used in the LES of a turbulent premixed burner with various methane–hydrogen mixtures. The results are compared against experimental data. First, predictions of the mean flame shape and length are evaluated, and then, the flame dynamics are analyzed through the unit impulse response and the flame transfer functions computed using system identification.¹³

II. CALIBRATION OF THE GLOBAL MECHANISM

The global mechanism used in this study is a three-step mechanism with an initial step for methane (CH₄) breakdown into carbon monoxide (CO) and hydrogen (H₂) and two additional steps for CO and H₂ oxidation into carbon dioxide (CO₂) and water (H₂O), respectively, as follows:



This mechanism is selected due to its simplicity and the good results for wide ranges of hydrogen content. In this mechanism, only the step for CO oxidation is reversible. The rate parameters of this mechanism are calibrated based on the methodology proposed by Polifke *et al.*,¹⁹ which allows calibrating each reaction step independently based on a target reaction progress rate. The methodology is divided in two parts:

First, a detailed mechanism is used to compute a 1D freely propagating laminar flame at a reference operating condition: pressure, temperature, hydrogen fraction, and equivalence ratio. The profiles of temperature T , species mole concentration $[C_i]$, and species production rates $\dot{\omega}_i$ are obtained from this simulation. Then, the goal is to determine the “target reaction rates” of the GM so that the production rate of the species in the GM matches the ones obtained with the DM along the 1D flame.

For a given detailed kinetic mechanism, the production rate of each species is given by

$$\dot{\omega}_i = \sum_{j=1}^M \nu_{i,j} r_j, \quad \text{with} \quad \nu_{i,j} = \nu''_{i,j} - \nu'_{i,j}, \quad (1)$$

where r_j is the reaction progress rate of the reaction j and $\nu'_{i,j}$ and $\nu''_{i,j}$ are the stoichiometric coefficient of species i in reaction j as reactant and product, respectively. For the whole system of N species and M reaction steps, Eq. (1) can be expressed in matrix form as

$$\mathbf{P}_{[N,1]} = \mathcal{M}_{[N,M]} \mathbf{r}_{[M,1]}, \quad (2)$$

where \mathbf{p} and \mathbf{r} are the vectors of production rates and reaction progress rates, respectively, and \mathcal{M} is the matrix of stoichiometric coefficients. The same applies for the GM, yielding

$$\hat{\mathbf{p}}_{[\hat{N},1]} = \hat{\mathcal{M}}_{[\hat{N},\hat{M}]} \hat{\mathbf{r}}_{[\hat{M},1]}, \quad (3)$$

where $\hat{\cdot}$ refers to the global mechanism. Then, the right-hand side of Eq. (3) is equaled to the left-hand side of Eq. (2) ignoring the production rates of the species in the DM not included in the GM, such as

$$\mathbf{P}_{[\hat{N},1]} = \hat{\mathcal{M}}_{[\hat{N},\hat{M}]} \hat{\mathbf{r}}_{[\hat{M},1]}. \quad (4)$$

Note that \mathbf{p} corresponds to the production rates of the species obtained from the 1D flame simulation using the DM. Then, Eq. (4) can be solved to obtain the reaction progress rates $\hat{\mathbf{r}}$ of the GM that produce the same species production rates that the DM. This, however, is not possible in general, because the matrix $\hat{\mathcal{M}}$ is not square ($\hat{N} > \hat{M}$). Polifke *et al.*¹⁹ addressed this issue by selecting a number \hat{M} of species in the GM, denoted “principal species,” to build a square

matrix $\hat{\mathcal{M}}$. The drawback of this approach is that the overall solution depends on the non-unique choice of these principal species. To overcome this limitation, a different approach is proposed in this work. It consists of solving Eq. (4) using the method of least squares so that all species production rates are considered for the reaction progress rates of the GM. The vector \hat{r}^* of the target reaction rates is, thus, defined as

$$\hat{r}^* = (\hat{\mathcal{M}}^T \hat{\mathcal{M}})^{-1} \hat{\mathcal{M}}^T \mathbf{p}. \quad (5)$$

This enhancement improves the accuracy of the calibration methodology and makes it more physics-driven.

The target rates for an example of GM calibration are shown in Fig. 1(a) with solid lines. The GM with the reaction rates \hat{r}^* closely reproduces the species production rates obtained with the detailed mechanism, as shown in Fig. 1(b). Note that only a single 1D laminar flame calculation is used to obtain the target reaction rates for each calibration, and no more are needed from now on.

The second part of the calibration is to adjust the rate parameters of each reaction step to match the target reaction progress rates \hat{r}_j^* . The reaction progress rate of each reaction step j is given by

$$\hat{r}_j = k_j \underbrace{\prod_{i=1}^{\tilde{N}} [C_i]^{\nu_{ij}}}_{\text{non-reversible}} - \underbrace{\frac{k_j}{K_{eqj}} \prod_{i=1}^{\tilde{N}} [C_i]^{\nu_{ij}'}}_{\text{reversible}}, \quad (6)$$

with $k_j = A_j T^{b_j} \exp\left(-\frac{E_{aj}}{RT}\right)$,

where A is the pre-exponential factor, b is the temperature exponent, E_a is the activation energy, R is the gas constant, and K_{eq} is the equilibrium constant as a function of T .

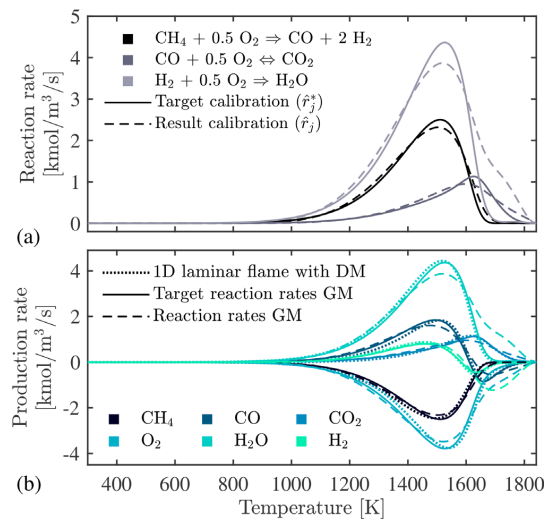


FIG. 1. Example of GM calibration, $X_{H_2} = 0$ and $\phi = 0.7$. (a) Reaction progress rates of GM. (b) Species production rates $\dot{\omega}_i$ from the 1D laminar flame, the GM target reaction rates, and the GM reaction rates after calibration.

The calibration of each reaction step is done using a genetic algorithm³¹ to minimize the cost-function¹⁹ relating \hat{r}_j and \hat{r}_j^* , where the values of T , $[C_i]$, and \hat{r}_j^* along the 1D laminar flame are the reference data and A_j , b_j , and E_{aj} are the parameters to be calibrated. For the nonreversible reaction steps, ν_{ij}' is also calibrated but restricted to be positive to increase the robustness of the GM.

The reaction progress rates obtained after the calibration are shown in Fig. 1(a) with dashed lines and agree reasonably well with the target reaction progress rates. The same applies to the species progress rates obtained with these reaction rates, as seen in Fig. 1(b). The higher difference is obtained for the H₂ oxidation step in the high-temperature region corresponding to the oxidation layer.

The reference operating condition for the calibration of the mechanism must agree with the operating condition in the LES, which, in the present work, corresponds to an atmospheric premixed CH₄-H₂-air flame with an equivalence ratio $\phi = 0.7$ and hydrogen fraction by volume of fuel $X_{H_2} = 0.0, 0.25, 0.57$, and 0.67 . The GM is calibrated for two conditions, $X_{H_2} = 0.0$ and $X_{H_2} = 0.57$, leading to two sets of parameters, referred to as 3S-00H and 3S-57H, respectively. The detailed kinetic mechanism UC San Diego,³² referred to as UC-SD, is used to compute the reference laminar flame for the calibration. The calibrated parameters for the three-step GM are presented in Table I.

III. VALIDATION OF GM IN 1D LAMINAR FLAMES

To verify that the GM can be used in the LES of the CH₄-H₂ flames, an evaluation of the global mechanism is done in the frame of 1D premixed laminar flames using the software Cantera.³³ Full multi-component mass diffusion and Soret effect are considered. The reference pressure and temperature of the reactants are equal to 101.3 kPa and 300 K, respectively. The global mechanism is compared with the detailed mechanism UC-SD used as a reference for the calibration and the well-known mechanism DRM19.³⁴ The latter as a reference for the accuracy of a skeletal mechanism.

A. Freely propagating premixed flame

The freely propagating premixed flame (free-flame) is used to compute the unstretched laminar flame speed S_L^0 and the unstretched thermal flame thickness defined by $\delta_T = (T_b - T_u) / \max(dT/dx)$, where subscripts u and b denote the unburnt and burnt sides of the flame, respectively. Figure 2 shows the results for $\phi = 0.7$ and

TABLE I. Global kinetic mechanism calibrated for CH₄-H₂-air. $\phi = 0.7$. 3S-00H → $X_{H_2} = 0.0$ and 3S-57H → $X_{H_2} = 0.57$. Units: cal, K, mol, cm³, s.

	A	b	E_a	ν_{CH_4}'	ν_{H_2}'	ν_{O_2}'
3S-00H						
(R1)	4.65×10^7	0.0	32 082	0.64	...	0.17
(R2)	1.51×10^9	0.33	24 334
(R3)	3.55×10^{13}	1.0	20 847	...	1.99	0.19
3S-57H						
(R1)	2.52×10^9	0.0	21 482	0.49	...	0.82
(R2)	1.68×10^9	0.0	15 694
(R3)	9.38×10^{11}	1.0	20 938	...	1.91	0.10

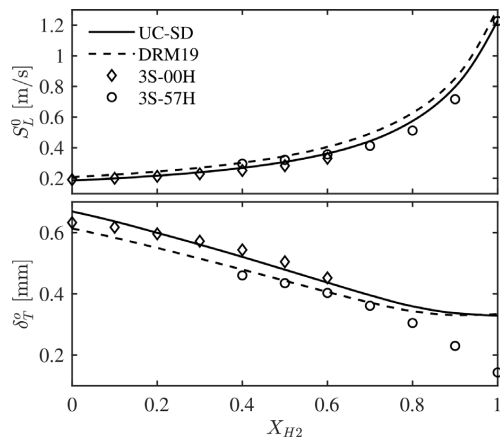


FIG. 2. Variation of unstretched laminar flame speed, S_L^0 , and thermal flame thickness, δ_T^0 , with hydrogen addition, X_{H_2} . $\phi = 0.7$.

CH_4 - H_2 mixtures ranging from pure methane to pure hydrogen. Both global mechanisms can predict the values of S_L^0 for a wide range of hydrogen concentrations although they are calibrated for only one specific condition. The GM calibrated for $X_{H_2} = 0.0$ shows better accuracy for low hydrogen additions, while the one calibrated for $X_{H_2} = 0.57$ has better accuracy for high hydrogen additions. In these ranges, the error in S_L^0 with the GM is less than 10% respect to the DM.

Regarding the flame thickness, the GM results are in good agreement with the detailed and skeletal mechanisms. However, the flame thickness is underpredicted for mixtures close to pure hydrogen where the GM effectively reduces to a one-step reaction.

Although only perfectly premixed flames are considered in this study, it is relevant to evaluate the accuracy of the global mechanism for various equivalence ratios ϕ since the latter may vary along the flame front due to preferential diffusion of hydrogen. Figure 3 shows the evolution of S_L^0 as a function of ϕ . The GM 3S-00H is used for the cases with $X_{H_2} = 0.0$ and 0.25, while the GM 3S-57H is used for $X_{H_2} = 0.57$ and 0.67, both will be referred to as GM hereafter. In all cases, the GM achieves a good accuracy for a wide range of equivalence

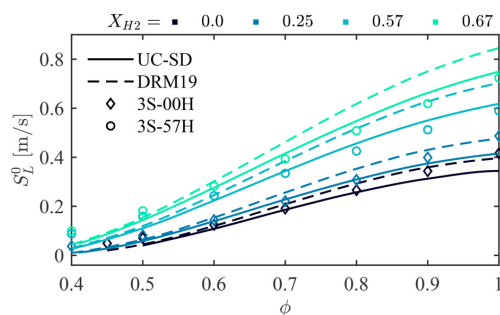


FIG. 3. Variation of unstretched laminar flame speed, S_L^0 , with equivalence ratio, ϕ .

ratios compared with the detailed and skeletal mechanisms. The DRM19 mechanism consistently over-predicts S_L^0 , especially for higher equivalence ratio and hydrogen addition. The accuracy of the GM diminishes when the equivalence ratio is far from the calibration condition. The GM could be tailored for rich and very lean mixtures by calibrating the mechanism for multiple equivalence ratios following the presented methodology and letting one of the Arrhenius coefficients vary with the equivalence ratio [e.g., $A_j = A_j(\phi)$], as can be found in the literature for CH_4 -air combustion.^{24,35}

In the present work, the global mechanism is calibrated for a reference temperature of 300 K. However, the GM is evaluated for various unburnt gas temperatures T_u ranging from 250 to 450 K, as it may be relevant to accurately represent flames with heat loss or gain. Figure 4 shows the evolution of S_L^0 as a function of T_u . For all cases, the effect of the unburnt gas temperature on the laminar flame speed is well captured by the GM. The major discrepancy with the detailed mechanism is presented at high T_u by the case with $X_{H_2} = 0.67$, a condition distinct from the one for the calibration. Nevertheless, the error is still in the magnitude range of the skeletal mechanism, showing the strength of the present calibration methodology.

A global mechanism calibrated with the present methodology can also resolve the internal structure of the laminar flame with reasonable accuracy, as shown in Fig. 5 for $X_{H_2} = 0.0$ and 0.57. The position across the free-flame x is normalized by the flame thickness δ_T^{REF} computed with the detailed mechanism, and the origin is located at $\max(dT/dx)$. The agreement between the GM and the DM is remarkable in the inner layer and around the peak value. The higher difference corresponds to the production rate of H_2 in agreement with the difference in the reaction rate of the H_2 oxidation step shown in Fig. 1. This difference may be related to the fact that in the GM chosen, all the hydrogen in the methane molecule has to pass through H_2 to oxidize to H_2O .

Nevertheless, the species mole fractions and temperature are also in good agreement with the DM, as shown in Fig. 6. The peak concentration of the intermediate species CO and H_2 in the case of pure methane is well predicted by the GM. The GM reaches the equilibrium condition sooner, which is inherent to the absence of more intermediate species.

B. Symmetric counterflow premixed flame

The transition from V- to M-shape flame induced by hydrogen addition has been related to the different response of the flame to stretch.^{5,10} Therefore, the symmetric counterflow premixed flame

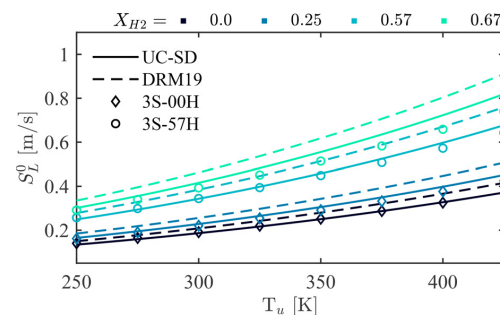


FIG. 4. Variation of unstretched laminar flame speed, S_L^0 , with unburnt gas temperature, T_u .

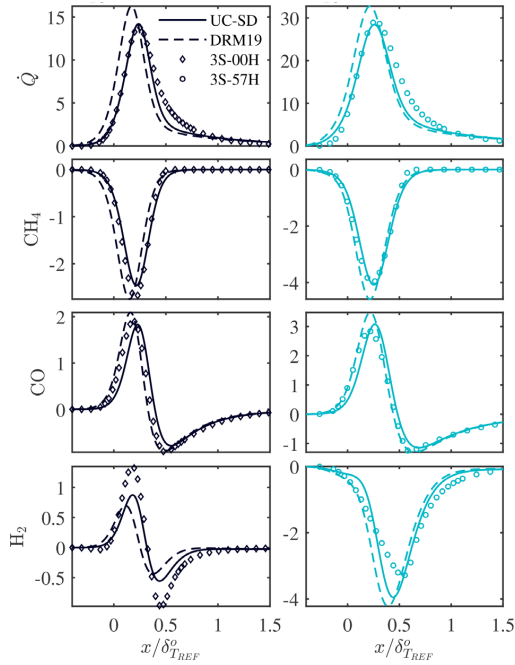


FIG. 5. Profiles of heat release rate, \dot{Q} , ($\times 10^8$ W/m³) and production rate, $\dot{\omega}_i$, of CH₄, CO, and H₂ (kmol/m³/s) across the freely propagating laminar flame, for cases with $X_{H_2} = 0.0$ (left) and 0.57 (right).

(twin-flame) is used to evaluate the capability of the GM to describe the response of the laminar flame to positive strain. Figure 7 shows the variation of the consumption speed with the increase in the strain rate, which is expressed in a dimensionless form using the Karlovitz number Ka . The results for $X_{H_2} = 0.57$ are not presented for the sake of conciseness, but the trend is the same. The consumption speed for the multicomponent fuel is defined in the present work as

$$S_c \equiv \frac{\sum_{i=1}^{N_f} \eta_i \int_{-\infty}^{\infty} \dot{\omega}_i dx}{\rho_u \sum_{i=1}^{N_f} \eta_i (Y_{i,b} - Y_{i,u})}, \quad (7)$$

where ρ is the density, Y_i is the mass fraction of the species i , $\eta_i = Y_{i,u}/Y_{f,u}$, and f denotes the fuel mixture. The GM can describe the increase in the flame speed with a strain rate produced by the effect of preferential diffusion. This result is especially relevant for hydrogen-enriched turbulent flames where the stretch induced by the turbulence produces local changes of the flame speed.^{14,15} The maximum S_c predicted by the GM in the twin-flame differs from the DM by less than 10%.

As shown in Fig. 8, the decrease in the flame thickness due to positive strain is also well described by the GM up to the maximum strain rate supported by the laminar twin-flame, known as the

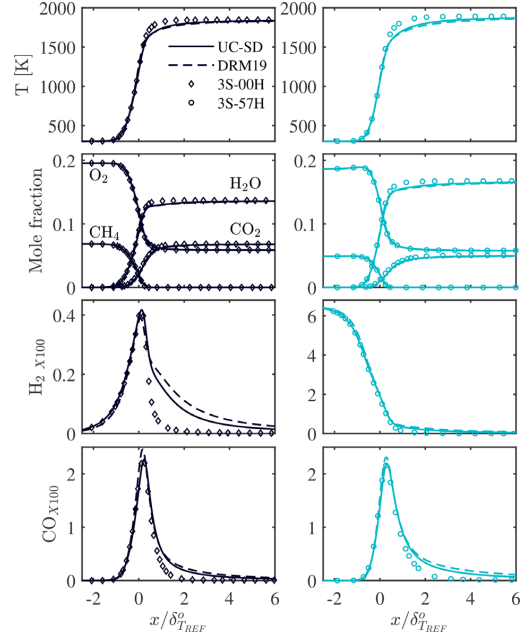


FIG. 6. Profiles of temperature and mole fractions of CH₄, O₂, H₂O, CO₂, CO, and H₂ across the freely propagating laminar flame, for cases with $X_{H_2} = 0.0$ (left) and 0.57 (right).

extinction strain rate. The values of the extinction strain rate computed with the GM are consistent with those obtained with the detailed and skeletal mechanisms. The skeletal mechanism consistently under-predicts the extinction strain rate in 17% compared to the DM, while the GM is in better agreement with the DM.

Another effect of preferential diffusion is the appearance of thermo-diffusive instabilities exhibited as cellular instabilities in the flame front. Such thermo-diffusive instabilities increase the flame

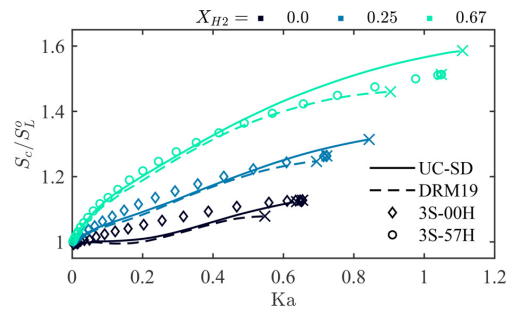


FIG. 7. Variation of consumption speed, S_c , with a strain rate. Extinction strain rate shown by the marker (x).

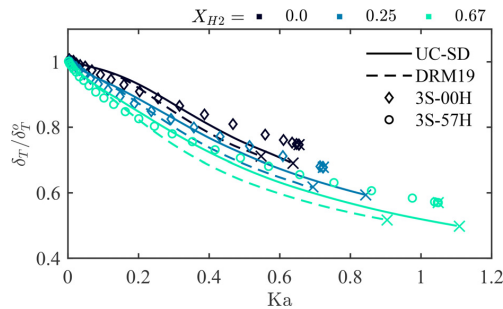


FIG. 8. Variation of thermal flame thickness, δ_T , with a strain rate. Extinction strain rate shown by the marker (x).

surface area, increasing the flame propagation speed even in turbulent flames.³⁶ An evaluation of the capability of the GM to capture thermo-diffusive instabilities is presented in the Appendix. However, it is not clear if this type of instability plays an important role in flame dynamics.

IV. SIMULATION OF TURBULENT CH₄-H₂ FLAME

The burner considered in the LES is a bluff body stabilized turbulent flame confined in a cylindrical combustion chamber open to the atmosphere, investigated extensively at NTNU.^{6,8,37} The numerical domain is shown in Fig. 9. The solid regions corresponding to the combustion chamber, the burner body, and the bluff body are

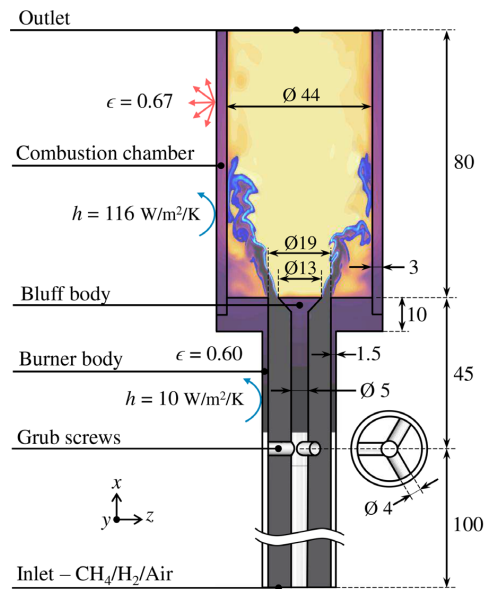


FIG. 9. Schematic of the computational domain used in the LES. The white solid regions are not considered for the CHT. Dimensions are given in mm.

included in the LES through conjugate heat transfer formulation (CHT). The combustion chamber is made of quartz, and all the other parts are made of SAE-316L stainless steel. The thermal power is fixed at 7 kW, and four hydrogen concentrations are evaluated, $X_{H_2} = 0.0, 0.25, 0.57,$ and 0.67 . Fuel and air are perfectly premixed, with a fixed equivalence ratio of $\phi = 0.7$. The Reynolds number and Karlovitz number for all flames at the dump plane are around 38 300 and 5, respectively.

A. Numerical model

The computational domain is discretized with a structured mesh of 7.82 M hexahedral cells, of which 0.34 M correspond to the solid regions. The mean cell size is 0.16 mm in the flame area and 0.25 mm in the space between the grub screws and the dump plane. The mesh is refined near the walls yielding a $y^+ \approx 1$. The software Simcenter STAR-CCM+³⁸ is used to solve the filtered incompressible multi-species Navier–Stokes equations. The sub-grid stress tensor is modeled by the WALE³⁹ model without using a wall function, and the PISO algorithm⁴⁰ is used for the pressure–velocity coupling.

Turbulence–flame interaction is considered with the thickened flame model (TFM). The flame thickness is discretized by at least five grid points, and the power law is used to model the sub-grid flame interactions and wrinkling.⁴¹ The reference flame thickness is computed as a function of T and S_L^0 . As for the 1D flames, GM 3S-00H is used for the cases with $X_{H_2} = 0.0$ and 0.25 , while GM 3S-57H is used for $X_{H_2} = 0.57$ and 0.67 . The dynamic viscosity is computed as a function of the temperature using the power-law, with the coefficients for air. The mixture thermal conductivity and the mass diffusion coefficient of each species are computed from the viscosity using constant Prandtl and species Schmidt numbers, respectively. These numbers are obtained from the mean values across the 1D laminar free-flame for each fuel mixture. Turbulent Prandtl and Schmidt numbers are set to 0.7. A second-order bounded-central difference scheme⁴² is used for the convective term of the momentum equation, while the second-order upwind scheme is used for enthalpy and mass species equations. The backward time difference scheme is used with a $2 \mu s$ time step to achieve a CFL below 0.9.

The energy conservation equation is solved in the solid regions of the burner to consider a proper wall temperature while the flame shape is changing with hydrogen addition. Wall heat loss by radiation and convection are considered with constant emissivity ϵ , and convective heat transfer coefficient h reported in Fig. 9 for the combustion chamber and the burner body. The period of transient heating of the solid regions is computed using the multi-timescale workflow⁴³ to reduce computational time. The LES statistics are calculated during six flow-through times (0.12 s) after the solid region has reached the steady-state thermal condition.

B. Flame shape

The flame shape is one of the main aspects to predict with the LES, since it plays an important role in the thermoacoustic instabilities.^{5,6} Figure 10 shows a comparison of the flame shape obtained from the experiments and the LES. The heat release rate \dot{Q} is used to characterize the flame shape in the LES, while the OH* chemiluminescence is used in the experiments.^{6,8} The LES with the global mechanism is able to reproduce the change of the flame shape with hydrogen addition. For pure methane, the flame is attached to the inner shear

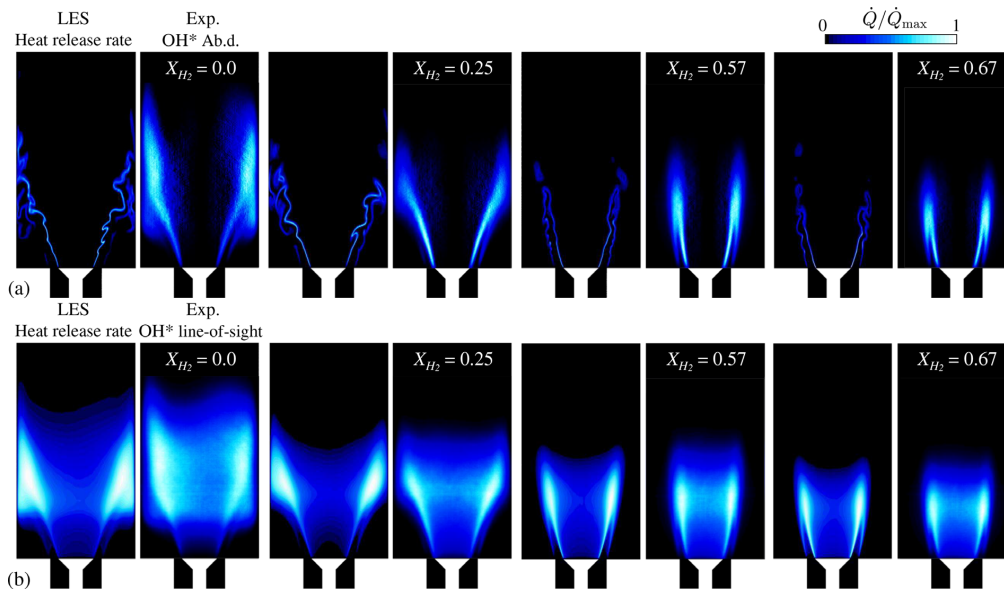


FIG. 10. Contours of heat release rate from LES and experimental OH* chemiluminescence. (a) Instantaneous \dot{Q} and Abel deconvolution of mean OH*. (b) Line-of-sight of mean \dot{Q} and line-of-sight of mean OH*.

layer with large portions of the flame brush in contact with the combustion chamber wall. The flame becomes more compact with hydrogen addition, and a transition from V to M shape occurs for X_{H_2} between 0.25 and 0.57.

A comparison of the flame length using the stream-wise profiles of heat release integrated along the transverse plane, $\bar{q}_x(x) = \iint \dot{Q}(x, y, z) dy dz$, is presented in Fig. 11. The OH* data are normalized such that the volume integral is equal to 7 kW. The general distribution of \bar{q}_x and the location of its maximum value are well reproduced by the LES for all methane-hydrogen mixtures. For the case of pure methane, the flame length is under-predicted by the LES. Good agreement is obtained near the dump plane so that the difference may be associated with the flame-wall interaction. A LES including radiation heat transfer with a gray gas model does not significantly improve the flame length discrepancy for pure methane, neither does a higher convective heat transfer coefficient outside of the combustion chamber. (These results are not presented for conciseness.) The difference is then attributed to a limitation of the global mechanism to describe direct wall-flame interaction. The lack of intermediate species may result in a flame less sensitive to direct contact with the wall. This is not a problem for cases where considerable portions of the flame are not attached to the chamber walls.

C. Flame dynamics

The dynamic response of a flame to upstream flow perturbations can be represented by the unit impulse response in the time domain and the flame transfer function (FTF) in the frequency domain, which are important to predict the acoustic response of a combustion system.

Computing the flame dynamics with LES is challenging for the combustion model, so it constitutes an excellent way to examine the performance of the LES based on global mechanisms. The flame dynamics are obtained from the LES data using a method based on system identification (LES-SysID).¹³ For this purpose, the flow is forced with a Daubechies wavelet-based broadband signal¹⁴ superimposed on the mean flow at the inlet. The length of the signal is 0.2 s, and its amplitude is 4% of the mean value. This amplitude is the same one used in the experiments to ensure a linear response of the flame. A reference velocity u_r is measured at the dump plane as the area-weighted average axial velocity. At the same time, the heat release rate \dot{Q} is integrated over the volume of the computational domain. The unit impulse response is determined by the optimal linear least squares estimation between the auto-correlation matrix and the cross correlation vector of the time series data u_r and \dot{Q} . Then, the FTF is obtained by a z-transformation of the unit impulse response.

It is important to note that the flame dynamics in thermoacoustics instabilities follow different mechanisms of the acoustics-flame interaction. In the case of perfectly premixed low Mach deflagration flames, heat release fluctuations induced by flow disturbances, such as reactant mass flow fluctuations and hydrodynamic fluctuations, are expected to be the most important since the effect of pressure, temperature, and strain rate perturbations directly accompanying the acoustic waves are pretty weak.^{45,46} The latter justifies the use of incompressible LES to characterize the flame dynamics of these types of flames. In the context of LES-SysID, the assumption of an incompressible flow not only decreases the computational cost of the LES but also breaks the coupling from the flame back to acoustics,

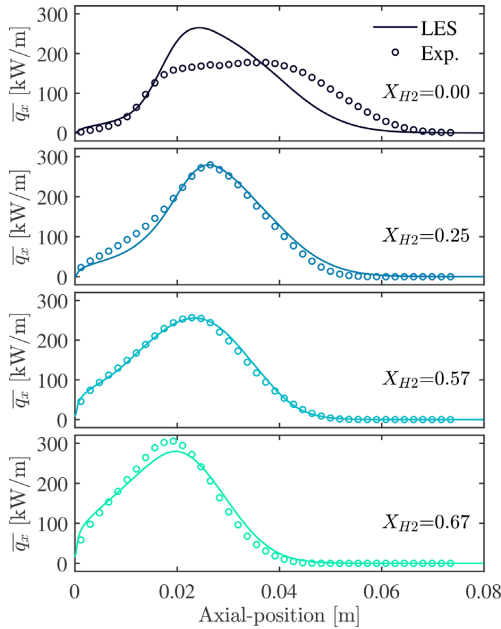


FIG. 11. Stream-wise heat release distribution, \bar{q}_x , for various hydrogen additions. The origin is located at the dump plane.

increasing the signal-to-noise ratio of the time series data u_r , and \dot{Q} since self-excited acoustics cannot occur.

The respective unit impulse response of the turbulent flames for the four hydrogen additions is presented in Fig. 12. All cases present a similar initial response to a sudden increase in axial velocity, which produces an increase in the mixture supplied to the flame. The extra mixture is transported through the flame as it burns and perturbs the flame surface area. This results in an overall increase in heat release, with a temporal distribution similar to the spatial distribution of heat release in the axial direction,⁴⁷ seen in Fig. 11. The increase in the heat release is followed by a decrease while the flame returns to its initial state. In the cases of high hydrogen addition, the heat release increases again when the vortices produced by the grub screws reach the flame. These vortex waves increase the flame surface area and then the heat release rate. Since the vortices do not supply more mixture to the flame, the increase in heat release is followed by a similar decrease due to mass and energy conservation.

The described flow-flame interaction is characterized by two different time-delays.⁵ The first time-delay from the dump plane to the mean flame length is

$$\tau_1 \approx H/u_p, \quad (8)$$

where u_p is the bulk velocity at the dump plane and H is the mean flame length defined by $H = \int x \bar{q}_x dx / \int \bar{q}_x dx$. The second time-delay from the screws to the mean flame length is

$$\tau_2 \approx L/u_b + H/u_p, \quad (9)$$

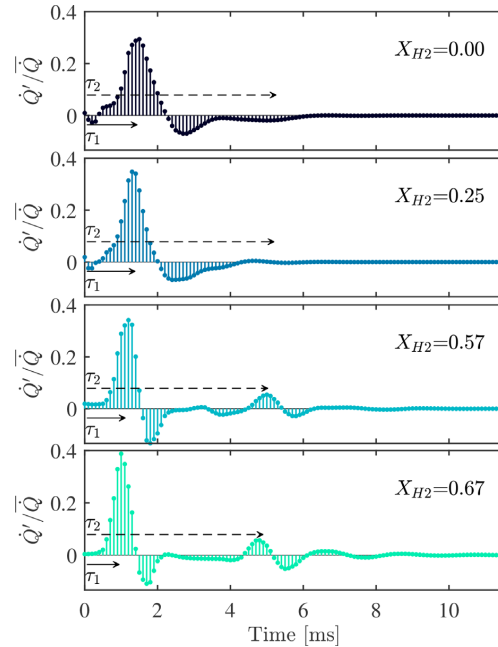


FIG. 12. Unit impulse responses for various hydrogen additions. τ_1 : time-delay from dump plane to mean flame length (\rightarrow). τ_2 : time-delay from screws to mean flame length (\dashrightarrow).

where u_b is the bulk velocity after the screws and L is the distance from the screws to the dump plane. Both time-delays are retrieved by the LES-SysID.

In the cases of low hydrogen addition, the effect of the vortices produced by the grub screws on the flame response is not significant. This happens when the frequency of the vortex waves is close or higher than the cutoff frequency of the flame response.³⁷ The cutoff frequency $f_c \approx 1/\tau_1$ defines the band of frequencies in which the flame is more sensitive to upstream flow fluctuations and acts as an amplifier.

For the cases with low hydrogen addition, $X_{H_2} = 0.0$ and 0.25 , the unit impulse response presents an initial decrease in the heat release before its main increase. This behavior may be related to a downstream movement of the leading edge of the flame closer to the dump plane produced by the higher axial velocity, momentarily decreasing the flame surface area. This initial decrease in the heat release does not happen for cases with high hydrogen addition, $X_{H_2} = 0.57$ and 0.67 , due to the higher flame speed that produces a more robust flame close to the dump plane, as shown in Figs. 10 and 11.

The flame transfer function is expressed as the ratio of the total heat release rate fluctuations to the fluctuations of the reference velocity in the frequency domain as

$$\text{FTF}(f) = \frac{\dot{Q}'(f)/\bar{Q}}{u_r'(f)/\bar{u}_r}. \quad (10)$$

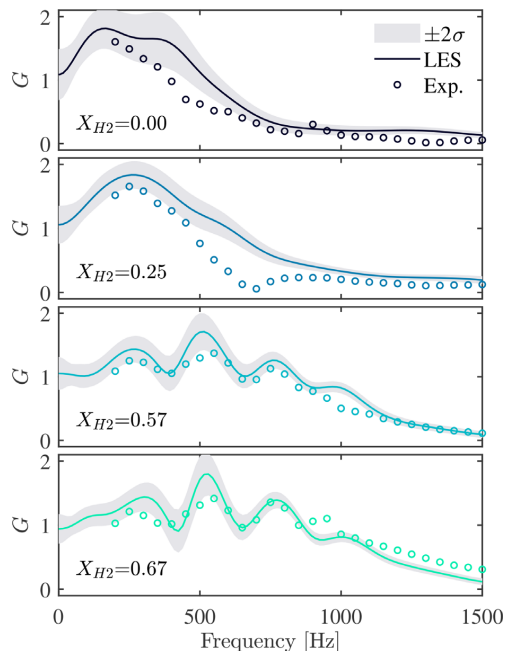


FIG. 13. Gain of the FTF for various hydrogen additions. Confidence interval from SysID (shaded area).

Figures 13 and 14 show the flame frequency response as $\text{FTF}(f) = G(f) \exp(i\theta(f))$, where G is the gain and θ is the phase. The confidence interval of the SysID is shown with two standard deviations σ , which represents the aleatory uncertainty caused by the resolved turbulent structures in the LES. The experimental FTF is measured at each frequency value as described by *Æsøy et al.*^{6,8} A remarkable agreement between the experiments and the LES-SysID is obtained, for both gain and phase, in particular for high hydrogen content. The latter is particularly important for thermoacoustic instability because it gives the time-delay, $\tau(f) = \theta/(2\pi f)$, between the upstream flow perturbations and the heat release fluctuations, where the average $\tau(f)$ is close to τ_1 . The LES-SysID method is able to reproduce well the modulation in the gain of the FTF, produced by the interaction between the flame and the vortex shedding from the grub screws.³⁷ The addition of hydrogen produces an increase in the cutoff frequency and a decrease in the time-delay. Both effects are related to the flame length and are captured very well by the LES using the global mechanism. In the case of pure methane, the time-delay is under-predicted in agreement with the shorter flame in the LES compared with the experiments.

The result of the FTF shows that the LES-SysID approach can predict the dynamics of turbulent $\text{CH}_4\text{-H}_2$ flames considering the different mechanisms of flow-flame interaction.

V. CONCLUSIONS

This work presents the large eddy simulation of a bluff-body stabilized turbulent flame with various methane-hydrogen mixtures

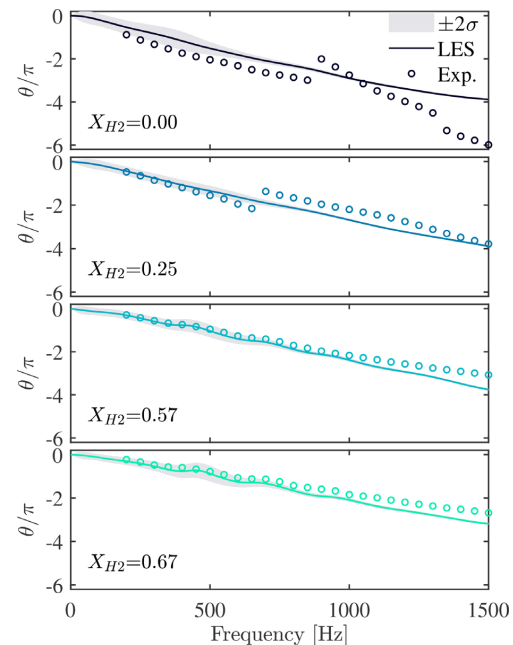


FIG. 14. Phase of the FTF for various hydrogen additions. Confidence interval from SysID (shaded area).

using calibrated global mechanisms. A three-step mechanism with a H_2 oxidation step was calibrated for various methane-hydrogen mixtures. A calibration methodology based on the computation of a single 1D laminar flame per calibration has been selected for its robustness and its time-efficiency. The calibration methodology has been enhanced in this work in order to make it more accurate and less user dependent. The calibrated global mechanisms accurately describe global flame parameters, such as the variation of the laminar flame speed and the thermal flame thickness with hydrogen addition and equivalence ratio, but also the internal flame structure and the response to positive strain rate.

Good prediction of the flame shape is obtained with the LES using thickened flame mode with GM, describing the transition from V- to M-shape flame induced by hydrogen addition. The axial distribution of the heat release and the flame length from the LES compares well with the experimental data. For the case of pure methane, where large portions of the flame are in contact with the walls, the flame length is under-predicted. Future work may focus on the effect of the GM and the reference conditions used for its calibration on the flame-wall interaction and the impact of the near-wall turbulence modeling.

The flame transfer functions computed from the LES data using system identification are in good agreement with the experiments. The effects of hydrogen addition on the flame frequency response are captured by the LES with the GM, including the modulation of the gain and phase produced by the flow-flame interaction. These results show

the potential of global kinetic mechanisms and the calibration methodology in large-eddy simulation of hydrogen blends for thermoacoustics applications. The same methodology can be applied for various fuel mixtures and operating conditions.

ACKNOWLEDGMENTS

This work was part of the Marie Skłodowska–Curie Innovative Training Network Pollution Know-How and Abatement (POLKA). We gratefully acknowledge the financial support from the European Union's Horizon 2020 research and innovation programme under the Marie Skłodowska–Curie Grant Agreement No. 813367. The authors would also like to thank Eirik Æsøy and co-workers at NTNU for the valuable information and experimental data provided.

AUTHOR DECLARATIONS

Conflict of Interest

The authors have no conflicts to disclose.

Author Contributions

Alex Mauricio García Vergara: Conceptualization (equal); Data curation (lead); Formal analysis (lead); Investigation (lead); Methodology (equal); Writing – original draft (lead); Writing – review and editing (lead). **Sophie Le Bras:** Conceptualization (equal); Formal analysis (equal); Funding acquisition (equal); Methodology (equal); Project administration (equal); Resources (equal); Supervision (equal); Writing – original draft (supporting); Writing – review and editing (equal). **Jens Prager:** Conceptualization (equal); Investigation (supporting); Methodology (equal); Software (equal); Writing – review and editing (supporting). **Matthias Häringer:** Investigation (equal); Methodology (equal); Writing – original draft (equal). **Wolfgang Polifke:** Conceptualization (equal); Formal analysis (equal); Funding acquisition (equal); Methodology (equal); Project administration (equal); Resources (equal); Supervision (equal); Writing – original draft (equal); Writing – review and editing (equal).

DATA AVAILABILITY

The data that support the findings of this study are available from the corresponding author upon reasonable request.

APPENDIX: THERMO-DIFFUSIVE INSTABILITIES WITH GM

The cellular instabilities in the flame front induced by thermo-diffusive instabilities are more easily observed in the absence of turbulence. Therefore, to evaluate the capability of the GM to capture thermo-diffusive instabilities, the simulation of the two-dimensional (2D) version of the symmetric counterflow premixed flame is performed. This configuration consists of two opposing streams of reactants, creating a stagnation point flow with a laminar flame located at each side of the stagnation point. The numerical domain with a symmetric boundary condition at the stagnation point is shown in Fig. 15. The domain has a width of 50 mm and a distance between the flow inlet and the stagnation point of 30 mm.

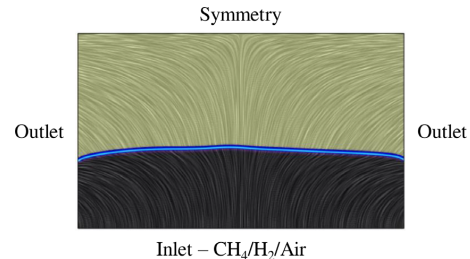


FIG. 15. Schematic of the computational domain used in the simulation of the 2D symmetric counterflow premixed flame.

It is discretized with a structured mesh of 0.11 M quadrilateral cells with a cell size of 0.1 mm in the flame area. The laminar flame is located where the flame speed balances the local axial velocity; thus, an inlet velocity of 2.5 times the unstretched laminar flame speed is specified to get a similar flame location for the various hydrogen fuel additions. The numerical setup is the same as the one used for the LES of the turbulent flame but with no turbulent model. The results obtained from the global mechanisms are compared with those obtained from the skeletal mechanism.

The results of the 2D simulation are presented in Fig. 16 using the heat release rate to characterize the flame shape. For high

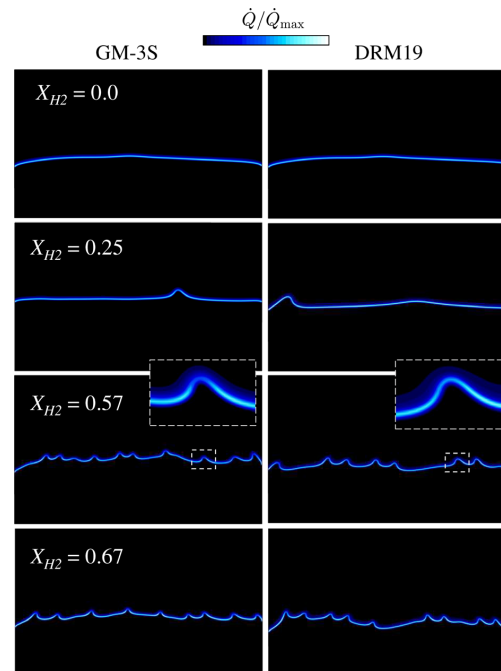


FIG. 16. Contours of instantaneous heat release rate.

hydrogen content, the flame front exhibits cellular structures. These cellular structures are induced mainly by a combination of thermo-diffusive and hydrodynamic instabilities. While the hydrogen addition increases, the flame becomes more thermo-diffusive unstable, increasing the number of cellular structures per unit of area. The heat release rate decreases in concavely curved flame regions due to preferential diffusion. In contrast, the opposite occurs in convexly curved regions but to a lesser extent due to the lower curvature. The GM seems to overpredict this effect. It may be due to the lack of intermediate species, particularly the radical H, which diffuses tangential to the flame front,⁴⁸ slightly attenuating the impact of the hydrogen differential diffusion. Nevertheless, the GM is able to capture the thermo-diffusive instabilities with good accuracy compared with the skeletal mechanism.

REFERENCES

- ¹K.-K. Lam, P. Geipel, and J. Larfeldt, "Hydrogen enriched combustion testing of siemens Industrial SGT-400 at atmospheric conditions," *J. Eng. Gas Turbines Power* **137**, 021502 (2015).
- ²G. Oztarlik, L. Selle, T. Poinso, and T. Schuller, "Suppression of instabilities of swirled premixed flames with minimal secondary hydrogen injection," *Combust. Flame* **214**, 266–276 (2020).
- ³I. Chtere, and I. Boxx, "Effect of hydrogen enrichment on the dynamics of a lean technically premixed elevated pressure flame," *Combust. Flame* **225**, 149–159 (2021).
- ⁴J. Zhang and A. Ratner, "Experimental study on the excitation of thermoacoustic instability of hydrogen-methane/air premixed flames under atmospheric and elevated pressure conditions," *Int. J. Hydrogen Energy* **44**, 21324–21335 (2019).
- ⁵S. Shanbhogue, Y. Sanusi, S. Taamallah, M. Habib, E. Mokheimer, and A. Ghoniem, "Flame macrostructures, combustion instability and extinction strain scaling in swirl-stabilized premixed CH₄/H₂ combustion," *Combust. Flame* **163**, 494–507 (2016).
- ⁶J. G. Aguilar, E. Åsøy, and J. R. Dawson, "Predicting the influence of hydrogen in combustion instabilities," in *Symposium on Thermoacoustics in Combustion: Industry Meets Academia (SoTIC 2021)* (Munich, Germany, 2021), p. 9.
- ⁷A. Ghani and W. Polifke, "Control of intrinsic thermoacoustic instabilities using hydrogen fuel," *Proc. Comb. Inst.* **38**, 6077–6084 (2021).
- ⁸E. Åsøy, J. G. Aguilar, S. Wiseman, M. R. Bothien, N. A. Worth, and J. R. Dawson, "Scaling and prediction of transfer functions in lean premixed H₂/CH₄ flames," *Combust. Flame* **215**, 269–282 (2020).
- ⁹T. F. Guiberti, D. Durox, L. Zimmer, and T. Schuller, "Analysis of topology transitions of swirl flames interacting with the combustor side wall," *Combust. Flame* **162**, 4342–4357 (2015).
- ¹⁰S. Taamallah, S. J. Shanbhogue, and A. F. Ghoniem, "Turbulent flame stabilization modes in premixed swirl combustion: Physical mechanism and Karlovitz number-based criterion," *Combust. Flame* **166**, 19–33 (2016).
- ¹¹R. Mao, J. Wang, W. Zhang, Z. An, W. Lin, M. Zhang, and Z. Huang, "Effect of high hydrogen enrichment on the outer-shear-layer flame of confined lean premixed CH₄/H₂/air swirl flames," *Int. J. Hydrogen Energy* **46**, 17969–17981 (2021).
- ¹²A. Gentemann, C. Hirsch, K. Kunze, F. Kiesewetter, T. Sattelmayer, and W. Polifke, "Validation of flame transfer function reconstruction for perfectly premixed swirl flames," in *ASME Turbo Expo 2004: Power for Land, Sea, and Air* (ASME, Vienna, Austria, 2004).
- ¹³L. Tay-Wo-Chong, T. Komarek, R. Kaess, S. Föller, and W. Polifke, "Identification of flame transfer functions from LES of a premixed swirl burner," in *Proceedings of ASME Turbo Expo 2010* (ASME, Glasgow, UK, 2010), pp. 623–635.
- ¹⁴E. R. Hawkes and J. H. Chen, "Direct numerical simulation of hydrogen-enriched lean premixed methane-air flames," *Combust. Flame* **138**, 242–258 (2004).
- ¹⁵M. S. Day, X. Gao, and J. B. Bell, "Properties of lean turbulent methane-air flames with significant hydrogen addition," *Proc. Combust. Inst.* **33**, 1601–1608 (2011).
- ¹⁶N. Zettervall, K. Nordin-Bates, E. Nilsson, and C. Fureby, "Large eddy simulation of a premixed bluff body stabilized flame using global and skeletal reaction mechanisms," *Combust. Flame* **179**, 1–22 (2017).
- ¹⁷A. Felden, P. Pepiot, L. Esclapez, E. Riber, and B. Cuenot, "Including analytically reduced chemistry (ARC) in CFD applications," *Acta Astronaut.* **158**, 444–459 (2019).
- ¹⁸D. Laera, P. Agostinelli, L. Selle, Q. Cazères, G. Oztarlik, T. Schuller, L. Gicquel, and T. Poinso, "Stabilization mechanisms of CH₄ premixed swirled flame enriched with a non-premixed hydrogen injection," *Proc. Combust. Inst.* **38**, 6355–6363 (2021).
- ¹⁹W. Polifke, W. Geng, and K. Döbbling, "Optimization of rate coefficients for simplified reaction mechanisms with genetic algorithms," *Combust. Flame* **113**, 119–134 (1998).
- ²⁰A. Abou-Taouk, B. Farcy, P. Domingo, L. Vervisch, S. Sadasivuni, and L.-E. Eriksson, "Optimized reduced chemistry and molecular transport for large eddy simulation of partially premixed combustion in a gas turbine," *Combust. Sci. Technol.* **188**, 21–39 (2016).
- ²¹J. Si, G. Wang, X. Liu, M. Wu, and J. Mi, "A new global mechanism for MILD combustion using artificial-neural-network-based optimization," *Energy Fuels* **35**, 14941–14953 (2021).
- ²²J. Armengol, O. L. Maitre, and R. Vicquelin, "Bayesian calibration of a methane-air global scheme and uncertainty propagation to flame-vortex interactions," *Combust. Flame* **234**, 111642 (2021).
- ²³G. Staffelbach, L. Y. M. Gicquel, G. Boudier, and T. Poinso, "Large Eddy simulation of self excited azimuthal modes in annular combustors," *Proc. Combust. Inst.* **32**, 2909–2916 (2009).
- ²⁴B. Franzelli, E. Riber, L. Y. Gicquel, and T. Poinso, "Large Eddy simulation of combustion instabilities in a lean partially premixed swirled flame," *Combust. Flame* **159**, 621–637 (2012).
- ²⁵S. Hermeth, G. Staffelbach, L. Y. M. Gicquel, and T. Poinso, "LES evaluation of the effects of equivalence ratio fluctuations on the dynamic flame response in a real gas turbine combustion chamber," *Proc. Combust. Inst.* **34**, 3165–3173 (2013).
- ²⁶C. Kraus, L. Selle, and T. Poinso, "Coupling heat transfer and large eddy simulation for combustion instability prediction in a swirl burner," *Combust. Flame* **191**, 239–251 (2018).
- ²⁷A. Ghani and T. Poinso, "Flame quenching at walls: A source of sound generation," *Flow, Turbul. Combust.* **99**, 173–184 (2017).
- ²⁸B. Rochette, F. Collin-Bastiani, L. Gicquel, O. Vermorel, D. Veynante, and T. Poinso, "Influence of chemical schemes, numerical method and dynamic turbulent combustion modeling on LES of premixed turbulent flames," *Combust. Flame* **191**, 417–430 (2018).
- ²⁹Y. Dagan, N. W. Chakroun, S. J. Shanbhogue, and A. F. Ghoniem, "Role of intermediate temperature kinetics and radical transport in the prediction of leading edge structure of turbulent lean premixed flames," *Combust. Flame* **207**, 368–378 (2019).
- ³⁰D. Brouzet, M. Talei, M. Brear, and B. Cuenot, "The impact of chemical modeling on turbulent premixed flame acoustics," *J. Fluid Mech.* **915**, A3 (2021).
- ³¹R. M. Solgi, see <https://pypi.org/project/geneticalgorithm/> for "Geneticalgorithm 1.0.2" (2020).
- ³²University of California at San Diego, see <http://ucsd.edu> for "Chemical-Kinetic Mechanisms for Combustion Applications" (2016).
- ³³D. G. Goodwin, H. K. Moffat, and R. L. Speth, *Cantera: An object-oriented software toolkit for chemical kinetics, thermodynamics, and transport processes*, version 2.4.0, Caltech, Pasadena, CA, 2009.
- ³⁴A. Kazakov and M. Frenklach, *Reduced Reaction Sets Based on GRI-Mech 1.2* (University of California at Berkeley, Berkeley, CA, 1994).
- ³⁵A. Abou-Taouk, S. Sadasivuni, D. Lörstard, and L.-E. Eriksson, "Evaluation of global mechanisms for LES analysis of SGT-100 DLE combustion system," in *Volume 1B: Combustion, Fuels and Emissions* (American Society of Mechanical Engineers, San Antonio, Texas, 2013), p. V01BT04A036.
- ³⁶L. Berger, A. Attili, and H. Pitsch, "Synergistic interactions of thermodynamic instabilities and turbulence in lean hydrogen flames," *Combust. Flame* **244**, 112254 (2022).
- ³⁷E. Åsøy, J. G. Aguilar, M. R. Bothien, N. A. Worth, and J. R. Dawson, "Acoustic-convective interference in transfer functions of methane/hydrogen and pure hydrogen flames," *J. Eng. Gas Turbines Power* **143**, 121017 (2021).

- ³⁸SID Software, *Simcenter STAR-CCM+* (Siemens, 2021).
- ³⁹F. Nicoud and F. Ducros, "Subgrid-scale stress modelling based on the square of the velocity gradient tensor," *Flow Turbul. Combust.* **62**, 183–200 (1999).
- ⁴⁰N. W. Bressloff, "A parallel pressure implicit splitting of operators algorithm applied to flows at all speeds," *Int. J. Numer. Methods Fluids* **36**, 497–518 (2001).
- ⁴¹F. Charlette, C. Meneveau, and D. Veynante, "A power-law flame wrinkling model for LES of premixed turbulent combustion Part I: Non-dynamic formulation and initial tests," *Combust. Flame* **131**, 159–180 (2002).
- ⁴²M. S. Darwish and F. H. Moukalled, "Normalized variable and space formulation methodology for high-resolution schemes," *Numer. Heat Transfer* **26**, 79–96 (1994).
- ⁴³M. Karalus, D. Brandt, A. Brown, and V. Lister, "A multi-timescale approach for the prediction of temperatures in a gas turbine combustor liner," in *Turbo Expo: Power for Land, Sea, and Air* (Virtual, Online, 2020), Vol. 84164, p. 11.
- ⁴⁴S. Föller and W. Polifke, "Advances in identification techniques for aero-acoustic scattering coefficients from large eddy simulation," in *18th International Congress on Sound and Vibration* (Rio de Janeiro, Brazil, 2011), Vol. 4, pp. 3122–3129.
- ⁴⁵T. Lieuwen, "Modeling premixed combustion—Acoustic wave interactions: A review," *J. Propul. Power* **19**, 765–781 (2003).
- ⁴⁶S. Ducruix, T. Schuller, D. Durox, and B. Candel, "Combustion dynamics and instabilities: Elementary coupling and driving mechanisms," *J. Propul. Power* **19**, 722–734 (2003).
- ⁴⁷W. Polifke, "Modeling and analysis of premixed flame dynamics by means of distributed time delays," *Prog. Energy Combust. Sci.* **79**, 100845 (2020).
- ⁴⁸X. Wen, T. Zirwes, A. Scholtissek, H. Böttler, F. Zhang, H. Bockhorn, and C. Hasse, "Flame structure analysis and composition space modeling of thermo-diffusively unstable premixed hydrogen flames—Part I: Atmospheric pressure," *Combust. Flame* **238**, 111815 (2022).